Measurements of the Double Helicity Asymmetry in Pion Production in Proton Collisions at $\sqrt{s} = 200$ GeV and the Resulting Constraints on the Polarized Gluon Distribution in the Proton

A Dissertation Presented

by

Kieran Peter Boyle

to

The Graduate School

in Partial Fulfillment of the Requirements

for the Degree of

Doctor of Philosophy

in

Physics

Stony Brook University

May 2008

Stony Brook University

The Graduate School

Kieran Peter Boyle

We, the dissertation committee for the above candidate for the Doctor of Philosophy degree, hereby recommend acceptance of this dissertation.

Abhay Deshpande – Dissertation Advisor
Professor, Department of Physics and Astronomy

Axel Drees – Chairperson of Defense
Professor, Department of Physics and Astronomy

George Sterman
Professor, Department of Physics and Astronomy

Alexander Bazilevsky
Associate Physicist
Brookhaven National Laboratory

This dissertation is accepted by the Graduate School.

Lawrence Martin
Dean of the Graduate School

Abstract of the Dissertation

Measurements of the Double Helicity Asymmetry in Pion Production in Proton Collisions at $\sqrt{s} = 200$ GeV and the Resulting Constraints on the Polarized Gluon Distribution in the Proton

by

Kieran Peter Boyle

Doctor of Philosophy

in

Physics

Stony Brook University

2008

Since the realization that the proton is a composite particle, much work has gone into understanding its structure and how the quarks and gluons that make up this structure lead to the proton's basic properties, such as charge, momentum, spin and magnetic moment. While much has been learned about some of these properties from several decades of experimental studies, knowledge of the spin structure has lagged behind, primarily due to the subtlety required for spin dependent measurements. The first results from polarized deep inelastic scattering (pDIS) experiments in the late 1980s and early 1990s revealed that contrary to the prevailing wisdom, quarks did not carry a significant fraction of the proton's spin. However, those experiments, which effectively probed the quark spins through their interactions via virtual photons, could not probe the charge-neutral gluons, and hence could only weakly

constrain the gluon's contribution to the nucleon's spin. Polarized proton-proton collisions at high center of mass energy employing the Relativistic Heavy Ion Collider (RHIC) at Brookhaven National Laboratory (BNL) provide a unique and direct way to access the gluon spin (ΔG) through measurements of the double helicity asymmetry A_{LL}.

In the present work, results for the double helicity asymmetry in neutral pion (π^0) production in polarized proton collisions from the 2005 and 2006 RHIC runs (Run5 and Run6, respectively) measured with the PHENIX detector are presented. Pions are abundantly produced in proton-proton collisions and so are a good candidate for a high statistics analysis. The PHENIX Electromagnetic Calorimeter has good energy resolution and high granularity which, when used with a high energy photon trigger, yield a substantial π^0 sample over a wide range in transverse momentum (p_T). The 2005 and 2006 polarized proton runs (at a center of mass energy of 200 GeV) saw large increases in luminosity (L) and polarization (P) compared to previous runs, resulting in a high figure of merit (P^4L). π^0 A_{LL} from RHIC Run5 and Run6 are precise enough to be sensitive to ΔG. A measurement of charged pion A_{LL} from RHIC Run5 is also presented, and examined as a complimentary analysis which can help determine the sign of ΔG. These are the first results from RHIC and BNL addressing the very important question of the role played by the gluons in determining the proton's spin.

Finally, the current understanding of the proton spin structure is examined considering this new data. A simple method for estimating the gluon spin structure in the proton is described, and indicates that the current data do offer a significant constraint. Even when using this method to consider theoretical uncertainties, which are large, the significance of the current data remains.

Contents

List of Figures xi

List of Tables xv

Acknowledgements xvii

1 Introduction: Proton Structure 1

1.1 Quarks and the Strong Force . . . 1
1.2 Experimental Techniques: Studying the Structure of Hadrons . 3
1.2.1 Deeply Inelastic Scattering . . . 3
1.3 The Parton Model . . . 5
1.3.1 Factorization and Universality . . . 6
1.4 Experimental Techniques, Continued . . . 7
1.4.1 Semi-Inclusive Deeply Inelastic Scattering . . . 8
1.4.2 Hadron-Hadron Scattering . . . 9
1.5 Proton Structure . . . 10
1.5.1 Results from Unpolarized Scattering . . . 10
1.5.2 Charge and Momentum . . . 15
1.6 Spin Structure . . . 16
1.6.1 Naive (and Slightly Less Naive) Quark Model . . . 18
1.6.2 EMC result . . . 19
1.6.3 A Broader Picture on Nucleon Spin: Complete Spin Sum Rule . . . 21
1.6.4 Modern Results for g1 . . . 21
1.6.5 Extracted Polarized Distribution Functions . . . 22
1.7 Accessing the Polarized Gluon Distribution through $p + p$ Collisions . . . 22
1.8 Measuring the Double Helicity Asymmetry . . . 24
1.9 Neutral and Charged Pion A_{LL} . . . 24
1.10 . . . 25

2 Polarized Protons at RHIC **27**
2.1 RHIC . . . 27
2.2 Siberian Snakes . . . 27
2.3 Source and Boosters . . . 29
2.4 RHIC Accelerator . . . 29
2.5 RHIC Polarimeters . . . 31
2.6 Spin Rotators . . . 32
2.7 Spin Pattern . . . 33
2.8 RHIC Performance . . . 34

3 PHENIX **37**
3.1 Luminosity Detectors . . . 39
3.1.1 Beam Beam Counters . . . 39
3.1.2 Zero Degree Calorimeters and Shower Maximum Detector 40
3.2 Electromagnetic Calorimetry . . . 42
3.3 Triggering . . . 42
3.3.1 BBC Level 1 Triggers . . . 43
3.3.2 ZDC Level 1 Triggers . . . 43
3.3.3 EMCal RICH Trigger . . . 43
3.3.4 GL1p Boards . . . 45
3.4 Tracking . . . 46
3.4.1 Magnets . . . 46
3.4.2 Drift Chamber . . . 47
3.4.3 Pad Chambers . . . 48
3.4.4 Track Determination and Momentum Reconstruction . . . 49
3.5 Particle ID . . . 50
3.5.1 Ring-Imaging Čerenkov Detector . . . 51

4 Measurement Requirements **52**
4.1 Luminosity Normalization: Relative Luminosity . . . 52
4.1.1 Run5 and Run6 Relative Luminosity . . . 56
4.1.2 Uncertainty in R and Propagation to A_{LL} . . . 57
4.1.3 Fill By Fill Results . . . 63
4.1.4 Future prospects . . . 63
4.2 Polarimetry (Magnitude) . . . 65
4.2.1 Polarized Hydrogen Jet Polarimeter . . . 66
4.2.2 Proton Carbon Polarimeter . . . 67
4.2.3 Polarization Normalization . . . 68
4.3 Local Polarimetry (Direction) . . . 69

4.3.1 Physics . . . 70
4.3.2 ZDC Measurement . . . 71
4.3.3 Analysis Method . . . 71
4.3.4 Results . . . 73
4.3.5 Implication for Bunch Pattern . . . 75

5 Event Selection, Particle Identification and Background Reduction 76
5.1 Event Selection . . . 76
5.1.1 Trigger Requirement . . . 77
5.1.2 BBC z-Vertex Cut . . . 78
5.2 ERT Trigger Requirement . . . 78
5.3 Neutral Pion Decay Kinematics . . . 79
5.4 Photon Identification . . . 80
5.5 Rejection of Clusters Due to Electronic Noise . . . 80
5.5.1 Warnmap . . . 80
5.6 Neutral Pion Mass Spectrum . . . 81
5.7 Neutral Pion Background Estimates . . . 81
5.8 Neutral Pion: Photon Cuts (Efficiencies, Studies) . . . 85
5.8.1 Shower Shape . . . 85
5.8.2 Time of Flight . . . 86
5.8.3 Charge Veto . . . 87
5.9 Neutral Pion Final Statistics . . . 88
5.10 Charged Pions: p_T Spectrum . . . 89
5.11 Charged Pions: Track Selection . . . 90
5.11.1 Track Quality . . . 90
5.11.2 RICH Requirement . . . 90
5.12 Charged Pions: Sources of Background . . . 91
5.12.1 Electron Background . . . 91
5.12.2 Hadronic Background . . . 93
5.12.3 Future Background Reduction . . . 94
5.13 Charged Pions: Cuts (Efficiencies, Studies) . . . 94
5.13.1 Matching Cuts . . . 94
5.13.2 Drift Chamber Acceptance Cut . . . 95
5.13.3 (Electromagnetic) Shower Shape . . . 96
5.13.4 $E/|\boldsymbol{p}|$ Cut . . . 97
5.13.5 p_T Dependent Energy Cut . . . 101
5.14 Charged Pions Background Estimates . . . 102
5.15 Charged Pions Final Statistics . . . 103

6 Double Helicity Asymmetry Measurement **104**
6.1 Neutral Pion . . . 104
6.1.1 Background Subtraction Method . . . 104
6.1.2 Odd and Even Requirement . . . 106
6.1.3 Statistical Uncertainty on A_{LL} . . . 106
6.1.4 Fill-by-fill A_{LL} Calculation . . . 106
6.1.5 Minbias Analysis . . . 108
6.1.6 Average p_T in p_T Bins . . . 109
6.1.7 Results . . . 109
6.2 Charged Pions . . . 109
6.2.1 Statistical Uncertainty on A_{LL} . . . 109
6.2.2 Fill-by-fill A_{LL} Calculation . . . 113
6.2.3 Background Discussion . . . 113
6.2.4 Results . . . 114

7 Systematic Uncertainties and Cross Checks **116**
7.1 Asymmetry in Background Sidebands . . . 116
7.2 Comparison of Different Detector and Trigger Results . . . 117
7.3 Neutral Pion A_{LL} for Different Signal Mass Ranges . . . 117
7.4 Longitudinal Single Spin Asymmetries . . . 120
7.4.1 Neutral Pion . . . 120
7.4.2 Charged Pions . . . 122
7.5 Parity Violating Double Helicity Asymmetries . . . 126
7.6 Transverse Double Spin Asymmetries (A_{TT}) . . . 126
7.6.1 Neutral Pion Results . . . 127
7.7 Bunch Shuffling . . . 128
7.7.1 Neutral Pion . . . 130
7.7.2 Charged Pions . . . 132
7.8 Systematic Uncertainty from Beam Polarization . . . 135
7.9 Summary of Systematic Uncertainties . . . 135
7.10 Final Combined Results for Neutral Pion A_{LL} from Run5 and Run6 . . . 136

8 Interpretation of A_{LL} Results **139**
8.1 Cross Section . . . 139
8.1.1 Comparison with Theory . . . 139
8.1.2 Charged Pions . . . 141

8.2 Comparison of Double Helicity Results with Expectations from Different Polarized DIS Fits . . . 142
8.3 Earlier Calculations of Spin Dependent PDFs . . . 142
8.4 Implications of A_{LL} for the Gluon Spin Distribution . . . 144
8.5 Effect of Experimental Systematic Uncertainties . . . 149
8.6 Effect of Theoretical Uncertainties . . . 151
8.6.1 Theoretical Scale Uncertainty . . . 151
8.6.2 Sensitivity to the Gluon and Quark Spin Distribution . . . 152
8.6.3 Sensitivity to Functional Form . . . 153
8.6.4 Uncertainty from α_s . . . 156
8.6.5 Uncertainty from the Unmeasured x Region . . . 156
8.6.6 Constraints on Positivity . . . 157
8.7 Extracting ΔG . . . 158
8.8 Recent Theoretical Studies . . . 159

9 Conclusions and Prospects **163**
9.1 Prospects for Constraining ΔG . . . 164

A Useful Mathematical Calculations **166**
A.1 k Factor Derivation . . . 166
A.2 Relations between Longitudinal Spin Parity Violating Asymmetries . . . 168
A.3 Relation between Asymmetries in FBF and Bunch Fitting Methods . . . 169

B Data Tables **171**

C Functional Forms Used in Fits of Polarized PDFs **180**
C.1 Common Assumptions . . . 180
C.2 GRSV . . . 181
C.3 BB . . . 182
C.4 DNS . . . 182
C.5 LSS . . . 183
C.6 GS-A,B,C . . . 184
C.7 Summary Table . . . 185

Bibliography **186**

List of Figures

1.1 Diagram of DIS 3
1.2 Diagram of DIS, SIDIS and hadron-hadron scattering in parton model discription 5
1.3 F_2^p vs. Q^2 11
1.4 MRST PDFs vs. x 12
1.5 CTEQ PDFs vs. x 13
1.6 Uncertainty in CTEQ PDFs vs. x 14
1.7 g_1^p vs. Q^2 17
1.8 Comparison of early SLAC and EMC results for A_1^p vs. x . . . 20
1.9 Comparison of early SLAC and EMC results for $\int_{x_m}^1 dx g_1^p(x)$ vs. x_m 20
1.10 $\Delta\Sigma$ and ΔG vs. x from various polarized fits 22
1.11 Relative fraction of produced pions from different subprocesses vs. p_T 25
1.12 A_{LL} expectation vs. p_T for three pion species 26

2.1 Diagram of RHIC 28
2.2 Effect of two full Siberian snakes in each RHIC ring 30
2.3 Diagram of pC polarimeter 32
2.4 Diagram of polarized HJet polarimeter 33
2.5 Run5 spin patterns 35
2.6 Run6 spin patterns 35

3.1 PHENIX detector diagram 38
3.2 Side view of ZDC 41
3.3 Diagram of ZDC location with respect to D_X magnets 41
3.4 Diagram of ERT trigger explaining overlapping trigger tile arrangement in the 4×4 tower triggers used for both π^0 and charged pion analyses. 44
3.5 PHENIX magnetic field set up in Run5 and Run6. 47
3.6 DC wire layout 48
3.7 Definition of α for charged tracks 50

4.1 Backgrounds in BBCs and ZDCs 54
4.2 Live trigger counts for BBCs and ZDCs 55
4.3 Relative Luminosity vs. fill number separately for odd and even crossings 56
4.4 Relative Luminosity vs. fill number for all crossings 57
4.5 Ratio of ZDCLL1 triggers to BBCLL1 triggers vs. crossing number 59
4.6 χ^2/NDF distributions for fits in Relative Luminosity study . . 59
4.7 Correlation plots of r to bunch crossing width 60
4.8 r vs. rate 62
4.9 $A_{LL}|_{ZDC/BBC}$ vs. fillnumber for different corrections 64
4.10 $A_{LL}|_{ZDC/BBC}$ vs. fill number for width corrected ratio 65
4.11 HJet target and beam asymmetries vs. recoil energy 67
4.12 Asymmetry in elastically scattered carbon atoms vs. ϕ 68
4.13 Final beam polarization vs. fill number 69
4.14 Diagram indicating which asymmetries are parity violating . . 70
4.15 Expected asymmetries vs. ϕ depending on beam polarization orientation 72
4.16 Neutron asymmetry results vs. fill number 74

5.1 Minbias π^0 efficiency vs. p_T 77
5.2 Example warnmap for π^0 analysis 82
5.3 Two photon invariant mass spectrum from PbGl 83
5.4 Two photon invariant mass spectrum from PbSc 84
5.5 Time of Flight distribution 86
5.6 Percentage background under π^0 peak vs. Time of Flight . . . 87
5.7 θ_{cv} distribution 88
5.8 Charged tracks p_T spectrum 89
5.9 Charged track p_T spectrum for different cuts in the analysis . 91
5.10 Diagram of reasons for incorrectly reconstructed p_T 93
5.11 Distributions of track matching variables 95
5.12 DC z distribution 96
5.13 Electromagnetic probability distribution 97
5.14 Distribution of electromagnetic (EM) probability vs. p_T 98
5.15 E/p distributions 99
5.16 E/p distribution for three p_T bins used in analysis 100
5.17 Energy vs. p_T distribution 101
5.18 p_T spectrum for different energy cuts 102
5.19 Final p_T spectra with fits for estimating background 103

6.1 Regions in two photon invariant mass spectrum used in $A_{LL}^{\pi^0}$ analysis 105

6.2 Example of π^0 A_{LL} vs. fill number from ERT data 107
6.3 π^0 A_{LL} vs. fill number from minbias data 110
6.4 $A_{LL}^{\pi^0}$ vs. p_T separately for even and odd crossings 111
6.5 $A_{LL}^{\pi^0}$ vs. p_T for ERT and minbias data 112
6.6 $A_{LL}^{\pi^0}$ vs. p_T for Run5 and Run6 112
6.7 Charged pion A_{LL} vs. fill number 114
6.8 Charged pion A_{LL} vs. p_T 115

7.1 Comparison of A_{LL} from π^0 background sidebands 117
7.2 $A_{LL}^{\pi^0}$ by EMCal type for ERT data in Run5 118
7.3 $A_{LL}^{\pi^0}$ by EMCal type for ERT data in Run6 119
7.4 $A_{LL}^{\pi^0}$ by EMCal type for minbias data in Run5 119
7.5 $A_{LL}^{\pi^0}$ for different π^0 mass widths 121
7.6 False parity violation due to ERT circuit 122
7.7 No false parity violation after separating into even and odd crossings 123
7.8 π^0 A_L for different trigger and EMCal types 123
7.9 π^0 A_L vs. p_T 124
7.10 Charged Pion A_L vs. p_T 125
7.11 Theoretical expectations for π^0 A_{TT} 128
7.12 π^0 A_{TT} vs. p_T 129
7.13 Example π^0 bunch shuffling results 131
7.14 π^0 bunch shuffling from incorrectly scaled minbias data 132
7.15 π^0 bunch shuffling from correctly scaled minbias data 133
7.16 Charged pion bunch shuffling results 134
7.17 Comparison of Run5, Run6 and Run5+6 $A_{LL}^{\pi^0}$ vs. p_T 137

8.1 π^0 cross section vs. p_T 140
8.2 $A_{LL}^{\pi^0}$ vs. p_T for Run5+6 with theoretical expectations 143
8.3 $A_{LL}^{\pi^0}$ vs. p_T compared with different expectations in the GRSV framework 145
8.4 Charged pion A_{LL} vs. p_T compared with different expectations in the GRSV framework 146
8.5 $x\Delta g(x)$ vs. x for different assumptions in the GRSV framework and the resulting A_{LL} expectations 147
8.6 χ^2 vs. $\Delta G_{\mathrm{GRSV}}^{x\in[0.02,0.3]}$ for Run5, Run6 and Run5+6 $A_{LL}^{\pi^0}$ results . 148
8.7 x_{gluon} distributions in π^0 production 148
8.8 χ^2 vs. $\Delta G_{\mathrm{GRSV}}^{x\in[0.02,0.3]}$ taking into account polarization uncertainty 150
8.9 χ^2 vs. $\Delta G_{\mathrm{GRSV}}^{x\in[0.02,0.3]}$ taking into account Relative Luminosity uncertainty 150
8.10 $A_{LL}^{\pi^0}$ vs. p_T expectations for different choices of theoretical scales 152

8.11 χ^2 vs. $\Delta G_{\mathrm{GRSV}}^{x\in[0.02,0.3]}$ taking into account theoretical scale uncertainty 153
8.12 χ^2 vs. $\Delta G_{\mathrm{GRSV}}^{x\in[0.02,0.3]}$ for different approaches to varying ΔG . . 154
8.13 χ^2 vs. $\Delta G_{\mathrm{GRSV}}^{x\in[0.02,0.3]}$ for different models 155
8.14 χ^2 vs. $\Delta G_{\mathrm{GRSV}}^{x\in[0.02,0.3]}$ after varying the location of a zero crossing 156
8.15 χ^2 profile for ΔG in DNS framework 158
8.16 Gluon spin distribution vs. x from AAC 160
8.17 Polarized PDFs from DSSV fit 161
8.18 χ^2 profile for ΔG from DSSV 161

List of Tables

2.1 RHIC performance statistics 36

3.1 Acceptance coverage of selected PHENIX detectors 39

4.1 Final luminosity weighted polarization values 69
4.2 Fraction of beam polarization in transverse and longitudinal directions 75

6.1 π^0 A_{LL} from Run5 and Run6 113
6.2 Charged pion A_{LL} vs. p_T 114

7.1 Summary of non-negligible systematic uncertainties in the A_{LL} measurements presented. Uncertainties from bunch (b.) shuffling for all results with $p_T > 1$ GeV/c were found to be negligible. 136
7.2 Results for combined Run5 and Run6 $A_{LL}^{\pi^0}$ 138

B.1 Run5 Warnmap statistics 171
B.2 Run6 Warnmap statistics 172
B.3 Run5 shower shape cut efficiency statistics 172
B.4 Run6 shower shape cut efficiency statistics 173
B.5 Run5 ToF cut efficiency statistics 173
B.6 Run6 ToF cut efficiency statistics 174
B.7 Run5 charge veto cut efficiency statistics 174
B.8 Run6 charge veto cut efficiency statistics 175
B.9 Run5 π^0 statistics 175
B.10 Run6 π^0 statistics 176
B.11 Charged pion statistics 176
B.12 $k^2_{enhance}$ for N^{π^0+BG} (N^{BG}) from Run5. 177
B.13 $k^2_{enhance}$ for N^{π^0+BG} (N^{BG}) from Run6. 177
B.14 Run5 π^0 A_L results 178
B.15 Run6 π^0 A_L results 178
B.16 Run5 charged pion A_L results 179
B.17 π^0 A_{TT} results 179

C.1 Information about constraints used in polarized fits 185

Acknowledgements

First, I would like to thank my advisor, Abhay Deshpande, for his help and encouragement over the past four and a half years. He constantly reminded me that graduate school is about learning, and so urged me to work on an array of projects throughout my time in PHENIX. Discussions over lunch, or dinner before a Spin PWG meeting, often forced me to consider the wider physics beyond a single thesis topic. Through probing questions, he challenged me to think beyond the current problems, and consider the deeper physics implication. The scope of this work would be much shallower if not for this support.

I would also like to thank the larger Stony Brook group: Professors Barbara Jacak, Axel Drees and Tom Hemmick as well as my fellow students who helped me start analyzing the multitude of different data sets in PHENIX, especially Matt Nguyen, Rob Bennett, and Sarah Campbell. Thanks also to the spin group post doc., Swadhin Taneja, for numerous hours of discussion on an array of topics. The final interpretation chapter of this thesis was significantly improved through these many discussions.

There are a number of people at BNL who helped me advance both my analysis and my working knowledge of physics including Gerry Bunce, Rachid Nouicer, Astrid Morreale, Christine Aidala, and many others. I specifically want to express my gratitude to all those who process and calibrate the huge amounts of data taken by PHENIX, an often thankless job without which none of these analyses would be possible.

I thank Sasha Bazilevsky, who always had the time to answer questions, and the knowledge to explain the answer thoroughly. He was willing to spend numerous hours trying to sort out differences in our π^0 yields, almost always due to a bug in my code. His guidance in my analysis, with his great grasp of seemingly all experimental and statistical techniques, were a considerable help for any problem I ran into. My appreciations also to Frank Ellinghaus for always being willing to answer my questions. It was great luck that he ended up sharing the Stony Brook office at BNL, as I was able to learn quite a lot from his knowledge both of experimental techniques and the larger field as a

whole.

This work was funded through the Research Foundation at Stony Brook with support from RIKEN through multiple Spinfests at BNL and in Wako, Japan. The impact of this work would have been much reduced if not for the support of RHIC by Jim Simons and associates through the funding of Run6.

I would like to thank my family for their strong support. I would not be where I am today if it were not for the the nurturing environment my parents created, or the willingness of my siblings to teach their little brother whatever they had learned in school that day.

Last, but certainly in no way least, I am grateful to my wife Amy for all her support over the last six years. From helping proofread my thesis (except the equations) to keeping our lives in one piece whenever a deadline approached, she was always there. I owe her greatly for all of this, and look forward to having the rest of our lives to repay her.

Chapter 1

Introduction: Proton Structure

Since measurements of the proton's magnetic moment revealed that the proton was not a point-like particle, the substructure of the proton has been studied intensely. By understanding the structure and composition of one of the basic particles that make up much of what we interact with daily, we have gained insight into the fundamental forces that govern our universe.

1.1 Quarks and the Strong Force

In 1964, Gell-Mann and Zweig independently proposed that all hadrons (which include baryons, such as the proton and neutron, and mesons, such as the pions) were composed of three types of *quarks* (q), defined as *up* (u), *down* (d) and *strange* (s). When combined with their antiparticles, all the hadrons seen at that time could be described as quark-anti-quark pairs ($q\bar{q}$), in the case of mesons, or a set of three quarks or anti-quarks (qqq or $\bar{q}\bar{q}\bar{q}$) for baryons.[1]

For quarks to remain bound in hadrons, or for protons and neutrons to remain bound in nuclei, a new force other than electromagnetism would be required.[2] Such a force would have to be stronger than electromagnetism on the scale of a nucleus (roughly several fm), and so was creatively named the strong force. The intermediary particle for the strong force is called a *gluon*. Gluons are massless, chargeless, spin 1 particles which carry the strong force equivalent of electric charge, called *color*. *Quantum Chromodynamics* (QCD), the theory of gluon and quark interactions, has been described in many introductory texts, such as [1–3]. For a more developed field theoretic

[1] Heavier particles containing the remaining 3 quarks in the standard model (SM) had not been seen at that time, and so only three quarks were required.

[2] Δ^{++}, which is composed of three up quarks, each with a charge of $+\frac{2}{3}$ clearly cannot be bound electromagnetism.

approach, see [4, 5].

While much of the interactions between quarks have analogs in the quantum theory of electromagnetism (called Quantum Electrodynamics or QED), there are a few very important differences. First, unlike in the case of the photon (the force carrier in QED), the gluon carries the color charge, and so can couple to other gluons directly. Second, and more significant, the coupling strength in QCD, α_s, becomes smaller as the distance of interaction becomes smaller. This has two direct implications: confinement and asymptotic freedom. Confinement implies that quarks and gluons will always be found in hadrons, as the field around a lone free quark (i.e. at large distance) is enough to create other quark-antiquark pairs from the vacuum. This is essentially what occurs in the process of fragmentation, which will be discussed later. In the other extreme, quarks become asymptotically free as the distance from a quark goes to zero.

This second point has a large impact on the ability of theory to make predictions. Quantum Mechanics requires that for a given starting and ending state, all possible intermediary states be considered, scaled by their probability. In any Quantum Field Theory (including QED and QCD), each intermediate state with an additional coupling (or vertex) carries an additional factor of the coupling constant in the calculation. If this coupling constant is sufficiently small, then the calculation of all possible intermediate states can be truncated at some order of the coupling constant, so that the required accuracy in the calculation is achieved. Such a calculation is called *perturbative*. In QED, perturbation theory is very successful, as the coupling constant, α, is small at large distances: $\alpha = 1/137$ on the scale of the Hydrogen atom.[3] However, in QCD, since α_s increases with distance, at large distances (on the order of the hadron's size), all extra couplings carry essentially the same weight. This implies that a description of the proton as 3 quarks, called *valance* quarks, is nearly as probable as a description with three valance quarks, many gluons, and also many quark-anti-quark pairs, called *sea* quarks. Therefore, to calculate anything, numerous possible intermediate states must be calculated. Currently, this is not possible, and so QCD predictions can only be made for very short distance reactions, where α_s is small, and again the calculation is perturbative. This theoretical frame work is called perturbative QCD (pQCD), and is currently the only type of QCD that can give firm predictions.[4] Therefore, we cannot use QCD to predict the structure of the hadrons.

So the question arises: Assuming that a proton is made up of quarks and

[3] In the case of QED, the scale at which this is not the case is extremely tiny, many times smaller than the Plank scale.

[4] Lattice QCD, which attempts to calculate a large number of the possible arrangements, and so approximate the composition of hadrons, may well allow us to move beyond pQCD.

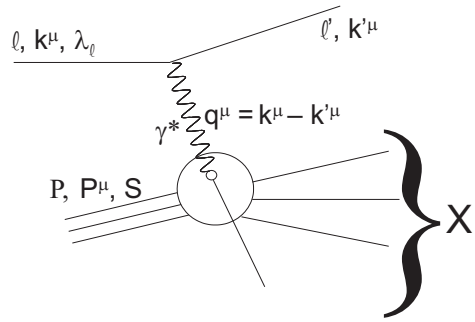

Figure 1.1: Diagram of Deeply Inelastic Scattering, in which a virtual photon, $\gamma*$, from a scattered lepton, ℓ, resolves substructure within the proton, P. The variables shown are discussed in the text.

gluons, how can we understand the structure of quarks and gluons in the proton? For this, we turn to experiment.

1.2 Experimental Techniques: Studying the Structure of Hadrons

The most straight forward way of understanding the proton structure is to understand how the basic properties of the proton such as charge, momentum, spin, etc., arise from the quarks and gluons that make it up. In order to achieve this goal, several experimental techniques are employed.

1.2.1 Deeply Inelastic Scattering

Deeply Inelastic Scattering (DIS) has been described in numerous texts, for example [2, 3]. Here, only a brief discussion of DIS will be given to introduce the relevant variables and concepts. Figure 1.1 shows the basic concept of DIS, in which a lepton is scattered off a nucleon (either a proton or neutron) and by measuring the change in the momentum of the lepton and the angle of scatter, information about the substructure can be determined. In general, this requires a measurement of the cross section $\sigma^{\ell+N\to\ell'+X}$ where ℓ (ℓ') denotes the lepton before (after) the collision, N denotes the nucleon, and X denotes the unmeasured final state.

The cross section for this process can be written as

$$d\sigma_{\ell N}^{DIS} = \frac{4\alpha^2}{s}\frac{d^3\boldsymbol{k}'}{2|\boldsymbol{k}'|}\frac{1}{Q^4}L^{\mu\nu}(k,q,\lambda)W_{\mu\nu}(P,q,S) \tag{1.1}$$

where α is the electromagnetic coupling constant, k^μ (k'^μ) is the incoming (outgoing) lepton 4-momentum, λ is the incoming lepton helicity, and $q^\mu = k^\mu - k'^\mu$ is the 4-momentum transferred to the nucleon. We define the variable $Q^2 \equiv -q^2$ as the virtuality of the photon. $L^{\mu\nu}$ is the leptonic tensor that describes the coupling of the lepton to the virtual photon and is know from QED. $W_{\mu\nu}(P, q, S)$ is the hadronic tensor which describes the coupling of the photon to the hadron, and depends on the 4-momentum of the nucleon, P, the 4-momentum transfer q, and the spin of the nucleon, S. Note that the final state momenta of the particles in X have been integrated out, and all possible final states X have been summed over.

In general, we define the Bjorken variable x such that

$$x \equiv \frac{Q^2}{2P \cdot q}. \tag{1.2}$$

Figure 1.1 can be redrawn in terms of the struck quark and the remainder of the proton, as can be seen in Fig. 1.2a. In this picture, x has the interpretation (at leading order in α_s) as the fraction of the total proton momentum, P, carried by the quark. Here, it is assumed that the quark has momentum parallel to the proton.

The hadronic tensor, $W_{\mu\nu}$, can be rewritten in terms of several structure functions as

$$\begin{aligned} W_{\mu\nu} &= -\left(g_{\mu\nu} - \frac{q_\mu q_\nu}{q^2}\right) F_1(x, Q^2) && (1.3) \\ &+ \frac{1}{P \cdot q}\left(P_\mu - q_\mu \frac{P \cdot q}{q^2}\right)\left(P_\nu - q_\nu \frac{P \cdot q}{q^2}\right) F_2(x, Q^2) && (1.4) \\ &+ \imath M \varepsilon^{\mu\nu\rho\sigma} q_\rho \left(\frac{S_\sigma}{P \cdot q} g_1(x, Q^2) + \frac{S_\sigma (P \cdot q) - P_\sigma (S \cdot q)}{(P \cdot q)^2} g_2(x, Q^2)\right) \end{aligned}$$

where $g_{\mu\nu}$ is the standard Minkowski metric tensor, M is the mass of the nucleon, $F_1(x, Q^2)$ and $F_2(x, Q^2)$ ($g_1(x, Q^2)$ and $g_2(x, Q^2)$) are the spin independent (dependent) structure functions to be determined from experiment. A fifth structure function, which arises from W boson exchange, for example in neutrino scattering, has been neglected. As $g_1(x, Q^2)$ and $g_2(x, Q^2)$ depend on the spin of the probed nucleon, these terms vanish if the initial spin states are summed over. In order to understand how these structure functions relate to the quarks and gluons, we turn to a second, complementary model for interpreting hadron structure.

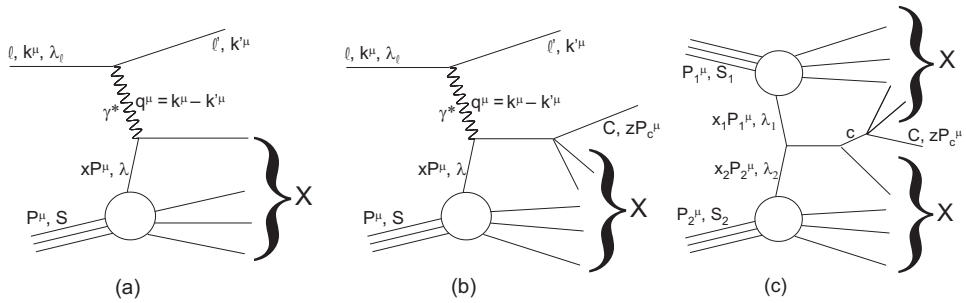

Figure 1.2: Diagrams of three experimental techniques: (a) Deeply Inelastic scattering, (b) Semi-Inclusive Deeply Inelastic Scattering, and (c) hadron-hadron scattering. These are used to access information on the structure of the proton. The variables shown are discussed in the text.

1.3 The Parton Model

Around the same time as Gell-Mann and Zweig were proposing the quark model, Feynman proposed the parton model of the nucleon, in which the nucleon is composed of particles, called partons, which interact with the virtual photon in DIS. Later, the partons were identified with the quarks and gluons in the nucleon.

The parton model states that the DIS cross section, $\sigma_{\ell N}^{DIS}$, can be written as the cross section, $\hat{\sigma}_{\ell f}^{\mathrm{el}}$, of an elastic scattering of a lepton off a parton, f, convoluted with a parton distribution function (PDF), $f(x, \mu_F^2)$:

$$\sigma_{\ell N}^{DIS} = \sum_{f=q,\bar{q},g} \int_0^1 dx\, \hat{\sigma}_{\ell f}^{\mathrm{el}}(xP, q, \mu_F^2, \mu_R^2) f(x, \mu_F^2)\,. \tag{1.5}$$

The PDF gives the probability of finding a parton with momentum fraction x (See Fig. 1.2a) when at a certain μ_F^2. μ_F^2 is defined as the factorization scale, which is a theoretical construct of order Q^2, and is a cutoff between hard and soft processes. The reason why this is needed is discussed in the next section. The renormalization scale, μ_R, is a second theoretical construct (See [4, 5] for details) and is normally set equal to μ_F in calculations. For the most part, from now on, the reliance on theoretical scales will be neglected, with the PDFs written as $f(x, Q^2)$. In Chapter 8, we will consider how the choice of these scales impact the interpretation of our result. As the integral in Eq. 1.5

is a convolution, it can be rewritten in a shorthand form:

$$\sigma_{\ell N}^{DIS} = \sum_{f=q,\bar{q},g} f(x, Q^2) \otimes \hat{\sigma}_{\ell f}^{\text{el}}(xP, q) \tag{1.6}$$

where $\otimes$ signifies a convolution.[5]

Note that even though the summation is over all partons, the cross section for a photon interacting with a gluon is suppressed as the colorless photon cannot couple directly to the chargeless gluon. Instead, a quark propagator is required, and so this interaction is suppressed by a factor of α_s. Therefore, in the Q^2 range where pQCD is applicable, information on the gluonic structure of the proton is suppressed.

In the parton model, it is the PDFs which contain information about the about the structure of the proton. The goal is to map out, as a function of x, the probability of finding a particular distribution of parton(s) with that specified momentum fraction.[6] To do this, we must use the experimental result for the structure functions, and relate these to the PDFs. This relation can be show to be

$$F_2(x) = \sum_i e_i^2 x f_i(x) \ . \tag{1.8}$$

1.3.1 Factorization and Universality

The parton model allows the measured cross section to be interpreted in terms of PDFs. However, implicit in the above discussion of the parton model interpretation of DIS is the assumption that the cross section can indeed be *factorized* in terms of a hard scattering process ($\hat{\sigma}$) between leptons, quarks and/or gluons, which is calculable using pQCD, and some number of soft (non-perturbative) QCD objects, i.e. the PDFs. (For other interactions, in which we also consider the final state hadrons, this also applies to the fragmentation functions. See Sec. 1.4). The factorization scale, μ_F, in Eq. 1.5, gives a cutoff for separating the soft and hard physics in theoretical calculations. This scale

[5]The technical definition of a convolution of two functions, f and g, is

$$[f \otimes g](x) = \int dx_1 dx_2 f(x_1) g(x_2) \delta(x - x_1 x_2) \, . \tag{1.7}$$

[6]Although the parton distributions mentioned previously are simply the distribution of a specified parton as a function of momentum fraction, there are other more complicated distributions, such as the difference between number of quarks and anti-quarks in a hadron, (for example, $u_v = u - \bar{u}$). The main body of this work will actually deal with the polarized parton distribution functions, which are a difference between a specified type of parton with spin aligned or anti-aligned to the spin of the parent hadron.

is an unphysical theoretical construct, dependent on the order of the perturbative calculation [6]. For next to leading order (NLO) in α_s pQCD calculations, it is generally taken to be equal to Q^2. In the case of a final state hadron, a second scale, the fragmentation scale μ'_F, exists for determining the separation between soft and hard physics in fragmentation. Normally μ'_F is taken to be the same as μ_F in calculations, though this is not necessary. In Chapter 8, the theoretical uncertainty in the expectations for A_{LL} calculated with NLO pQCD due to the choice of scales (μ_F, μ'_F and μ_R) will be studied.

Factorization, by itself, only allows us to describe the structure of the proton in a particular arrangement. While this is useful, the real goal is an understanding of the proton (and other hadrons) independent of the particular experimental method being used. Therefore, the PDFs (and fragmentation functions) measured in any one method must be the same as those measured by another process, i.e., they must be *universal*. Without universality, measuring the structure of the proton is nonsensical, as the measurement would imply nothing inherent about the proton, but only how it behaves in a very specific situation.

Both factorization and universality are assumptions, and have been shown to hold in only a limited number of cases [7]. In the case of observing final state hadrons in any interaction, factorization has not been proved. However, in order to attempt to understand non-perturbative QCD objects, we must rely on factorization and universality.

This is not to say that they cannot be tested. In the case of fragmentation functions (FFs), differences between Semi-Inclusive DIS (See Sec. 1.4.1) and e^+e^- have been examined in [8] and [9] and the FFs from both processes were found consistent. Similarly, de Florian, Sassot and Stratmann (DSS) [10] found that the fragmentation in e^+e^-, Semi-Inclusive DIS and hadron-hadron scattering can be described with a single set of functions (one for each parton fragmenting to a specified hadron). Both of these result imply that universality and factorization hold, at least in the case of FFs, at the present experimental and theoretical accuracy.

Now that we understand the two main assumptions in the parton model, we can return to considering experimental techniques used to measure nucleon structure.

1.4 Experimental Techniques, Continued

The DIS interaction can be generalized to account for many other experimental methods. Consider the scattering $A + B \rightarrow C + D + X$ where A and B are composite particles with interacting partons a and b, respectively, which are

involved in hard scattering $a+b \to c+d$. C and D are final state observables originating from c and d, respectively, and X is everything else.

In this case, Eq. 1.5 generalizes to

$$\begin{aligned}\sigma^{A+B\to C+D+X} &= \sum_{f_a,f_b}\int_0^1 dx_a \int_0^1 dx_b \int_0^1 dz_C \int_0^1 dz_D \\ &\quad \hat{\sigma}^{\mathrm{el},a+b\to c+d}(x_aP_A, x_bP_B, P_c/z_C, P_d/z_D, Q^2) \\ &\quad f_a(x_a,Q^2)f_b(x_b,Q^2)D_C^c(z_C,Q^2)D_D^d(z_D,Q^2)\,.\end{aligned} \tag{1.9}$$

where x_a and x_b are the momentum fractions carried by the interacting partons in A and B, P_A and P_B are the momenta of the scattering particles (leptons or hadrons), P_c and P_d are the momenta carried by the outgoing partons, and z_C and z_D are the fraction of the outgoing parton's energy carried by the measured particle(s). f_a and f_b are the PDFs and D_C^c and D_D^d are the FFs, which give the probability that a parton of type c will fragment into a measured particle with momentum z_CP_c.

In the case of DIS, particles A and D are the incoming and outgoing lepton. As leptons are effectively structureless at the energies probed in existing experiments, the PDFs and FFs for a lepton are simple delta functions at $x_a = 1$ and $z_D = 1$ respectively. D_C^c in this case is included in the final stated X, as is the integral over z_C. Performing the integrals over x_a and z_D will then give back Eq. 1.5.

Equation 1.10 can be written similar to Eq. 1.6 as

$$\begin{aligned}\sigma_{\ell N}^{DIS} &= \sum_{f_a,f_b} f_a(x_a,Q^2)\otimes f_b(x_b,Q^2) \\ &\quad \otimes\hat{\sigma}^{\mathrm{el},a+b\to c+d}(x_aP_A, x_bP_B, z_CP_c, z_DP_d, Q^2) \\ &\quad \otimes D_C^c(z,Q^2)\otimes D_D^d(z,Q^2)\,.\end{aligned} \tag{1.10}$$

With this generalization in mind, we can consider a few more complicated experimental techniques, which are currently used to understand the structure of the proton.

1.4.1 Semi-Inclusive Deeply Inelastic Scattering

Semi-inclusive DIS (SIDIS) is similar to DIS, except that (at least) one hadron in the final state is observed, i.e. the interaction measured is $\ell+N \to \ell'+h+X$. As with DIS, particles A and D are the incoming and outgoing lepton, and so the $f_a(x_a,Q^2)$ and $D_D^d(z,Q^2)$ are simple delta functions at $x_a = 1$ and $z_D = 1$ respectively. In SIDIS, however, $D_C^c(z,Q^2)$ is not included in the sum over X.

The cross section is then

$$\sigma_{\ell N}^{SIDIS} = \sum_{f=q,\bar{q},g} f(x,Q^2) \otimes \hat{\sigma}^{\rm el}_{\ell f \to cX}(xP,q) \otimes D_h^c(z,Q^2)\,. \tag{1.11}$$

This process is shown diagrammatically in Fig. 1.2b. Again note that, similar to DIS, the sensitivity of SIDIS to the gluon is reduced due to the fact that the photon and the gluon do not directly couple. For a thorough description of SIDIS, see [11].

1.4.2 Hadron-Hadron Scattering

A third approach to understanding the nucleon structure is through hadron-hadron collisions. In this case, both quarks and gluons interact in leading order. The basic interaction considered in this work is $p + p \to X$, and is shown in Fig. 1.2c.[7] However, in proton-proton ($p+p$) inelastic scattering, as neither the proton nor the remnant is measured, a final state created in the interaction (for example, a hadron h, a jet, or a direct photon) is observed in the final state.[8] In all measurements discussed in this work, we assume only one final state particle (or jet), and so $D_D^d(z,Q^2)$ is included in the sum over X. As both incoming particles are protons, there are two PDFs contributing to the cross section:

$$\begin{aligned}\sigma^{p+p\to h+X} \quad = \quad & \sum_{f_{a,b}=q,\bar{q},g} f_a(x_a,Q^2) \otimes f_b(x_b,Q^2) \\ & \otimes \hat{\sigma}^{a+b\to c+X}(x_aP_1, x_bP_2, q, zP_c) \otimes D_h^c(z,Q^2)\,. \end{aligned} \tag{1.12}$$

Here, the final state observable is assumed to be a hadron. In this work, the final state observable is either a charged or neutral pion. Note that in the case of $p + p \to jet + X$ or $p + p \to \gamma + X$, the FF is simply a delta function at $z = 1$.

A drawback of $p+p$ collisions is that neither x nor Q^2 are directly measured in the interaction. Instead, for the requisite hard scale needed for theoretical interpretation (normally $\mu^2 = Q^2$ in DIS and SIDIS), the transverse momentum, p_T, of the measured probe is used.

[7] Here, and in the following, both hadrons are assumed to be protons.

[8] As is discussed in Chapter 3.3, experimentally we require some additional particles to be seen by our event trigger.

1.5 Proton Structure

With the experimental techniques described above, much can be learned about the structure of the proton. In the following, we first look at what has been learned from unpolarized scattering in terms of the charge and momentum of the proton, and then move on to spin.

1.5.1 Results from Unpolarized Scattering

Fig. 1.3 shows the proton structure function F_2 as a function of Q^2 plotted in bins of fixed x measured from unpolarized DIS. These results cover a large x and Q^2 range. Results at different Q^2 can be related using the DGLAP evolution equations [13–15]. These equations use the gluon and quark splitting functions, which describe how quarks radiate gluons, and how gluons produce quark-antiquark pairs. Given some initial PDFs and a specified Q^2, the DGLAP equation are used to get the PDFs at any other Q^2.[9]

Figures 1.4 and 1.5 show the resulting (unpolarized) PDFs from two example fits of these data for F_2, as well as some results from hadron-hadron scattering and neutrino scattering, from the MRST [16] and CTEQ [18] groups, respectively. The MRST result uses pQCD calculated to Next to Next to Leading Order (NNLO), while CTEQ uses NLO pQCD. The results agree well for $10^{-3} \lesssim x \lesssim 0.7$, where the majority of the data exists.

Figure 1.6 shows the estimated percentage uncertainty in the three light quark distributions as well as the gluon distribution as fit by CTEQ.[10] The majority of the data used in these fits come from DIS, in which gluons do not interact at LO, and so the gluon distribution constraint comes largely from evolution with the DGLAP equations. The large range in Q^2 of the data in Fig. 1.3 is the dominant constraint of the gluon distribution, as the quark distribution at other Q^2 will be directly affected by the quark and gluon splitting functions through the DGLAP evolution. Even so, the gluon is less constrained than the light quarks, as is evident from Fig. 1.6. As we will see later, the lack of such a large Q^2 range in polarized DIS data leads to large uncertainty in the polarized gluon distribution. First, however, we consider what we can learn about the basic properties of the proton from these unpolarized PDFs.

[9] DGLAP equations may not be valid when evolving down to very low Q^2 as they rely on the applicability of pQCD.

[10] Here, CTEQ uncertainties are shown as representative of NLO pQCD fit results. NLO pQCD will be used to interpret the results presented in this work, and so are most relevant here.

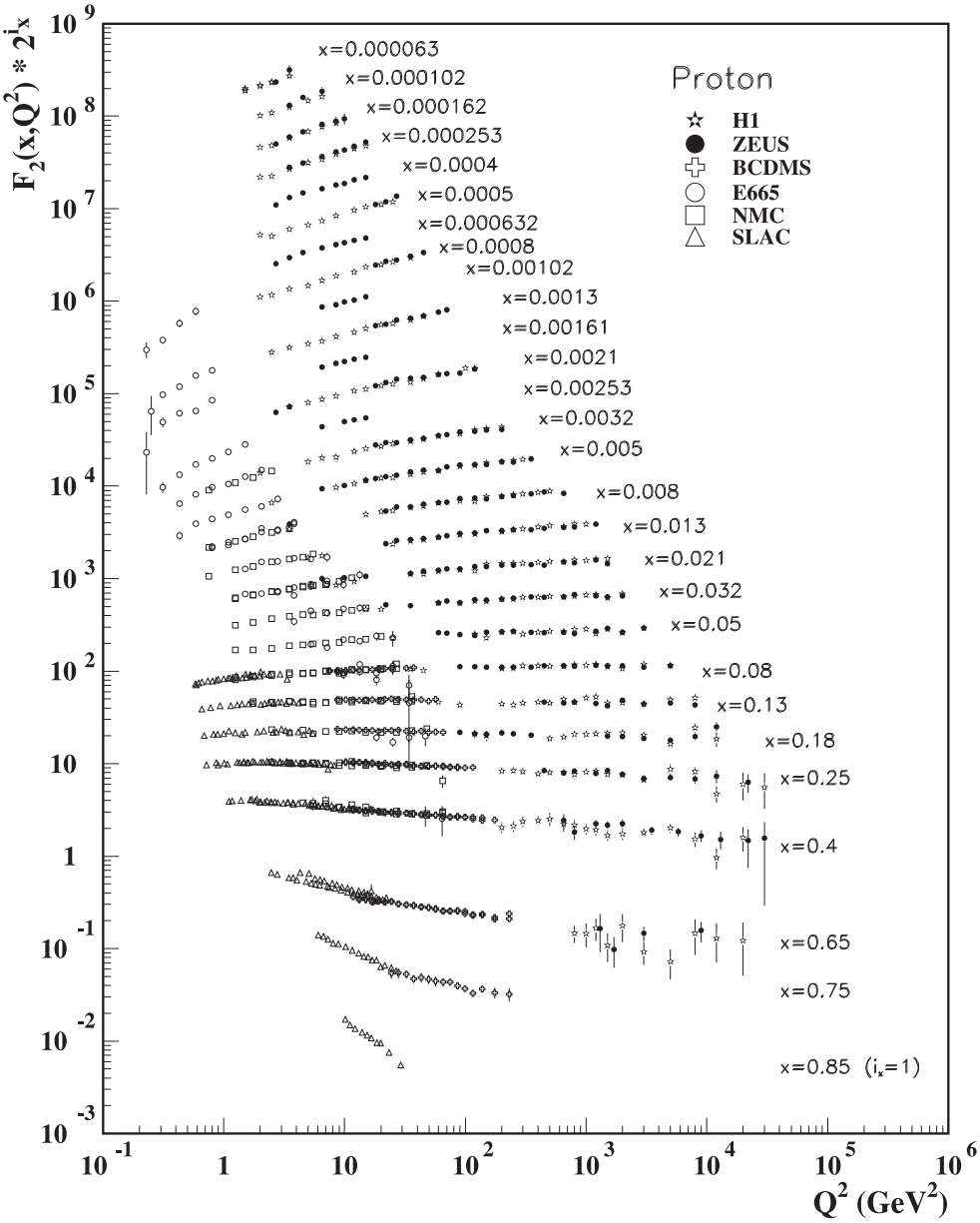

Figure 1.3: Proton structure function F_2^p measured by DIS. Data was compiled the Particle Data Group [12], and is meant to be representative of the current world data.

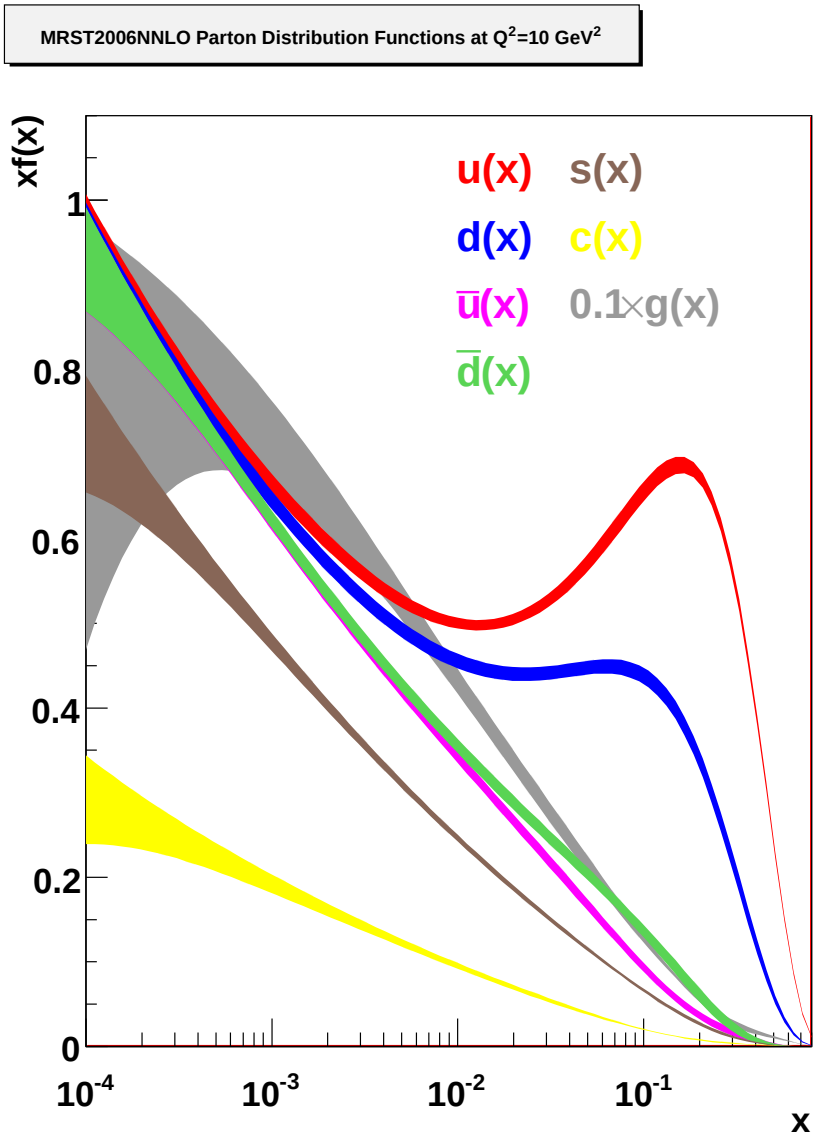

Figure 1.4: Parton Distribution Functions for up (red), down (blue), antiup (purple), antidown (green), strange (brown) and charm (yellow) quarks and gluons (grey) as a function of x at $Q^2 = 10$ GeV^2 using the MRST 2006 NNLO fits [16]. Note that the gluon is scaled down by a factor of ten. Bands represent uncertainties estimated by MRST calculated by PDF calculator at [17].

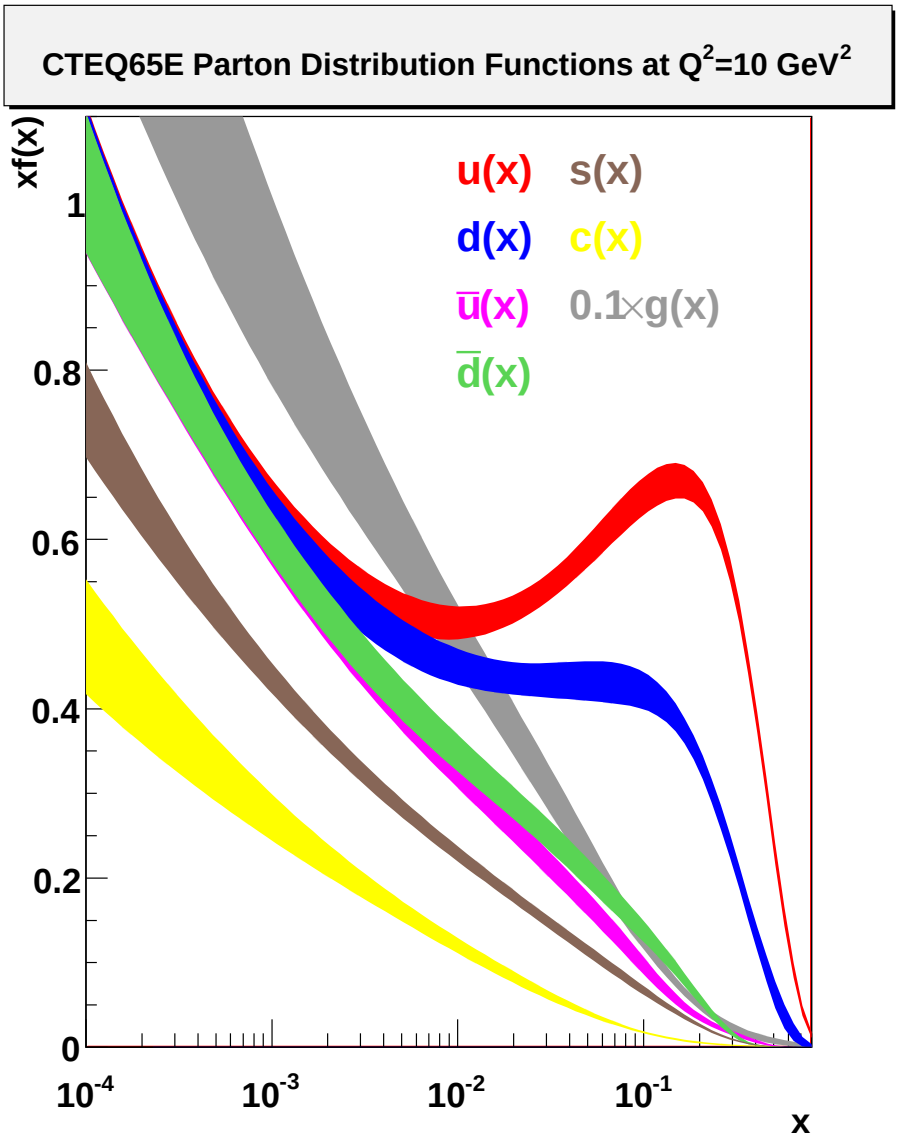

Figure 1.5: Parton Distribution Functions scaled by x for up (red), down (blue), antiup (purple), antidown (green), strange (brown) and charm (yellow) quarks and gluons (grey) as a function of x at $Q^2 = 10$ GeV^2 using the CTEQ6.5 NLO fits [18]. Note that the gluon is scaled down by a factor of ten. Bands represent uncertainties estimated by CTEQ calculated by PDF calculator at http://durpdg.dur.ac.uk.

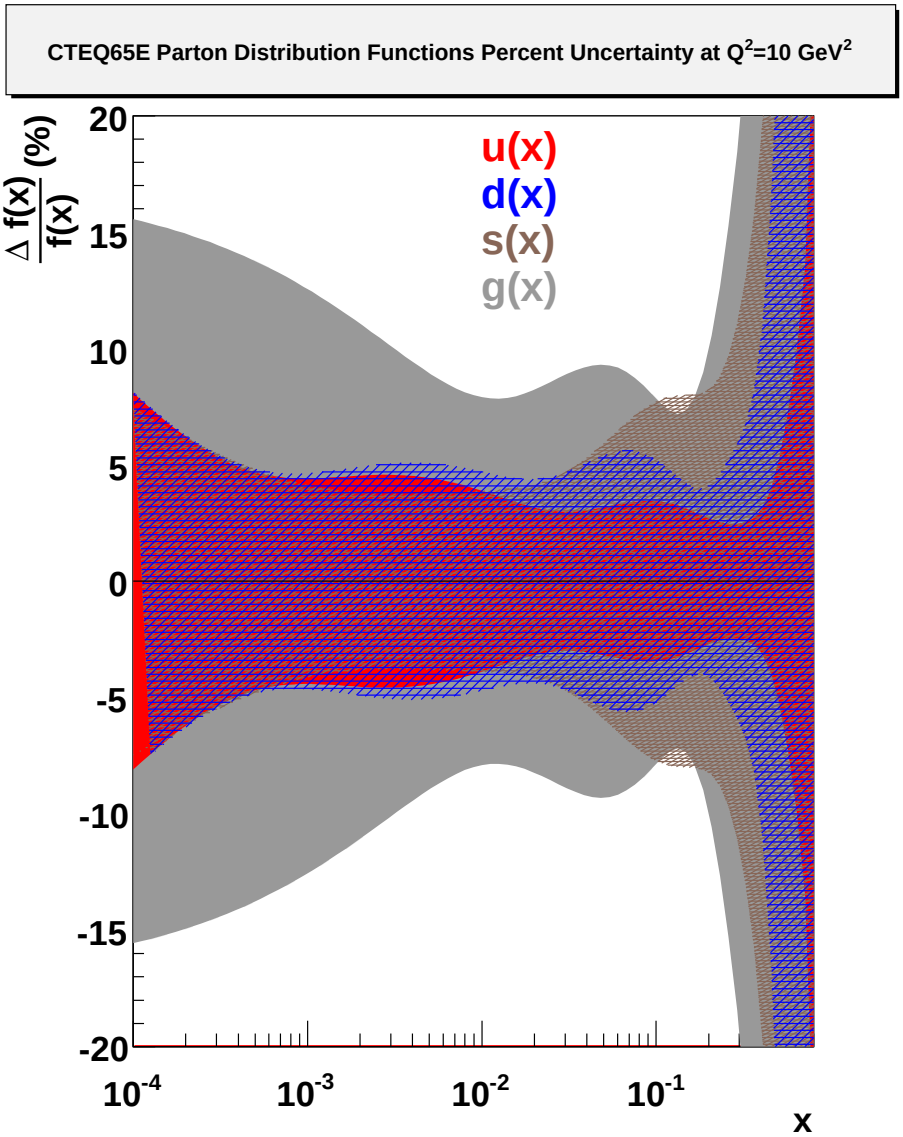

Figure 1.6: Estimated percentage uncertainty in the up (red), down (blue), and strange (brown) quarks and gluons (grey) as a function of x at $Q^2 = 10$ GeV^2 using the CTEQ6.5 NLO fits [18]. Uncertainties estimated by CTEQ calculated by PDF calculator at [17].

1.5.2 Charge and Momentum

In terms of charge, understanding the proton (or other hadron) structure is rather simple, as the quarks must have charges such that the charge of the proton, neutron, and other hadrons are simply the sum of the charged particles within. As the gluon is electromagnetically neutral, and quark-anti-quark pairs in the sea are also electromagnetically neutral, this leaves only the charge of the valance quarks. This leads to up, charm, and top with $q = +\frac{2}{3}e$ and down, strange and bottom with $q = -\frac{1}{3}e$ where e is the charge of the positron.

Using these charge values for the quarks, we can write a charge sum rule as

$$\begin{aligned} +1 &= \sum_q e_q \int_0^1 dx\{q(x) - \bar{q}(x)\} \\ &= +\frac{2}{3}\int_0^1 dx\{u(x) - \bar{u}(x)\} - \frac{1}{3}\int_0^1 dx\{d(x) - \bar{d}(x)\} \\ &\quad + \sum_{s,c,b,t} e_q \int_0^1 dx\{q(x) - \bar{q}(x)\} \\ &= +\frac{2}{3} * 2 - \frac{1}{3} * 1 + 0\,. \end{aligned} \tag{1.13}$$

Here, gluons, which carry no charge, are excluded and the following relations are used.

$$\begin{aligned} \int_0^1 dx\{u(x) - \bar{u}(x)\} &= \int_0^1 dx u_v(x) = 2 \\ \int_0^1 dx\{d(x) - \bar{d}(x)\} &= \int_0^1 dx d_v(x) = 1 \\ \int_0^1 dx\{q(x) - \bar{q}(x)\} &= \int_0^1 dx q_v(x) = 0 \qquad \text{for } \; q = s, c, b, t\,. \end{aligned} \tag{1.14}$$

Here, u_v, d_v and q_v are just the valence distributions for the quarks in a proton. As there are no valence distributions the strange, charm, bottom or top quark, they contribute no charge to the proton.

Next, consider momentum. A very simple (and naive) assumption would be to assume that the three valance quarks carry all the momentum in equal amounts (i.e. $x = \frac{1}{3}$). However, once gluonic interactions between the quarks are allowed, the momentum fractions carried by the quarks get smeared out. If $q\bar{q}$ pair production is also taken into account, then a long tail is found at

small x. With this in mind, a momentum sum rule can be written as:

$$1 = \sum_q \int_0^1 dx x\{q(x) + \bar{q}(x)\}\,. \tag{1.15}$$

However, results from DIS measurements showed this picture to be too naive. Using PDFs such as those in Fig. 1.4 and 1.5, it was shown that the quarks (both valence and sea) carry only about 50% of the proton momentum. This missing momentum is actually carried by the gluon, and can be viewed as an indication of the existence of gluons. Including the gluons in Eq. 1.15 then gives a complete momentum sum rule:

$$1 = \sum_q \int_0^1 dx x\{q(x) + \bar{q}(x)\} + \int_0^1 dx x g(x)\,. \tag{1.16}$$

1.6 Spin Structure

Next, consider the proton spin, $\langle S_P \rangle = \frac{1}{2}$, given in the unit of angular momenta, $\hbar = 1.05457148 \times 10^{-34}$ m^{2}kg/s.[11] Similar to the momenta and charge of the proton, its spin should be the sum of its part, and so, to understand origin of the proton spin, we must understand the spin (or polarized) structure of the proton.

The polarized structure of the proton is much less well understood than the unpolarized structure needed to understand charge and momentum. This is primarily due to the added difficulty in experimentally measuring spin structure.[12] As was mentioned in Sec. 1.2.1, the spin structure functions, g_1 and g_2 (see Eq. 1.5), can only be measured if the initial spin states are not summed over. Experimentally, this requires that measurements are made with both a polarized lepton beam and a polarized hadron target. The difficulties in producing both of these at collider energies has limited the x and Q^2 range of polarized DIS measurements. Figure 1.7 shows current experimental data for g_1 for the proton as a function Q^2. The lack of polarized DIS data at high Q^2 and/or low x is evident when compared with the unpolarized case (Fig. 1.3). In the remainder of this section, we examine initial expectations for these data and how the interpretation of these results have evolved since experiments first indicated that the proton spin was not primarily due to the intrinsic quark spin.

[11] From here on, we will neglect the units when discussing angular momenta.

[12] Additional theoretical advances were also required, as the NLO pQCD calculations needed for polarized and unpolarized cross sections differ significantly.

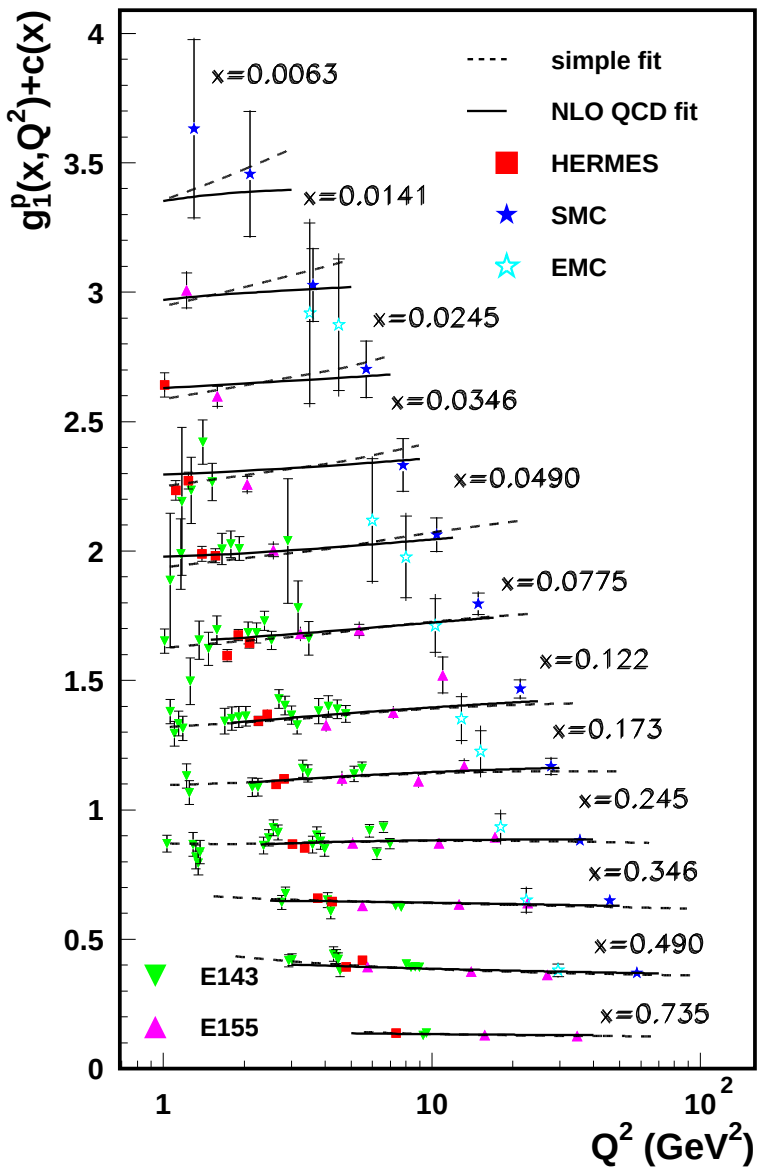

Figure 1.7: Proton structure function g_1^p measured by polarized DIS. Data was compiled by S. Bass [19], and is meant to be representative of the current world data.

1.6.1 Naive (and Slightly Less Naive) Quark Model

The spin of mesons and baryons were found to be describable simply in terms of the valence quark spin [2]. With such a very naive understanding of quarks, one may expect that, for a proton with spin $\frac{1}{2}$ made up of three valence quarks of spin $\frac{1}{2}$, two quarks have spins aligned to the proton, and one is anti-aligned. However, this assumption is similar to assuming that each quark carries one third of the proton momentum. The fraction of the proton spin is instead smeared out over the quarks analogous to the smearing of the fractional momentum.

This slightly less naive model would assume that the spin of a proton is given by

$$\langle S_P \rangle = \frac{1}{2} = \frac{1}{2}\Delta\Sigma \tag{1.17}$$

where

$$\Delta\Sigma = \sum_{q=u,d,s,c,b,t} \{\Delta q(x) + \Delta\bar{q}(x)\}\,. \tag{1.18}$$

$\Delta q(x)$ ($\Delta\bar{q}(x)$) is the polarized quark (antiquark) PDF. Defining two new PDFs, $q_+(x)$, the probability of finding a quark with momentum fraction x and helicity aligned to the proton helicity, and $q_-(x)$, the probability of finding a quark with momentum fraction x and helicity opposite the proton helicity, we define

$$\Delta q(x) \equiv q_+(x) - q_-(x)\,. \tag{1.19}$$

Note that the unpolarized quark PDF $q(x)$ is just the sum of the two helicity dependent PDFs, namely

$$q(x) = q_+(x) + q_-(x)\,. \tag{1.20}$$

In Eq. 1.18, although the sum is over all quarks, in general only the three light quarks are expected to have significant contributions to the proton spin.

Ellis-Jaffe Sum Rule

In 1974, Ellis and Jaffe [20] proposed independent sum rules for the proton and neutron spin structure using what has become known as the "naive quark model" (NQM), assuming that the strange quark sea was (nearly) unpolarized.

From this sum rule, the value of $\Delta\Sigma$ is reduced to 0.6 due to relativistic motion of the quarks. Similar estimates were derived from other models [21]. Sehgal [22] identified the difference from $\Delta\Sigma$ =1 as the quark orbital angular momentum contribution, L_z^q, in effect acknowledging that the net orbital angular momentum due to the quarks is the sum of intrinsic and orbital angular

momentum. In this case, Eq. 1.17 becomes

$$\langle S_P \rangle = \frac{1}{2} = J_z^q = \frac{1}{2}\Delta\Sigma + L_z^q \tag{1.21}$$

where J_z^q is the total angular momentum of the quarks.

1.6.2 EMC result

The first experimental measurements of polarized DIS were performed at the Stanford Linear Accelerator (SLAC) with polarized electrons and polarized protons [23–25]. The actual measured asymmetry is

$$A_1^p = \frac{\sigma^{\uparrow\uparrow} - \sigma^{\uparrow\downarrow}}{\sigma^{\uparrow\uparrow} + \sigma^{\uparrow\downarrow}} \quad , \tag{1.22}$$

where $\uparrow\uparrow$ ($\uparrow\downarrow$) signify the ℓp cross section when the lepton and proton polarizations are aligned (anti-aligned). The SLAC results plotted in Fig. 1.8 agreed with the expectation from the Ellis-Jaffe sum rule, but were limited to large x (>0.1).

Several years later, the European Muon Collaboration (EMC) at CERN used a polarized muon beam incident of polarized protons to extend the measured x range down to 0.01. The EMC result for A_1^p is plotted in Fig. 1.8 [26], and is seen to agree with the SLAC results in the overlapping x range measured by the two experiments.

However, when this result is converted into g_1^p, using

$$A_1(x, Q^2) = \frac{g_1(x, Q^2)}{F_1(x, Q^2)}, \tag{1.23}$$

it was found to disagree with the Ellis-Jaffe sum rule, as can be seen in Fig. 1.9. This plot shows $\int_{x_m}^1 dx g_1^p(x)$, the integral of $g_1^p(x)$ over x from a lower x value, x_m, to 1, vs. x_m. Excluding a large increase in $g_1^p(x)$ at some value of $x<0.01$, the Ellis-Jaffe sum rule is clearly violated. The larger implication [27] of this violation was that the quark spins did not contribute much to the proton spin, i.e.

$$\Delta\Sigma = 0.120 \pm 0.094 \pm 0.138 \tag{1.24}$$

where the first uncertainty is statistical and the second is systematic.

A second implication from the EMC results, in the framework of the NQM, was that the strange quark polarization was not zero, but large and negative: $\Delta s + \Delta\bar{s} = -0.095 \pm 0.016 \pm 0.023$.

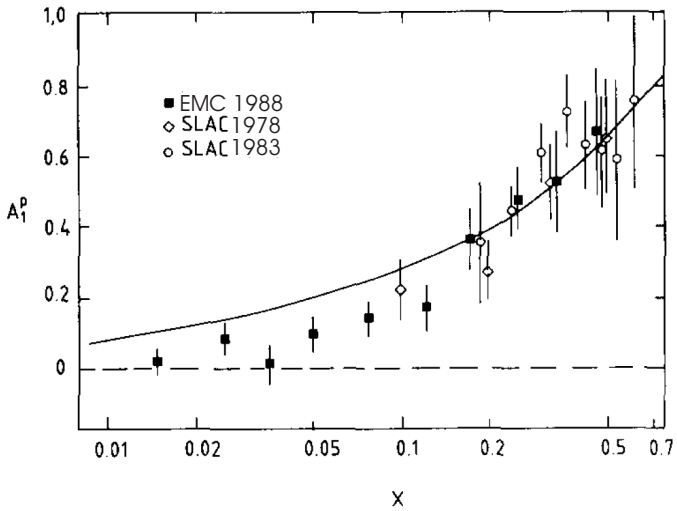

Figure 1.8: Early results from SLAC (open circles [23, 24] and diamonds [25]) and EMC (closed squares) for A_1^p vs. x. Solid line is expectation if Ellis-Jaffe spin sum rule for the proton held. Plot taken from [26]

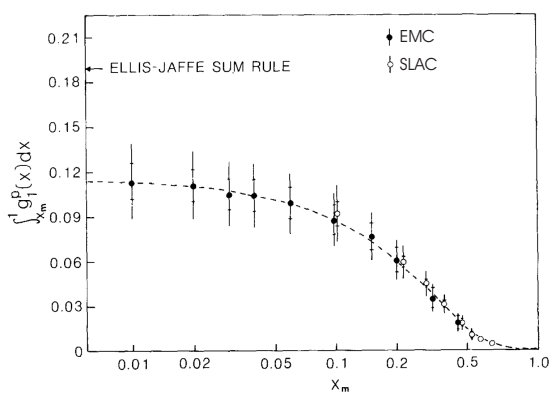

Figure 1.9: Early results from SLAC (open) and EMC (closed) for $\int_{x_m}^1 dx g_1^p(x)$ vs. x_m, where x_m is the value of x at the low edge of each bin. The dashed line is a parametrization of A_1^p. For details, see [27].

1.6.3 A Broader Picture on Nucleon Spin: Complete Spin Sum Rule

The failure of the NQM to describe the proton spin as composed simply by the quarks led the broader conception of the spin sum rule for the proton given in Eq. 1.21. By including the possible contribution from gluon angular momentum, both intrinsic ($\Delta G = G^+ - G^-$) and orbital (L_g), a complete spin sum rule of the proton is given as

$$\langle s_z^P \rangle = \frac{1}{2} = \frac{1}{2}\Delta\Sigma + L_q + \Delta G + L_g \,. \tag{1.25}$$

Note here that this sum rule is only valid in the infinite momentum framework. Some theoretical predictions [28–30] indicated that an extremely large polarized gluon distribution ($\Delta G \sim 3$ or 4) could restore the measured value of $\Delta\Sigma$ to about 0.6 through anomalous gluon contribution to $\Delta\Sigma$:

$$\Delta\Sigma_{\text{measured}} = \Delta\Sigma_{\text{real}} + \frac{\alpha_s}{2\pi}\Delta G \,.$$

However, it is important to note that even a smaller gluon contribution on the order of 0.5 would satisfy the spin sum rule (Eq. 1.25) while having little effect on the value of $\Delta\Sigma$.

1.6.4 Modern Results for g1

Numerous other DIS experiments have been performed at CERN (μp) [31], SLAC (ep) [32–34] and DESY (ep) [35] which confirmed the EMC result. They have also expanded the covered range of x and Q^2 and obtained the neutron structure function, g_1^n, through deuteron and ^{3}He (helium atoms with a single neutron and two protons) measurements. g_1^p as a function of Q^2 for different fixed x values is plotted in Fig. 1.7 for a representative subset of the world data from polarized DIS.

Both the Q^2 and x ranges of the g_1^p data are two orders of magnitude smaller than the F_2^p data shown in Fig. 1.3. This is primarily due to the lack of a polarized electron polarized proton collider, as all polarized DIS experiments to date are fixed target and therefore limited in energy. As was discussed earlier, the large Q^2 range measured in unpolarized DIS were significant in constraining the unpolarized gluon distribution. As we will see, the lack a large Q^2 range in the polarized DIS data leads to large uncertainty in the polarized gluon distribution.

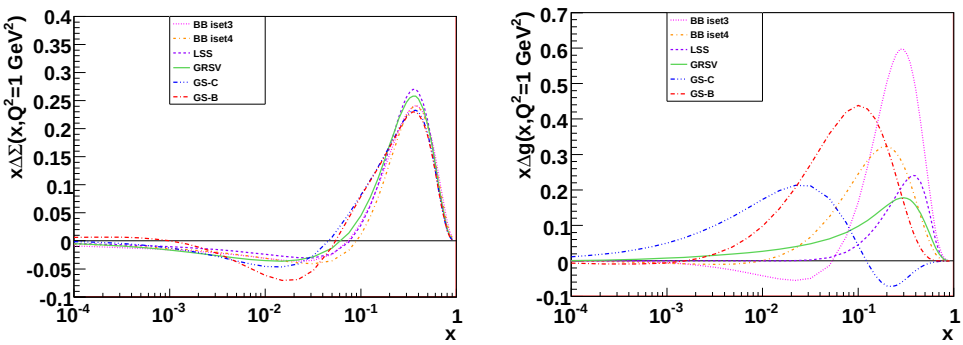

(a) (b)

Figure 1.10: Spin dependent PDFs for (a) $\Delta\Sigma$ and (b) ΔG vs. x at Q^2=1 GeV^2, as extracted by different NLO pQCD fits to polarized DIS data. While the total quark contribution agrees well in all fits, the polarized gluon distributions vary significantly, due to the poor constraining power of fixed target polarized DIS.

1.6.5 Extracted Polarized Distribution Functions

Since the mid-1990's, a number of theoretical and experimental groups have tried to extract the polarized parton distribution functions from fits of the world data on g_1^p. A brief summary of a number of these fits is given in Appendix C. The results for $\Delta\Sigma$ and ΔG are plotted in Fig. 1.10.

As can be clearly seen in Fig. 1.10, $\Delta\Sigma$ is quite consistent in all fits, indicating that the existing polarized DIS data offer a reasonable constraint. ΔG, however, varies significantly indicating it is poorly constrained by the current fixed target polarized DIS data. In order to more precisely determine ΔG, we turn to interactions in which the gluon interacts at leading order, specifically $p+p$ scattering.

1.7 Accessing the Polarized Gluon Distribution through $p+p$ Collisions

Unpolarized $p+p$ scattering was described in Sec. 1.4.2. In the case of longitudinally polarized $p+p$ scattering, Eq. 1.12 becomes

$$\Delta\sigma^{p+p\to h+X} = \sum_{f_{a,b}=q,\bar{q},g} \Delta f_a(x_a,Q^2)\otimes\Delta f_b(x_b,Q^2) \otimes\Delta\hat{\sigma}^{a+b\to c+X}(x_a,x_b,Q^2,z)\otimes D_h^c(z,Q^2)\,. \quad (1.26)$$

Here, $\Delta\sigma$ is defined as

$$\Delta\sigma = \sigma_{++} + \sigma_{--} - \sigma_{+-} - \sigma_{-+} \tag{1.27}$$

where the '+' and '−' signs indicate the helicity state of the two longitudinally polarized protons in the case of $\Delta\sigma^{p+p\to h+X}$ or the two partons in the case of $\Delta\hat{\sigma}^{a+b\to c+X}$.[13] Therefore, by measuring $\Delta\sigma^{p+p\to h+X}$, we could gain access to the polarized structure functions. Equation 1.27 is generally written in the shorter form

$$\Delta\sigma = \sigma_{++} - \sigma_{+-} \tag{1.29}$$

where '++' ('+−') indicate same (opposite) helicity collisions.

Experimentally, however, there are often large systematic uncertainties due to detector acceptance and efficiencies, which make such a cross section measurement difficult. Instead, by measuring the ratio of the polarized and unpolarized cross sections, such systematic uncertainties will largely cancel. This ratio is defined as the double helicity asymmetry, or double longitudinal spin asymmetry, A_{LL}:

$$\begin{aligned} A_{LL} &= \frac{\Delta\sigma^{p+p\to h+X}}{\sigma^{p+p\to h+X}} && (1.30)\\ &= \frac{\sum_{f_{a,b}=q,\bar{q},g} \Delta f_a \otimes \Delta f_b \otimes \Delta\hat{\sigma}^{a+b\to c+X} \otimes D_h^c}{\sum_{f_{a,b}=q,\bar{q},g} f_a \otimes f_b \otimes \hat{\sigma}^{a+b\to c+X} \otimes D_h^c} \\ &= \frac{\sigma_{++} - \sigma_{+-}}{\sigma_{++} + \sigma_{+-}} && (1.31) \end{aligned}$$

where the functional dependencies on x_a, x_b, z and Q^2 have been suppressed.

To interpret this measurement in terms of ΔG, we rely on elements from a number of sources: unpolarized PDFs (See Sec. 1.5.1), fragmentation functions in the case of a final state hadron, and polarized and unpolarized partonic cross sections calculable in pQCD, as well as the polarized PDFs of the quarks from polarized DIS. In Chapter 8, we examine how the results from $p + p$ scattering can be used to determine the polarized gluon distribution, as well as how uncertainties from these components affects this determination. First, however, we turn to the measurement itself.

[13] We can also define the unpolarized cross section, σ, in terms of the four helicity combinations in Eq. 1.27 as

$$\sigma = \sigma_{++} + \sigma_{--} + \sigma_{+-} + \sigma_{-+}\,. \tag{1.28}$$

1.8 Measuring the Double Helicity Asymmetry

A cross section can be written as

$$\sigma = \frac{N_{corr}}{L} \tag{1.32}$$

where N_{corr} is the measured yield (N) corrected for the efficiencies in reconstruction (ϵ_{reco}), trigger bias (ϵ_{bias}) and detector acceptance (ϵ_{acc})

$$N_{corr} = \frac{N}{\epsilon_{\text{bias}}\epsilon_{\text{acc}}\epsilon_{\text{reco}}} \ , \tag{1.33}$$

and L is the luminosity. Therefore, A_{LL} can be written as

$$\begin{aligned} A_{LL} &= \frac{\sigma_{++} - \sigma_{+-}}{\sigma_{++} + \sigma_{+-}} \\ &= \frac{\frac{\left(\frac{N^{++}}{\epsilon^{++}_{\text{bias}}\epsilon^{++}_{\text{acc}}\epsilon^{++}_{\text{reco}}}\right)}{L^{++}} - \frac{\left(\frac{N^{+-}}{\epsilon^{+-}_{\text{bias}}\epsilon^{+-}_{\text{acc}}\epsilon^{+-}_{\text{reco}}}\right)}{L^{+-}}}{\frac{\left(\frac{N^{++}}{\epsilon^{++}_{\text{bias}}\epsilon^{++}_{\text{acc}}\epsilon^{++}_{\text{reco}}}\right)}{L^{++}} + \frac{\left(\frac{N^{+-}}{\epsilon^{+-}_{\text{bias}}\epsilon^{+-}_{\text{acc}}\epsilon^{+-}_{\text{reco}}}\right)}{L^{+-}}} \ . \end{aligned} \tag{1.34}$$

In general, for any asymmetry measurement, the efficiencies in the measurement need to largely cancel to achieve the required accuracy. As will be described later, a polarized proton accelerator offers a unique environment, where we can safely take $\epsilon^{+-} = \epsilon^{++}$ for the above efficiencies. This allows Eq. 1.34 to be rewritten in a simpler form

$$A_{LL} = \frac{1}{P_B P_Y} \frac{\frac{N^{++}}{L^{++}} - \frac{N^{+-}}{L^{+-}}}{\frac{N^{++}}{L^{++}} + \frac{N^{+-}}{L^{+-}}} \tag{1.35}$$

where P_B and P_Y are the polarization of the two beams at RHIC, which are used to normalize the measured asymmetry so the physics asymmetry can be calculated.

1.9 Neutral and Charged Pion A_{LL}

Equation 1.35 gives the basic method for measuring a double helicity asymmetry. In this work, we focus on the measurement of neutral and charged pions. As we will see in Chapter 3, PHENIX is very well suited for measuring a large sample of π^0s. However, even with large statistics, additional probes

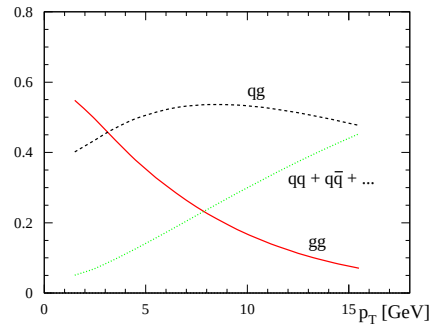

Figure 1.11: Relative fraction of produced pions originating in gluon-gluon (gg, solid red), gluon-quark (qg, dashed black) and quark-quark (qq, dotted green) scattering as a function of p_T. Calculated with NLO pQCD. Taken from [36]

such as the charged pions can help elucidate aspects of ΔG that are difficult to measure, such as the sign of ΔG.

Figure 1.11 shows as a function of p_T the fraction of pions produced for the three possible interactions in $p + p$ collisions: gluon-gluon (gg), gluon-quark (qg) and quark-quark (qq). At low p_T, gg scattering dominates, and so A_{LL} given in Eq. 1.31 effectively probes ΔG^2. Figure 1.12 shows the expectations for charged and neutral pions based on the GRSV framework. At low p_T, the expectations for a given ΔG are similar, because all pions have equal likelihood to come from gluons, which dominate in this p_T range. The difference between the three pion species at higher p_T coincides with the p_T range in which qg scattering becomes more significant. This arises due to the coupling of two effect. First, the u and d quarks have different likelihoods of fragmenting into each type of pion, with π^+s ($u\bar{d}$) more likely to come from u quarks than d quarks, and visa versa for the π^-s ($d\bar{u}$), while the π^0s ($[u\bar{u}+d\bar{d}]/2$) do not favor either. Second, Δu_v and Δd_v have opposite sign. Combining these two fact, we anticipate an ordering of the expected A_{LL} results for the three species. By studying the three separate pion species in the mid p_T range, it may be possible to extract the sign of ΔG more accurately than from the π^0 alone.

1.10

The remainder of this work, excluding the last two chapters, will focus on the measurement of A_{LL} for neutral and charged pions, including the assumptions

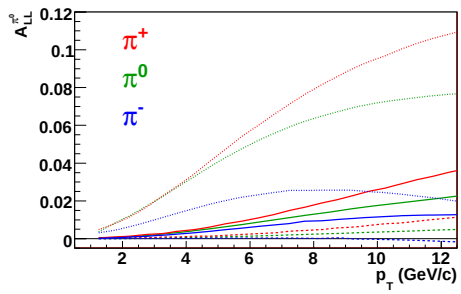

Figure 1.12: A_{LL} expectations for π^+ (red), π^0 (green) and π^- (blue) based on the GRSV fit with three input values of ΔG: the best fit (solid), $\Delta G = 0$ (dashed) and $\Delta G = G$ (dotted).

that went into Eq. 1.35. In Chapter 2, we focus on the design of RHIC as a polarized proton collider and how it allows the difference between efficiencies in '++' and '+−' collisions to be reduced to essentially zero. In Chapter 3, the PHENIX detector will be described, with emphasis on the systems used in the present work. Chapter 4 will discuss the luminosity normalization, as well as how both the magnitude and direction of the longitudinal polarization is measured. Chapter 5 will define the criteria for event selection and describe the particle identification methods used. The results for A_{LL} of $\pi^{\pm}$ and π^0 will be given in Chapter 6. Chapter 7 will detail a number of systematic cross checks, and a discussion of the final systematic uncertainty in the A_{LL} measurements.

With these results, Chapter 8 will examine how the current measurement of $A_{LL}^{\pi^0}$ in particular can be used to constrain the polarized gluon distribution of the proton, as well as discuss the current status of the theoretical and experimental uncertainties in such a constraint. Finally, in Chapter 9, we briefly discuss the future in terms of both measurements and theoretical interpretation we can expect.

Chapter 2

Polarized Protons at RHIC

2.1 RHIC

The Relativistic Heavy Ion Collider (RHIC) at Brookhaven National Laboratory (BNL) was designed to study the both the proton spin structure, through polarized proton collisions, and the state of matter created in Heavy Ion, primarily Au-Au, Collisions. In this dissertation, we focus on proton spin structure, and more precisely, the gluon spin contribution to the proton's spin. Therefore, only the elements of RHIC related to polarized protons will be discussed here. Figure 2.1 shows the RHIC facility layout, including the proton source and booster rings.

There are six possible Interaction Points (IP) in RHIC. During the 2005 run (Run5), there were four experiments that saw $p + p$ collisions: BRAHMES, PHENIX, PHOBOS and STAR. PHOBOS was decommissioned before the 2006 run (Run6). During Run6, there were only collisions at BRAHMES during the $\sqrt{s}$ =62.4 GeV running period, and a few days prior to the switch from $\sqrt{s} = 200$ GeV. The reduced number of collision points was a significant reason for the increased luminosity seen in Run6.

For specific details about accelerating and storing polarized protons at RHIC, see [37].

2.2 Siberian Snakes

For a particle in a synchrotron with no electric field, the equation of motion is given by

$$\frac{d\boldsymbol{\beta}}{dt} = -\frac{e}{\gamma m}\boldsymbol{\beta} \times \boldsymbol{B}_{\perp} \tag{2.1}$$

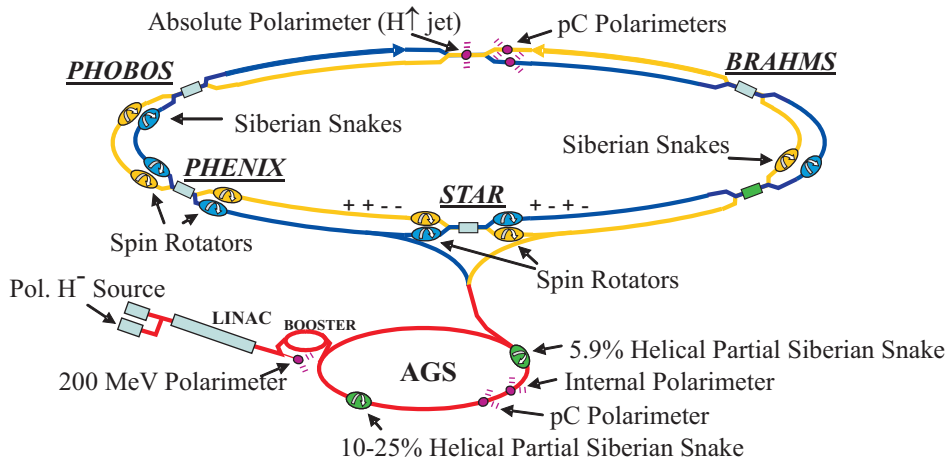

Figure 2.1: Diagram of the Relativistic Heavy Ion Collider Complex in 2006. Only elements specific to the spin program are shown. The accelerator components are discussed in the text.

where e and m are the charge and mass, respectively, of the particle, γ is given by E/m, $\boldsymbol{\beta}c$ is the velocity of the particle, and $\boldsymbol{B}_\perp$ is the magnetic field perpendicular to the particles motion. The equation of motion of the spin vector in the rest frame of the particle (assuming no electric field) is given by the Thomas-BMT equation

$$\frac{d\boldsymbol{S}}{dt} = -\frac{e}{\gamma m}\boldsymbol{S} \times \left[(1+G\gamma)\boldsymbol{B}_\perp + (1+G)\boldsymbol{B}_\parallel\right] . \tag{2.2}$$

Here, G is the anomalous magnetic moment ($G = 1.7928$ for a proton [12]), $\boldsymbol{S}$ is the particle spin vector in the particles rest frame and $\boldsymbol{B}_{\parallel(\perp)}$ is the magnetic field parallel (perpendicular) to the particle's motion. At high energies (large γ), the $B_\perp$ dominates, and $G\gamma$ gives the number of spin precessions per revolution, called the spin tune ν_{sp}.

If the spin precession frequency coincides with the frequency of a perturbation of the spin due to the magnetic field, a resonance will occur with any depolarization affects amplified. During acceleration, polarization can be lost due to such resonances which are mainly of two types: intrinsic, resulting from the period of betatron oscillation matching the period of spin procession, and imperfection, resulting from imperfections in the magnet field experienced by the spin vector each revolution. In order to reduce the impact of such resonances at high energies, sets of helical dipole magnets, called *Siberian snakes*, are used. These dipoles create a field perpendicular to the spin vector, rotating

the direction of the spin vector. If the vector is flipped 180°, then we called the snake a *full* snake. In the ideal case, a (set of) Siberian snake(s) precess(es) the polarization vector by 180° per revolution. The effect of this is to ensure that in any two revolutions, precessions of the spin vector due to resonances cancel. If the spin vector precession is not 180°, multiple orbits are needed to cancel out depolarizing effects. These depolarizing effects may not fully cancel if the beam is accelerating during these multiple orbits. Note that in the ideal case (180° precession), the spin tune is set to be $\frac{1}{2}$, ensuring that at least imperfection resonances are canceled.

2.3 Source and Boosters

Polarized protons are produced from a optically pumped polarized H^- source (OPPIS) with a polarization of ∼80%. After stripping the hydrogen of their electrons, the protons are accelerated through a spin transparent LINAC and are injected into a low energy booster. Proton bunches are injected into the Alternating Gradient Synchrotron (AGS) from the booster ring with proton energy of 2 GeV. The bunches are then accelerated to ∼23 GeV, and then injected into RHIC. There are many depolarizing resonances during the ramp in the AGS, and so controlling the polarization is very important for achieving high polarization in RHIC. Due to the small size of the AGS, and the lack of straight sections in which a full Siberian snake can be inserted, there are no full Siberian snakes in the AGS. A 5% snake was used in combination with an RF dipole to reduce depolarization prior to 2005. In 2005, a 15% "cold" snake was commissioned, greatly reducing polarization loss in the AGS [38].The use of the 15% "cold" snake was the primary reason for the increase of polarization seen in RHIC in 2006 (see Table 2.1).

2.4 RHIC Accelerator

Proton bunches are accelerated from RHIC injection energy up to a maximum energy of 250 GeV. For the analyses in this work, only data using beams accelerated to 100 GeV were used. RHIC contains two full snakes (180° flip) in each ring to reduce the effects of depolarizing resonances. This leads to a stable beam polarization in the vertical direction.

Figure 2.2 shows the effect of two snakes. As discussed above, depolarization will occur when a spin precession frequency coincides with the revolution frequency in the accelerator. In Fig. 2.2a, the polarization vector is slightly different from vertical due to a depolarizing resonance. After passing through

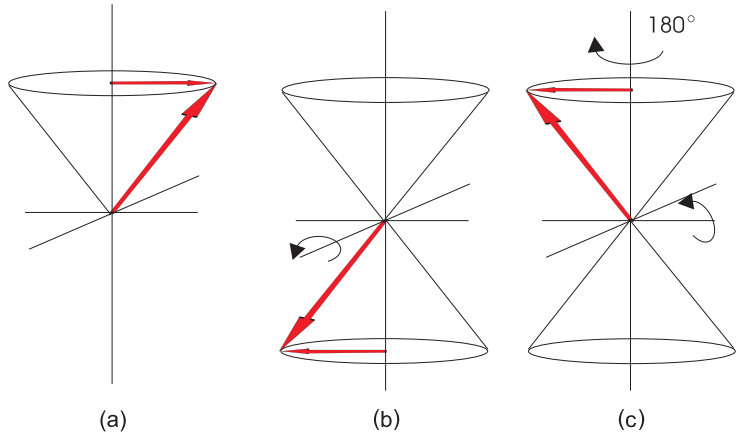

Figure 2.2: Effect of two full Siberian snakes in each RHIC ring. The spin vector precesses about the vertical (y) axis. (a) Spin vector at some point in the ring. (b) Spin vector after going through one full snake and so rotated 180° about x-axis. (c) Spin vector after going through the second full snake and so rotated 180° about z-axis, effectively returning to the position in (a), but with the spin vector precessed by 180° about the vertical axis.

the first rotator, the polarization vector is rotated about one horizontal axis (Fig. 2.2b). It is then rotated about the second horizontal axis (Fig. 2.2c) returning the polarization vector to the original orientation at the original point in the ring, except with a phase difference of 180° with respect to the vertical axis. The net effect is a cancelation of depolarization due to resonances, resulting in a stable vertical polarization in RHIC.

RHIC has a total of 120 fillable bunches in each ring, counted as bunch 0 through bunch 119. In each ring, nine bunches are left empty so that the beam can be dumped cleanly. These nine bunches are referred to as an "abort gap". Bunch numbering in each beam is defined with bunch 0 as the first bunch after the abort gap. At PHENIX in Run5 and Run6, bunch 0 in the blue ring is set to collide with bunch 80 in the yellow ring. Such a collision point is defined as a *crossing*, with crossing number coinciding with blue bunch number. As the blue and yellow beams are shifted with respect to each other, there are two abort gaps at PHENIX: crossings 31-39 and 111-119.

Prior to the 2005 run, RHIC operated in "60 bunch mode", which meant that only even bunches were filled in both rings. In order to increase the luminosity, RHIC switched to "120 bunch mode" on May 10, 2005, allowing up to 111 bunches filled in each ring. For most of Run5, however, the odd bunch crossings were not all filled as the effects of filling more bunches were

being studied. For Run6, all bunches (excluding abort gaps) were filled.

To achieve maximum luminosity during the running time, fills in RHIC normally last 7-8 hours, where a *fill* is the time from initial injection into RHIC until the beam is dumped. In general, beam parameters can change in between fills. Therefore, in the A_{LL} analysis, the measurement is done on a fill by fill basis to reduce possible beam related systematic uncertainties from such variations.

2.5 RHIC Polarimeters

In order to achieve the required accuracy for the RHIC spin goals, beam polarization must be measured to better than 5% per beam. To achieve this goal, RHIC has two different types of polarimeters for measuring the magnitude of the beam polarization.

The first of the two polarimeters used in RHIC relies on proton Carbon (pC) elastic scattering. This polarimeter has been described in detail [39], and so here only a brief description is given. Figure 2.3 shows the configuration. A thin vertical or horizontal carbon target of about 25 nm thickness is moved into the path of the polarized beam. Carbon atoms are elastically scattered nearly perpendicular to the beam. Six silicon strip detectors are placed inside the beam pipe such that, for a vertical carbon target (as shown in Fig. 2.3), they lie at $\pm 45°$, $\pm 90°$ and $\pm 135°$ with respect to the plane of the vertical target. Although only the two detectors at $\pm 90°$ are needed for measurement with a vertical target, the other four detectors allow for systematic control, as well as measurement with a horizontal target. Two different types of measurements can made with either vertical or horizontal targets: *fixed*, where the target position is constant in the measurement, and *scan*, where the target is placed at a number of points across the beam. In Run5, nearly all measurements were fixed, but indications of a polarization profile led to the decision to use scan measurements at least once per fill in Run6. As is shown if Fig. 2.1, each beam has its own pC polarimeter, as does the AGS.

This measurement has high rates (20 million events in 10 s), and so is used at RHIC for multiple measurements over the course of every fill to measure fill by fill polarization, as well as tracking any changes in polarization within a fill. However, as the analyzing power is not directly measured, this measurement is only relative, and alone carries a large uncertainty (31% relative error per beam). In order to reduce this uncertainty to the stated goal of 5% per beam, a second polarimeter is needed to measure the absolute polarization.

This second polarimeter used in RHIC relies on a polarized hydrogen gas jet (HJet) polarimeter, described in detail at [40]. Figure 2.4 shows the

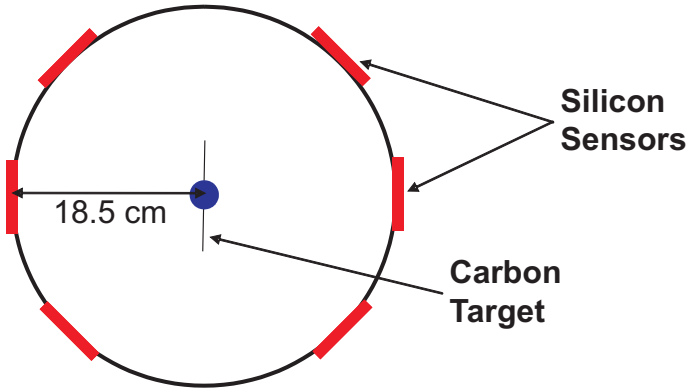

Figure 2.3: Beam view of pC polarimeter. Beam (blue) is into the page, incident on the carbon target (center). Recoil Carbon atoms are measured with 6 silicon strip detectors (red).

configuration used in Run5 and Run6. Hydrogen gas is polarized and ionized, and passed through the beam pipe, where it scatters from the beam. After exiting the beam pipe, the polarization is measured with a Breit-Rabi polarimeter. The HJet polarization was stable throughout both Run5 and Run6 and measured to be 96%. Molecular hydrogen can form as the HJet passes through the apparatus, and will dilute the polarization. The actual polarization in the region of the scattering is estimated to be 92.4±1.8%, with the uncertainty largely due to the uncertainty in the amount and effect of the molecular component on polarization.

Polarized protons from the HJet are scattered at near perpendicular angles to the beam direction. A set of three silicon detectors sit on each side of the beam perpendicular to both the beam and HJet axis, allowing for the measurement of a left right asymmetry. Due to the fact that the HJet is polarized, both target and beam asymmetries are measurable, allowing an absolute polarization measurement. However, the low rate of this detector means that many fills are required to have an accuracy of 1-2% needed to achieve the total polarization uncertainty (statistical and systematic) of 5% per beam.

2.6 Spin Rotators

As was stated above, the stable direction for polarization at RHIC is vertical. However, in order to make a measurement of A_{LL}, longitudinal polarization is required. Therefore, sets of four helical dipole magnets on each side of the

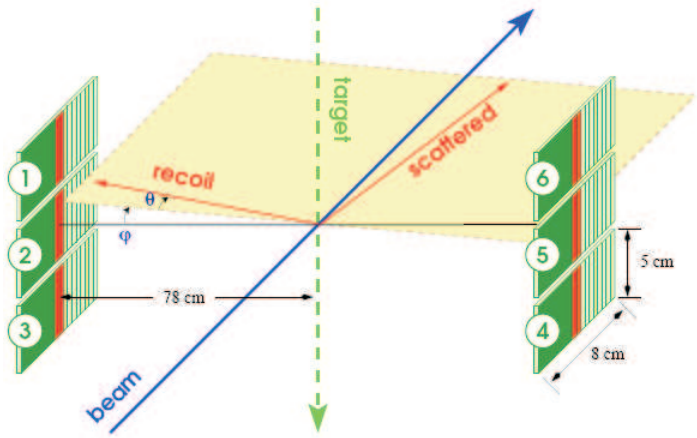

Figure 2.4: Diagram of polarized HJet polarimeter. Target protons are scattered by the beam at small recoil angles (θ) to one of six silicon strip detectors. The six silicon detectors each have 18 vertical strips, eight of which are used to detect forward scattered protons (shown in white).

PHENIX (and STAR) interaction point are used to rotate the polarization vector from the vertical axis to the longitudinal axis. These spin rotators are shown in Fig 2.1, and are described in detail in [37].

The spin rotators are designed to work independently at STAR and PHENIX, allowing each experiment to decide the polarization direction. In Run6, the STAR rotators were turned on, switching the polarization direction at STAR from vertical to longitudinal, during longitudinal running at PHENIX. As is described in Chapter 4.3, PHENIX has developed a method using a forward neutron asymmetry to determine beam direction. Several runs were taken consisting of primarily events using a special trigger for neutrons to study if any effect could be seen at PHENIX. The measured neutron asymmetry agreed well with the asymmetry prior to the turn on of the STAR rotators, indicating that the two systems are independent. However, throughout both Run5 and Run6, the PHENIX and STAR rotator currents, as well as that of the four RHIC Siberian snakes, were monitored. No runs showed unexpected values, and so no runs were discarded from the A_{LL} analyses.

2.7 Spin Pattern

The polarization pattern for bunches in RHIC can be controlled. Therefore, all four possible combinations (‘++’,‘+−’,‘−+’ and ‘−−’) can collide at PHENIX

(or any interaction point) within 4 filled crossings. In 2005, the time between crossings varied from 106 ns to 212 ns due to the changing number of filled crossings. In 2006, all crossings were filled, and so the time between crossings was 106 ns. Therefore, within 848 ns (412 ns) in the worst (best) case scenario, all possible combinations are examined, greatly reducing the systematic effects in any measured asymmetry due to detector efficiency fluctuations.

In Run5, one polarization pattern shown in Fig. 2.5a was used for all fills prior to May 26, 2005 while all four patterns in Fig. 2.5 were used afterwards. By cycling patterns, effects in any specific crossings which could adversely impact asymmetry measurements are reduced as the polarization directions associated with the specific crossings vary from fill to fill. As will be discussed in Chapter 3.3.3, different sets of electronics are used in even and odd crossings in the primary trigger for the A_{LL} analyses. This can lead to potential false asymmetry measurements, and so the asymmetries are calculated separately for even and odd crossings to prevent this possible problem. Parity violating single spin asymmetries (see Chapter 7.4), which offer a useful systematic cross check, cannot be measured when one specific crossing polarization coincides with one trigger circuit. In Fig. 2.5, an example of this is given, showing in (a) blue even crossings (colored red) always coinciding with '+' and blue odd crossings (colored blue) always coinciding with '−'. Clearly, in this case odd or even crossings will only sample two of the four possible spin combinations, and so the measurable asymmetries are limited. In 60 bunch mode, this situation never arose, but in 120 bunch mode it is possible, and did occur at the end of Run5 in a few fills. For the large majority of Run5 fills, however, this did not occur, and so the measurement was not adversely affected.

In Run6, RHIC filled 111 bunches in both rings, and so this matching of '+' to even and '−' to odd crossings described above would occur for all fills. This would badly impact PHENIX results, including A_{LL}, as the measurement of the parity violating single asymmetry would be impossible. Therefore, the spin pattern for Run6 was changed to those shown in Fig. 2.6, which ensure that all four combinations occur in both even and odd crossings. These patterns were cycled with each new fill to reduce systematic affects similar to the case of Run5.

2.8 RHIC Performance

In Table 2.1, the machine performance is listed for the parameters that most directly influence the statistical uncertainty in A_{LL}: average polarization ($\langle P \rangle$) and recorded integrated luminosity ($\int L dt$). The uncertainty in A_{LL} goes roughly as the inverse of polarization squared (actually, $frac1P_B \cdot P_Y$) times

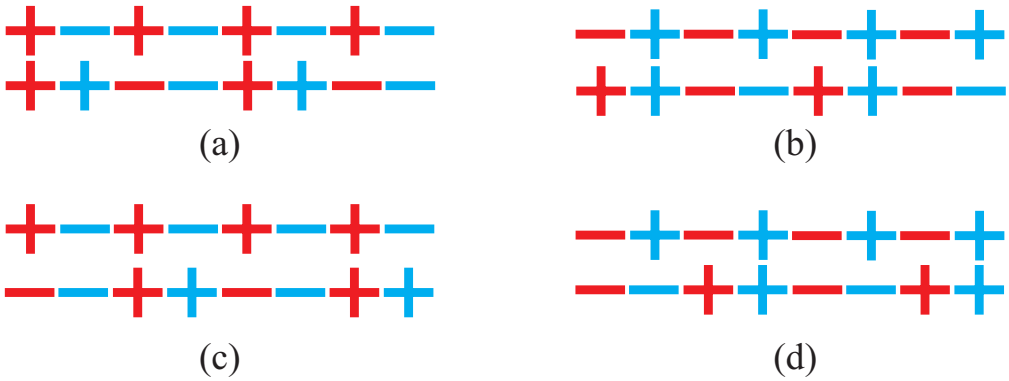

Figure 2.5: Four spin patterns used in RHIC for the two beams during Run5. In each set, top is blue ring spin pattern and bottom is yellow ring spin pattern. Red and blue colors signify even and odd crossing when all bunches are filled.

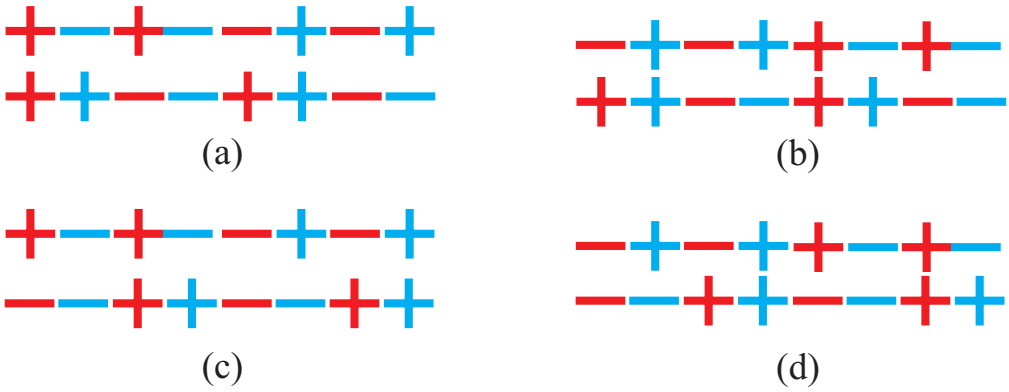

Figure 2.6: Four spin patterns used in RHIC for the two beams during Run6. In each set, top is blue ring spin pattern and bottom is yellow ring spin pattern. Red and blue colors signify even and odd crossing when all bunches are filled. In these patterns, as opposed to those used in Run5 (Fig. 2.5), both even (red) and odd (blue) crossings contain all four possible spin combinations.

the square root of the integrated luminosity. Therefore, defining the square of this quantity as the figure of merit (FOM), we have

$$FOM = \langle P \rangle^4 \cdot \int L dt \,. \tag{2.3}$$

From this definition, it is clear that a doubling of polarization is equivalent to a factor of 16 increase in luminosity. This effect is the reason that the Run6 data, with a little over twice the luminosity, is about four times more precise. From Table 2.1, it is also evident that Run5 and Run6 were the first significant data sets for measuring A_{LL}.

Table 2.1: Average polarization ($\langle P \rangle$), integrated luminosity ($\int Ldt$) and figure of merit ($P^4 L$) for the four longitudinally polarized RHIC runs with $\sqrt{s}$ = 200 GeV to date.

Year	Run	$\langle P \rangle$ (%)	$\int Ldt$ (pb^{-1})[1]	FOM (pb^{-1})
2003	Run3	27	0.35	0.002
2004	Run4	40	0.12	0.003
2005	Run5	49	3.4	0.200
2006	Run6	57	7.5	0.790

Chapter 3

PHENIX

The PHENIX Detector [41] is designed to measure rare physics probes with high rate data collection and high resolution. PHENIX consists of 4 arms: the west and east central arms, shown in the top half of Fig. 3.1, and the north and south muon arms, seen in the bottom half of Fig. 3.1. Two sets of global detectors, the beam beam counters and zero degree calorimeters can also be seen in the lower half of Fig. 3.1.

The central (east and west) arms consist of several subsystems for tracking, particle identification, and energy measurements. Each arm covers a pseudorapidity[1] range of $|\eta| < 0.35$ and $90°$ in ϕ. In each central arm, a drift chamber and a set of pad chambers (2 in the east arm, 3 in the west) are used for tracking. Both of these detectors sit outside of the azimuthal magnetic field region. A ring imaging Čerenkov detector in both arms is used primarily for electron identification. Electromagnetic calorimeters are used for energy reconstruction and event triggering.

In this work, a subset of central arm detectors, along with the global detector systems, are used, and so only those detectors are described here. For information about other PHENIX subsystems, see [41].

The coordinate system at PHENIX is defined such that the z-axis lies along the beam direction, with the positive direction taken as pointing towards the north muon arm (pointing right in lower half of Fig. 3.1). The angle ϕ is calculated with respect to the x-axis, which points into the west arm. Using a right handed coordinate system, the positive y axis is taken as the up direction.

[1] Pseudorapidity is defined as

$$\eta = -\ln\left[\tan\left(\frac{\theta}{2}\right)\right] \tag{3.1}$$

where θ is defined with respect to the beam axis.

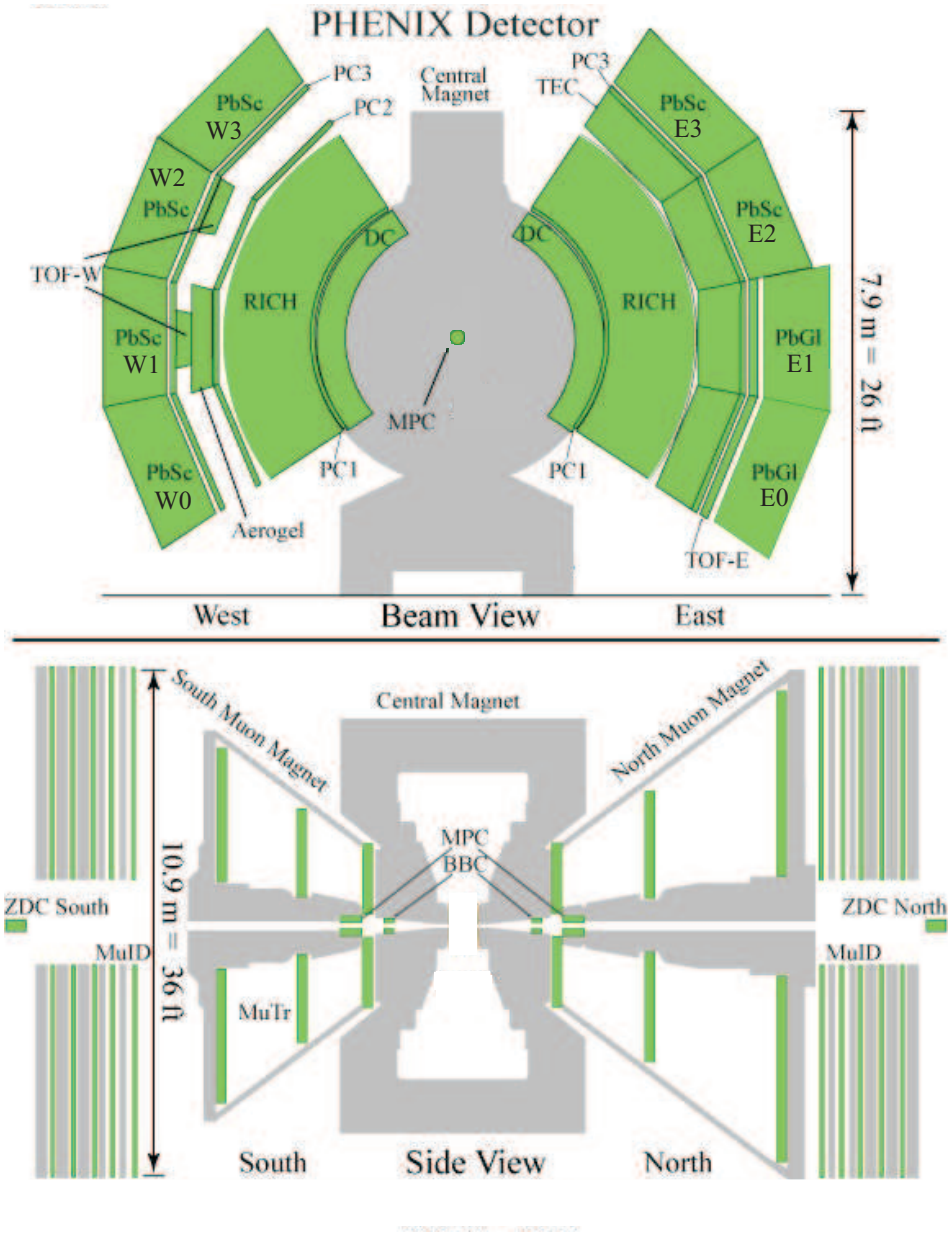

Figure 3.1: PHENIX detector set up. Not drawn to scale. Top picture shows central arm detectors with the beam into the page. Bottom picture shows the side view cross section of the detector, and the location of the global detectors (the ZDCs are located further from the IP than shown).

Table 3.1: Acceptance coverage of PHENIX detectors used in the following analyses.

Detector System	$\Delta\eta$	$\Delta\phi$
BBC	$\pm$(3.1-3.9)	360°
ZDC	>6 and <-6	360°
PbSc EMCal	$\pm$0.35	90° + 45°
PbGl EMCal	$\pm$0.35	45°
DC	$\pm$0.35	90° $\times$2
PC1 and PC3	$\pm$0.35	90° $\times$2
RICH	$\pm$0.35	90° $\times$2

Table 3.1 lists the η and ϕ coverage of the different detectors discussed in this chapter.

3.1 Luminosity Detectors

3.1.1 Beam Beam Counters

The Beam Beam Counters (BBC) [42] have three main purposes at PHENIX:

- Trigger for collisions (see Sec. 3.3)
- Vertex determination for collision
- definition of t0 for Time of Flight (ToF)

Each BBC consists of 64 photomultiplier tubes. Each tube has a quartz crystal at its head, which acts as a Čerenkov radiator. The BBCs sit at $\pm$1.44 m (in the z-direction) from the nominal center of the PHENIX detector (see Fig. 3.1), cover a pseudorapidity range of $3.0 < |\eta| < 3.9$ and have full ϕ coverage. For hadron identification with the PHENIX Time of Flight (ToF) detector [43], very good accuracy in t_0, the initial collision time measured by the BBCs, is required. Therefore, the BBC timing resolution is 52$\pm$4 ps for a single PMT. The accuracy in t_0 determination can also be used for photon identification, as is described in Chapter 5.8.2 with respect to the π^0 analysis.

The timing information in the two BBCs allow the calculation of both t_0 and the vertex position, z_{BBC}:

$$\begin{aligned} z_{\mathrm{BBC}} &= c * (t_S - t_N)/2 \\ t_0 &= (t_S + t_N)/2 \end{aligned} \tag{3.2}$$

where c is the velocity of the particles, and t_S (t_N) is the average time of prompt particles as seen by the BBC South (North). With the good timing resolution, the resulting resolution in the vertex position determined by the BBC is ∼5 cm online and ∼2 cm offline.[2] This vertex resolution is acceptable for the tracking needs in PHENIX, and the needs of the analyses in this work, but is too coarse to be able to determine secondary vertices from heavy flavor quark decays. This is a primary reason for the Silicon Vertex Detector (VTX) [44] which will be installed in 2010.

One byproduct of using Eq. 3.2 to calculate the vertex is that it assumes only a single collision per crossing. In the case of a multiple collision, the reconstructed vertex will be from particles from the two separate vertices, and therefore will actually be reconstructed as between the two real vertices. The number of multiple collisions will be correlated with the luminosity in the experiment. With the Run6 peak luminosity, multiple collision rates were ∼5%, but were much smaller for most of the running time. At the RHIC design luminosity, the multiple collision rate may be as high as 25%. Offline, the VTX detector will help distinguish multiple collisions after it is installed.

For spin dependent analyses, the BBCs are also used for spin dependent luminosity normalization, as is discussed in Chapter 4.1.

3.1.2 Zero Degree Calorimeters and Shower Maximum Detector

The Zero Degree Calorimeters (ZDC) [45] are a second collision detector system, which are the same for all 4 experiments at RHIC. The Collider-Accelerator Department (CAD) at BNL uses the ZDCs for luminosity determination at all interaction points around RHIC. For this reason, a number of triggers have been set up with the ZDCs (see Sec. 3.3).

The ZDCs are hadronic calorimeters, designed to measure very forward hadrons. Each ZDC consists of three modules with optical fiber sandwiched between Tungsten layers, which correspond to 1.7 nuclear interaction length (λ_I) per module (see Fig. 3.2). The ZDCs are located ±18 m (in the z-direction) from the center of the PHENIX detector (see Fig. 3.1). The ZDCs cover a cone of 2 mrad about the beam axis (z axis) corresponding to $|\eta| > 6$. This coverage is limited due to the space constraints between the yellow and blue beam pipes. As the ZDCs are primarily used for neutron tagging, the detector is positioned past the D_X bending magnet as seen in Fig. 3.3. The D_X bending magnets are used to steer the two proton beams back into the

[2] This resolution varies as a function of the vertex position, but is very consistent within ±30 cm of the PHENIX IP.

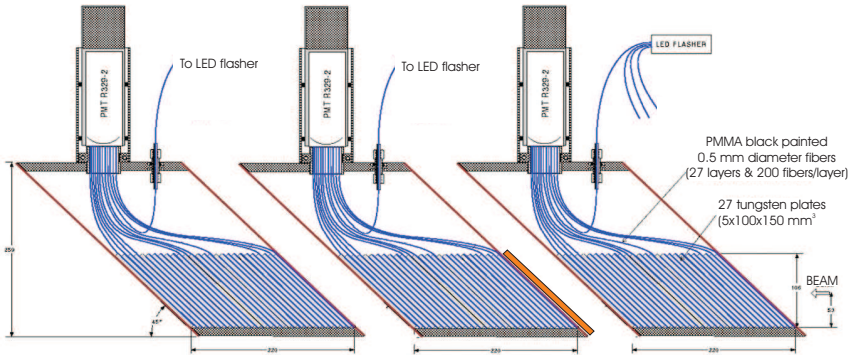

Figure 3.2: Cross section of the ZDC. Each ZDC consists of three modules. Particles created in collisions come in from the right. The SMD (orange) lies on the front of the second module, behind the first module.

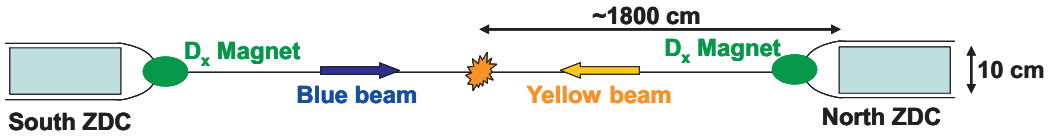

Figure 3.3: Top down view (not drawn to scale) of the location of the ZDCs with respect to the PHENIX IR and the D_X bending magnets.

two accelerator rings. This limits the detector acceptance for charged particles created in the very forward direction in the initial event.[3]

The z vertex position and t_0 can also be determined by the ZDCs, but the poorer timing resolution (∼150 ps) and the greater distance from the interaction point lead to poorer resolution in both compared to the BBCs.

A Shower Maximum Detector (SMD) sits between the first and second module of each ZDC and is used to determine the position of the hadronic shower. Photon showers are primarily contained in the first module, and so showers detected in the SMD are expected to be largely neutrons. The detector consists of 7 strips of vertical scintillator and 8 strips of horizontal scintillator, from which the x and y coordinates of the shower position can be determined.

For spin dependent analyses, the ZDCs are used in conjunction with the BBCs to estimate the uncertainty from luminosity normalization in our final asymmetry results, as is discussed in Chapter 4.1.2. The ZDCs, along with the SMDs, are used to measure the polarization direction at PHENIX on a fill

[3] A nice study of the ZDC acceptance for charged particles, primarily from protons which shower in the D_X magnet, is given in [46].

by fill basis, as is discussed in Chapter 4.3.

3.2 Electromagnetic Calorimetry

The PHENIX Electromagnetic Calorimeter (EMCal) [47] covers the full central arm acceptance, and is divided into four sections per arm. It is primarily designed to measure the position and energy of photons and electrons in the central arms.

Six sections (four in the west arm, W0-W3, and two in the east, E2 and E3, see Fig. 3.1) comprise the Lead Scintillator (PbSc) EMCal. Each sector contains 36×72 towers and cover $|\eta| < 0.35$ and $\phi = 22.5°$. Each tower is 5.5×5.5 cm^2 and consists of 66 sampling cells, composed of 1.5 mm lead slabs in front of 4 mm of scintillating material. This corresponds to 18 radiation lengths (X_0), or 0.85 λ_I. From test beam data, the energy resolution is

$$\frac{\sigma_E}{E} = 2.1\% \oplus \frac{8.1\%}{\sqrt{E}} \,. \tag{3.3}$$

The detector was calibrated using test beam data, minimum ionizing particles, and the π^0 mass peak.

The final two calorimeter modules in the east arm (E1 and E2) are comprised of lead glass (PbGl). Each sector contains 48×96 towers and cover $|\eta| < 0.35$ and $\phi = 22.5°$. Each tower is 4.0×4.0 cm^2 and consists of homogenous lead glass Čerenkov radiator. This corresponds to 14.4 X_0, or 1.1 λ_I. The energy resolution was measured at WA98, and is

$$\frac{\sigma_E}{E} = 0.8\% \oplus \frac{5.9\%}{\sqrt{E}} \,. \tag{3.4}$$

The two different types of EMCal at PHENIX allow for a systematic cross check of measurement results. In Chapter 7.2, the results for π^0 A_{LL} for the two different EMCal types are compared.

3.3 Triggering

Due to the limited luminosity available, and rareness of the physics events of interest, a number of triggers have been designed to ensure a significant fraction of these events are recorded. The triggers consist of two type: event, in which a global requirement is met, and particle, in which the event has a high likelihood of containing a specific particle of interest. Here, only the

triggers used in the A_{LL} analyses and related spin measurements are discussed.

3.3.1 BBC Level 1 Triggers

The main trigger for events in PHENIX relies on a coincidence between the two BBCs. For $p+p$ running, a minimum requirement of 1 tube per side is required. Two triggers are defined in this manner. The first, *BBCwide*, triggers based on any such coincidence. The second, *BBCLL1*, requires the event to occur in a limited z range. A vertex position (z_{BBC}) is reconstructed using Eq. 3.2 with an online resolution of 5 cm. For BBCLL1, an online cut of $|z_{BBC}| < 30$ cm is applied to all events in BBCwide. BBCLL1 is defined as our minimum bias (minbias) trigger condition for all events used in the following analyses.

The cross section sampled by the BBC was measured, and found to be 21.8(9.6%) mb [48]. This cross section is used to normalized all cross sections measured at PHENIX. It is also used to determine the size of any data sample solely from the number of minbias events.

3.3.2 ZDC Level 1 Triggers

For spin dependent analyses at PHENIX, there are three important triggers incorporating the ZDCs. For luminosity determination, two triggers are used which require a coincidence between the two ZDCs. Again, using timing differences between hits in the ZDCs, an online vertex (z_{ZDC}) can be reconstructed with a resolution of roughly 30 cm. Two triggers are defined based on online vertex cuts. The *ZDCnarrow* trigger requires a reconstructed vertex with $|z_{ZDC}| < 30$ cm, in nominal agreement with the minbias cut. As is discussed in Chapter 4.1.2, a comparison in luminosity measured with the minbias and ZDCnarrow triggers is used for estimating the systematic uncertainty in luminosity normalization. The *ZDCwide* trigger requires $|z_{ZDC}| < 150$ cm, and is primarily used to correct for the poor resolution of the ZDC in the luminosity analysis.

Another important ZDC dependent trigger in spin analyses is used for Local Polarimetry as described in Chapter 4.3. This *LocalPol* trigger requires an energy deposit in one ZDC (north or south) in coincidence with a minbias trigger, and is used to tag events with a very forward neutron.

3.3.3 EMCal RICH Trigger

In order to record rare events, such as particles with high transverse momentum (p_T), an additional trigger is required beyond minbias. The EMCal RICH

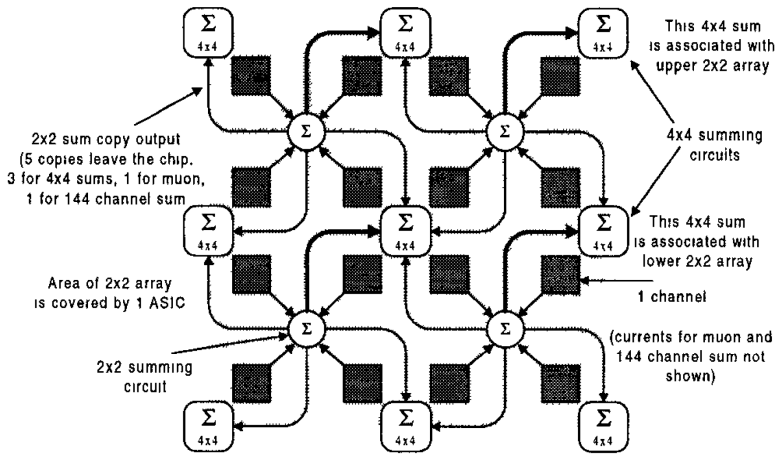

Figure 3.4: Diagram of ERT trigger explaining overlapping trigger tile arrangement in the 4×4 tower triggers used for both π^0 and charged pion analyses.

Trigger (ERT) triggers on events in which there is a large localized energy deposit in the EMCal.[4] The EMCal towers are grouped in sets of 2×2 towers, which make up a basic trigger tile. The concept is that if some energy deposit is above a threshold in one tile, then the event will be triggered. However, in this case, if a high energy particle splits its energy in neighboring tiles, the threshold might not be met for any one individual tile. Therefore, overlapping trigger tiles are set up, consisting of 2×2 neighboring basic tiles, to create a 4×4 tower trigger. There are 3 versions of this trigger, which differ only in the threshold energy. 4×4a, 4×4b, and 4×4c, as they are named, require respectively a 2.1, 2.8 and 1.4 GeV energy deposit in a 4×4 tower block made up of 4 neighboring basic tiles. A diagram of the circuit is shown in Fig. 3.4.

Sets of 12×12 towers are grouped into supermodules, which are used in the trigger logic for event triggering. Supermodules are the smallest triggering unit written in the output data.

For the Run5 π^0 and charged pion results, only events triggered with 4×4c (the lowest threshold) was used. However, in Run6, the PbGl section of the ERT had many noisy trigger tiles, and so only 50% of the lowest threshold ERT trigger was live in these sections. Therefore, the 4×4a trigger was also

[4]For triggering on electrons, a corresponding signal in the RICH can also be required in the trigger, which is why the trigger is called the EMCal *RICH* Trigger. However, for the analyses in the present work, only the sufficient energy deposit is required.

used in Run6, recovering most of the noisy trigger tiles at this higher energy threshold. In the remainder of this work, the trigger requirement will be called the ERT trigger, signifying 4×4c in Run5 and the 'OR' of 4×4c and 4×4a in Run6.

Trigger Problem

In Run5, for the first time RHIC ran in 120 bunch mode (see Chapter 2). This required both even and odd bunches to be filled. As is discussed in [49], the ERT trigger reset takes about 140 ns, longer than the 106 ns between RHIC bunches in 120 bunch mode. In order for the trigger to work in 120 bunch mode, the trigger was designed as two alternating sets of circuits distinct for odd and even crossings. For asymmetry measurements such as A_{LL}, we assume that efficiency issues are helicity and crossing independent. However, if the trigger efficiency is not the same for the two distinct ERT trigger circuits, then the assumption fails. This is seen very clearly in Fig. 7.6, where a clear false parity violating asymmetry is seen towards the end of the 2005 running period. During this period of large false asymmetry, the blue spin pattern completely matched the two circuits (i.e. blue '+' with odd crossings, blue '−' with even), as is shown in Fig. 2.5. Such a false asymmetry indicates that the trigger efficiencies for the two circuits differ, and so one cannot correctly measure asymmetries using all bunches. This is most significant in the p_T range where the efficiencies are rapidly changing. For this reason, all asymmetries are measured separately for odd and even crossings if ERT triggered events are used in a p_T region of changing ERT trigger efficiency.

3.3.4 GL1p Boards

It is very important for measuring A_{LL} to have an accurate count of the luminosity for different helicity states. The average rate for minbias events in 2005 (2006) was 60 kHz (200 kHz). Even with the very high rate of data taking with the PHENIX Data Acquisition System (DAQ) [50], which can record up to 7 kHz of data, most triggers are prescaled (only every jth event is recorded). If one simply uses the number of prescaled minbias events, N_{pre}, scaled up by the prescale factor (j), giving a luminosity $L = jN_{pre}$, the uncertainty in luminosity is

$$\sigma_L = j\sqrt{N_{pre}}$$

as j is a constant. If the total number of triggers (N_{tot}) is recorded, then the uncertainty in luminosity measured this way ($L' = N_{tot}$) is simply

$$\sigma_{L'} = \sqrt{N_{tot}}.$$

Now if we assume

$$N_{tot} = jN_{pre} + n$$

where $0 < n < j$, then

$$\sigma_{L'} = \sqrt{jN_{pre} + n} \simeq \sqrt{jN_{pre}} = \frac{\sigma_L}{\sqrt{j}} \,. \tag{3.5}$$

Thus we see that the uncertainty in luminosity increases by a factor of $\sqrt{j}$ if we simply define $L = jN_{pre}$.

In order to get a more accurate luminosity measurement, a set of scaler boards called the GL1p boards are used [50]. These boards record the total number of triggers per beam crossing when the DAQ was live (able to take data) for up to four different triggers. For both the 2005 and 2006 runs, the minbias (BBCLL1), ZDCnarrow and ZDCwide triggers were used. In 2005, the fourth trigger used was the ERT4x4c trigger, not in coincidence with the minbias trigger. In 2006, the fourth trigger was CLOCK, which triggers on every bunch crossing when the DAQ is live regardless of whether a collision occurs.

Aside from having a very accurate luminosity, because these boards record triggers for each bunch crossing, they also allow measurement of helicity dependent asymmetries in the luminosity measurement. Such studies are discussed in Chapter 4.1.

3.4 Tracking

PHENIX uses two detectors, the Drift Chamber (DC) and three layers of Pad Chambers (PC1, PC2, and PC3), primarily for tracking in the central arm. These detectors can be seen in Fig. 3.1.

3.4.1 Magnets

Before discussing tracking in PHENIX, we must first consider the magnetic field required to measure such charged tracks. The PHENIX magnet system [51] consists of three independent magnets, the north and south muon magnets and the Central Magnet (CM). Only the field of the CM is germane to this work, and so we focus on it here. The CM consists of two independent concentric coils and provides a field parallel to the z-axis. In Run5 and Run6, the fields from the two coils were set so they added ('++' configuration), yielding a magnetic field integral of $\int \boldsymbol{B} \cdot d\boldsymbol{\ell} = 1.15$ T m. The field lines in the CM '++' configuration can be seen in Fig. 3.5, along with those of the muon magnets.

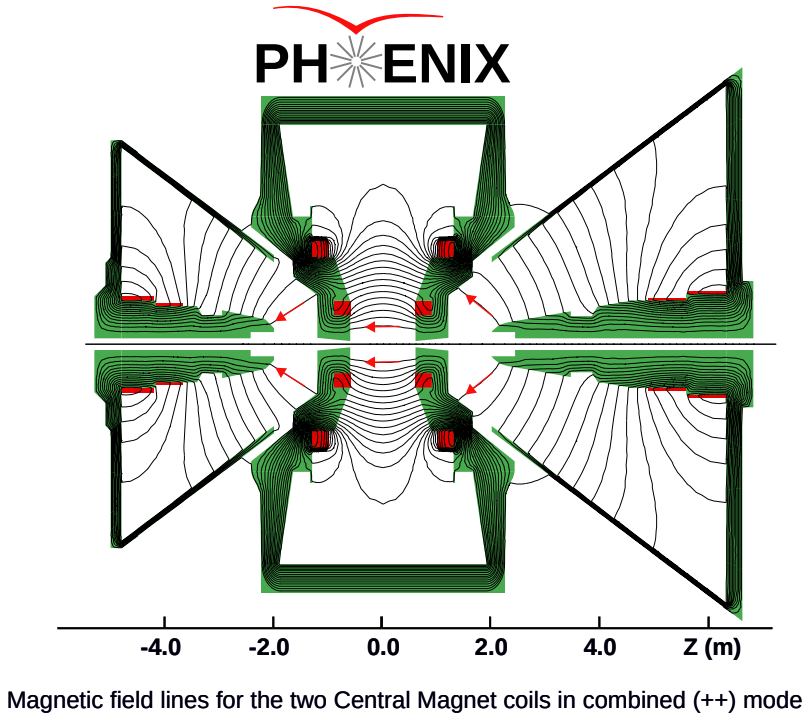

Figure 3.5: PHENIX magnetic field set up in Run5 and Run6.

The magnet was designed so that it was outside of the acceptance of the central arms. Therefore, the pole tips of the central magnet sit at z=±40 cm from the center of PHENIX. The CM was also design so that the field strength is significantly reduced in the region of the central arm detectors ($r > 2$ m), and is small enough such that $\int_{2.4}^{4.0} \boldsymbol{B} \cdot d\boldsymbol{\ell} < 0.01$ T m, where this is the region covered by the RICH (see Fig. 3.1).

3.4.2 Drift Chamber

The Drift Chamber (DC) has been described in detail in [52]. Each central arm contains an independent DC (see Fig. 3.1), composed of an multiwire gas chamber, filled with a 50%/50% mixture of Argon and Ethane gas.

A cross section of the detector is shown in Fig. 3.6. Six sets of wires are stacked radially. The X1 and X2 wires run parallel to the beam pipe, and are the main elements in determining p_T for charged particles. The U and V wires run slightly off parallel to the X wires, as is seen on the right of Fig. 3.6, and give some resolution in the ϕ direction. To reduce the occupancy in heavy ion collisions, the detector is split at the z=0 plane, with wires on each side

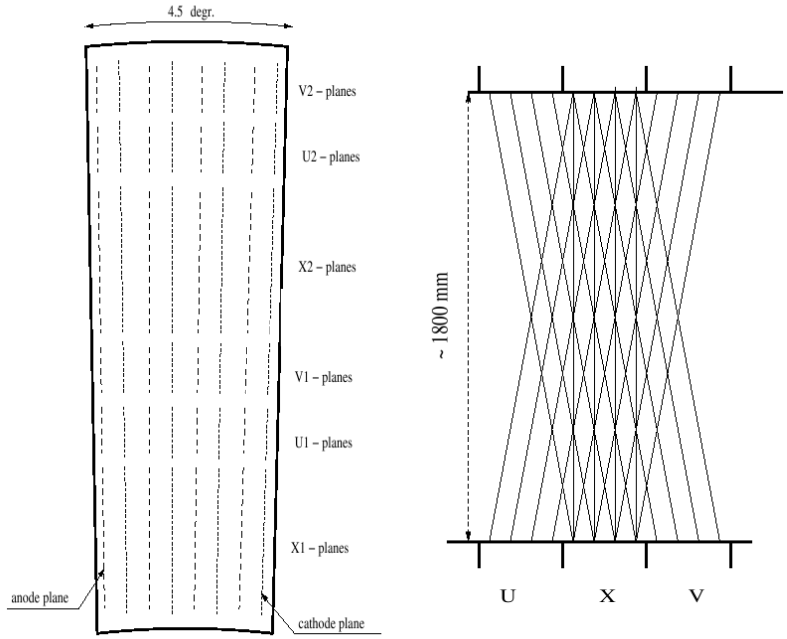

Figure 3.6: Left: Cross section of the DC in the r-ϕ plane showing wire layout. Right: Top view of same section, showing crossing angle of X, U and V strips.

readout independently. Therefore tracks traveling through this region may not generate the expected signal.

The DC covers the full acceptance of the central arms, with $\Delta\eta$=0.7 and $\Delta\phi$=90° in the each of the central arms. The DC is the closest detector to the beam pipe in the radial direction, located from 2-2.4 m radially from the z-axis. The front and back (radially) walls of the DC consist of thin Aluminum mylar window 125 μm thick. This wall was designed to have a small radiation length to reduce the number of photon conversions, as the DC is the first tracking detector in the radial direction.

3.4.3 Pad Chambers

There are three separate layers of multiwire proportional chambers that compose the PHENIX Pad Chamber (PC) as seen in Fig. 3.1. The first layer of PC (PC1) sits just after the DC (with respect to the beam), covering the full acceptance of the central arms (90° $\times$2, $|eta| < 0.35$), and is used in conjunction with the DC to determine the momenta of charged particles (see next section).

In the west arm only, a second layer of PC lies just behind the RICH. However, as the acceptance is limited, it will not be used in the following analyses. A third layer of PC (PC3) sits 20 cm in front of the EMCal, and also covers the full central arm acceptance. This layer is primarily used as a veto on poorly reconstructed tracks in charged particle analyses. In the π^0 analysis, it is used as a method of vetoing clusters in the EMCal associated with charged tracks.

3.4.4 Track Determination and Momentum Reconstruction

Tracks in PHENIX are defined using hits from the PC1 and the two X and UV layers in the DC. The quality of the track depends on whether there are hits in each of these detector layers. While the acceptable quality varies for different analyses, in general most require hits in all layers. For the charged pion analysis in this work, the required track quality is discussed in Chapter 5.11.1.

In most experiments,[5] tracking detectors are placed in the region of high magnetic field so that multiple points along the bent path are determined in order to get an accurate momentum measurement. In PHENIX, the DC and PC are outside the region of strong magnetic field, and so a different method is required.

Fig. 3.7 shows the basic method of determining the momentum of a track in the r-ϕ plane. Charged particles will bend in the strong magnetic field in the interior of PHENIX. This field is significantly smaller at the DC, and so the track is (nearly) straight. To determine the track p_T, we define two vectors in the r-ϕ plane: (1) the line that best describes the hits in the DC and PC1 associated with the track and (2) the line which intersects this line at the midpoint in the DC (r=2.2 m) and goes through the vertex (dotted line in Fig. 3.7).[6] The angle between these vectors is defined as α, and is used to define the momentum of the track, as it defines the deviation of the track arc from a straight line (*i. e.*, infinite momentum).

To get the z momentum of a track, a hit in the PC1 is required, which gives a single space point associated with the track. Assuming the track originated at the vertex, the total momentum can be calculated as the track will not bend in the z direction.

[5]This includes the PHENIX Muon arms and in the future, will include the central arms after the Silicon Vertex Detector is installed.

[6]The vertex may not necessarily lie at $x = 0$, $y = 0$. The actual vertex is calculated in special runs when the magnetic field is turned off. In this case all charged tracks are straight, and point to the real x, y of the vertex. It is this point from which tracks are assumed to originate in all other running times.

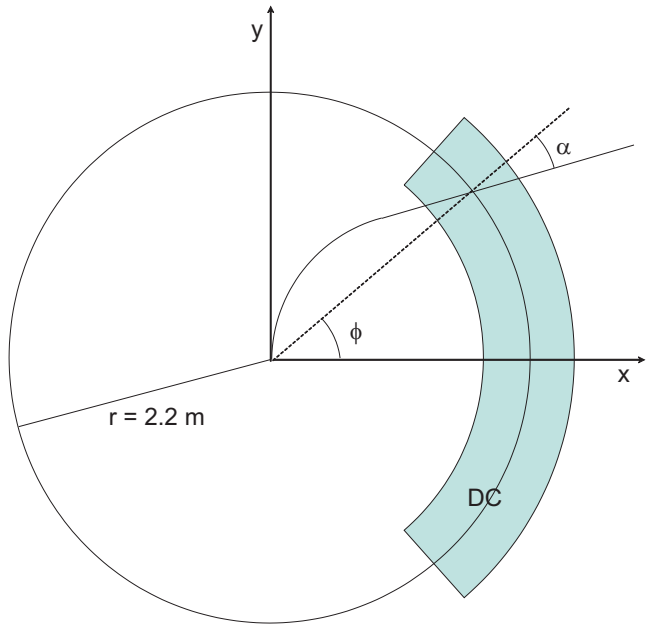

Figure 3.7: Definition of α for a charged track bent in the magnetic field. p_T is proportional $1/\alpha$.

As will be discussed in Chapter 5.12, a side effect of measuring charged particle momenta in the region outside of the magnetic field is that late conversion before the tracking detector may generate tracks with larger momenta than they actually have. To reduce the amount of such conversions, in Run5 a helium bag was inserted between the beam pipe and the DC. In Run6, a helium bag was not installed as it interfered with a prototype of the Hadron Blind Detector (HBD) [53]. The HBD prototype sat well within the magnetic field region, and so the momenta of conversion electrons were nearly correct. However, this did create a slightly larger overall background in the π^0 measurement after the HBD prototype was installed.

3.5 Particle ID

The PHENIX ToF [43] cannot distinguish charged pions from other hadrons above 2.8 GeV. In order to identify high p_T charged pions from other hadrons, a ring-imaging Čerenkov (RICH) detector is used.

3.5.1 Ring-Imaging Čerenkov Detector

The PHENIX RICH [43] is filled with CO_2 gas and sits between the PC1 and PC2/3 detectors in both arms, as seen in Fig. 3.1. It is primarily used for discriminating electrons from charged hadrons in electron analyses. The index of refraction, n, for CO_2 is 1.000449, and so the threshold momentum for producing Čerenkov light is 17 MeV/c for electrons, 4.7 GeV/c for charged pion and 16.5 GeV/c for kaons. Therefore, for $4.7 < p_T < 16.5$ GeV/c, the RICH can be used for identifying charged pions from other hadrons.

Chapter 4

Measurement Requirements

As was written in Chapter 1.8, A_{LL} can be written as

$$A_{LL} = \frac{1}{P_B P_Y} \frac{\frac{N^{++}}{L^{++}} - \frac{N^{+-}}{L^{+-}}}{\frac{N^{++}}{L^{++}} + \frac{N^{+-}}{L^{+-}}} \ . \tag{4.1}$$

In order to measure A_{LL}, three items are required: luminosity normalization, polarization, and particle yields. In this chapter, we focus on the on the first two of these, and leave the last for Chapter 5.

4.1 Luminosity Normalization: Relative Luminosity

Luminosity measured with a detector can be written as

$$L = \frac{N}{\sigma_{det}} \tag{4.2}$$

where N is the number of $p + p$ collisions measured by the detector and σ_{det} is the inelastic $p + p$ cross section measured by the detector, defined as

$$\sigma_{det} = \sigma_{\text{inelastic}}^{pp \to X} * \varepsilon_{eff} \tag{4.3}$$

Here, $\sigma_{\text{inelastic}}^{p+p \to X}$ is the total inelastic $p+p$ cross section, and ε_{eff} is the efficiency of the detector. As was discussed in Chapter 2, the bunch pattern at RHIC allows us treat this efficiency as spin independent.

If we consider the ratio of luminosities from the two spin states, defined as

relative luminosity,

$$R = \frac{L_{++}}{L_{+-}} \ , \tag{4.4}$$

then the spin independent efficiencies will cancel. If we likewise assume that the polarized cross sections measured by the detector are helicity independent, we merely must count the number of collisions in '++' and '+−' crossings, N^{++}_{Lum} and N^{+-}_{Lum} respectively, and take the ratio. In this case, Eq. 4.1 can be rewritten as

$$A_{LL} = \frac{1}{P_B P_Y} \frac{N^{++} - RN^{+-}}{N^{++} + RN^{+-}} \tag{4.5}$$

where now R is now given by

$$R = \frac{N^{++}_{Lum}}{N^{+-}_{Lum}} \ . \tag{4.6}$$

The validity of this assumption is discussed in Sec. 4.1.2, and leads to the largest systematic uncertainty in the final results for A_{LL}.

At PHENIX, the two main detectors used for luminosity measurements are the BBCs and the ZDCs. For luminosity normalization, we require a detector with (1) low background and (2) high statistics that (3) samples the z-vertex region which corresponds to that of our asymmetry data sample ($|z_{BBC}| < 30$ cm, see Chapter 5.1.2). The first two requirements are obvious of any detector, so here only the third is discussed in detail.

For measurements with the central arms (including π^0 and $\pi^{\pm}$), the z-vertex range is restricted to 30 cm on either side of the IP. There are two main reasons for this restriction. First, the number of collisions within the region does not change much with z as the collision distribution width is about 60 cm, whereas the number drops off quickly outside of 35 cm. Second, the iron magnet pole tips are located at $z = \pm 40$ cm, blocking the central arm acceptance from events outside the accepted region. For luminosity normalization, we need to measure the luminosity which can actually affect the measurement. A simple example will clarify this point.

Assume two bunch crossings are to be measured, one with same helicity bunches, and the other with opposite helicity. Assume that the same helicity crossing has N collisions for $|z| < 30$ cm evenly distributed, while the opposite helicity crossing has $2N$ collisions for $|z| < 60$ cm evenly distributed. Therefore both bunches would have the same number of collisions for $|z| < 30$ cm. If the relative luminosity is calculated using only the z region which is used in the analysis, R=1. However, if the full luminosity is used for both crossings, R=$\frac{1}{2}$, which will clearly skew the results incorrectly.

Figure 4.1 shows the background levels in the BBCs and the ZDCs for

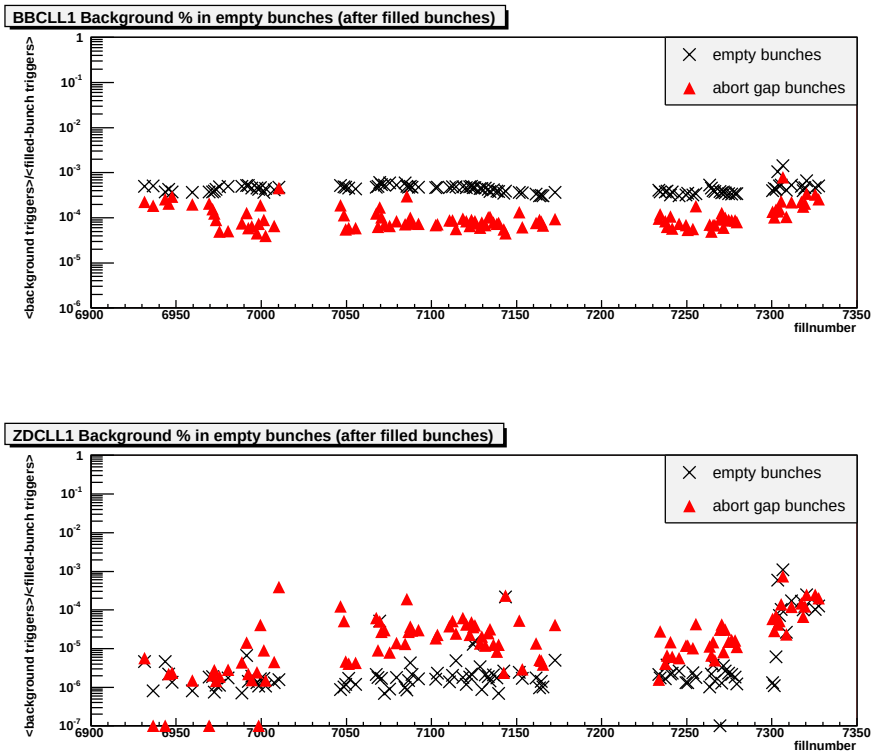

Figure 4.1: Average percentage background in live triggered events for "empty" (black ×'s) and abort gap (red triangles) crossings vs. fill number for BBCLL1 (top) and ZDCLL1 (bottom). See text for definition of abort gap and "empty" crossings.

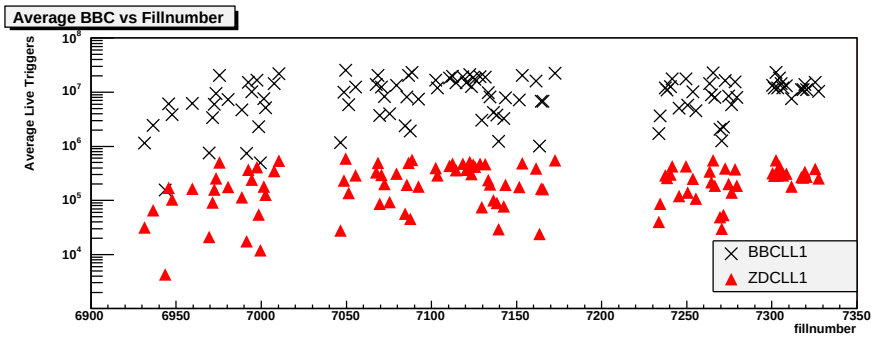

Figure 4.2: Live trigger counts averaged over good filled crossings vs. fill number for BBCLL1 (black ×) and ZDCLL1 (red triangles).

empty and abort gap crossings. For this background study only, an "empty" crossings is defined to be an unfilled crossing following a filled crossing, while abort gap crossings were set to be 32-39 and 112-119 (the first abort gap crossing was excluded because normally it follows a filled bunch). The two types of empty crossings are separated in order to see if there is any effect in a crossing (filled or empty) following a filled bunch. From Fig. 4.1(top), there is roughly 5 times higher background on average in "empty" crossings compared to abort gap crossings, indicating a small ($< 0.1\%$) background in crossings that may be attributed to other filled bunches nearby. The primary cause of this effect is due to afterpulses in the BBCs either in coincidence with beam gas or an afterpulse in the second BBC. This effect should not be spin dependent, and the use of four spin patterns in RHIC means that no one helicity pairing is more highly favored in terms of increased statistics due to background. Fig. 4.1(bottom) shows that the background in the ZDC is also less than 0.1%.

Figure 4.2 shows the fill dependent BBCLL1 (black ×'s) and ZDCLL1 (red triangles) live trigger counts averaged over good filled crossing. The BBCLL1 trigger records ∼40-45 times more events than the ZDCLL1.

Finally, as discussed in Chapter 3.3, the online resolution of the BBC is ∼5 cm, while the online ZDC resolution is ∼30 cm. Therefore, the z-vertex region sampled by the BBCs much more accurately matches the actual offline z-vertex region used in the analysis ($|z_{BBC}^{\text{offline}}|<30$ cm). As the BBCs offer (1) greater statistical precision than the ZDCs with (2) an acceptably small background and (3) a more accurate description of the z-vertex acceptance, they (specifically BBCLL1 triggered events) are used for Relative Luminosity.

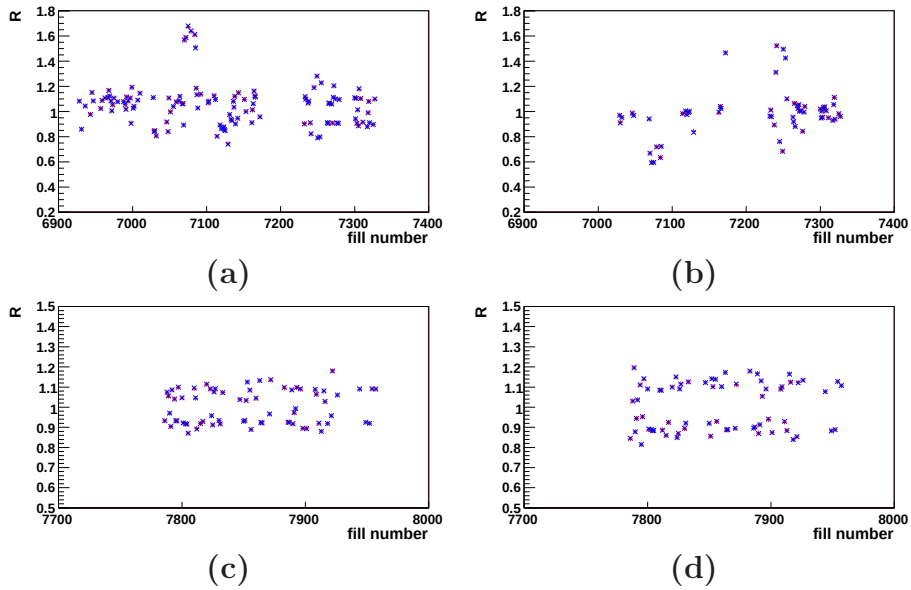

Figure 4.3: Relative Luminosity vs. fill number as measured by the BBCs (red +'s) and ZDCs (blue x's) for (a) even and (b) odd crossings separately for Run5 and (c) even and (d) odd crossings separately for Run6. As fills prior to fill 7046 in Run5 were in 60 bunch mode, only even bunches were filled, and hence there is no Relative Luminosity for odd bunches in these fills.

4.1.1 Run5 and Run6 Relative Luminosity

Figures 4.3a, 4.3b, and 4.4 show the Relative Luminosity from BBCLL1 (red +'s) and ZDCLL1 (blue ×'s) triggered events vs. fill number using only "good" even crossing, only "good" odd crossings, and all "good" crossings, respectively. "Good" crossings are defined as filled crossings with a reasonable ratio of BBCLL1 and ZDCLL1 triggers. Figures 4.3c, 4.3d, and 4.4 show the same for Run6. All fills shown are from longitudinal $\sqrt{s}$ =200 GeV running. Data for BBCLL1 and ZDCLL1 come from the GL1p board (see Chapter 3.3.4.

By comparing the ZDC values of Relative Luminosity with those of the BBC, we can look for systematic uncertainties in the assumption used to get Eq. 4.6, i.e. that σ_{BBC} is spin independent. In the following sections, a more sophisticated test will be applied.

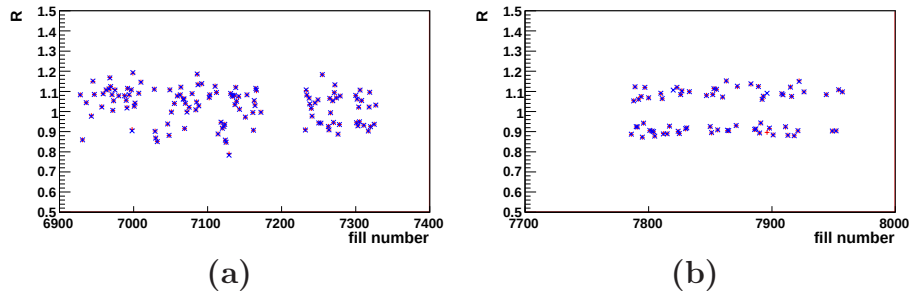

(a) (b)

Figure 4.4: Relative Luminosity vs. fill number for (a) Run5 and (b) Run6 as measured by the BBCs (red +'s) and ZDCs (blue x's) for all (even *and* odd) bunches.

4.1.2 Uncertainty in R and Propagation to A_{LL}

Using standard error propagation and Eq. 4.5, the uncertainty in A_{LL} due to the uncertainty in Relative Luminosity is found to be

$$\delta A_{LL}|_R = \frac{1}{|P_B||P_Y|}\frac{2N_{++}N_{+-}}{(N_{++}+RN_{+-})^2}\delta R\,. \tag{4.7}$$

For the case of small asymmetries, where $N_{++} \simeq RN_{+-}$, then we have

$$\delta A_{LL}|_R \sim \frac{1}{|P_B||P_Y|}\frac{2N_{+-}^2 R}{(2N_{+-}R)^2}\delta R = \frac{1}{|P_B||P_Y|}\frac{\delta R}{2R}\,. \tag{4.8}$$

As discussed above, Relative Luminosity is measured using the BBCs. $\delta R/R|_{stat}$ for an average (8 hour long) fill for Run5 (Run6) is less than $2\times 10^{-2}\%$ ($4\times 10^{-3}\%$), which is essentially negligible. The two largest systematic sources of uncertainty are a possible asymmetry in the measured cross sections for different helicities and inaccurately measuring the total luminosity.

Through comparison with luminosity measured by the ZDCLL1 trigger, both of these systematics can be estimated.

Method

Due to the large systematic uncertainties ($\sim 10\%$) in the measured BBC cross section, determination of whether or not it is helicity independent cannot be done directly. Therefore, we look for a possible double spin asymmetry in the ratio of the number of triggered events from the two luminosity detectors, BBC and ZDC. This asymmetry, $A_{LL}^{ZDC/BBC}$, can be measured using Eq. 4.5. However, bunch to bunch variations which may lead to a systematic uncertainty

can be missed. As the statistics measured by both detectors is large, a crossing by crossing analysis is used instead.

For a crossing i, we define the ratio

$$r(i) = \frac{N_{ZDC}(i)}{N_{BBC}(i)} \ , \tag{4.9}$$

where $N_{BBC}(N_{ZDC})$ are the total triggered events in a fill for the BBCLL1 (ZDCLL1) in crossing i. If there is no asymmetry in the ratio, the ratio should be described by a constant fit. The ratio is plotted for a Run6 fill vs. crossing number in Fig 4.5a.

To account for a possible asymmetry, the data is actually fit with the function [54]

$$r(i) = c[1 + \epsilon_{LL} S_B(i) S_Y(i)] \tag{4.10}$$

where $S_{B(Y)}(i)$ is the sign of the polarization of the ith bunch in the blue (yellow) beam, and c and ϵ_{LL} are the two fit parameters. c is the constant expected if there is no asymmetry, and ϵ_{LL} is the raw asymmetry, related to A_{LL} by

$$A_{LL} = \frac{\epsilon_{LL}}{P_B P_Y}. \tag{4.11}$$

The asymmetry in Eq. 4.10 is equivalent to that measured using Eq. 4.5, as is shown in Appendix A.3. This method, however, can make it easier to identify bunch to bunch systematic uncertainties, as will be seen below.

If ϵ_{LL} is consistent with zero, then the asymmetry in the BBCLL1 is the same, within uncertainties, as the asymmetry in the ZDCLL1. The BBCs and ZDCs cover very different pseudorapidities (see Table 3.1) and trigger on different particles, and so if the asymmetries of the two detectors are consistent, then the asymmetries are most likely zero.

The χ^2 per degrees of freedom (χ^2/DOF) distribution for fits to all fills in Run5 and Run6 is shown in black in Fig. 4.6a and Fig. 4.6b, respectively. The DOF vary in Run5 from 43 to 97, due the varying number of filled bunches used that year. In Run6, the DOF varied from 90 to 96. The distribution in both cases is wide and not peaked at 1, indicating that there are unaccounted for systematic uncertainties in the ratio r.

Width Correction

As was discussed above in Sec. 4.1, the ZDCLL1 resolution is ∼30 cm, and so smears out the measured vertex position. Therefore, the sampled vertex in the online trigger differs between the two detectors. Fig. 4.7a shows r vs. the width of the z-vertex distribution from ZDC triggered events. A clear correlation is

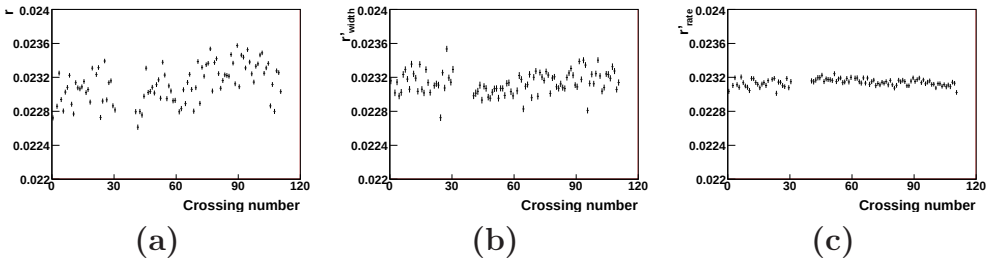

Figure 4.5: Ratio of ZDCLL1 triggers to BBCLL1 triggers vs. crossing number for (a) uncorrected, (b) width corrected and (c) rate corrected.

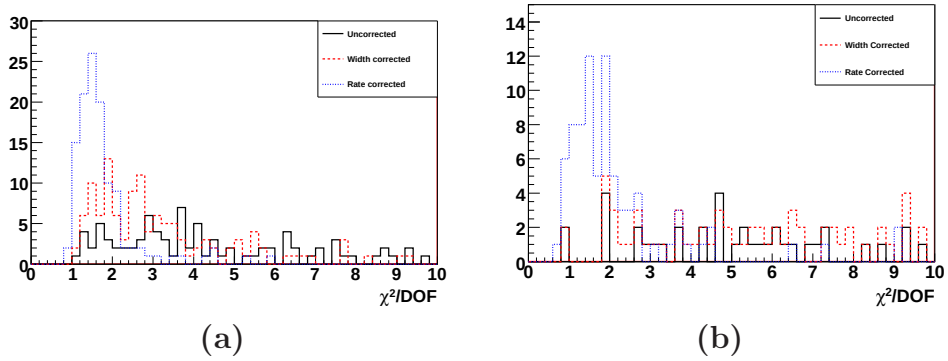

Figure 4.6: χ^2/NDF distributions from all fills in (a) Run5 and (b) Run6 from fits using the uncorrected (black solid line), width corrected (red dashed line) or rate corrected (blue dotted line) ratio.

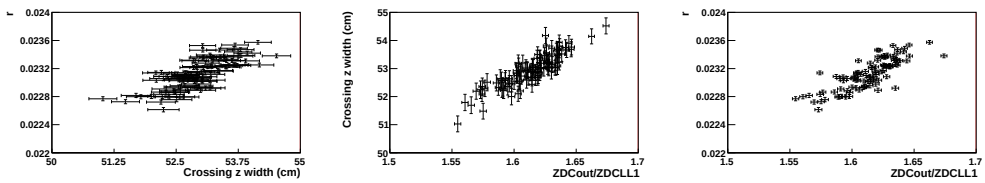

(a) (b) (c)

Figure 4.7: (a) r vs. the bunch crossing distribution width. (b) bunch crossing distribution width vs. the ratio of ZDCout to ZDCLL1. (c) r vs. the ratio of ZDCout to ZDCLL1. Points correspond to individual crossings in a single fill.

visible. Given the two ZDC triggers available, ZDCwide ($|z| < 150$ cm) and ZDCLL1 ($|z| < 30$ cm), we define

$$ZDCout = ZDCwide - ZDCLL1. \tag{4.12}$$

Fig. 4.7b shows a clear correlation between $ZDCout/ZDCLL1$ and the width of the z-vertex distribution from ZDC triggered events. As the amount of ZDC triggered data recorded during regular data taking is small, and this data would be needed to reconstruct the ZDC z-vertex distribution, we use the GL1p scalers to calculate the ratio $ZDCout/ZDCLL1$. Fig. 4.7c shows that r and $ZDCout/ZDCLL1$ are correlated, indicating it is a good proxy for ZDC width.

By applying a linear fit to plots similar to Fig. 4.7c for each fill, the correlation between r and the ZDC z-vertex width can be parameterized on a fill by fill basis [54]. $r(i)$ can then be corrected for this ZDC smearing issue using the formula

$$r'_{width}(i) = \langle r(i) \rangle \frac{r(i)}{p0 + p1(N_{ZDCout}/N_{ZDCin})} \tag{4.13}$$

Fig. 4.5b shows r'_{width} vs. crossing number. Although some systematics have been removed by this correction, other systematic sources clearly exist. This is also seen in the red χ^2/DOF distributions in Fig. 4.6a and b, which, while closer to what is expected for a pure statistical distribution, still has a peak significantly great than 1.

Rate Correction

As discussed in Chapter 3, both the BBCLL1 and ZDCLL1 triggers cannot distinguish between single and multiple collisions. As the luminosity increases, so does the number of events with more than one collision, called multiple collision events. However, a detector with a smaller cross section (ZDCLL1)

will (naively) be less affected in determining the total cross section than a detector with larger cross section.

This can be seen by a simplified example[1]. Assume there are 100000 measured events, and 10% are multiple (for simplicity, double) collisions. Also assume the luminosity is measured with two sets of detectors, A and B, which sample 25% and 2% of total collisions. For the 90000 single collision events, detector A (detector B) records 22500 (1800) collisions. For the 10000 double collision events, detector A (detector B) will see 5000 (400) collisions,[2] but 625 (4) collisions will be in events with another collision, and so only 4375 (396) events will be recorded. The actual number of collisions was 110000, while detector A (detector B) gives the number of events as 26875 (2196) which, when scaled by efficiency, gives the total number of events as 107500 (109800). Such scaling factors drop out in any A_{LL} calculation, and so the BBCLL1 statistically is the better luminosity detector, but this does indicates that for a detector which samples a large fraction of the $p+p$ cross section, multiple collision issues becomes a larger problem as the rate increase.

As the ZDCLL1 sees fewer events than BBCLL1 (see Fig. 4.2), the ZDC can in principle be used to test for BBCLL1 rate effects and how r is affected. Fig. 4.8 shows r plotted vs. ZDCout/CLOCK for a fill from Run6, where ZDCout is defined as in Eq. 4.12. We use ZDCout as it is uncorrelated with r. As CLOCK was not in the GL1p scalers in Run5, the Run Length from the database was used. Due to DAQ problems at the end of a small number of runs, not all fills have a properly calculated Run Length[3]. A clear correlation is visible, implying that rate effects are affecting the Relative Luminosity error estimate.

Again, a linear fit to plots similar to Fig. 4.8 for each fill[4] are made, and the correlation between r and the collision rate as seen by the ZDCout trigger can be parameterized on a fill by fill basis. $r(i)$ can then be corrected for this BBC rate issue using the formula

$$r'_{rate}(i) = \langle r(i) \rangle \frac{r(i)}{p0 + p1(N_{ZDCout}/N_{CLOCK})} \tag{4.14}$$

Fig. 4.5c shows r'_{rate} vs. crossing number. The resulting values appear to have a more statistical distribution, as is also seen in the blue χ^2/DOF distributions

[1]Statistical fluctuations are ignored.

[2]Here, in this simple description, we neglect events in which neither collision would trigger an event, but combined they do. However, this type of event is not negligible in practice.

[3]This is why CLOCK was added to the GL1p scalers in Run6.

[4]In Run5, each fill in which all runs ended properly and have a reasonable Run Length.

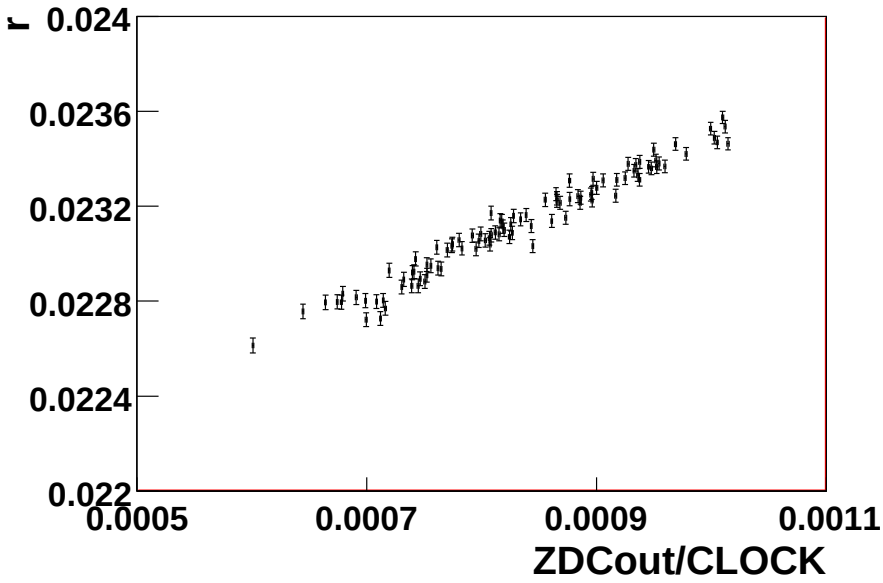

Figure 4.8: Ratio of ZDCLL1 triggers to BBCLL1 triggers (uncorrected) vs. the rate of ZDCout triggers, given by ZDCout/CLOCK.

in Fig. 4.6a and b.

The above argument seems to indicate the effect in the data is due to an issue in the BBC. Clearly, when there are two or more collisions with $|z_{BBC}| <$ 30 cm, the number of recorded events is underestimated. However, a second process due again to multiple collisions may increase the number of recorded events. Collisions that are actually outside of the (online) $|z_{BBC}| < 30$ cm, for example $z_{BBC} < (-30 - \delta)$ cm, may be reconstructed as within $|z_{BBC}| < 30$ cm due to a second collision with $z_{BBC} > (-30 + \delta')$ cm if $\delta < \delta'$. A simulation study was performed [55] which indicated that in Run6, these two effects nearly canceled. The systematic uncertainty from the rate effect on the relative luminosity measured with the BBC was estimated to be less than 10^{-4}. This indicates that the rate effect seen in Fig. 4.8 may actually be due to rate effects in the ZDC, which may not cancel well. As this study is ongoing, the rate correction, while clearly indicating the existence of a systematic uncertainty, is not used. As we will see in the next section, the systematic uncertainty in A_{LL} using only the width correction is small compared to the statistical uncertainty in Run5 and Run6. However, this will not be the case in future runs.

4.1.3 Fill By Fill Results

The results for ϵ_{LL} are scaled by the polarization values (using Eq. 4.11) on a fill by fill basis, giving $A_{LL}|_{ZDC/BBC}$, and are plotted for Run6 in Fig. 4.9 when using the uncorrected ratio, r (top), the rate corrected ratio, r'_{rate} (middle) and the width corrected ratio, r'_{width} (bottom). From the χ^2 values of the results, it is clear that significant systematic uncertainties remain in the measurement of the uncorrected ratio, with only minor improvement for the asymmetry of the width corrected ratio. The asymmetry of the rate corrected ratio shows much less of a systematic problem, which agrees with the interpretation of Fig 4.6. However, as was said above, due to uncertainty in the cause of the rate effect, it is not used in the final result. Instead we use the result from the width corrected ratio.

To account for the systematic uncertainty, two methods are used. In the first, the uncertainty in $A_{LL}|_{ZDC/BBC}$ is scaled by the $1/\sqrt{\chi^2_{fill}/\text{DOF}}$. The results are plotted in Fig 4.10a along with the unscaled errors. The χ^2/DOF value from fitting $A_{LL}|_{ZDC/BBC}$ is 46.8/66, indicates an overestimation of the uncertainties.

The second approach is to fit the distribution of central values for $A_{LL}|_{ZDC/BBC}$ with a gaussian, and take the width, σ_g, as a systematic uncertainty on all fills. Then the statistical uncertainty for each fill is added in quadrature with this systematic uncertainty. The result is plotted in Fig. 4.10b The χ^2/DOF from fitting $A_{LL}|_{ZDC/BBC}$ with a constant is 51.2/66, indicating a more reasonable error.

The two methods yield consistent result, indicating a 3.2 or 2.7 σ deviation from zero. The results from Run5 were more consistent with zero with an uncertainty on $A_{LL}|_{ZDC/BBC}$ of 0.00021. This measured asymmetry can arise from several sources including physics or systematic variation in the accelerator. It is unclear whether it is due to the BBC or the ZDC, or some combination of both. Therefore, we assume that it is the BBC, and take the measured asymmetry plus the uncertainty as the size of the possible effect of the measured pion A_{LL}. The estimated uncertainties for both RHIC runs are given in Table 7.1.

4.1.4 Future prospects

For future A_{LL} measurements, the systematic uncertainty in Relative Luminosity, at the level of Run6, will dominate the statistical uncertainty at low p_T. At $\sqrt{s}$ =500 GeV, the expected asymmetry will be less than 10^{-3}, and so any measurement will require smaller systematic uncertainties. Rate effects

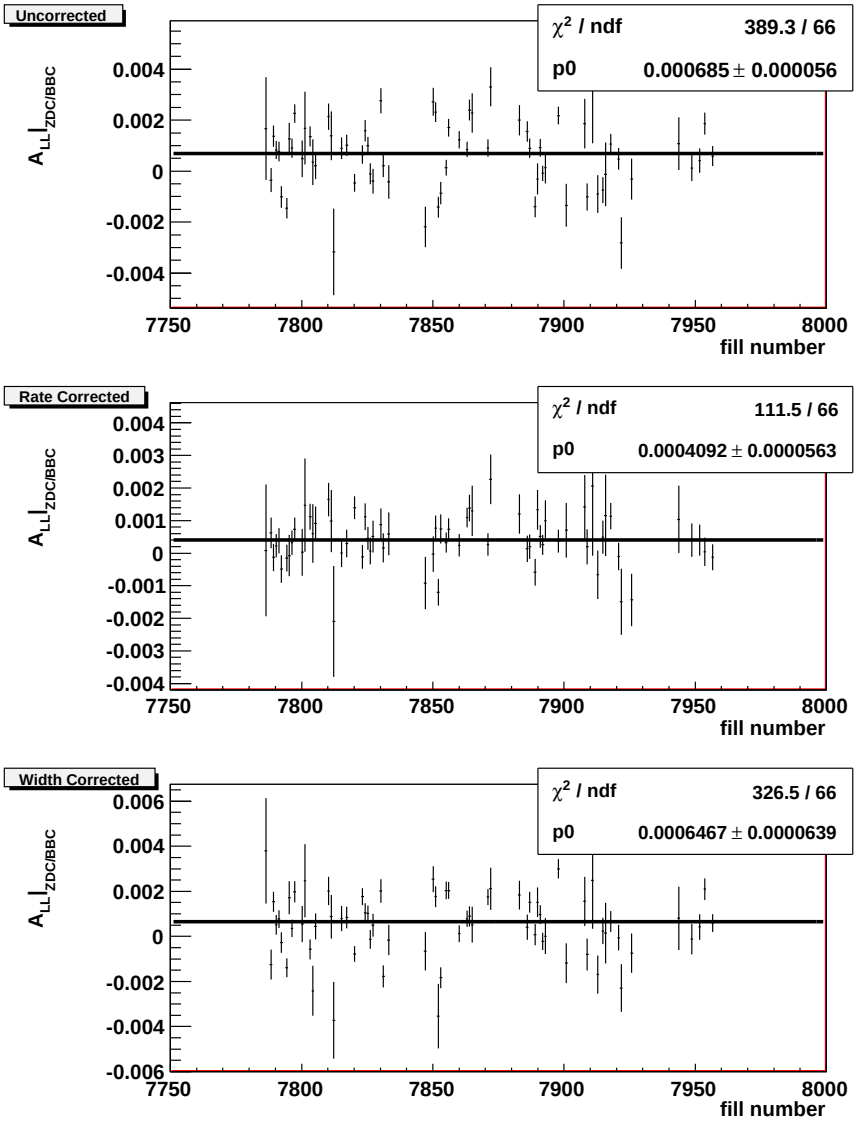

Figure 4.9: $A_{LL}|_{ZDC/BBC}$ as a function of fill number for the uncorrected (top), rate corrected (middle) and width corrected (bottom) ratio of luminosity measured by the ZDC to that measured by the BBC.

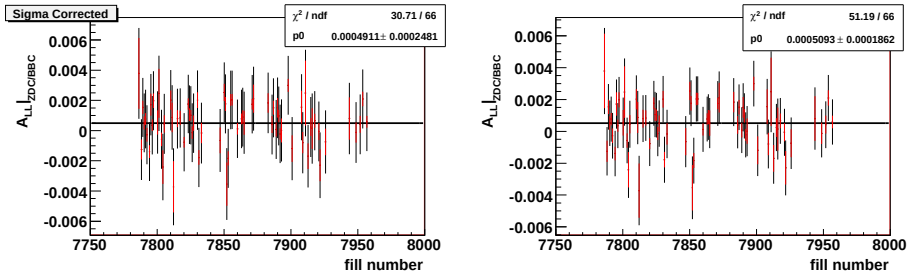

(a) (b)

Figure 4.10: $A_{LL}|_{ZDC/BBC}$ as a function of fill number for the width corrected ratio, r'_{width}. Red points are the same in both (a) and (b) and include statistical errors only. Black points have the same central value as the red points, but with statistical errors (a) scaled by $\sqrt{\chi^2/DOF}$ or (b) summed in quadrature with σ_g. Fit is done with black errors.

discussed above will become more important as luminosity increases, and will need to be better understood.

Another prospect is the use of a spin flipper, which can flip the spins in a single beam, essentially turning same helicity crossings into opposite helicity crossing and visa versa. This should greatly reduce systematic uncertainties due to bunch to bunch differences, extending the systematic reduction from using different bunch patterns in RHIC between fills. If spins can be flipped multiple times during a fill, then the effect of rate differences on luminosity normalization will also be reduced. Such a device has been proposed [37], and has been studied at RHIC [56]. The possible commissioning of this device in Run9 (2009), along with higher luminosity and polarization, will greatly enhance the extent of the A_{LL} measurements at RHIC.

4.2 Polarimetry (Magnitude)

For a double helicity measurement, longitudinally polarized protons are required. In this section, we first examine how the magnitude of the polarization vector is measured at RHIC with elastic proton-Carbon and $p+p$ scattering. In the next section, the method used to determine the direction of the polarization vector at PHENIX is described.

Two separate polarimeters are used at RHIC to measure the magnitude of polarization in RHIC: the pC polarimeters, which make quick relative measurements several times per fill for each beam, and a polarized HJet polarimeter, which makes an absolute determination of the beam polarization but at a

much lower data rate. The absolute HJet measurement is used to normalize the pC measurement. Both measurements are made with vertically polarized protons, and exploit asymmetries in elastic scattering in the Coulomb-Nuclear Interference (CNI) region. The CNI region is defined as the energy range in elastic scattering in which the Coulomb and Nuclear forces are of the same strength, and therefore can interfere with each other, inducing a spin flip, observable as an asymmetry [57, 57, 58]. As both detectors were briefly described in Chapter 2, here we give only a quick description of the measurements.

4.2.1 Polarized Hydrogen Jet Polarimeter

The apparatus for the HJet polarimeter has been described in Chapter 2.5. In this section, the measurement of absolute beam polarization magnitude is described briefly. For more detail, see [59] for Run5 results or [60] for Run6.

The main purpose of the HJet polarimeter is to give a normalization for the quicker but relative pC polarimeters. As both the beam and target are polarized in the $p+p$ scattering with the HJet, two different single spin asymmetries can be measured: the raw beam asymmetry, ϵ_B, where the beam is treated as polarized and the target unpolarized, and the raw target asymmetry, ϵ_T, where the target is treated as polarized and the beam unpolarized.

During standard running, only one beam is incident on the target at a time so as to reduce background. The on target beam is switched between yellow and blue several times during the running period. Figure 4.11 shows the raw asymmetries for the beam and target for blue and yellow running period (when the specified beam was incident on the target) in Run5 and Run6.

The physical asymmetry measured for the target and beam are the same. The difference in raw asymmetry seen in Fig. 4.11 is simply due to the difference in beam and target polarizations. Defining the physical asymmetry as

$$A_N = \frac{\epsilon}{P} \,, \tag{4.15}$$

we can relate the measured asymmetries for the target and the beam as

$$\frac{\epsilon_B}{P_B} = \frac{\epsilon_T}{P_T} \,. \tag{4.16}$$

This can be rewritten so that the beam polarization can be calculated as

$$P_B = \frac{\epsilon_B}{\epsilon_T} P_T \,. \tag{4.17}$$

With the polarization determined by the HJet polarimeter, we move to the quick relative polarization measurements from the pC polarimeters which are

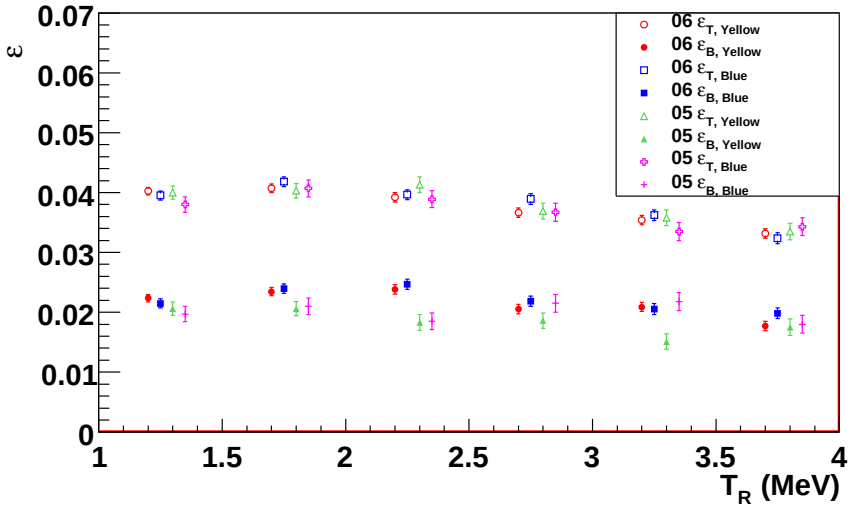

Figure 4.11: Target (T) and Beam (B) asymmetry during the 2005 and 2006 running periods for the two beams as a function of the recoil energy of the scattered proton (T_R).

used to give final fill by fill polarization magnitudes.

4.2.2 Proton Carbon Polarimeter

The set up for the pC polarimeter was described in Chapter 2.5. Here we focus briefly on the measurement, described in more detail in [39] and [61] for Run5 and Run6, respectively. The asymmetry from a single measurement with a vertical target is plotted in Fig. 4.12 as a function of the angle ϕ. As was described in Chapter 2.5, measurements can be made with either a fixed target or a target which is scanned across the beam. Fixed target measurements measure the polarization at a point near the maximum beam intensity, and are all that is required if the beam has no polarization profile, i.e. polarization does not change as a function of position in the beam. Scan measurements are used to study if there is a beam profile, and how large it is. In Run5 and Run6, polarization profiles were found, and the resulting systematic uncertainty was the largest uncertainty from the pC polarimeters.

4.2.3 Polarization Normalization

The results from the pC polarimeters have been normalized by the results from the HJet. The normalizations from Run5 and Run6 were found to differ

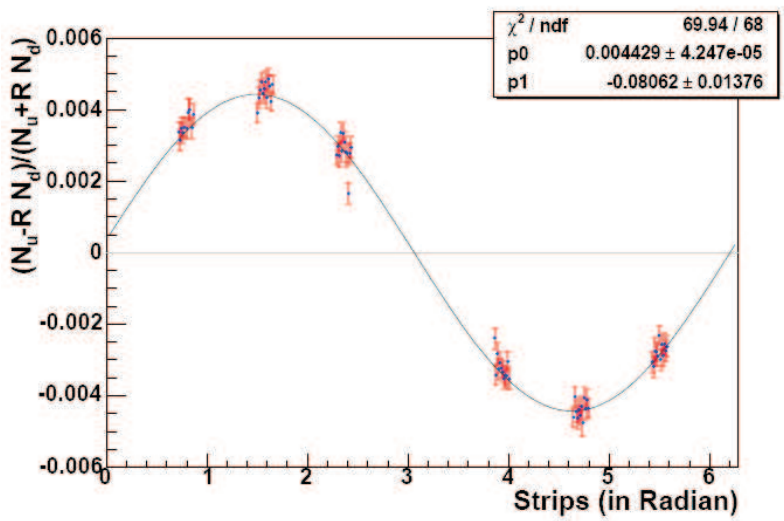

Figure 4.12: Asymmetry in elastically scattered carbon atoms vs. ϕ. Taken from [62].

substantially between the two years, highlighting the necessity for normalization with the HJet each year until the pC analyzing power is better understood. Figure 4.11, which shows the target and beam asymmetries for Run5 and Run6, clearly indicate the validity of the HJet measurement, as the target asymmetry is consistent between Run5 and Run6.[5] Figure 4.13a and b show the polarizations measured for the blue and yellow beam as a function of fill number for Run5 and Run6, respectively.

Final luminosity weighted polarizations and uncertainties are given in Table 4.1 for both runs. The uncertainties are separated into two sources of systematic and statistical (which includes fill to fill uncorrelated systematic uncertainties). The "systB" and "systY" terms are correlated between fills, but uncorrelated between the Yellow and Blue beams. The global uncertainty ("systG") is correlated between fills and between beams, and includes uncertainties from the polarization and background of the HJet.

4.3 Local Polarimetry (Direction)

As described in Chapter 2.6, for measurements using longitudinally polarized beams, such as A_{LL}, spin rotators are used to rotate the direction of the beam

[5]Note that the target polarization was the same in both years, allowing a direct comparison of the asymmetries. This is not necessarily true of the beam asymmetries.

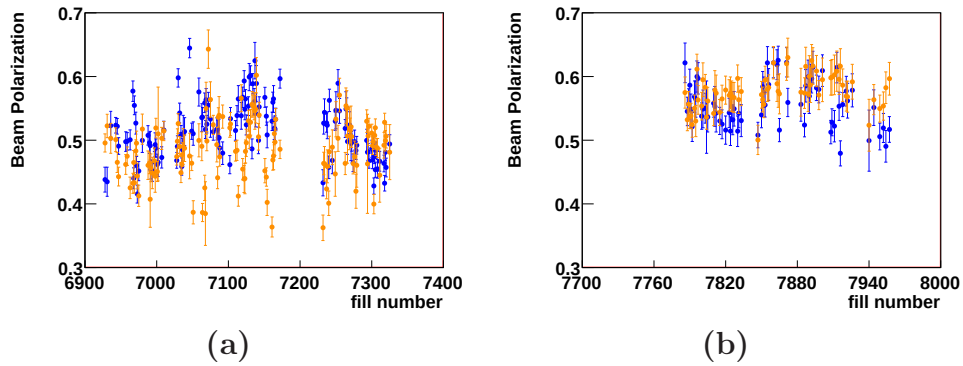

(a) (b)

Figure 4.13: Blue (blue) and Yellow (orange) beam polarization vs. fill number from (a) Run5 and (b) Run6. Errors are statistical uncertainties summed in quadrature with fill by fill uncorrelated systematic uncertainties.

Table 4.1: Final luminosity weighted average polarization values for Run5 and Run6, along with the overall systematic uncertainty.

Year	Blue Beam (%)				Yellow Beam (%)			
	$\langle P \rangle$	ΔP_{stat}	ΔP_{systB}	ΔP_{systG}	$\langle P \rangle$	ΔP_{stat}	ΔP_{systY}	ΔP_{systG}
Run5	50	0.2	2.5	1.4	49	0.2	2.7	1.4
Run6	56	0.2	1.8	1.9	57	0.2	1.9	2.0

polarization from vertical to longitudinal (parallel to the beam momentum direction). In reality, there will always be some remaining transverse component. This remaining component reduces the sensitivity to A_{LL}, while increasing the sensitivity to A_{TT}, the transverse equivalent of A_{LL}. Therefore, it is very important to check that the polarization direction is correct at PHENIX. A set of "local" polarimeters, composed of the ZDCs and SMDs, are used towards this objective. As the polarization direction can only be measured at PHENIX, this analysis is referred to as *local polarimetry*.

4.3.1 Physics

The polarization direction cannot be measured directly. We can simply measure an asymmetry due to the degree of polarization. As we need to know the polarization direction of the two proton beams independently, we choose to look at a single spin asymmetry (SSA).

Figure 4.14a show two protons scattering such that the scattering plane is in

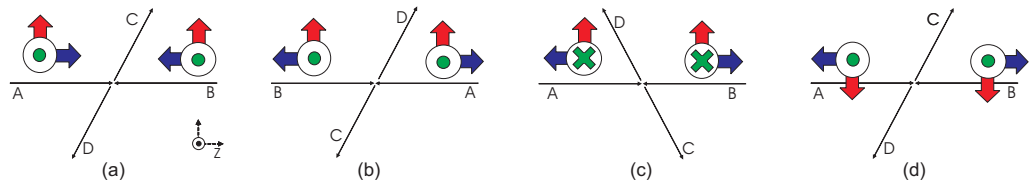

Figure 4.14: Diagrams of polarized proton collision with the scattering plane in the plane of the page. (a) Proton(s) are polarized longitudinally (blue) or transversely in the scattering plane (red) or perpendicular to it (green). Three transformations are applied: (b) parity, then (c) rotation about the x-axis and then (d) rotation about the z-axis. Note that parity flips vectors, such as momentum, but not pseudovectors, such as spin.

the plane of the page.[6] In this case we consider proton "B" to be unpolarized. Parity and two rotations are applied, such that the in the unpolarized case, (a) and (d) are the same.[7] In the case of including spin, we see that in certain spin orientations with respect to the scattering plane, the diagrams differ. Rotations are simply a change of coordinate system, and should have no effect on the actual physics. Therefore, any difference between the measured results in (a) and (d) indicate that parity is not conserved. As the strong force conserves parity, only asymmetries that do not violate parity can be observed.[8] Any SSA with the spin vector in the scattering plane is parity violating, including when the spin vector is parallel to the beam momentum direction, *i. e.* longitudinally polarized.

Figure 4.14 shows that a transverse SSA is not parity violating when the spin is perpendicular to the scattering plane, and so is not necessarily zero. Indeed, many transverse SSA have been seen in $p + p$ scattering [64–66] at large positive values of Feynman x (x_F), defined as

$$x_F \equiv \frac{p_z}{\sqrt{s}/2} \,. \tag{4.18}$$

Large positive x_F in a collider at $\sqrt{s} = 200$ GeV is equivalent to the large η

[6]This concept was taken from [63].

[7]This can be generalized. Assume we have a state ψ_a. We can define a different state $\psi_d = R_x(\pi)R_z(\pi)\Pi\psi_a$, where $R_x(\phi)$ and $R_z(\phi)$ are rotations of ϕ about the x-axis and z-axis, respectively, and Π is the parity operator. A measurement of ψ_a-ψ_d then can only be nonzero if parity is violated.

[8]In the case of the future W boson program at RHIC, the fact that parity is violated by the weak force and conserved by the strong force will be exploited to measure the spin dependent and flavor dependent distribution of the quark sea.

range in the forward direction with respect to the polarized beam. As listed in Table 3.1, the only detectors at large η are the BBC and ZDC.[9] An SSA in the angular distribution of neutrons produced at very large positive pseudorapidities in $\sqrt{s} = 200$ GeV $p + p$ scattering was first found at the IP12 experiment at RHIC [67]. The cause of this asymmetry is still under debate, but for our purposes, a fuller understanding is not required.

4.3.2 ZDC Measurement

At PHENIX, the ZDCs give energy of forward scattered hadrons, as well as discrimination between hadronic and electromagnetic showers (which have a high probability of depositing all energy in the first ZDC module). As was discussed in Chapter 3.1.2, the location of the ZDCs outside the DX magnet, at very forward scattering angles, makes it a very good candidate for measuring neutrons with low background from charged hadrons. Combined with the SMDs, which are used to determine the localized position of the hadronic shower associated with a neutron candidate, an asymmetry can be measured [46, 68]. To have enough statistics for this analysis, a special trigger was designed, called the *LocalPol* trigger (see Chapter 3.3.2).

4.3.3 Analysis Method

Candidate neutrons used in the local polarimetry analysis must leave a hit in the SMD, which is between the first and second ZDC modules. This greatly reduces the contribution from photons, as each ZDC module is 51 electromagnetic interaction lengths. Due to the design of the ZDC, particles hitting the top of the ZDC can shower into the bare readout fibers, and appear to deposit very large energies. Nominally, we should not expect any particles with energy greater than beam energy, i.e. 100 GeV. However, due to the low energy resolution of the detector (± 20 GeV) the energy of a candidate neutron is required to be from 20 to 120 GeV [68].

The hit position in the SMD is defined using the center of gravity of the deposited energy in the SMD scintillators. The hits are then divided into quadrants (up, down, left and right). The measured asymmetry is calculated for left and right or up and down using the square root formula [69]:

$$A(\phi) = \frac{1}{P_{\text{Beam}}} \frac{\sqrt{N_L^+ N_R^-} - \sqrt{N_L^- N_R^+}}{\sqrt{N_L^+ N_R^-} + \sqrt{N_L^- N_R^+}} \tag{4.19}$$

[9] The Muon Piston Calorimeter (see Fig. 3.1) was not installed in Run5 and was not fully operational in Run6.

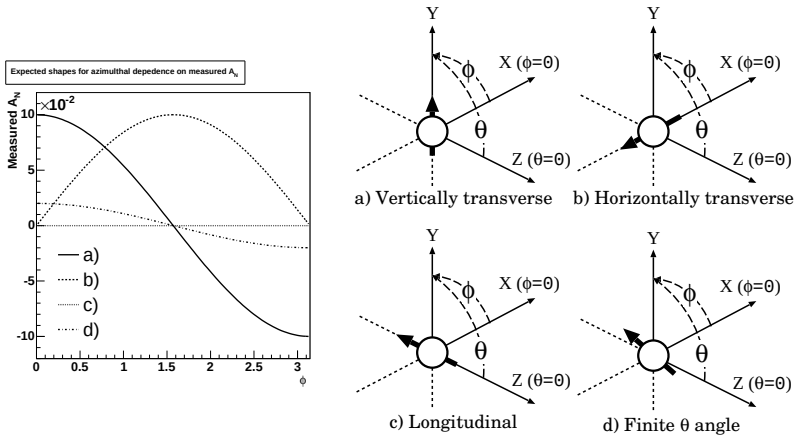

Figure 4.15: Expected neutron asymmetry if the beam is polarized (a) vertically transverse, (b) horizontally transverse, (c) completely longitudinally or (4) longitudinally with a remaining small transverse component. Taken from [46].

which reduces the affect of luminosity difference between + and − polarized bunches and detector acceptance differences between the opposite sides of the detector. Figure 4.15a and b shows the expected asymmetry as a function of ϕ with vertically and horizontally polarized beams. Here ϕ is defined in the counterclockwise direction with respect to the beam direction with $\phi = 0$ at $y = 0$. As discussed in Chapter 2, the stable beam direction is vertical, and so with spin rotators turned off, the beam is polarized as shown in Fig. 4.15a. Figure 4.15c shows the same neutron asymmetry when the spin rotators are on such that the beam polarization direction is expected to be longitudinal. In reality, there is always some remaining transverse component, such as shown in Fig. 4.15d.

The amplitudes of the asymmetry in Fig. 4.15a and d can be compared, and the ratio

$$\frac{A_{N,\text{long}}}{A_{N,\text{vert}}} = \frac{\epsilon_{\text{long}}/P_{\text{long}}}{\epsilon_{\text{vert}}/P_{\text{vert}}} \tag{4.20}$$

gives an estimate the remaining transverse beam polarization. Note that here beam polarizations must be included as it will vary from fill to fill, and so only the effective analyzing power,

$$A_{N,eff} = \frac{\epsilon}{P} \ , \tag{4.21}$$

should remain constant between fills.

4.3.4 Results

Commissioning of the spin rotators occurs at the start of each RHIC run to ensure that the beam polarization is correct. Data is taken in several RHIC fills maximizing the data acquisition bandwidth of the LocalPol trigger in order to commission the spin rotators. The asymmetry is measured with vertical polarization with high precision, giving the denominator in Eq. 4.20, which we define as A_N^{com}. After the spin rotators are turned on, another fill is taken maximizing the data acquisition bandwidth of the LocalPol trigger. Comparing the result before and after the rotator is turned on, we can ensure the rotator is working correctly.

During normal data taking, the majority of bandwidth is reserved for the main physics triggers, such as the ERT, and so only a small bandwidth of 200 Hz is allocated for the LocalPol trigger. Up-down (UD) and left-right (LR) asymmetries are measured fill by fill, yielding a result with about 1% statistical uncertainty per fill, assuming 50% beam polarization.

Results for the up-down and left-right forward neutron asymmetries measured in Run5 are plotted as a function of fill number in Fig. 4.16 for the blue and yellow beam. These results can be fit with a constant to estimate the size of the polarization vector in the vertical (horizontal) direction, P_y (P_x). From the χ^2 values, the fits are reasonable, indicating that the beam polarization direction was stable during the run. Similar results were found for Run6.

The total polarization vector can be written as the sum of its components in cartesian coordinates as

$$\boldsymbol{P} = P_x\hat{x} + P_y\hat{y} + P_z\hat{z} \ . \tag{4.22}$$

From the fit results in Fig. 4.16, the fraction of the beam polarization in the transverse directions can be calculated as

$$\frac{P_x}{P} = \frac{A_N^{UD}}{A_N^{com}} \quad \text{and} \quad \frac{P_y}{P} = \frac{A_N^{LR}}{A_N^{com}} \tag{4.23}$$

while the total transverse component can be given by

$$\frac{P_T}{P} = \sqrt{\left(\frac{A_N^{UD}}{A_N^{com}}\right)^2 + \left(\frac{A_N^{LR}}{A_N^{com}}\right)^2} \ . \tag{4.24}$$

From this, the longitudinal component is given as simply

$$\frac{P_L}{P} = \sqrt{1 - \left(\frac{P_T}{P}\right)^2} \ . \tag{4.25}$$

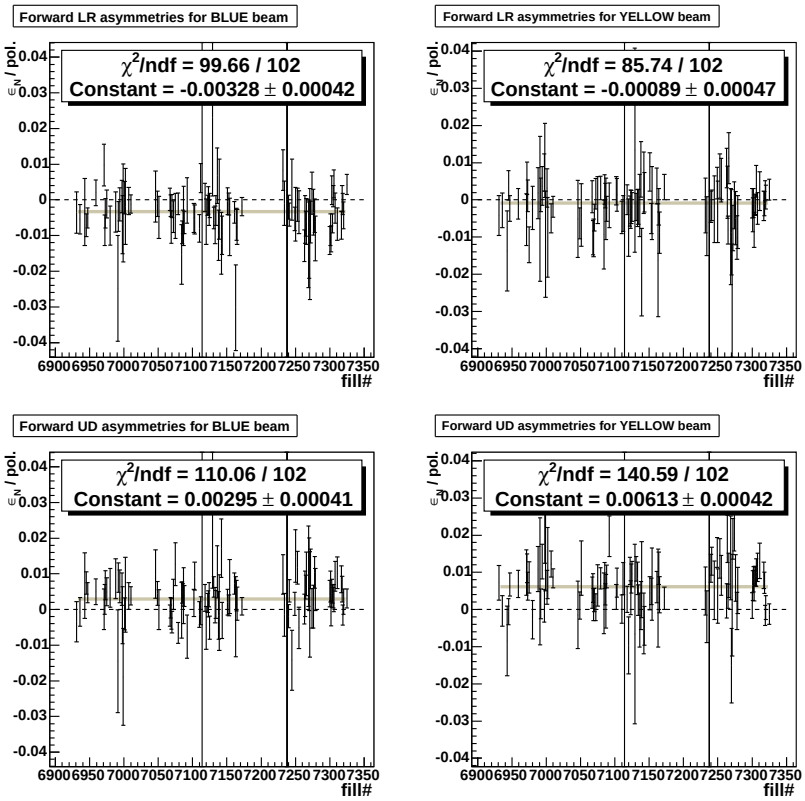

Figure 4.16: Results for left-right (top) and up-down (bottom) forward neutron asymmetry scaled by beam polarization vs. fill number for blue beam (left) and yellow beam (right) from Run5. The small size of the asymmetry indicates that the beams polarization is almost completely longitudinal, and that the polarization direction was very stable throughout Run5. The nonzero asymmetries also indicate that the spin pattern used in the analyses is correct, as the expected result from commissioning is recovered.

Table 4.3.4 lists the values of P_T/P and P_L/P for the blue and yellow beam for Run5 and Run6. As can be seen there, both beams were almost completely longitudinally polarized in both years. The effect of the remaining transverse polarization will be considered in Chapter 7.6.

	Run5		Run6	
	Blue	Yellow	Blue	Yellow
P_T/P (%)	9.6±1.6	13.8±1.6	12.1±2.4	11.2±2.3
P_L/P (%)	99.5±0.1	99.0±0.1	99.2±0.4	99.3±0.3

Table 4.2: Percentage of the beam polarization in transverse and longitudinal directions for Run5 and Run6.

4.3.5 Implication for Bunch Pattern

While it may seem logical that the transverse component should be reduced as much as possible, so that it is consistent with zero, having a small nonzero component can be a very useful systematic cross check that the spin pattern is correct. When measuring an unknown asymmetry such as A_{LL}, there is a danger that an incorrect result could be due to an incorrect spin pattern. The spin pattern used in measuring the remaining forward neutron transverse SSA is the same used for measuring A_{LL}. This indicates that the spin pattern has been correctly recorded, ensuring it is not a source of error in the following analyses.

Chapter 5

Event Selection, Particle Identification and Background Reduction

In this chapter, the criteria for selecting events used in the analysis is presented. Then, the requirement imposed on all candidate particles due to the use of the ERT trigger in event selection is discussed. Finally, the methods used for identifying neutral and charged pions are detailed.

For neutral pion identification, π^0 kinematics, photon identification, and reduction of electronic noise in the data are described. Several cuts are then discussed to reduce non-photonic contamination.

The second half of this chapter focuses on charged pion identification. Here, the largest background is due to electron contamination, mostly from conversions. Cuts are presented which reduce this contamination, and estimates of the background are given.

5.1 Event Selection

There are two requirements for any event used in the following analyses:

- trigger requirement: The event must be triggered by a coincidence between the ERT trigger and a BBCLL1 trigger. In minbias events, only the BBCLL1 trigger is required.

- z-vertex requirement: Offline reconstructed BBC z-vertex must be within ± 30 cm of the nominal interaction point (denoted as $|z_{BBC}| < 30$ cm).

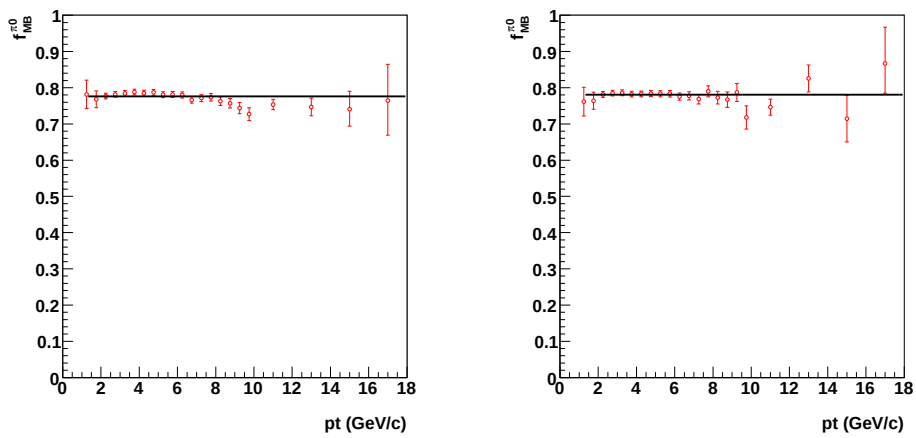

(a) (b)

Figure 5.1: The fraction $f_{\pi 0}$ of the π^0 s in events triggered only by the ERT for which the minimum bias trigger bit was also set as a function of the p_T of the π^0 in PbSc (a) or PbGl (b). Lines are fits to a constant.

5.1.1 Trigger Requirement

There are two trigger requirements used in this analysis: event trigger and particle trigger. The first gives a high likelihood for a $p+p$ collision, while the second significantly increases the chance that the event has a high momentum particle.

For the following analyses, the event trigger used is the minimum bias trigger (BBCLL1) described in Chapter 3.3.1. This gives us events with an acceptable z-vertex (nominally $|z| < 30$ cm online with a resolution of 5 cm), and low noise, ensuring that the majority of our data is usable. This trigger requirement samples roughly 50% of all $p+p$ events, but samples roughly 80% of all π^0 events in the PHENIX acceptance, as can be seen in Fig. 5.1.

This condition is necessary, but not complete.[1] Due to the relatively low cross section of high p_T pions, we must also trigger on the particle of interest. For this, we require that there is additionally an ERT trigger (see Chapter 3.3.3) in coincidence with the minimum bias trigger. This ERT trigger is a particle based trigger, as it does not measure a global condition of the entire event (such as z-vertex position) but whether a particle with certain properties existed in an event. In reality, it actually checks whether properties consisted

[1]For the minbias data analysis, the ERT trigger is not required.

with a specific particle (large energy deposits in a small region of the EMCal in these analyses) are present in the event.

5.1.2 BBC z-Vertex Cut

Although the minbias trigger requirement requires a reconstructed z_{BBC} to be within ± 30 cm of the nominal interaction point, the actual distribution is wider due to the 5 cm online resolution and the actual settings on the trigger ($-34 < z_{BBC} < 37$ cm). As the magnetic pole tips sit at ± 40 cm, and as events close to the pole tips will see a limited acceptance and higher background, an offline cut of $|z_{BBC}^{\text{offline}}| < 30$ cm is imposed. This cut ensures that events analyzed see the full PHENIX central arm acceptance. This cut removes about 15% of recorded data.

5.2 ERT Trigger Requirement

In Sec. 5.1.1, the ERT trigger requirement for event selection was described. However, it is important to not only require that the candidate particle is in such a triggered event, but actually triggered the event itself. Particles in an event which are not associated with an ERT trigger in that event are called *random benefit*. It is difficult to understand the trigger bias for such particles. For a cross section measurement which requires that the trigger bias is understood, it is clear that such particles must be excluded. As will be discussed in Chapter 8.1, we must rely on the fact that pQCD describes the measured cross section in order to use pQCD to interpret A_{LL}. For the comparison to be valid, data sets with the same understood trigger bias should be used for the cross section and A_{LL} analyses. Therefore, random benefit particles are excluded from the following A_{LL} analyses. To do this, the particle are required to be associated with an ERT trigger.

The best way to ensure that a particle is associated with a trigger is to limit the size of the trigger region. As discussed in Chapter 3.3.3, the smallest component of the ERT trigger used is a 4×4 block of towers. However, in the final data files, only the supermodule (12×12 tower) information is available. The actual requirement differs for neutral and charged pions.

For π^0, which are reconstructed from two photons, we require that the higher energy photon candidate is centered on a tower in a triggered supermodule.[2] This is the same requirement as was used for the π^0 cross section result [70]. Variations of this trigger requirements, such as requiring the higher

[2]For the minbias data analysis, no such requirement is used.

energy photon candidate to be the highest energy cluster in the supermodule, were shown to yield very similar results.

For charged pions, we require that the central tower of the cluster associated with the candidate charged pion be in a triggered supermodule. As $\sim 40\%$ of the charged pions deposit only a minimum ionizing energy (250 MeV) in the EMCal, and the lowest trigger threshold is nominally 1.4 GeV, all minimally ionizing particles (MIPs) are excluded from our sample by this requirement. The trigger efficiency is lower still as many charged pions that do shower in the EMCal will not deposit enough energy in the EMCal to trigger, as energy will be lost out the back of the EMCal. For this reason, the statistics of the charged pion sample is expected to be less than half that of the π^0 simply due to this trigger requirement.

5.3 Neutral Pion Decay Kinematics

The π^0 decays to two photons 98.798±0.032% of the time[12] and is the decay channel studied in this analysis. Conservation of momentum tells us then that in any frame

$$p^{\mu}_{\pi^0} = p^{\mu}_{\gamma_1} + p^{\mu}_{\gamma_2} \,. \tag{5.1}$$

The square of the momentum is a Lorentz invariant, and in the rest frame of any particle is simply the particle's mass squared:

$$p^{\mu}_{\pi^0} p_{\pi^0,\mu} = m^2_{\pi^0} \,, \tag{5.2}$$

$$p^{\mu}_{\gamma} p_{\gamma,\mu} = 0. \tag{5.3}$$

In the lab frame, the four vector momentum for the two photons can be written as $p^{\mu}_{\gamma_i} = (E_i, \boldsymbol{p_i})$. Squaring both sides of Eq. 5.1, and using the relations in Eq. 5.2 and 5.3, we have

$$m^2_{\pi^0} = 2(E_1 E_2 - \boldsymbol{p_1} \cdot \boldsymbol{p_2}) \,. \tag{5.4}$$

Given Eq. 5.3, we can also derive that

$$p^{\mu}_{\gamma} p_{\gamma,\mu} = E^2_{\gamma} - |\boldsymbol{p_\gamma}|^2 \tag{5.5}$$

$$\Rightarrow E_{\gamma} = |\boldsymbol{p_\gamma}| \,. \tag{5.6}$$

As $\boldsymbol{p_1} \cdot \boldsymbol{p_2} = |\boldsymbol{p_1}||\boldsymbol{p_2}| cos\theta$, where θ is the angle between the two photon 3-momentum vectors in the lab frame, we can rewrite Eq. 5.4 as

$$m^2_{\pi^0} = 2E_1 E_2 (1 - cos\theta) \,. \tag{5.7}$$

5.4 Photon Identification

The PHENIX EMCal is the primary detector used in identifying photons, from which π^0s are reconstructed. Chapter 3.2 gives the energy resolution of this detector. In order to reduce backgrounds in the π^0 sample, several sources of background must be rejected including noisy detector components, non-event related background and hadrons. In the next several sections, we discuss how we reject such false photon candidates.

5.5 Rejection of Clusters Due to Electronic Noise

Two methods are used to reduce the effects due to electronic noise. The first method is to exclude very low energy clusters, in effect placing a higher threshold on the cluster energy than is used when the event is written to tape. Due to the different nature of the two types of EMCal's at PHENIX, two different minimum energy cuts are applied: $E < 100$ MeV for PbSc and $E < 200$ MeV for PbGl. Such a cut has a small effect on the sample of π^0s. At low p_T, such a requirement greatly reduces the background under the π^0 mass peak, while at high p_T, only decays with extremely asymmetric energies are cut. This energy asymmetry is due to the angle between the momentum vector of the π^0 and the direction of decay in the π^0 rest frame, which should be independent from the partonic distributions in the proton in the initial state. Therefore, such a cut can be safely made, without biasing the spin asymmetry measurement.

The second method to reduce the effects due to electronic noise defines a map of bad towers, called a warnmap, which are excluded from the analysis.

5.5.1 Warnmap

The EMCal consists of 24768 individual towers. Some number of these towers can be either dead, *i. e.* they do not register energy deposits, or hot, *i. e.* electronically noisy. Such towers can lead to false signals or wrongly reconstructed cluster energy. These towers, as well as towers which could not be calibrated, comprise the basis of a warnmap. All clusters centered on any tower in the warnmap are excluded from analysis.

The edgemost towers for all sectors of the EMCal are not well calibrated, as shower energy can be lost into the space next to the calorimeter. Therefore, a one tower edge is included in the warnmap. All towers that are declared hot, dead, uncalibrated, and edge cannot be used in good clusters. The average

electromagnetic shower in the EMCal is roughly 2 towers wide. Therefore, towers in a 3×3 box around these bad towers are also included in the warnmap, as the reconstructed energy of any cluster centered on these "neighbor" towers may be incorrect. Note that this means that effectively a two tower edge is used for all sectors of the EMCal.

Figure 5.2 shows a tower map from Run6 of the 8 EMCal sectors, with hot, dead and failed calibration/edge towers labeled red, black and blue. Neighboring towers included in the warnmap are colored yellow. Green towers are good towers. Table B.1 (B.2) lists the number of masked towers (excluding 2 tower edge) and edge towers by sector for Run5 (Run6).

5.6 Neutral Pion Mass Spectrum

Figures 5.3 and 5.4 show the two photon invariant mass spectrum (using Eq. 5.7) for the different p_T bins for ERT events (ERT trigger in coincidence with minbias trigger) from PbSc and PbGl, respectively, used in the Run6 analysis. The black line is the spectrum before any cuts other than warnmap and minimum energy, while the red line includes all cuts.

5.7 Neutral Pion Background Estimates

The following sections discuss different cuts applied to both photon candidates in the invariant mass pair. In order to understand the effectiveness of these cuts, we define three quantities:

- π^0 efficiency: $N^{\pi^0}_{after}/N^{\pi^0}_{before}$
- Background (BG) suppression: $1 - N^{BG}_{after}/N^{BG}_{before}$
- Remaining background contribution: $N^{BG}_{after}/(N^{BG}_{after} + N^{\pi^0}_{after})$.

Here, N^{π^0} (N^{BG}) is the fraction of candidate photon pairs under the π^0 mass peak ($0.112 < m_{\gamma\gamma} < 0.162$ MeV/c^2) from π^0s (background). In order to estimate the remaining background contribution under the π^0 mass peak, the invariant mass spectrum from 50 MeV to 300 MeV is fit with a gaussian plus third order polynomial.

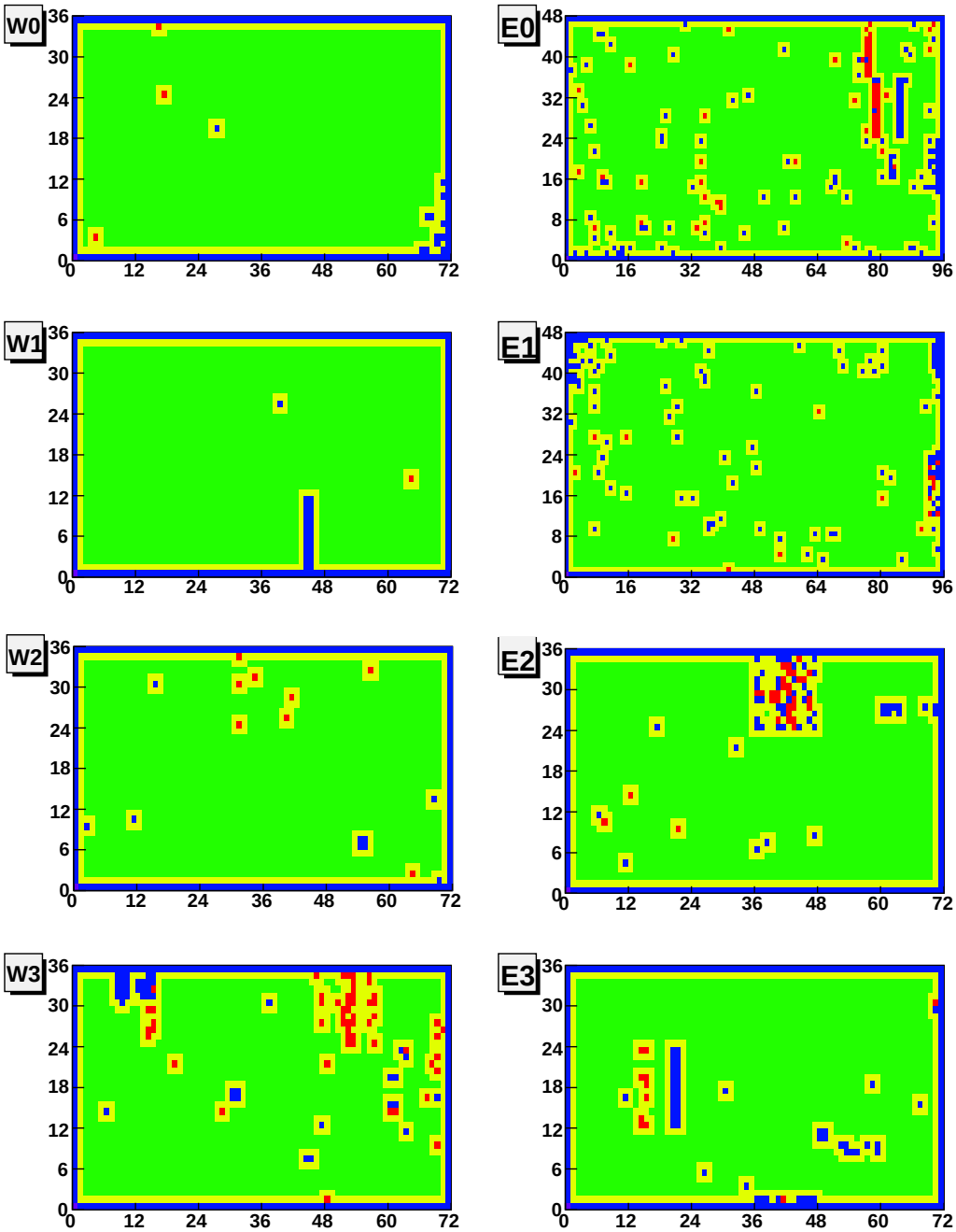

Figure 5.2: Run6 warnmap for the 8 EMCal sectors. The different colors indicate tower quality: good (green), hot (red), dead (black), uncalibrated or one tower edge (blue) and neighboring towers (yellow).

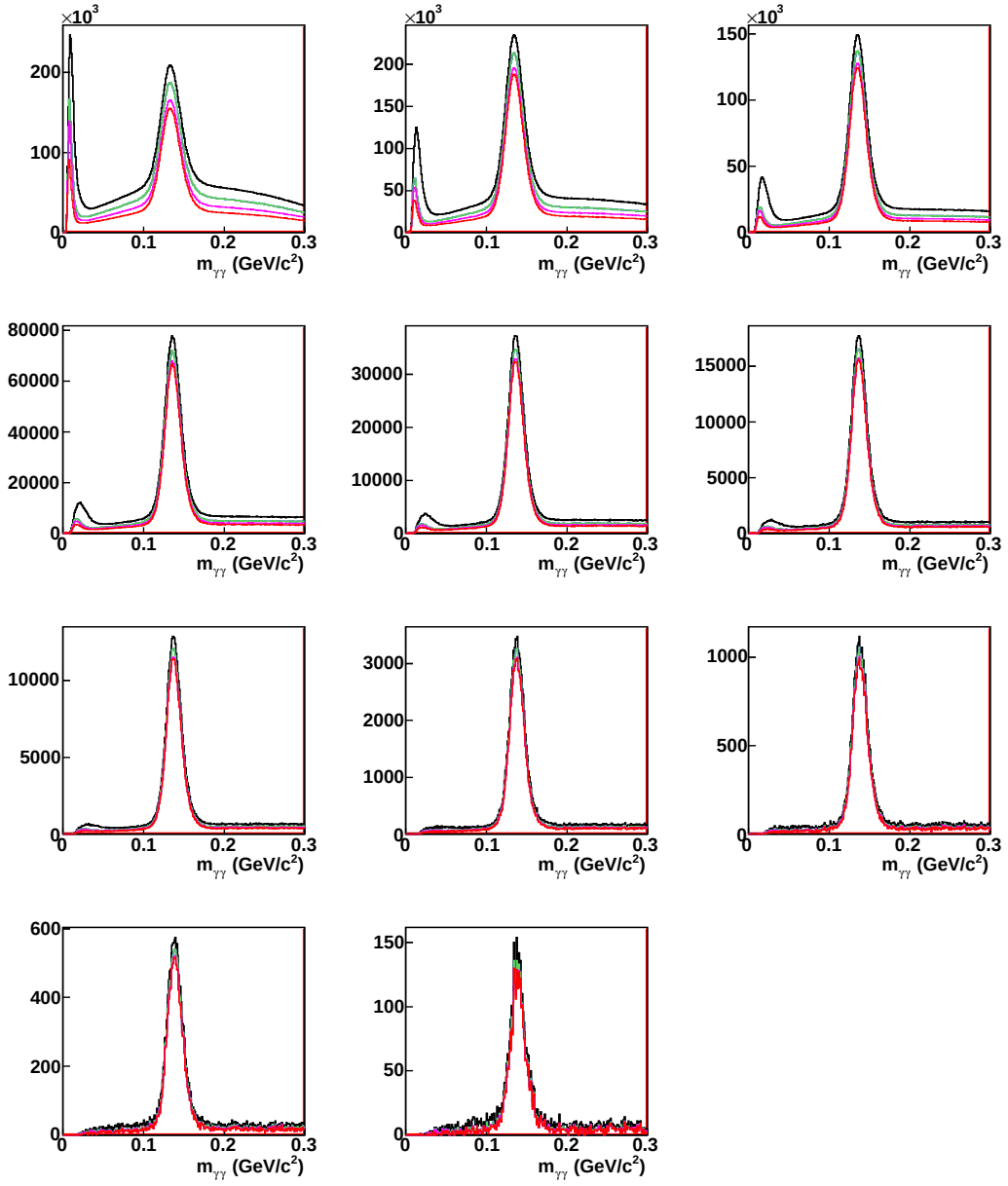

Figure 5.3: Two photon invariant mass distribution from *PbGl* only for ERT triggered events in Run6 for 11 photon pair p_T bins used in this analysis. Top row, from left to right: 1.0-1.5, 1.5-2.0, 2.0-2.5 GeV/c. Second row, from left to right: 2.5-3.0, 3.0-3.5, 3.5-4.0 GeV/c. Third row, from left to right: 4.0-5.0, 5.0-6.0, 6.0-7.0 GeV/c. Bottom row, from left to right: 7.0-9.0 and 9.0-12.0 GeV/c. Black line includes only warnmap and minimum energy cut. The effect of additional cuts are shown in green (shower shape), pink (ToF) and red (charge veto).

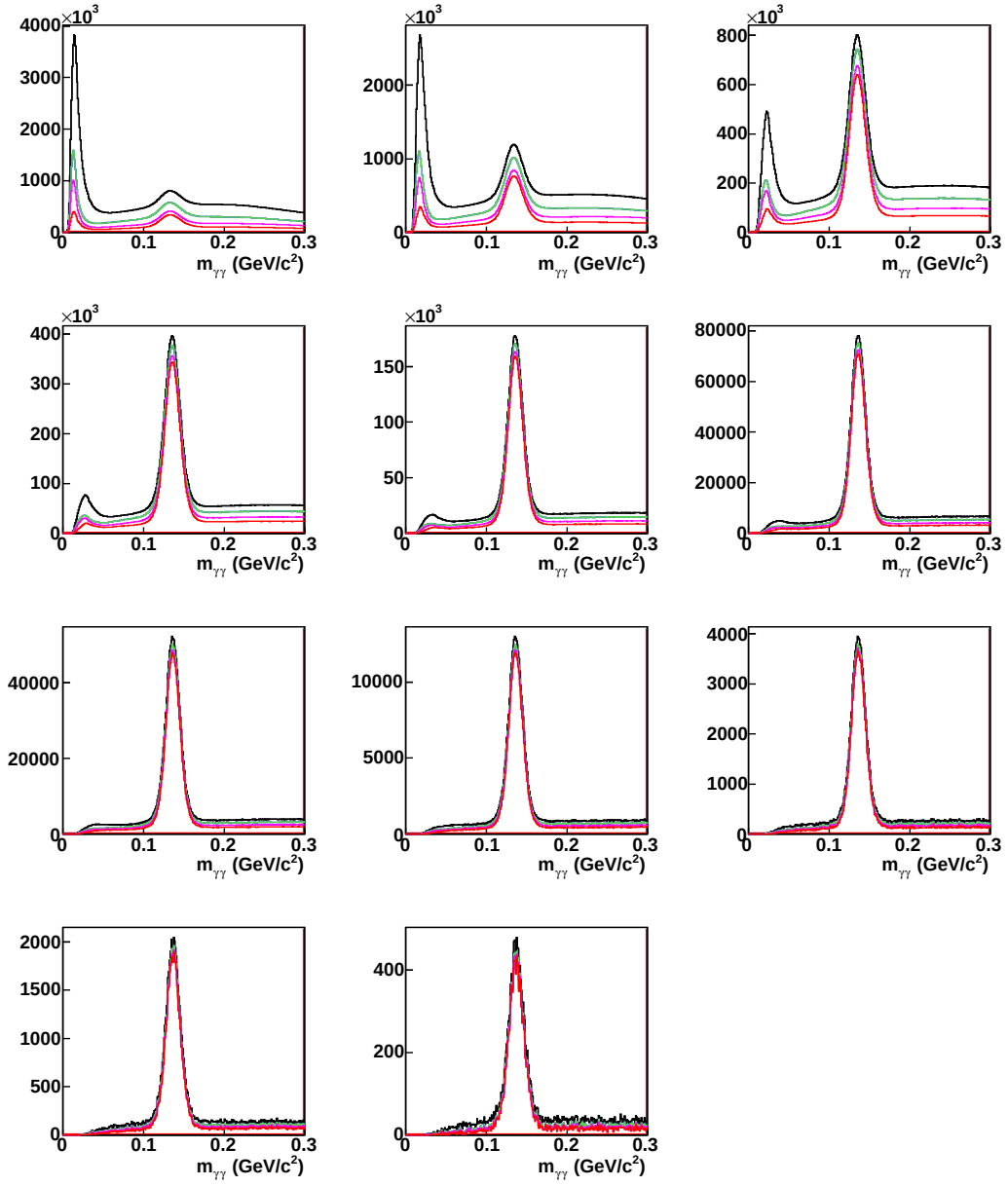

Figure 5.4: Two photon invariant mass distribution from *PbSc* only for ERT triggered events in Run6 for 11 photon pair p_T bins used in this analysis. Top row, from left to right: 1.0-1.5, 1.5-2.0, 2.0-2.5 GeV/c. Second row, from left to right: 2.5-3.0, 3.0-3.5, 3.5-4.0 GeV/c. Third row, from left to right: 4.0-5.0, 5.0-6.0, 6.0-7.0 GeV/c. Bottom row, from left to right: 7.0-9.0 and 9.0-12.0 GeV/c. Black line includes only warnmap and minimum energy cut. The effect of additional cuts are shown in green (shower shape), pink (ToF) and red (charge veto).

5.8 Neutral Pion: Photon Cuts (Efficiencies, Studies)

After applying event selection, trigger requirements, minimal energy cuts and the warnmap, we apply several cuts to reduce the combinatorial background under the π^0 peak in the two photon invariant mass spectrum. These include:

- Shower shape
- Time of flight
- Charge veto.

In the following sections, each of these is discussed in detail.

5.8.1 Shower Shape

Photons, electrons and hadrons all will shower in an infinite calorimeter. However, hadrons interact with the material via the strong force, while photons and electrons interact electromagnetically. Therefore, due to the much shorter range of the strong force, hadrons will typically travel farther in the material before interacting. (This is why the nuclear interaction length is about 18 times larger than the radiation length in the PHENIX EMCal.) Similarly, due to the different forces involved, the average shape of the shower is different in the two cases. Here, we will use this difference to exclude showers that have a low probability to be electromagnetic.

As the PHENIX EMCal is not segmented in the radial direction (i.e. depth of shower direction), we cannot use the different interaction lengths to distinguish between the two types.[3] Instead the 2-dimensional shower shape is used.

Using a test beam of $E = 1$ GeV photons [47], the shower shape in towers similar to those in the EMCal was measured. The fractional energy per tower was calculated for each electromagnetic cluster, and an average distribution was determined. By fitting the fractional energy per tower for each candidate cluster in PHENIX, the probability (calculated from the χ^2 of the fit) that the cluster fits the expected distribution for an electromagnetic shower is determined.

In the π^0 analysis, all clusters that have a less than 2% probability of being electromagnetic are excluded. Table B.3 (B.4) lists the π^0 efficiency,

[3]However, as the calorimeter is "short" in the radial direction, ∼40% of hadrons will not shower at all in the EMCal, and those that do will on average only deposit a third of their energy, reducing the contamination at high energy.

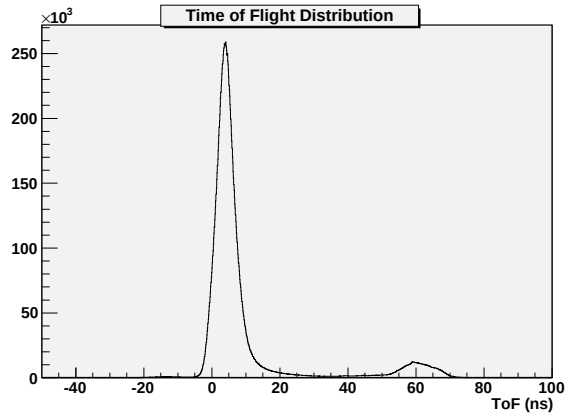

Figure 5.5: Time of Flight distribution for all clusters after warnmap, shower shape and low energy cuts are applied.

background suppression and the remaining background contribution for each p_T bin used in this analysis from Run5 (Run6).

5.8.2 Time of Flight

The time of flight (ToF) of a particle associated with an a energy cluster in the EMCal is defined as

$$ToF = t_{emc} - t_{bbc} \tag{5.8}$$

where t_{emc} is the time difference between the RHIC clock and the time the particle hits the EMCal, and t_{bbc} is the time difference between the RHIC clock and the time the collision occurs, as determined by the BBCs. The resolution of the ToF in PHENIX is 120 ps (200 ps) for PbSc (PbGl) for energy deposits above ∼0.5 GeV [47].

Figure 5.5 shows the ToF distribution for photon candidates. A clear peak is visible at 2 ns, but a long tail and second peak are also visible at longer times. Figure 5.6 shows, for three different p_T ranges, the background percentage in the π^0 mass region for 1 ns ToF bins, where for each bin, at least one candidate photon in the pair must have the ToF of that bin. As the background percentage in the ToF range corresponding to the large peak in Fig. 5.6 is small, this peak is clearly dominated by photons. However, the long tail and the second peak are associated with a very large background percentage, indicating that these clusters are not from (π^0) photons. Such clusters are removed in this analysis.

Table B.5 (B.6) lists the π^0 efficiency, background suppression and the

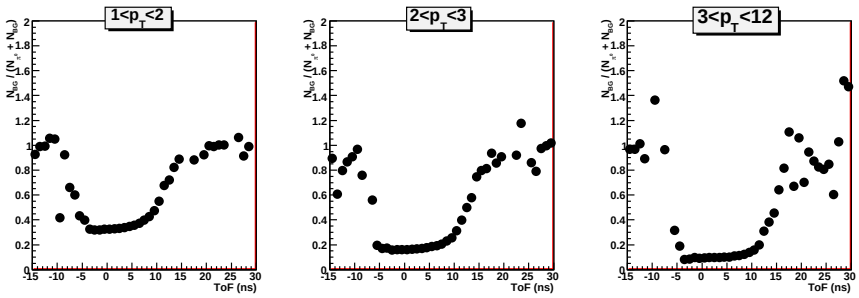

Figure 5.6: Background percentage under π^0 mass peak vs ToF when requiring one of the two clusters has a given ToF, for two low p_T bins, and all high p_T pions.

remaining background contribution for the ToF cut from Run5 (Run6).

5.8.3 Charge Veto

Yet another method of reducing hadron contamination is to apply a veto on clusters associated with charged tracks [71]. For this, we look for hits in the PC3, which is about 20 cm closer radially to the z-axis than the EMCal. We define two vectors: the first from the vertex $(0, 0, z_{BBC})$ to the cluster position in the EMCal, and the second from the vertex to the nearest hit in the PC3. The angle between these two vectors is defined as θ_{cv}.

Figure 5.7a shows the distribution of θ_{cv} from a subset of the Run6 data set in a limited p_T range. If all clusters were unrelated to hits in the PC3, then an even distribution as a function of θ_{cv} is expected, similar to the blue region in Fig. 5.7a. For charged particles, which yield a candidate cluster in the EMCal, originate from the vertex, and have bent trajectories due to the magnetic field, the expected distribution would be peaked about some set θ_{cv}, which would depend on the particle momentum. Therefore, cutting clusters within some set θ_{cv} for a set energy[4] should reduce this background contribution.

Figure 5.7b shows the two photon invariant mass spectrum for three ranges of θ_{cv}. The blue spectrum requires a cluster from the blue region of the θ_{cv} distribution in Fig. 5.7a, which should contain actual photons, and, as a π^0 peak is clearly seen at the expected mass peak, obviously does. The red spectrum, which shows no π^0 peak, requires a cluster from the red region of Fig. 5.7a. The lack of a π^0 peak indicates that the a majority of clusters in

[4]Here, the cluster energy is used as an approximation of the particle momentum, as it is independent of whether or not a track associated with the PC3 hit.

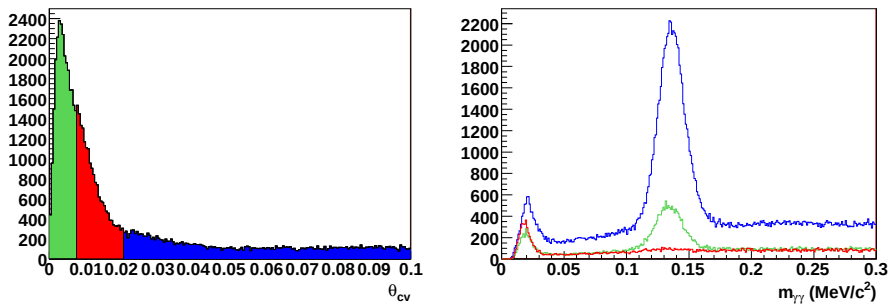

(a) (b)

Figure 5.7: (a) θ_{cv} distribution. Colors are described in text. (b) Two cluster invariant mass distributions for the three regions in (a).

this region are not photons, yielding an invariant mass spectrum of nearly all background.

A perhaps surprising result from Fig. 5.7b is the clear π^0 mass peak when requiring a cluster associated with a PC3 hit at a very small θ_{cv} (green). However, this is easily explained by realizing that the θ_{cv} spectrum for photons has two components. The first is due to unassociated PC3 hits, which should have, as stated above, a flat distribution. A small fraction ($\sim$2%) of photons will convert to e^+e^- pairs in the region of the PC3, leaving a hit in the PC3. These e^+e^- pairs will not diverge, as there is only a very small residual magnetic field at the radius of the PC3, and so the cluster will look electromagnetic. They will deposit essentially the full energy of the parent photon in the EMCal. In effect, the PC3 acts as a first conversion layer of the EMCal. Therefore, to remove hadron contamination while keeping conversion photons, only clusters in the red region in Fig. 5.7a are excluded.

Table B.7 (B.8) lists the π^0 efficiency, background suppression and the remaining background contribution for the charge veto cut from Run5 (Run6). Inefficiency in this cut is primarily due to the dead areas in PC3. As these dead area are spin independent, this inefficiency cancels in calculating A_{LL}. $A_{LL}^{\pi^0}$ was analyzed with and without charge veto, and no significant difference was found.

5.9 Neutral Pion Final Statistics

Table B.9 (B.10) lists the final π^0 statistics and background fraction r after all cuts are applied for Run5 (Run6) ERT triggered data.

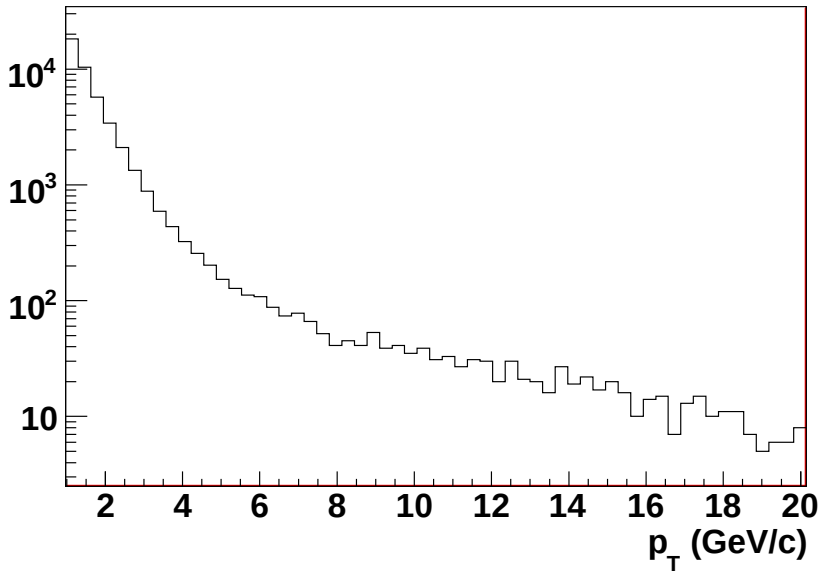

Figure 5.8: Example p_T spectrum for all negatively charged high quality tracks from a small subset of the data.

5.10 Charged Pions: p_T Spectrum

Unlike π^0s, charged pions are directly observed at PHENIX, as they have a significantly longer life time: $2.6033 \pm 0.0005 \times 10^{-8}$ s for charged pions as compared to $8.4 \pm 0.6 \times 10^{-17}$ s for the π^0 [12]. In this case, there is no simple background estimation, as there was for π^0. Therefore, exact percentages for efficiencies and background reduction will not be given. Instead, the effectiveness of each cut will be shown graphically.

The p_T spectrum of all charged tracks[5] in the central arm from a subset of the data is shown in Fig. 5.8. This contains not only charged pions, but also electrons–real (defined as electrons from the interaction and prompt decays from heavy quark hadrons), conversion, and late decay from long lived hadrons–as well as other hadrons, primarily kaons and (anti)protons, and some electronic noise.

In this analysis, only high quality tracks which are associated with Čerenkov radiation in the RICH are used. The primary background consists of conversion electrons close to the DC. To reduce the background contamination in the charged pion sample used in the final A_{LL}, several cuts are applied:

[5]Track quality is already applied.

- PC3 and EMCal matching cut
- DC acceptance cut
- Shower shape cut
- $E/|\boldsymbol{p}|$ cut
- p_T-dependent energy cut.

5.11 Charged Pions: Track Selection

5.11.1 Track Quality

As described in Chapter 3.4, tracks in PHENIX are constructed from hits in four layers of the DC and the first layer of the PC. In this analysis, only the best quality tracks are used, which require both X1 and X2 hits, as well as associated UV and PC1 hits. If there are multiple PC1 hits which could be associated with a candidate track, then the track is used only if there is a best choice based on the UV layers. The number of tracks used in this analysis which are not top quality (*i. e.*, the PC1 hit is not unique) was 1.7%.

5.11.2 RICH Requirement

PHENIX has two methods of identifying charged pions. The first is based on the time of flight of low p_T hadrons (see for example [72]). However, pion-kaon separation is not possible above 2.8 GeV/c. The second method relies on the PHENIX RICH.

As is stated in Chapter 3.5.1, charged pions begin to Čerenkov radiate at 4.7 GeV/c, allowing charged pions to be distinguished from all other (more massive) hadrons up to a p_T of $\sim$17 GeV/c, at which point kaons also Čerenkov radiate. For this analysis, a RICH associated track is defined as a track with two or more triggered PMTs in a disc centered on the track position extrapolated to the RICH. Figure 5.9 shows the p_T spectrum for high quality RICH associated negative (left) and positive (right) charged tracks. The rise near $p_T = 4.7$ GeV/c is due to charged pions above the Čerenkov threshold.

It is an overstatement to define this method as particle identification, as it is difficult to use the RICH to distinguish charged pions from background electrons radiating in the RICH.[6] The source of electrons in PHENIX, and the

[6]For electron analyses in PHENIX, the angle of Čerenkov radiation is used to remove charged pion background. As the size of the angle of Čerenkov radiation depends on the

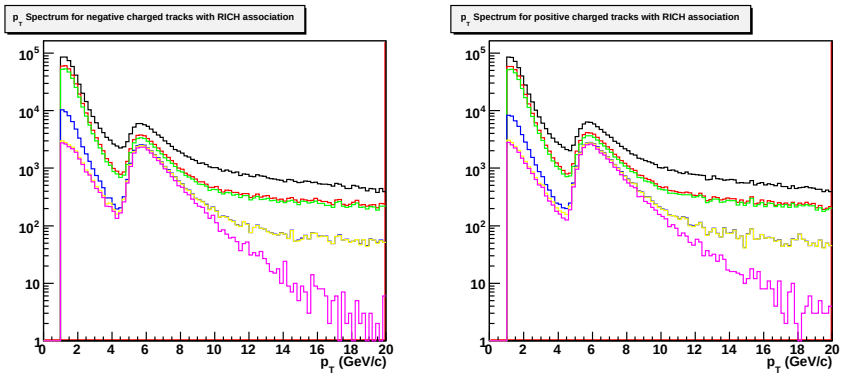

Figure 5.9: Transverse momentum spectra for high quality RICH associated ERT trigger tracks with negative (left) and positive (right) charge in black. A clear rise in the spectrum is seen at 4.7 GeV/c, the Čerenkov threshold for charged pions in $C0_2$. The colored spectra show the effects of adding the following cuts to the previous spectra: matching (red), DC acceptance (green), electromagnetic probability (blue), $E/|\boldsymbol{p}|$ (yellow) and momentum dependent energy (pink) cuts.

methods used to remove them from the final sample are the topic of the rest of this chapter.

5.12 Charged Pions: Sources of Background

5.12.1 Electron Background

There are three major sources of electrons[7] in $p+p$ scattering in PHENIX. The first are physics electrons from the vertex. This sample includes electrons from heavy quark hadron decay, as there is no way to distinguish these electrons from those actually originating at the real interaction vertex with the present PHENIX vertex resolution.[8] The momentum of such electrons is correctly

p_T of the particle when close to threshold, the cone size for a 5 GeV/c pion would be on average smaller than that of an electron with a p_T >200 MeV/c. The light from charged pions will then be reflected onto a smaller number of PMTs. The light from electrons would be reflected onto a ring of PMTs whose radius is correlated to the angle of Čerenkov radiation. This difference was studied for this analysis for a possible purification of the charged pion sample. Evidence of the difference was found, but the effectiveness of a cut based on this appeared low and dropped quickly towards higher p_T, and so no cut was used.

[7]Throughout the following, we use "electron" to describe both positrons and electrons.

[8]This is the primary reason the VTX is being built.

reconstructed (within the stated uncertainty). However, for $p_T > 5$ GeV/c, the cross section for these electrons is about three orders of magnitude lower than that of charged pions [73]. Therefore, prior to any cuts, such electrons already are an insignificant background.

This leaves two remaining sources of electrons in the candidate charged pion sample: "slow" decays from light hadrons and photon conversions.

Photons can convert anywhere in matter. Therefore, in PHENIX there are four different conversion types: (1) conversions in the beam pipe (or other nearby material) where the magnetic field is strong, conversions in the central arm acceptance (2) prior to the DC (including the front window of the drift chamber) or (3) after the first DC X layer and (4) conversions outside of the acceptance (for example in the pole tip or magnet) which scatter back into the acceptance. Type (3) will not have a hit in the first X layer of the DC, and so are already excluded by track quality. Conversions of type (4) are expected to be limited to the edges of the acceptance, and are primarily removed by an acceptance cut on tracks in the DC (Sec. 5.13.2).

For types (1) and (2), the probability to have a conversion electron with $p_T > 5$ GeV/c is very small due to the small yield of photons with $p_T > 5$ GeV/c and the small radiation length of the material prior to the drift chamber. Therefore, most conversion electrons will have low p_T. Conversion electrons from (or near) the beam pipe will experience the strong magnetic field, and the reconstructed momentum will be nearly the actually momentum. Thus, conversion electrons from the beam pipe with a reconstructed $p_T > 5$ GeV/c are not a significant background for charged pions.

However, for conversion of type (2), there is a problem in the reconstructed momentum due to the method described in Chapter 3.4. This method assumes that the track originated at the vertex, and experienced the large magnetic field near the beam pipe. Instead, for an electron (see Fig 5.10) from a photon which converts near the front of the drift chamber, the angle α is uncorrelated to the actual momentum. The momentum is instead correlated with the angle of its trajectory at creation and the bend it undergoes in the weaker magnetic field at the DC. Therefore, these electrons can have a large reconstructed momentum, even if their actual momentum is quite small. Many of the cuts described below are designed to reduce the contamination of these fake high p_T electrons.

Finally, for leptonic decays from long lived particles away from the interaction vertex, the largest sample will be from low momentum hadrons decaying prior to the RICH. From the branching ratios [12], only charged kaons decay into a final state including an electron a significant amount of the time ($\sim$5%). If the decay occurs after the RICH, then the parent kaon would not radiate in

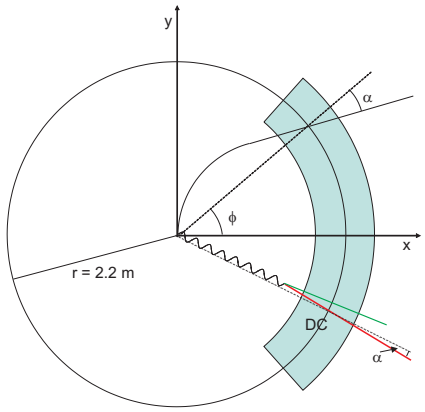

Figure 5.10: A real track (black) bends in the magnetic field, and so α is correctly related to momentum. A photon which converts before the DC into an e^+e^- pair can give tracks which have incorrectly calculated momenta. The same holds for long lived neutral hadrons which decay into charged pions.

the RICH (unless it has very high p_T), and the track would not be a candidate in the charged pion sample. On the other hand, if the decay occurs prior to the RICH, as long as the decay electron has $p > 17$ MeV/c, it will radiate in the RICH. Due to decay kinematics, the p_T of these tracks may be incorrectly reconstructed. Such tracks can primarily be rejected by matching the expected hit location in the PC3 and EMCal with the actual hit location, as will be discussed in Sec. 5.13.1.

5.12.2 Hadronic Background

There are two sources of hadronic background in $p+p$ collisions that we briefly consider here: hadronic showers from the pole tips, and charged pions from other hadronic decays.

Hadronic showers from the pole tips, resulting in high p_T charged pions, are removed with a acceptance cut. Charged pions originating from other hadronic decays are a source of background when measuring A_{LL}, as we are interested in charged pions from the initial fragmentation. Similar to electrons from kaon decays, the momentum may be incorrectly reconstructed, especially if the parent hadron has neutral charge (see Fig. 5.10, where the photon is replaced by a neutral hadron, and the e^+e^- pair by a $\pi^+\pi^-$ pair). However, to be included in the signal, they must Čerenkov radiate, implying their $p_T >$ 4.7 GeV/c and that the parent hadron has very high p_T. The small likelihood of these events implies that this is only a significant problem when the real

charged pion yield is low, *i. e.* for $p_T > 10$ GeV/c, where matching cuts can mostly remove them.

5.12.3 Future Background Reduction

Note that the VTX detector will essentially remove almost all of the false high p_T background when it is installed in Run10 by requiring tracking points in the magnetic field region.

5.13 Charged Pions: Cuts (Efficiencies, Studies)

5.13.1 Matching Cuts

For background from decays, in the center of mass frame of the parent hadron, the decay is isotropic. Therefore, when boosted into the lab frame, the decay electron or charged pion trajectory will differ from that of the parent hadron (though the difference decreases on average with the parent hadron momentum, *i. e.* a larger boost). If the candidate track is extrapolated from the DC and PC1, assuming it originated at the BBC vertex, to either the PC3 or the EMCal, decay particles would on average be further from the extrapolated value than tracks actually from the vertex. This concept is used in this analysis in the form of PC3 and EMCal matching cuts [74].[9]

Such a cut can also reduce the conversion electron contamination for types (2) and (4) from above. Some fake high p_T conversions of type (2) will be cut, as their trajectory due to bending in the residual magnetic field will disagree with the expected trajectory for such high p_T particles. Conversion electrons (type (4)) and hadrons from showers in the magnet are also unlikely to follow a trajectory extrapolated using the vertex and the DC/PC1 hits.

The basic concept of track matching is to extrapolate the track defined by the DC, PC1, and vertex to the PC3 or EMCal, and check how well this coincides with the nearest hit in that detector. To define how well a track matches, a distribution of the difference between the expected and actual hit location, Δz ($\Delta\phi$), in the z (ϕ) direction, is plotted.

The resulting distribution is then fit so that a resolution (σ of the distribution) can be defined. The top (bottom) plots in Fig. 5.11 show example distributions for negatively charged tracks with $6 < p_T < 7$ GeV/c with σ normalized to one for (a) Δz and (b) $\Delta\phi$, respectively, using the PC3 (EMCal).

[9] Due to the limited acceptance of PC2, it is not used in this analysis.

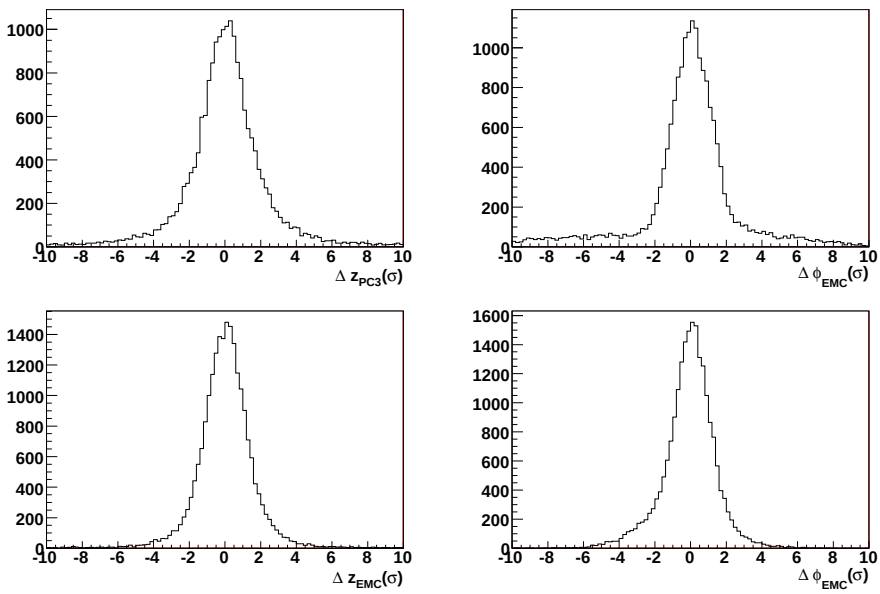

(a) (b) (c)

Figure 5.11: Distributions of the difference between the expected and actual hit location in the PC3 (top) and EMCal (bottom) in the (a) z and (b) ϕ directions for high quality RICH associated ERT trigger tracks with $6 < p_T < 7$ GeV/c.

Essentially, the distribution consists of a gaussian distribution for tracks originating from the vertex on top of several wider distributions related to the different mechanism discussed above for generating "false" tracks. This is the main reason why tails of the distributions in Fig. 5.11 are not Gaussian.

The effect of this cut can be seen in Fig. 5.9. The black line shows the p_T distribution for all high quality RICH associated ERT trigger tracks while the red line shows the same distribution after applying matching cuts. The greater reduction in yields for $p_T < 5$ GeV/c (effectively all background) than for $5 < p_T < 7$ GeV/c clearly indicate the usefulness of this cut.

5.13.2 Drift Chamber Acceptance Cut

As was discussed above, a potential source of hadronic background and conversion electrons in PHENIX is the central magnet (including the CM poletips). We define the DC z position as the z coordinate of the mid-point of the track in the DC at r=2.2 m (see Fig. 3.7). Figure 5.12 shows the charged pion candidate track distribution for the different charges as a function of the DC z position for all high quality RICH associated ERT trigger tracks. The black

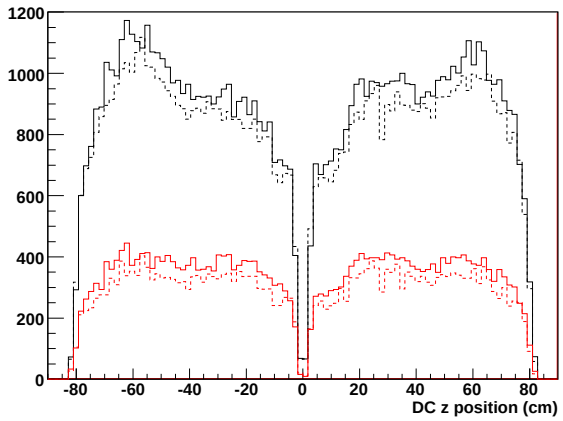

Figure 5.12: DC z position (see text for definition) for negatively (solid) and positively (dashed) charged high quality RICH associated ERT trigger tracks with only matching cuts (black) or with all cuts except DC acceptance cut (red). The dip near $z = 0$ is due to the readout "spine" of the DC.

distribution have only matching cuts, while the red distribution includes only tracks passing all other cuts (excluding DC z position). To reduce the background contamination from these tracks, which can include charged pions, an acceptance cut is applied to the z-position of the track in the DC. The effect of including this cut can be seen from the green spectra in Fig. 5.9.

5.13.3 (Electromagnetic) Shower Shape

The following three cuts rely on using the energy deposit in the EMCal to distinguish electrons, which deposit their full energy in electromagnetic showers, from charged pions, which on average deposit only a third of their energy over a larger number of towers. Note that the trigger requirement for candidate tracks (see Sec. 5.2) excludes all minimally ionizing tracks.

The first cut using the full information in the EMCal relies on the shower shape associated with a candidate track. As was described in Sec. 5.8.1, the EMCal can be used to determine the probability that the shape of the cluster associated with the track is electromagnetic.[10] By requiring that there is less than a 20% probability that the cluster is electromagnetic, 80% of all electrons from all sources are excluded from the charged pion sample [74].

[10]In this case, as the cluster is associated with a charged track, "electromagnetic" is assumed to indicate the deposit is from an electron.

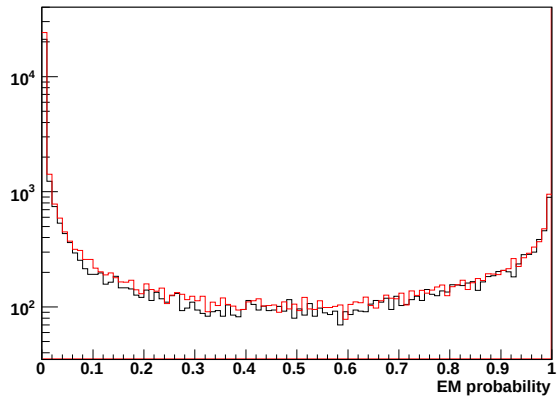

Figure 5.13: Electromagnetic (EM) probability distribution for negatively (red) and positively (black) charged high quality RICH associated ERT trigger tracks with matching and DC acceptance cuts applied. Only tracks with $5 < p_T < 10$ GeV/c, the p_T range used in the A_{LL} analysis are shown.

Figure 5.13 shows the distribution of electromagnetic probability for all high quality RICH associated ERT trigger tracks after matching and DC acceptance cuts have been applied with $5 < p_T < 10$ GeV/c. Figure 5.14 shows the 2-D distribution of electromagnetic probability vs. p_T for these tracks (neglecting the constraint). The charged pion turn on in the RICH is clearly seen at low probability, and drops quickly towards high probability. This trend is clearly different from the trend below the charged pion Čerenkov radiation turn on at 4.7 GeV/c. Clearly, the majority of charged pions are not well described as "electromagnetic", and so survive this cut.

In Fig. 5.9, the reduction in background can be seen as the blue spectra. This clearly reduces the yield for $p_T < 5$ GeV/c and $p_T > 7$ GeV/c while only slightly reducing the yield from $5 < p_T < 7$ GeV/c where it is dominated by charged pions.

5.13.4 $E/|\boldsymbol{p}|$ Cut

Figure 5.15 shows (blue line) the ratio of energy to (total) momentum (E/p) for all high quality RICH associated ERT trigger positively charged tracks after matching and DC acceptance cuts with $p_T > 1$ GeV/c. A clear peak is seen centered near $E/p = 1$. This peak is associated with "physical" electrons, defined as those with properly reconstructed momentum, *i. e.* electrons from the vertex and beam pipe conversions (Type (1) in Sec. 5.12). A second

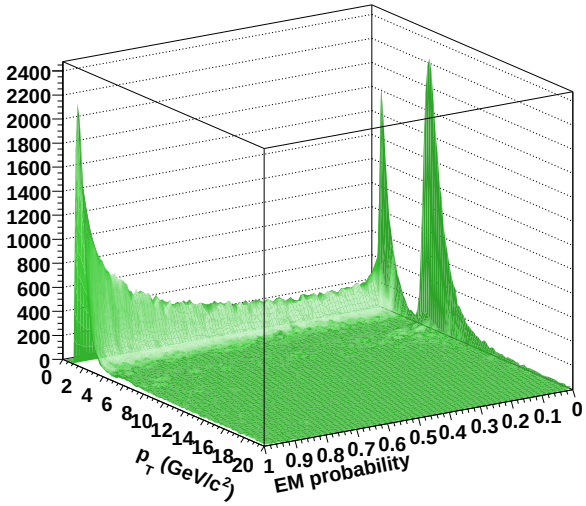

Figure 5.14: Distribution of electromagnetic (EM) probability vs. p_T for negatively charged high quality RICH associated ERT trigger tracks with matching and DC acceptance cuts applied. A clear rise in the spectrum is seen at 4.7 GeV/c at low EM probability, but is nearly invisible at high EM probability.

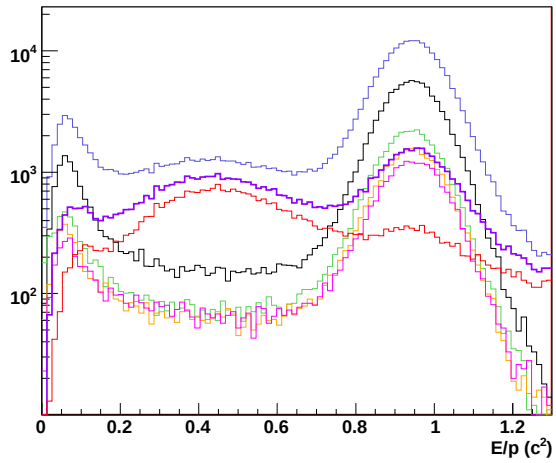

Figure 5.15: Distribution of E/p for positively charged high quality RICH associated ERT trigger tracks with matching and DC acceptance cuts applied and $p_T > 1$ GeV/c. The different distribution are for different electromagnetic probability ranges: 0-1 (blue), 0.8-1.0 (black), 0.6-0.8 (green), 0.4-0.6 (orange), 0.2-0.4 (pink), 0.0-0.2 (thick purple), 0.00-0.01 (red). The thick purple line corresponds to the spectrum after the electromagnetic probability cut actually used in the analysis.

wider peak is visible centered around $E/p \sim 0.4$. Recall that the EMCal is about 1 nuclear interaction length, and so charged pions will on average deposit $1/e$ of their energy, which for high momentum particles coincides with $\langle E/p \rangle = 1/e \sim 0.4$. To see this more clearly, E/p has also been plotted in Fig. 5.15 for different ranges of electromagnetic probability. It is evident that at high probability (probability>0.6, in black and green) there is no peak centered on $E/p \sim 0.4$, while there is clearly a peak at $E/p \sim 1$. The peak at $E/p \sim 0.4$ is visible at very low probability (probability< 0.01, in red), while the peak at $E/p = 1$ associated with "physical" electrons is quite reduced. The thick purple line corresponds to probability< 0.2, which is the actual cut used in the analysis.

To remove the contamination from "physical" electrons, all tracks with $E/p > 0.9$ are excluded from the charged pion sample. Figure 5.16 show the E/p distributions for high quality RICH associated ERT trigger tracks with matching, DC acceptance and EM probability cuts applied for the three p_T bins used in the A_{LL} analysis.

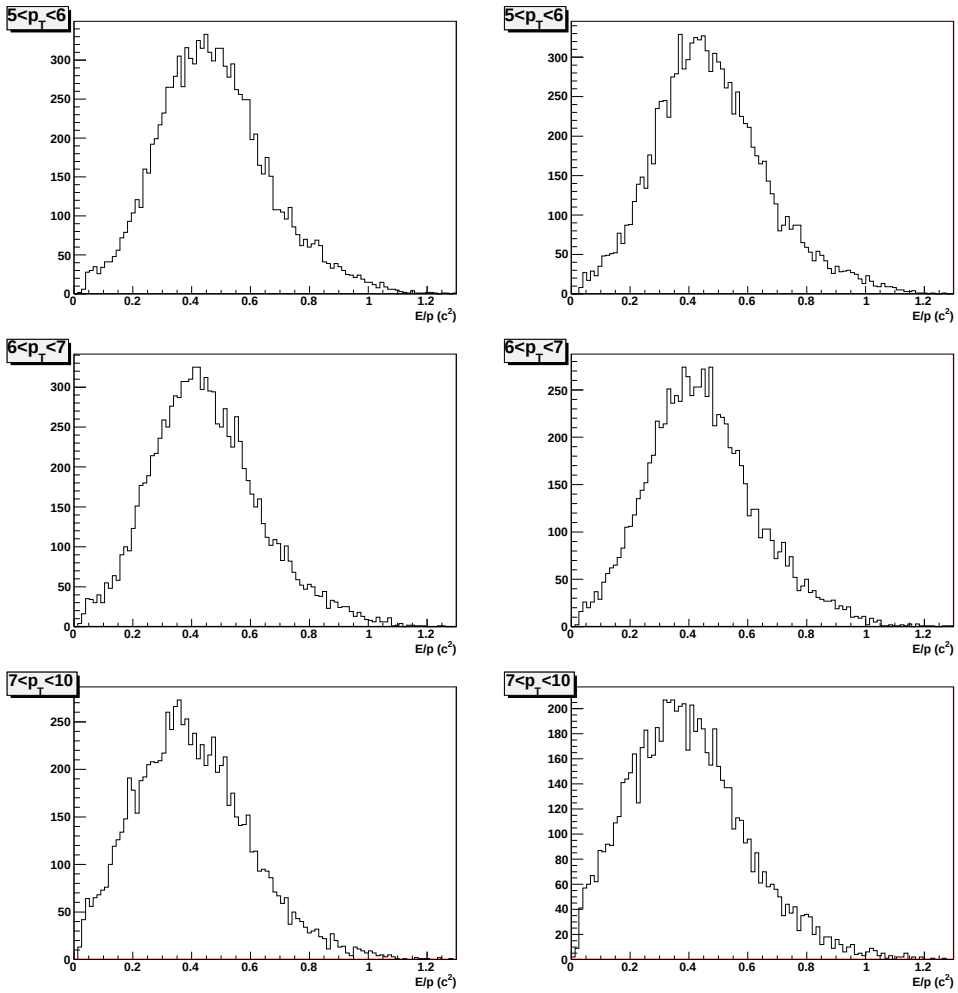

(a) **(b)**

Figure 5.16: Distribution of E/p for (a) negatively and (b) positively charged high quality RICH associated ERT trigger tracks with matching, DC acceptance and electromagnetic probability cuts applied with $5 < p_T < 6$ GeV/c (top row), $6 < p_T < 7$ GeV/c (top row) and $7 < p_T < 10$ GeV/c (top row).

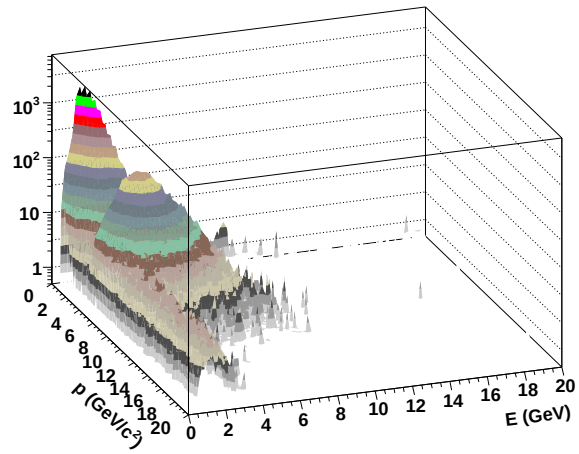

Figure 5.17: Distribution of energy vs. p_T for positively charged high quality RICH associated ERT trigger tracks with matching, DC acceptance and electromagnetic probability cuts applied.

5.13.5 p_T Dependent Energy Cut

A third structure can be seen in Fig. 5.15 at low E/p. This structure is clearly electromagnetic, as it appears at all values of EM probability except those very close to zero. This structure is due to conversion electrons of Type (2) (see Sec. 5.12). Figure 5.17 shows a 2-D surface histogram of energy vs. momentum with all cuts described above except E/p included. Three structures are visible: (1) a peak at $E/p \sim 1$, (2) the charged pion turn on in the RICH and (3) a long ridge at near constant energy of $\sim$2 GeV.

This ridge corresponds to the low E/p peak in Fig. 5.15, and is due to conversion electrons of type (2) which have incorrectly reconstructed high p_T. As the amount of material in front of the X1 layer in the DC is small, the large majority of these electrons will originate from low energy photons. Therefore, the energy of the conversion electrons will be much smaller than the reconstructed momentum.[11] To reduce this electron contamination, a momentum dependent energy cut is applied [74]. Figure 5.18 shows the p_T spectrum of candidate charged pions where matching cuts, DC acceptance, electromagnetic probability and E/p cuts are applied in black. The effect of the ridge in Fig. 5.17 can be seen as the flat background at high p_T. The red, green,

[11] While the majority of such electrons will have very small energy, the trigger requirement will select higher energy electrons. The average energy is around 2 GeV due to the trigger turn on effect.

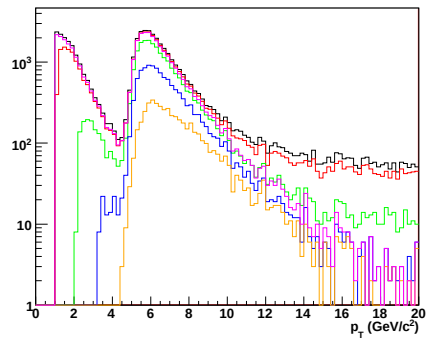

Figure 5.18: Transverse Momentum Distribution for positively charged high quality RICH associated ERT trigger tracks with matching, DC acceptance, electromagnetic probability and E/p cuts applied. Different spectra are for different minimal energy cut: no cut (black), $E > 1$ GeV (red), $E > 2$ GeV (green), $E > 3$ GeV (blue), $E > 4$ GeV (orange), and $E > 0.3 + 0.15p_T$ GeV (pink).

blue, and orange lines represent different minimal energy cuts. While cuts of $E > 3$ GeV remove most of this background, there is also a large reduction in charged pion statistics. Instead, a momentum dependent energy cut was developed, and is applied in this analysis. The effect of this cut is clearly visible in the pink spectra in Fig. 5.9.

5.14 Charged Pions Background Estimates

Figures 5.19 show the p_T spectrum for positive and negative charged pions after all cuts. Two simple fits can be applied to the data to estimate the background. The idea is to extrapolate the charged particle yield seen in the low p_T region ($p_T < 4$ GeV/c) into the signal region. In general, we expect that the charged pion p_T spectra at high p_T should be described by a power law. Therefore, we can use the sum of two functions: a power law describing the high p_T charged pions and either a exponential or power law fit to the low p_T particles radiating in the RICH. In order to account for the turn on for pions radiating in the RICH, a Fermi function is multiplied by the power law describing high p_T charged pion, giving

$$N_{yield} = N_{\pi^\pm} f_{\pi^\pm}(p_T) + N_{BG} f_{BG}(p_T) \tag{5.9}$$

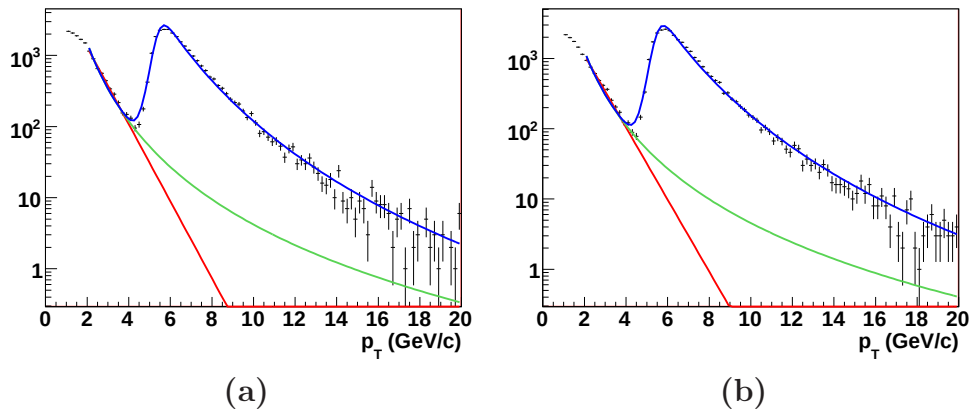

Figure 5.19: Final p_T spectrum after all cuts for (a) positive and (b) negative charged pions. Blue line is data fit with Eq. 5.9 with Type 2 background. Green line shows Type2 background function. Similar fit with was done using Eq. 5.9 with Type1 background, and was nearly the same as blue line in signal region. Red line is Type1 background from this second fit.

where

$$f_{\pi^\pm}(p_T) = \frac{1}{e^{\frac{p_T - a0}{a1}+1}} p_T^{a2} \tag{5.10}$$

and

$$Type1 \quad : \quad f_{BG}(p_T) = e^{-a3 p_T} \tag{5.11}$$

$$Type2 \quad : \quad f_{BG}(p_T) = p_T^{a3}. \tag{5.12}$$

The results of the fits are also shown in Fig. 5.19 assuming a background of Type2 (in blue). The fit with background of Type1 was very similar in the signal region. The background functions from the fits also are plotted in red and green for Type1 and Type2 respectively. Neither fit indicates a large background for $5 < p_T < 10$ GeV/c, the p_T range used in the A_{LL} analysis, and both are likely overestimates. However, for the current exploratory analysis, they are acceptably small.

5.15 Charged Pions Final Statistics

Table B.11 gives the final statistics for tracks satisfying all cuts described above in the three p_T bins used for the A_{LL} analysis, as well as charged pion yield and the background percentage assuming a Type2 background.

Chapter 6

Double Helicity Asymmetry Measurement

As discussed in Chapter 1, a double helicity asymmetry (A_{LL}) is defined as

$$A_{LL} = \frac{\Delta\sigma}{\sigma}. \tag{6.1}$$

Experimentally, we actually measure the difference in luminosity normalized yields as given in Eq. 4.5. The necessary ingredients for measuring the double helicity asymmetry in neutral and charged pions have been discussed in Chapters 4 (luminosity normalization and polarization) and 5 (event selection and yields). In this Chapter, the methods used for calculating A_{LL} and its statistical uncertainty $\sigma^{stat}_{A_{LL}}$ are discussed. For π^0 A_{LL}, the asymmetry of the background is estimated, and subtracted from the signal asymmetry. For charged pion A_{LL}, the estimated backgrounds are quite small, and no background asymmetry is estimated. Two possible methods are available for calculating A_{LL}: bunch fitting, which was used for relative luminosity (see Chap. 4.1), or calculating Eq. 4.5 fill by fill (FBF). As bunch fitting divides the sample by a factor of 50-100, large statistics are required. Therefore, we use Eq. 4.5 to calculate A_{LL} for each fill, and then take the uncertainty weighted average over all fills in either Run5 or Run6 for the final result.

6.1 Neutral Pion

6.1.1 Background Subtraction Method

For calculating the π^0 asymmetry, we include all two photon invariant mass pairs in the mass range of $112 < m_{\gamma\gamma} < 162$ MeV/c^2. In Fig. 6.1, this region

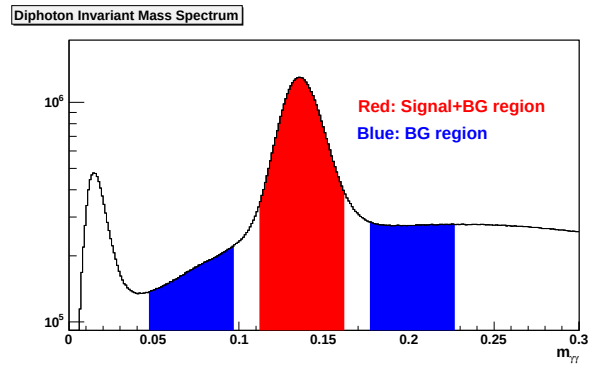

Figure 6.1: Two photon invariant mass spectrum. The red region under the π^0 peak ($112 < m_{\gamma\gamma} < 162$ MeV/c^2) is used in this analysis to measure $A_{LL}^{\pi^0+BG}$. The background contribution is estimated by measuring the asymmetry (A_{LL}^{BG}) in the two blue regions on the sides of the π^0 peak ($50 < m_{\gamma\gamma} < 100$ MeV/c^2 and $170 < m_{\gamma\gamma} < 220$ MeV/c^2).

is shown in red and roughly corresponds to two sigma around the peak. As the number of counts in this region under the peak include both signal (N_{π^0}) and combinatorial background (N_{BG}), the measured asymmetry, defined as $A_{LL}^{\pi^0+BG}$, is a combination of $A_{LL}^{\pi^0}$ and the asymmetry in the combinatorial background, A_{LL}^{BG}. By fitting the two photon invariant mass spectrum with a Gaussian plus a third order polynomial, the fraction of background under the peak, r, can be estimated. The measured asymmetry can then be written as

$$A_{LL}^{\pi^0+BG} = (1-r)A_{LL}^{\pi^0} + rA_{LL}^{BG} \quad \text{where} \quad r = \frac{N_{BG}}{N_{BG} + N_{\pi^0}} \tag{6.2}$$

and r is given in Tables B.9 and B.10 for Run5 and Run6.

The asymmetry of the background under the π^0 mass peak cannot be measured directly, so instead the asymmetry of the two sidebands, ($50 < m_{\gamma\gamma} < 100$ MeV/c^2 and $170 < m_{\gamma\gamma} < 220$ MeV/c^2), shown in blue in Fig. 6.1, is used. The validity of this assumption is considered in Chapter 7.1. Using Eq. 6.2, the final π^0 asymmetry is given by

$$A_{LL}^{\pi^0} = \frac{A_{LL}^{\pi^0+BG} - rA_{LL}^{BG}}{1-r} \quad , \qquad \sigma_{A_{LL}^{\pi^0}} = \frac{\sqrt{\sigma^2_{A_{LL}^{\pi^0+BG}} + r^2\sigma^2_{A_{LL}^{BG}}}}{1-r}. \tag{6.3}$$

The asymmetries for $A_{LL}^{\pi^0+BG}$ and A_{LL}^{BG} are measured fill by fill, and the fit with a constant. These constants are then used in Eq. 6.3 to calculate $A_{LL}^{\pi^0}$ for

the entire RHIC run.

6.1.2 Odd and Even Requirement

As was discussed in Chapter 3.3.3, due to two different ERT electronics chains, all data are analyzed separately for even and odd crossings. These two data sets are statistically independent. Therefore, the final A_{LL} are calculated as the uncertainty weighted average:

$$A_{LL} = \frac{\frac{A_{LL}^{\text{even}}}{(\delta A_{LL}^{\text{even}})^2} + \frac{A_{LL}^{\text{odd}}}{(\delta A_{LL}^{\text{odd}})^2}}{\frac{1}{(\delta A_{LL}^{\text{even}})^2} + \frac{1}{(\delta A_{LL}^{\text{odd}})^2}} , \qquad \delta A_{LL} = \sqrt{\frac{1}{\frac{1}{(\delta A_{LL}^{\text{even}})^2} + \frac{1}{(\delta A_{LL}^{\text{odd}})^2}}} . \tag{6.4}$$

6.1.3 Statistical Uncertainty on A_{LL}

The uncertainty in the two photon yield, $\Delta N_{\gamma\gamma}$, is not simply $\sqrt{N_{\gamma\gamma}}$ as there may be more than one photon pair per event in the specified mass range. The number of photon pairs can be written as

$$N_{\gamma\gamma} = \sum_{i=1}^{N_{ev}} k_i = \bar{k} N_{ev} \tag{6.5}$$

where k_i is the multiplicity per event, N_{ev} is the number of events and $\bar{k}$ is the average multiplicity. As is shown in Appendix A.1, the uncertainty in $N_{\gamma\gamma}$ is instead given by

$$\sigma_{N_{\gamma\gamma}} = \sqrt{\frac{\bar{k^2}}{\bar{k}} N_{\gamma\gamma}} . \tag{6.6}$$

We define $k_{enhance} = \sqrt{\frac{\bar{k^2}}{\bar{k}}}$ as the enhancement in the uncertainty compared to the Poissonian uncertainty, $\Delta N_{\gamma\gamma} = \sqrt{N_{\gamma\gamma}}$. In the limit of either $k = 0$ or $k = 1$, then $k_{enhance} \rightarrow 1$ and we recover Poisson statistics.

Table B.12 (B.13) lists the mean $k^2_{enhance}$ for each p_T bin from Run5 (Run6) for both N^{π^0+BG} and N^{BG}.

6.1.4 Fill-by-fill A_{LL} Calculation

Equation 4.5 is calculated for both the signal and background regions for each fill. A sample of the results are shown in Fig. 6.2 for the peak region asymmetry ($A_{LL}^{\pi^0+BG}$) from Run6 in even crossings plotted as a function of fill number.

The red lines in Fig. 6.2 are fits of the data to a constant. This fit of A_{LL} vs. fill number simply returns the uncertainty weighted average. The χ^2 values

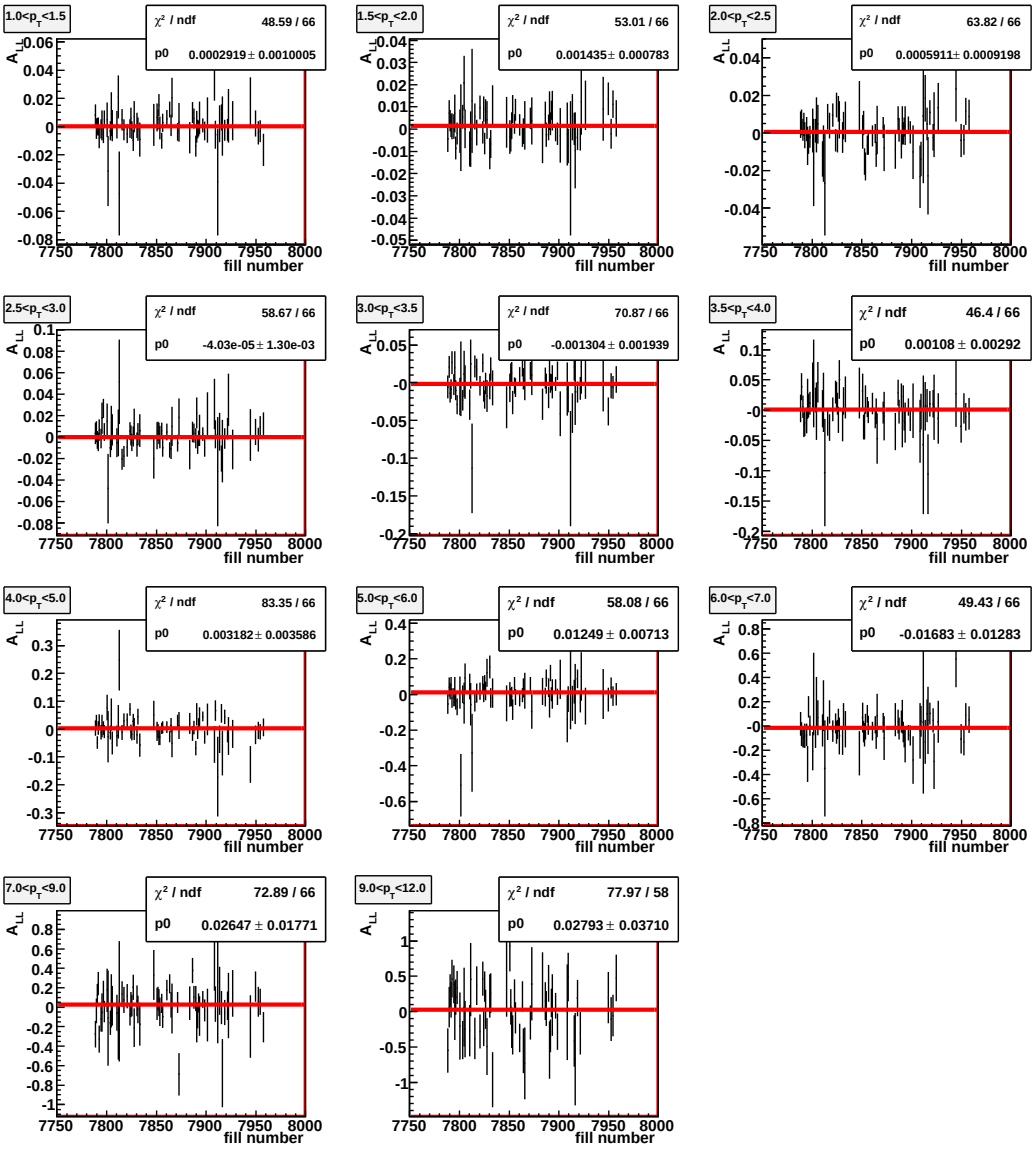

Figure 6.2: $A_{LL}^{\pi^0+BG}$ vs. fill number for the ERT data set using only even crossings for 11 photon pair p_T bins used in the Run6 analysis. Top row, from left to right: 1.0-1.5, 1.5-2.0, 2.0-2.5 GeV/c. Second row, from left to right: 2.5-3.0, 3.0-3.5, 3.5-4.0 GeV/c. Third row, from left to right: 4.0-5.0, 5.0-6.0, 6.0-7.0 GeV/c. Bottom row, from left to right: 7.0-9.0, 9.0-12.0 GeV/c. The line is a fit to a constant.

from the fits, though, are an indication of how reasonably well the FBF results are described by a constant. If a fill to fill systematic uncertainty remained, we would expected the fit to be poor, and so the χ^2/DOF would be large. In all cases, the χ^2/DOF appears reasonable. In Chapter 7.7, a more robust way of checking for systematic uncertainties based on this χ^2 evaluation will be presented.

6.1.5 Minbias Analysis

A FBF analysis has also been performed using minbias triggered events. Normally, this is done solely as a cross check as only a small fraction of the DAQ bandwidth is dedicated to minbias triggers, and so the ERT data yields a significantly larger π^0 sample. However, in 2005, $A_{LL}^{\pi^0}$ was measured for $0.5 < p_T < 1.0$ GeV/c. In this p_T range, the ERT trigger efficiency is so low that the minbias data contains many times more π^0 s. Therefore, we present here the results for all minbias data from Run5, but for the final result will use only the data with $0.5 < p_T < 1.0$ GeV/c.

For minbias events, we do not use the ERT trigger and so there is no reason to calculate odd and even separately. Also, we do not apply the ERT trigger check (see Chapter 5.2) for minbias data. A complication in the minimum bias data set comes from the trigger prescale, which allow only every ith minbias event to be recorded. Data at PHENIX is taken in one hour runs, with about seven or eight runs per fill. As prescales are set on a run by run basis, the prescale can (and often does) change during a fill in order to maximize the DAQ bandwidth. Therefore, the prescale does not cancel out in Eq. 4.5. For example, if we have two runs in a fill, with prescales a_1 and a_2, then

$$L_{fill} = \frac{L_1}{a_1} + \frac{L_2}{a_2} \tag{6.7}$$

and so

$$R = \frac{L_{fill}^{++}}{L_{fill}^{+-}} = \frac{\frac{L_1^{++}}{a_1} + \frac{L_2^{++}}{a_2}}{\frac{L_1^{+-}}{a_1} + \frac{L_2^{+-}}{a_2}} \,. \tag{6.8}$$

Clearly, the prescales will not cancel. (No prescales were used for the ERT trigger in Run5. In Run6, a few runs had the lowest energy trigger prescaled and were excluded from the analysis.) Note that both the luminosity and the uncertainty are scaled equally, *i. e.*

$$L_{prescaled} = \frac{L}{a} \,, \quad \sigma_{L,prescaled} = \frac{\sqrt{L}}{a} \,. \tag{6.9}$$

The FBF results from Run5 using the minbias data sample for $A_{LL}^{\pi^0+BG}$ and A_{LL}^{BG} from *all* crossing are in Fig. 6.3. Only the two lowest p_T bins which are used in the final result are shown.

6.1.6 Average p_T in p_T Bins

Average π^0 p_T in each p_T bin is calculated from the average p_T ($\langle p_T \rangle$) of the signal window ($\pi^0 + BG$) and background (BG):

$$\langle p_T^{\pi^0} \rangle = \frac{\langle p_T^{\pi^0+BG} \rangle - r \langle p_T^{BG} \rangle}{1 - r}, \tag{6.10}$$

where r is background contribution from Table B.9 or B.10 defined in Eq. 6.2. The mean p_T values are summarized in Table 6.1.

6.1.7 Results

The result for $A_{LL}^{\pi^0}$ is calculated using Eq. 6.3. The final results for $A_{LL}^{\pi^0}$ from ERT trigger events in even and odd crossings separately is shown in Fig. 6.4 for Run5 and Run6 respectively. In both cases, the data are seen to be consistent.

ERT data from odd and even crossings are combined using Eq. 6.4. As the minbias data is used for the π^0 result with $p_T < 1.0$ GeV/c, Fig. 6.5 shows the Run5 minbias result along with the ERT result after combining odd and even crossings. In Run6, the minbias prescales were quite large, and so the Run6 data is not more significant compared to Run5. Therefore, the data below $p_T = 1$ GeV/c was not updated in Run6. The final results for Run5 and Run6 are plotted together in Fig. 6.6. The data from Run5 include the minbias results with $p_T < 1$ GeV/c. All other data is from ERT triggered events. The results from the two years are consistent. The final results from Run5 and Run6 are listed in Table 6.1.

6.2 Charged Pions

6.2.1 Statistical Uncertainty on A_{LL}

The measured charged pion yield is roughly 20% of the π^0 yield due to reduced trigger efficiency. In the same p_T range as the charged pion data, $k^2_{enhance} \leq 1.03$ for the π^0. Therefore, for the charged pion analysis, Poisson statistics were assumed, as the likelihood of triggering on two high p_T charged pions is negligible.

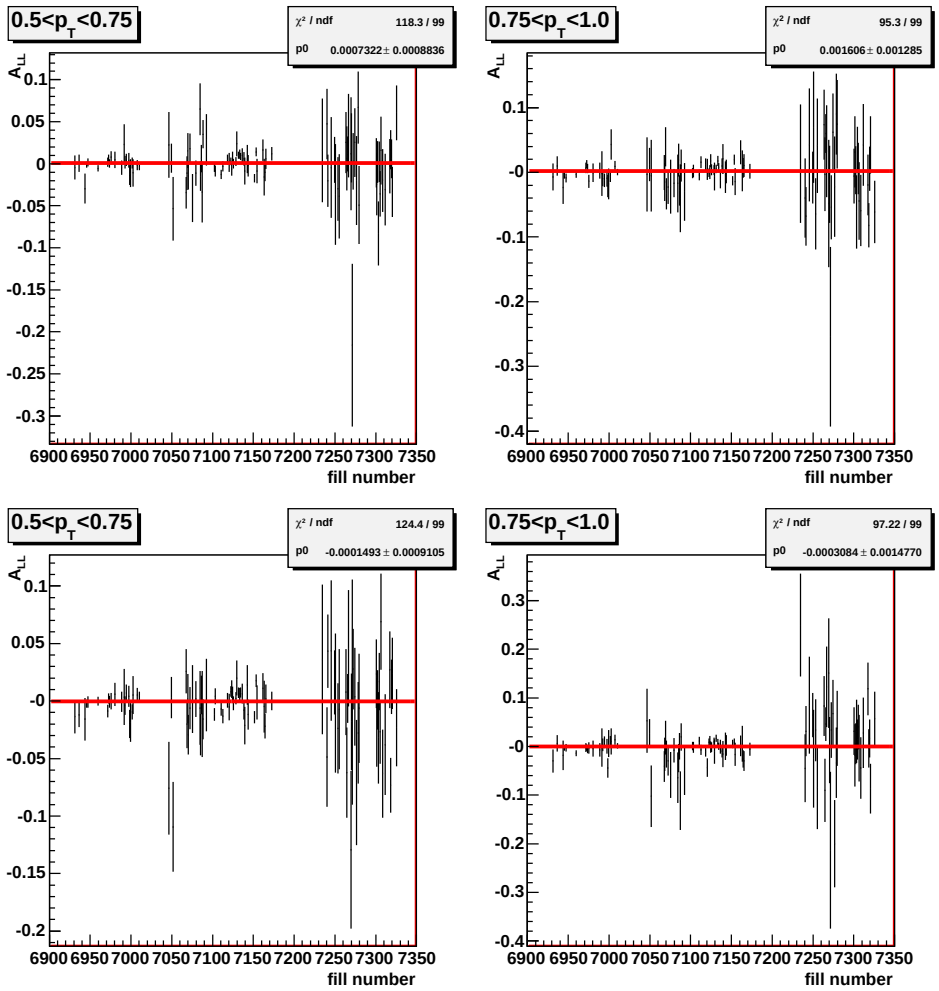

Figure 6.3: $A_{LL}^{\pi^0+BG}$ (top) and A_{LL}^{BG} (bottom) vs. fill number for the minbias data set using both odd and even crossings for the 2 photon pair p_T bins used in the final result: 0.5-0.75 (left) and 0.75-1.0 GeV/c (right). The line is a fit to a constant.

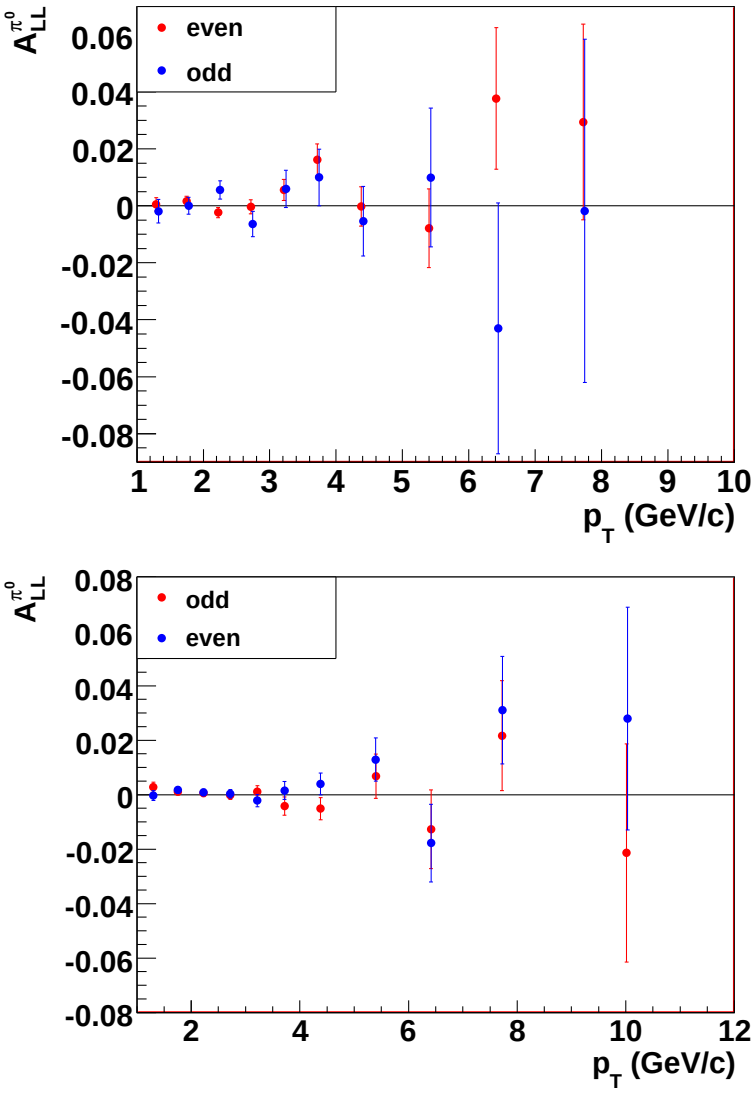

Figure 6.4: $A_{LL}^{\pi^0}$ vs. p_T from ERT triggered events in even crossings (red) and odd crossings (blue) from Run5 (top) and Run6 (bottom).

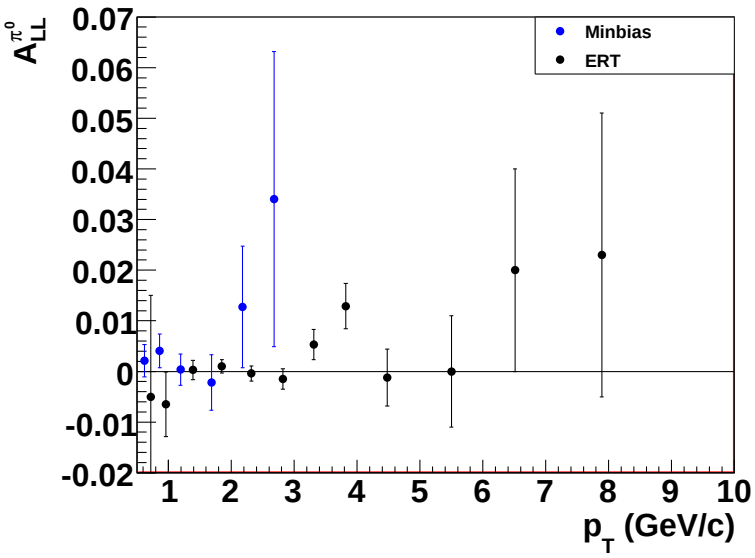

Figure 6.5: $A_{LL}^{\pi^0}$ vs. p_T in Run5 from minbias (blue) and ERT (red) after combining even and odd crossings.

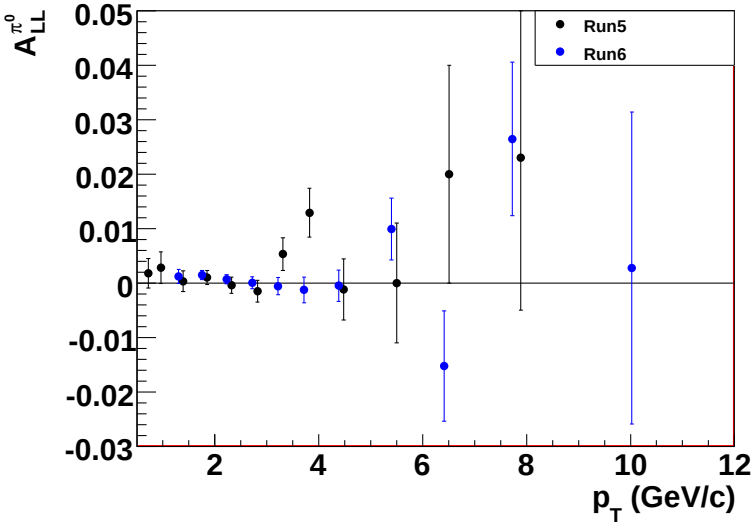

Figure 6.6: $A_{LL}^{\pi^0}$ vs. p_T from Run5 and Run6.

p_T bin (GeV/c)	$\langle p_T \rangle$ (GeV/c)	Run5 (%)	Run6 (%)
0.5-0.75	0.62	0.21±0.32	
0.75-1.0	0.86	0.40±0.33	
1.0-1.5	1.30	0.03±0.19	0.12±0.13
1.5-2.0	1.75	0.10±0.13	0.146±0.082
2.0-2.5	2.23	-0.04±0.15	0.070±0.084
2.5-3.0	2.72	-0.15±0.20	0.00±0.11
3.0-3.5	3.22	0.53±0.30	-0.06±0.16
3.5-4.0	3.72	1.29±0.45	-0.13±0.23
4.0-5.0	4.38	-0.12±0.56	-0.05±0.29
5.0-6.0	5.40	0.0±1.1	0.99±0.57
6.0-7.0	6.41	2.0±2.0	-1.5±1.0
7.0-9.0	7.74	2.3±2.8	2.6±1.4
9.0-12.0	10.02		0.3±2.9

Table 6.1: π^0 A_{LL} from Run5 and Run6. The width of the p_T bin is listed in the first column while the average p_T ($\langle p_T \rangle$) for each bin is shown in the second. Errors are statistical only.

6.2.2 Fill-by-fill A_{LL} Calculation

For charged pion A_{LL}, only ERT data is used, as the minbias sample has negligible statistics. Results for positive and negative charged pion A_{LL} using Eq. 4.5 as a function of fill number are shown in Fig. 6.7 for the three p_T bins used in this analysis: 5-6, 6-7 and 7-10 GeV/c. The results from a constant fit are also given in Fig. 6.7. In all cases, the χ^2/DOF appear reasonable, indicating that any fill to fill systematic uncertainties are negligible with respect to the statistical uncertainties.

6.2.3 Background Discussion

As discussed in Chapter 5.14, the background was estimated to be quite small in the three p_T bins used. The electron background is dominated by tracks with incorrectly reconstructed p_T, due mostly to conversions. The majority of these photons will be from π^0, and as the results in Sec. 6.1.7 are quite small, we can roughly assume the same asymmetry for this conversion electron background. As this will be scaled by the small percentage of background in this region, the net effect on charged pion A_{LL} will be negligible. The background from decay charged pions is expected to be small, and so for now, this is neglected. In the future, much of this background from tracks with incorrectly reconstructed p_T

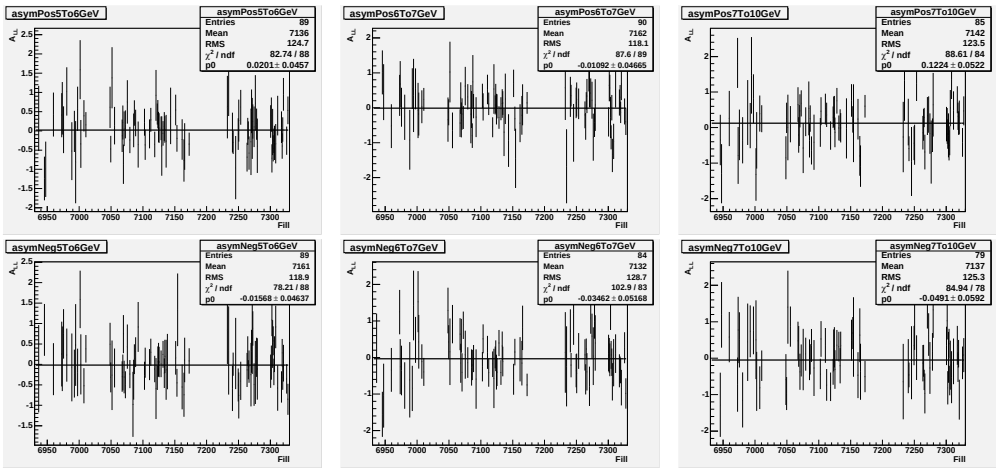

(a) **(b)** **(c)**

Figure 6.7: A_{LL} vs. fill number for π^+ (top) and π^- (bottom) in three p_T bins used in this analysis: (a) 5-6, (b) 6-7 and (c) 7-10 GeV/c. Results from a fit to a constant are shown.

	π^+			π^-		
p_T bin	$\langle p_T \rangle$ (GeV/c)	A_{LL}	$\sigma_{A_{LL}}$	$\langle p_T \rangle$ (GeV/c)	A_{LL}	$\sigma_{A_{LL}}$
5.0-6.0	5.59	0.020	0.046	5.56	-0.016	0.046
6.0-7.0	6.45	-0.011	0.047	6.44	-0.035	0.052
7.0-10.0	7.98	0.122	0.052	7.99	-0.049	0.059

Table 6.2: Final positive and negative charged pion A_{LL} results from Run5, along with the average p_T in each p_T bin.

will be removed after the installation of the VTX detector.

6.2.4 Results

Final results for Run5 positive and negative charged pion A_{LL} are show in Fig 6.8, plotted along side the final Run6 $A_{LL}^{\pi^0}$ result. Note that the highest p_T bin differs for neutral and charged pions. With the current statistics from Run5 for charged pions, it is difficult to see any ordering of the different pion species. The results are given in Table 6.2.

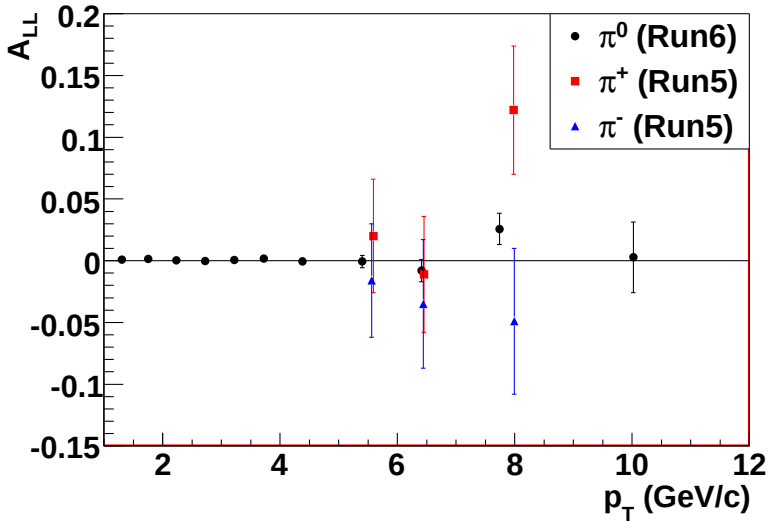

Figure 6.8: A_{LL} vs. p_T for π^+ and π^- from Run5, along with the Run6 result for π^0.

Chapter 7

Systematic Uncertainties and Cross Checks

The results given in Chapter 6 consider only statistical uncertainty. In this chapter, we consider several different possible sources of systematic uncertainties. We also present two measurements of other physics observables, which offer a systematic cross check of our A_{LL} measurements. Finally, we present all significant systematic uncertainties in the measurements of neutral and charged pion A_{LL}.

7.1 Asymmetry in Background Sidebands

As was described in the Chapter 6, the asymmetry in the combinatorial background under the π^0 mass peak cannot be measured directly. Therefore, the asymmetry in the sideband regions shown in blue in Fig. 6.1 is measured and assumed to have an A_{LL} equal to that of the combinatorial background under the π^0 mass peak. To test the assumption that the background asymmetry is roughly constant in the region around the π^0 mass peak, the asymmetry in each sideband is independently measured to see that they are consistent.

Figure 7.1 shows A_{LL} for the $50 - 100$ MeV/c^2 (BG1) and the $170 - 220$ MeV/c^2 (BG2) sideband for Run6 separately from odd and even crossings. The background A_{LL} in the two sidebands agree. Similar results were found in Run5.

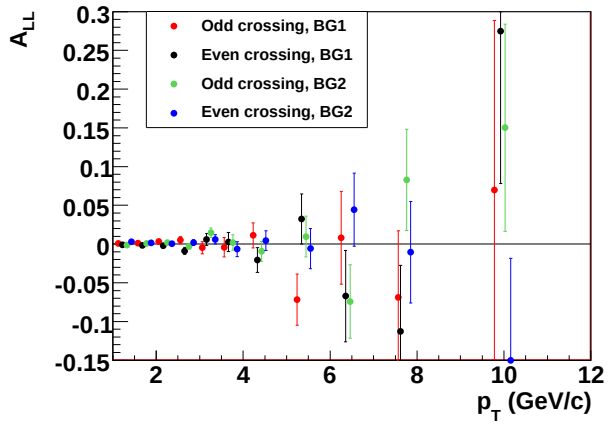

Figure 7.1: A_{LL} vs. p_T from Run5 for N^{BG} separately for the two sideband regions in Fig. 6.1: BG1 ($50 < m_{\gamma\gamma} < 100$ MeV/c^2) and BG2 ($170 < m_{\gamma\gamma} < 220$ MeV/c^2).

7.2 Comparison of Different Detector and Trigger Results

The FBF analysis described in Chapter 6.1.4 was also performed for the two different types of EMCal in PHENIX independently. Results for N^{π^0+BG} and N^{BG} A_{LL} as a function of p_T are shown in Fig. 7.2 and Fig. 7.3 for Run5 and Run6, respectively, for ERT triggered events in even and odd crossings separately using the PbSc only (red), PbGl only (blue) or full EMCal (black). No dependence on EMCal type was seen.

Results for N^{π^0+BG} and N^{BG} A_{LL} as a function of p_T are shown in Fig. 7.4 for minbias triggered events in all filled crossings from Run5. (Prescales are taken into account.)

7.3 Neutral Pion A_{LL} for Different Signal Mass Ranges

The two photon mass range used for the signal region was varied to see if there was any affect on $A_{LL}^{\pi^0}$. Figure 7.5 shows $A_{LL}^{\pi^0}$ vs. p_T for analysis done as described in Chapter 6.1 with three different signal mass ranges. Red points are from a narrower 30 MeV/c^2 mass range (122-152 MeV/c^2) and blue points are from a wider 70 MeV/c^2 mass range (102-172 MeV/c^2) while black points are from the standard mass range (112-162 MeV/c^2). Background side bands

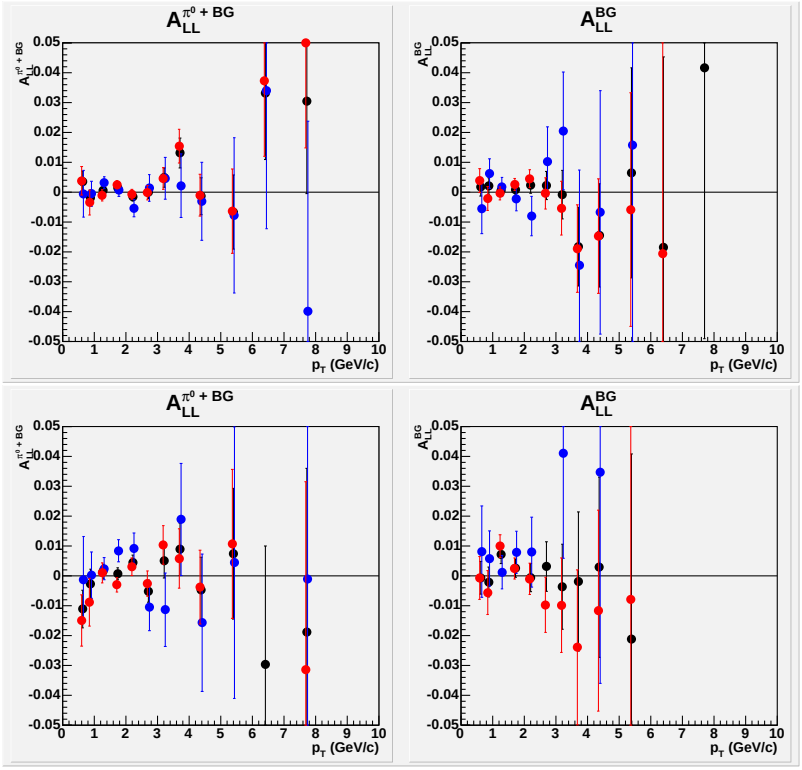

Figure 7.2: A_{LL} vs. p_T from Run5 for N^{π^0+BG} (left) and N^{BG} (right) from ERT triggered events in even (top) and odd (bottom) crossings. Red is PbSc only, blue is PbGl only, and black is from the full EMCal (PbGl+PbSc).

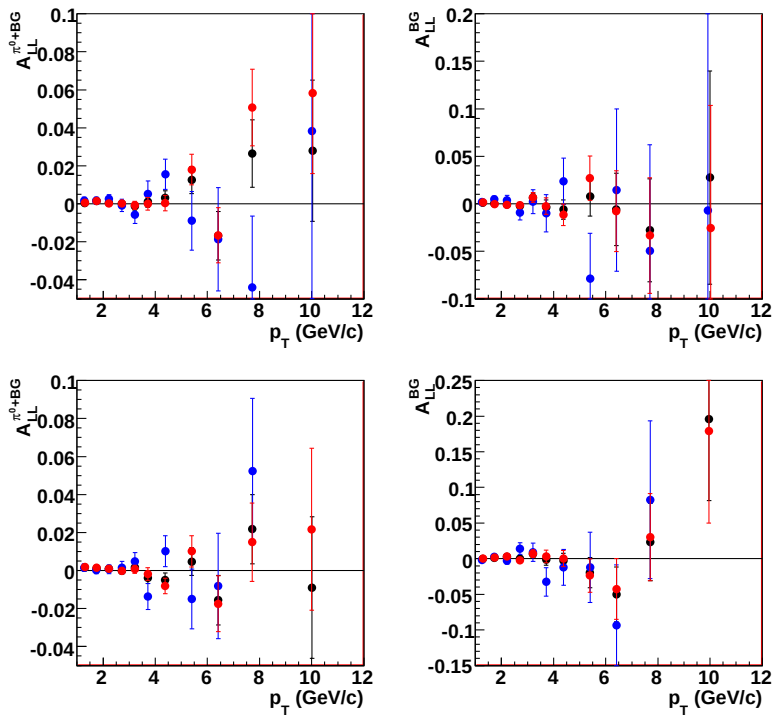

Figure 7.3: A_{LL} vs. p_T from Run6 for N^{π^0+BG} (left) and N^{BG} (right) from ERT triggered events in even (top) and odd (bottom) crossings. Red is PbSc only, blue is PbGl only, and black is from the full EMCal (PbGl+PbSc).

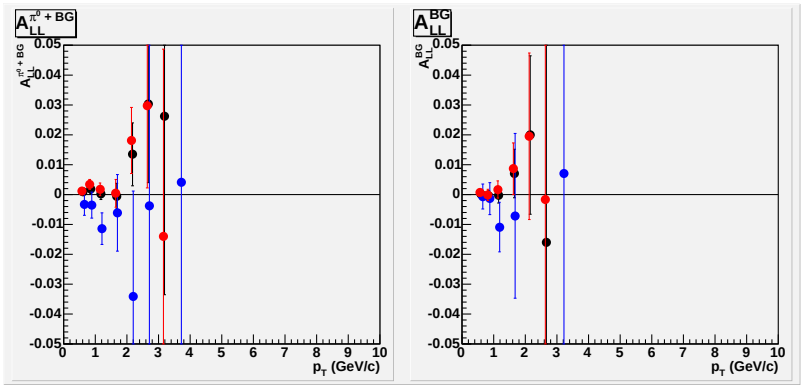

Figure 7.4: A_{LL} vs. p_T from Run5 for N^{π^0+BG} (left) and N^{BG} (right) from minbias triggered events in all crossings. Red is PbSc only, blue is PbGl only, and black is from the full EMCal (PbGl+PbSc).

were the same for the three cases (see Fig. 6.1). No significant affect is seen when varying the signal mass range.

7.4 Longitudinal Single Spin Asymmetries

As was discussed in Chapter 4.3, longitudinal SSA's are parity violating. Therefore, by measuring such SSA's in the helicity dependent production, called A_L, of either π^0 or charged pions, systematic problems in the data not evident in the measurement of A_{LL} may be found. Non zero A_L in π^0 production from Run5 lead to the realization that the A_{LL} analysis should done separately in even and odd crossings.

In this case, we are interested only in production asymmetries, and so the formula is similar to that of A_{LL}, namely

$$A_L^{\text{Beam}} = -\frac{\sigma_+ - \sigma_-}{\sigma_+ + \sigma_-} \tag{7.1}$$

where σ_+ (σ_-) is the cross section of positive (negative) helicity bunches for one beam (the other beam polarization states are summed over). This can then be rewritten in terms of yields and relative luminosity as

$$A_L^{\text{Beam}} = -\frac{1}{P_{\text{Beam}}}\frac{N^+ - R_{\text{Beam}}N^-}{N^+ + R_{\text{Beam}}N^-}\ , \qquad R_{\text{Beam}} = \frac{L^+}{L^-} \tag{7.2}$$

where N_+ (N_-) are the particle yields in collisions with the positive (negative) helicity crossings in the set beam, and P_{Beam} is the polarization for that beam. Note that the relative luminosity in this case has a different definition than in A_{LL}. A_L for the blue and yellow beams can be measured simultaneously as the asymmetries are actually independent linear combinations (along with the total cross section and A_{LL}) of the four double helicity combinations.

7.4.1 Neutral Pion

A_L is measured using the FBF method that was used for A_{LL}. Figure 7.6 shows π^0 A_L as a function of fill number from Run5 without separating odd and even bunches for the blue beam for $1 < p_T < 2$ GeV/c. A clear $\sim 10\sigma$ asymmetry is seen in the last few fills of Run5. This period had all crossings filled (except abort gaps), using the patterns shown in Fig. 2.5. Clearly blue '+' align with even crossings and blue '−' with odd crossings. Due to the different trigger thresholds (See Chapter 3.3.3) in even and odd crossings, the trigger efficiencies were effectively not spin independent, and resulted in a large

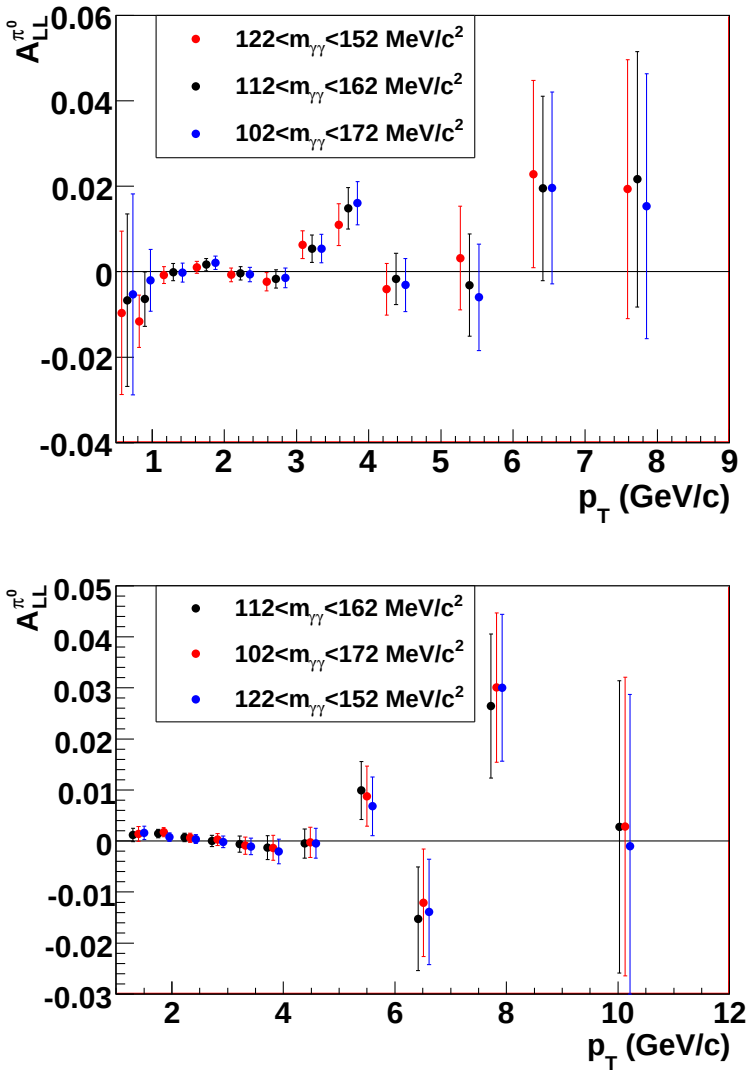

Figure 7.5: $A_{LL}^{\pi^0}$ from Run5 (top) and Run6 (bottom) calculated with three different signal ranges (see Fig. 6.1) in the two photon mass spectrum. Black data points use 50 MeV/c^2 bin used for final result. Red point are for a 30 MeV/c^2 wide (122-152 MeV/c^2) signal region, and blue for a 70 MeV/c^2 wide (102-172 MeV/c^2) signal region. Background side band for all three analyses are the same (see Fig. 6.1).

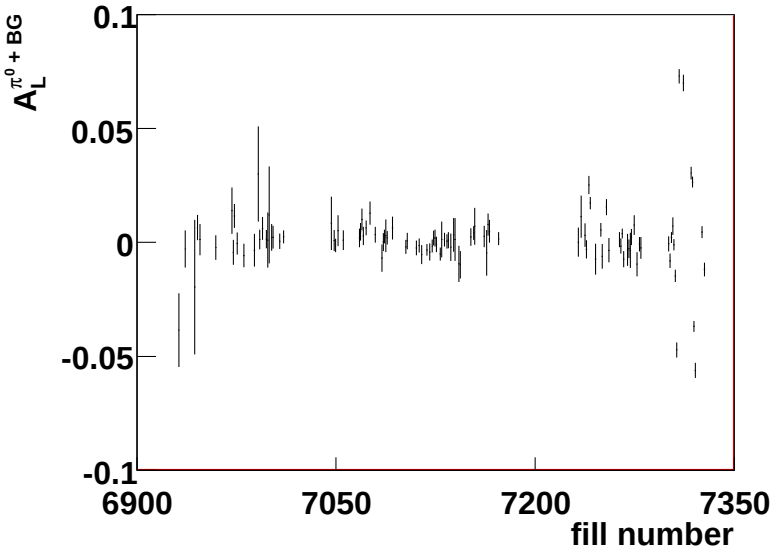

Figure 7.6: Blue beam π^0 A_L vs. fill number for ERT triggered events without separating into odd and even crossing in Run5. Due to trigger difference (see Chapter 3.3.3) for odd and even bunches, a clear large false parity violating asymmetry is measured.

false A_L. Figure 7.7 shows the same p_T bin as Fig. 7.6 but with the analysis done separately for odd and even crossings. Clearly, the problem leading to the false asymmetry has been corrected.

Figure 7.8 shows π^0 A_L for the two beams calculated from ERT triggered events for odd and even bunches separately, and for minbias events from Run5. The results are consistent with zero.

After merging odd and even bunches, the final results for blue and yellow beam A_L from the two RHIC runs are plotted in Fig. 7.9. The final values are listed in Table B.14 and B.15 for Run5 and Run6, respectively. The results in all cases are consistent with zero, as expected.

7.4.2 Charged Pions

Figure 7.10 shows the results for parity violating A_L for the Blue and Yellow beam for π^+ and π^-. The results are consistent with zero, as expected. The results are listed in Table B.16.

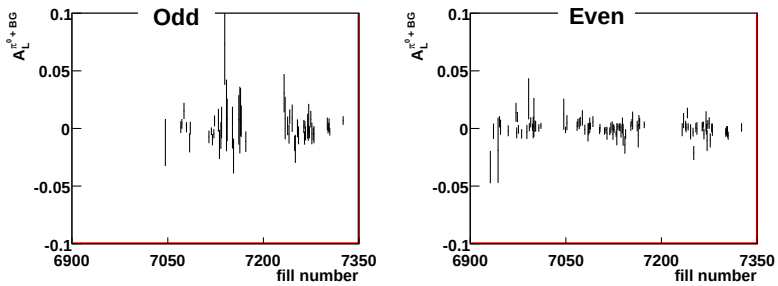

Figure 7.7: Blue beam π^0 A_L vs. fill number for ERT triggered events for same p_T bin as in Fig. 7.6 analyzed separately for odd and even crossing. This false parity violation is removed.

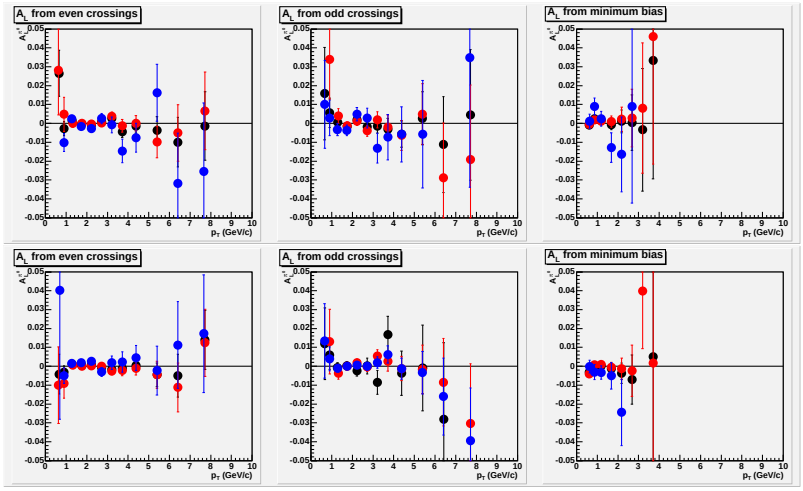

Figure 7.8: Blue (top) and Yellow (bottom) π^0 A_L vs. p_T for ERT triggered events in even (left) and odd (middle) crossings, and from minbias triggered events in all crossings (right). Red is PbSc only, blue is PbGl only, and black is from the full EMCal (PbGl+PbSc).

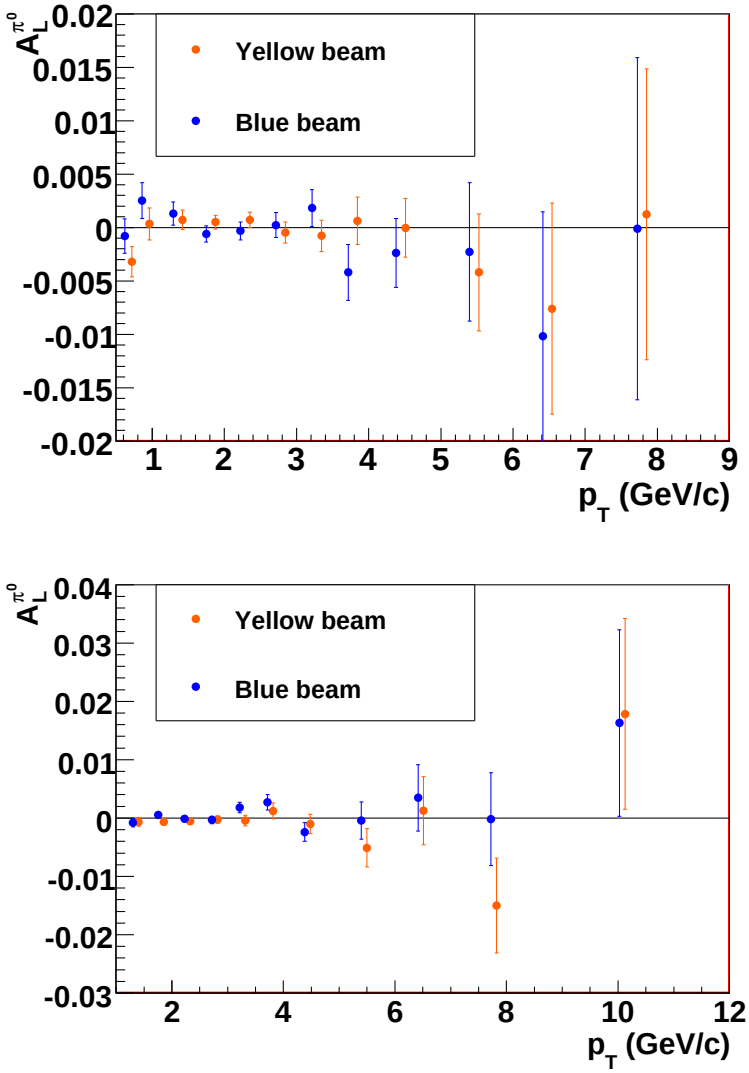

Figure 7.9: π^0 A_L vs. p_T for ERT triggered events after combining even and odd crossings for Blue (blue) and Yellow (orange) beams for Run5 (top) and Run6 (bottom).

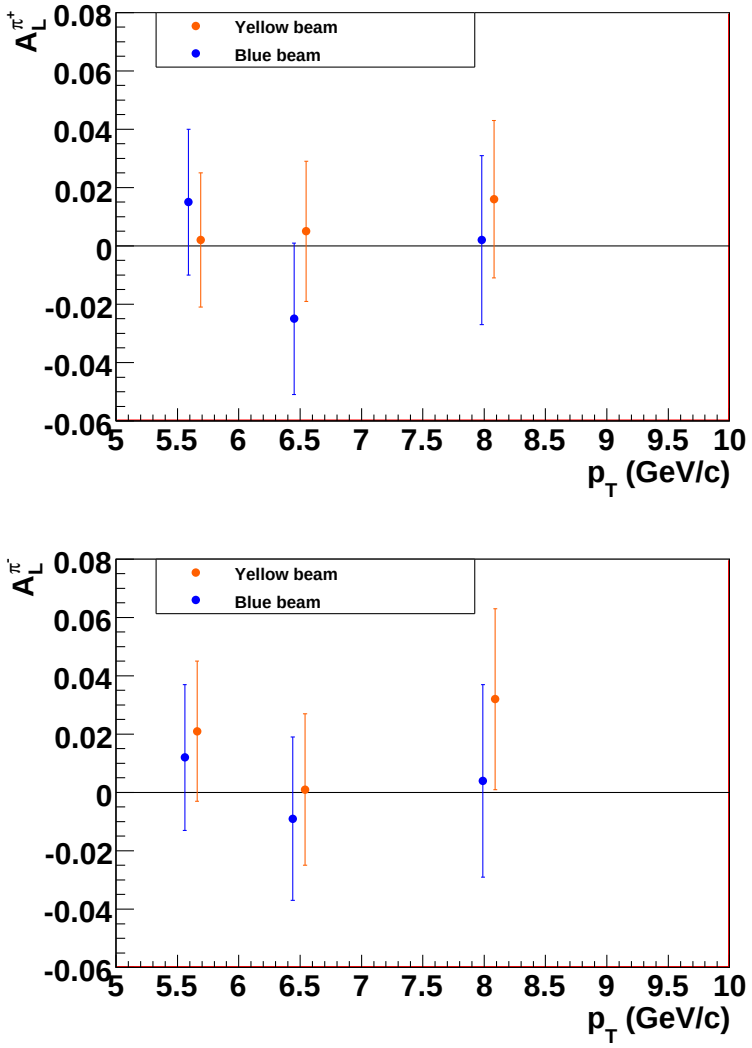

Figure 7.10: A_L vs. p_T for positive (top) and negative (bottom) charged pions from Run5 for Blue (blue) and Yellow (orange) beams.

7.5 Parity Violating Double Helicity Asymmetries

Any nonzero difference between σ_{++} and σ_{--} or between σ_{+-} and σ_{-+} would imply parity violation (see Appendix A.2). For a systematic cross check, double helicity asymmetries for these combinations can be measured, similarly to the measurement of A_L. However, as is shown in Appendix A.2, these asymmetries give no new information compared to the A_L of the two beams. Therefore, we do not calculate these asymmetries.

7.6 Transverse Double Spin Asymmetries (A_{TT})

As was discussed in Chapter 4.3.4, there is a remaining transverse component of the proton beam polarization at PHENIX. This fraction can reduce the measured A_{LL}, and also lead to a possible inclusion of a double transverse spin asymmetry, A_{TT} affecting the measured value. A_{TT} is defined as

$$A_{TT} = \frac{1}{|P_B P_Y|} \frac{N_{\uparrow\uparrow} - R_T N_{\uparrow\downarrow}}{N_{\uparrow\uparrow} + R_T N_{\uparrow\downarrow}}, R_T = \frac{L_{\uparrow\uparrow}}{L_{\uparrow\downarrow}} \ . \tag{7.3}$$

When calculating an asymmetry such as in Eq. 4.5, we assume that the beam is longitudinally polarized only, so

$$A_{LL} = \frac{1}{P_B P_Y} \epsilon_{LL} \tag{7.4}$$

where ϵ_{LL} is the same as in Eq. 4.11. In reality, we measure

$$A_{LL}^{real} = \frac{1}{P_{B,L} P_{Y,L}} \epsilon_{LL} \tag{7.5}$$

where $P_{B(Y),L}$ is the longitudinal beam polarization. Dividing Eq. 7.5 by Eq. 7.4 gives

$$A_{LL} = \frac{P_{B,L} P_{Y,L}}{P_B P_Y} A_{LL}^{real}. \tag{7.6}$$

Similarly,

$$A_{TT} = \frac{P_{B,T} \cdot P_{Y,T}}{P_B P_Y} A_{TT}^{real} \simeq \frac{P_{B,T} P_{Y,T}}{P_B P_Y} A_{TT}^{real} \tag{7.7}$$

where we have assumed that the transverse polarization components are parallel.

The actual asymmetry measured at PHENIX can be written as

$$A_{meas} = A_{LL} + A_{TT} \tag{7.8}$$

$$= \frac{P_{B,L}P_{Y,L}}{P_B P_Y} A_{LL}^{real} + \frac{P_{B,T}P_{Y,T}}{P_B P_Y} A_{TT}^{real} . \tag{7.9}$$

Therefore, solving Eq. 7.9 for A_{LL} gives

$$A_{LL}^{real} = \frac{1}{\frac{P_{B,L}}{P_B}\frac{P_{Y,L}}{P_Y}} A_{meas} - \frac{\frac{P_{B,T}}{P_B}\frac{P_{Y,T}}{P_Y}}{\frac{P_{B,L}}{P_B}\frac{P_{Y,L}}{P_Y}} A_{TT}^{real}. \tag{7.10}$$

As is stated in Chapter 4.3.4, the remaining transverse component in Run5 (Run6) was 10±2% (12±6%) and 14±2% (11±4%) for the blue and yellow beam, respectively. Therefore, any possible effect from A_{TT} will be scaled by the product of these components, or roughly 0.01.

Non-zero A_{TT} theoretically arises from parton transversity distributions, $\delta f(x, Q^2)$, which describe the difference in the number density of partons with the same and different polarization as the proton, when transversely polarized. As the gluon is a massless spin 1 particle, $\delta g(x, Q^2) = 0$. Therefore, the numerator in Eq. 7.3 depends only on quark transversity. As both quarks and gluons contribute to π^0 production, the denominator includes both quark and gluon interactions. Thus, A_{TT} is expected to be quite small.

7.6.1 Neutral Pion Results

Theory has predicted a small A_{TT} in π^0 production of order 10^{-4} in the measured p_T range at $\sqrt{s} = 200$ GeV [75], with a maximal value given by the curves shown in Fig. 7.11. At $\sqrt{s} = 200$ GeV (larger valued curves), $A_{TT}^{\pi^0}$ is expected to be less than 0.05% at p_T=5GeV/c. All curves in this plot assume a value of $\delta f(x, Q^2)$ set by the Soffer bound [76]

$$2|\delta q(x)| \leq q(x) + \Delta q(x). \tag{7.11}$$

The bound is satisfied at an input scale of $\mu_0^2 \simeq 0.6$ GeV^2 using the best fit GRV and GRSV densities for $q(x)$ and $\Delta q(x)$. Varying the input scale can lead to a slightly higher A_{TT}. However, as the curves in Fig. 7.11 assume the bound is saturated at the input scale, the actual asymmetry is most probably smaller. As is discussed above, the impact on our A_{LL} measurements is reduced by a factor of 100. Therefore, the effect of A_{TT} on the measured A_{LL} should be negligible ($\mathcal{O}(10^6)$).

In Run5, a small data set (4 fills) was taken with spin rotators turned off

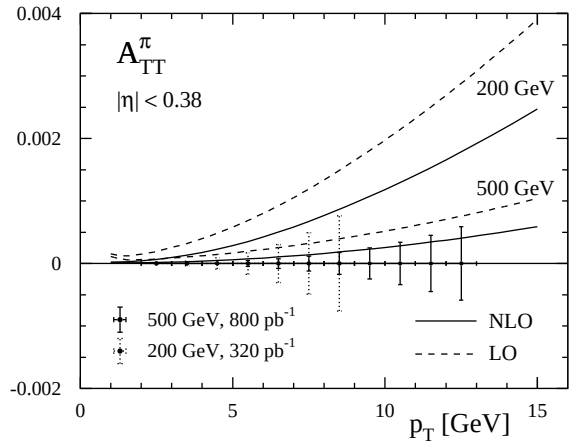

Figure 7.11: Theoretical estimates [75] of upper bound of π^0 A_{TT} at $\sqrt{s}$ = 200 GeV.

so that A_{TT} could be measured, to ensure that A_{TT} is indeed small. Figure 7.12 shows $A^{\pi^0}_{TT}$ vs. p_T, and the results are listed in Table B.17. The result is consistent with zero at all measured p_T, with statistical uncertainty of roughly 4.7 times that of the statistical uncertainty on Run5. Due to the large statistical uncertainty in A_{TT}, the measurement is not sensitive to the size of the transversity distribution in the proton. However, we do see that there is no unexpectedly large asymmetry which could influence the measured A_{LL} through the small remaining transverse beam polarization at PHENIX. When scaled by the small remaining transverse component, the effect of A_{TT} on the measured A_{LL} is negligible.

As discussed above, the actual normalization is the dot product of the two polarization vectors, and so one can in the future significantly reduce the possible effects of an A_{TT} contamination of A_{LL} by requiring that the transverse components of the two polarization vectors are perpendicular. This would have the same effect as having no transverse components, while retaining the ability to ensure the spin pattern is correct as discussed in Chapter 4.3.5.

7.7 Bunch Shuffling

Bunch shuffling is a technique used to ensure that any systematic uncertainty from bunch to bunch or fill to fill correlations is less than the current statistical

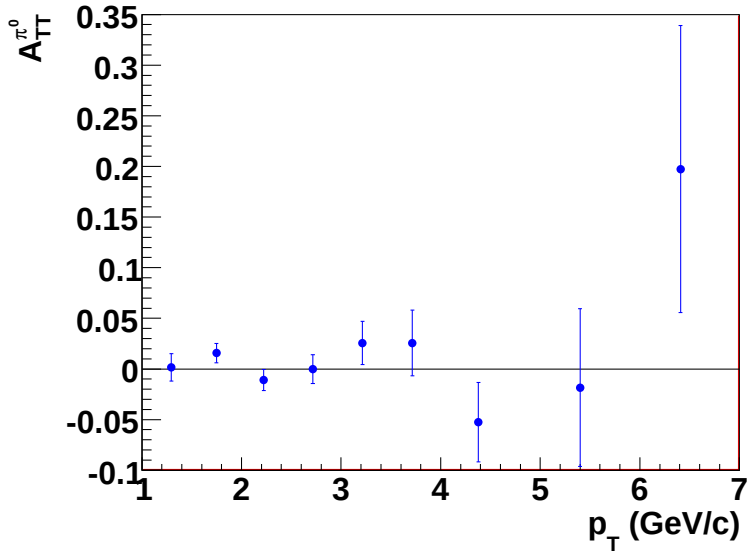

Figure 7.12: π^0 A_{TT} at $\sqrt{s} = 200$ GeV measured during four days of transverse polarization running in Run5.

uncertainty. In the case of a bunch fitting analysis, such as that used for Relative Luminosity, a χ^2 is available for each fill, and the resulting distribution of χ^2/DOF can be studied to see if there is any such bunch to bunch systematic uncertainty. However, in the FBF method used for the final A_{LL} results, there is only one χ^2 per p_T bin for the fit of A_{LL} vs. fill number. As we have only one sample, it is not necessarily clear how to interpret this lone χ^2 value in terms of the likelihood of remaining systematic uncertainties. It is much easier to interpret a distribution of χ^2 values.

Bunch shuffling allows the creation of multiple samples needed to differentiate indications of systematic uncertainties from normal fluctuations in χ^2. To create a "new" sample, the helicity for all bunches in the data sample (Run5 or Run6 in this case) are randomly assigned (or shuffled). The A_{LL} can be calculated using the FBF method, and a new χ^2 value is returned. Doing this numerous times, in the following cases 10,000 times, will give a χ^2 distribution. If the distribution differs from the expected distribution for a set number of degrees of freedom, in this case the number of fills available, it is an indication of systematic uncertainty.

7.7.1 Neutral Pion

ERT Triggered Events

Bunch Shuffling was performed for each π^0 p_T bin separately for even and odd crossings for both the signal and background sideband regions. A sample of the results from the ERT analysis are shown in Fig 7.13. The red curve is the expected χ^2/DOF distribution for a given number of DOF set equal to the number of fills per running year. As can be seen in the results for the low p_T bins, there are no indications of systematic uncertainties.

The 7-9 GeV/c p_T bin in Fig. 7.13 show some divergence from the expected distribution. This can be understood as a combination of two effects due to low statistics.

First, in the very high p_T bins, the number of photon pairs per fill in the measured mass range is small. In a shuffled sample, the actual number of same or opposite helicity counts may be less than ten. Therefore, the standard error, $\sqrt{N}$, while still Poissonian, is no longer Gaussian, and can incorrectly influence the fit, which assumes Gaussian errors. This effect will lead to a larger value of χ^2 on average, and result in a distribution such as in the 7-9 GeV/c p_T bin.

Second, although bunches may be filled, at such high p_T, not all will have photon pairs. This leads to a decrease in the number of possible bunch shuffled configurations. For example, if only two filled bunches have photon pairs, then there are only four random helicity configurations from which an A_{LL} can be calculated. When this occurs, it does not mean we have assigned the wrong uncertainties. Instead, it is a failing of bunch shuffling.

Note that in both of these cases, the effect is only seen at high p_T. In general, bunch to bunch or fill to fill systematic uncertainties are very unlikely to only be seen in the highest p_T bins, but instead should affect all p_T bins.

Results from all p_T bins in even and odd crossings using ERT triggered events were studied for both Run5 and Run6. The results indicated that any bunch to bunch or fill to fill systematic uncertainty was negligible compared to the statistical uncertainty of the present $A_{LL}^{\pi^0}$ results.

Minbias Triggered Events

As discussed in Chapter 6.1.5, multiple runs are taken during any one fill, and the prescales on the minbias trigger can and do often change run to run. Results from minbias data for Run5 for the signal region are show in Fig. 7.14 without properly taking into account prescales and in Fig. 7.15 when they are correctly incorporated. At high p_T, the effect of low statistics can be seen in the deviation from the expected distribution. in the low p_T region, there is disagreement in both cases. However, the disagreement is much larger

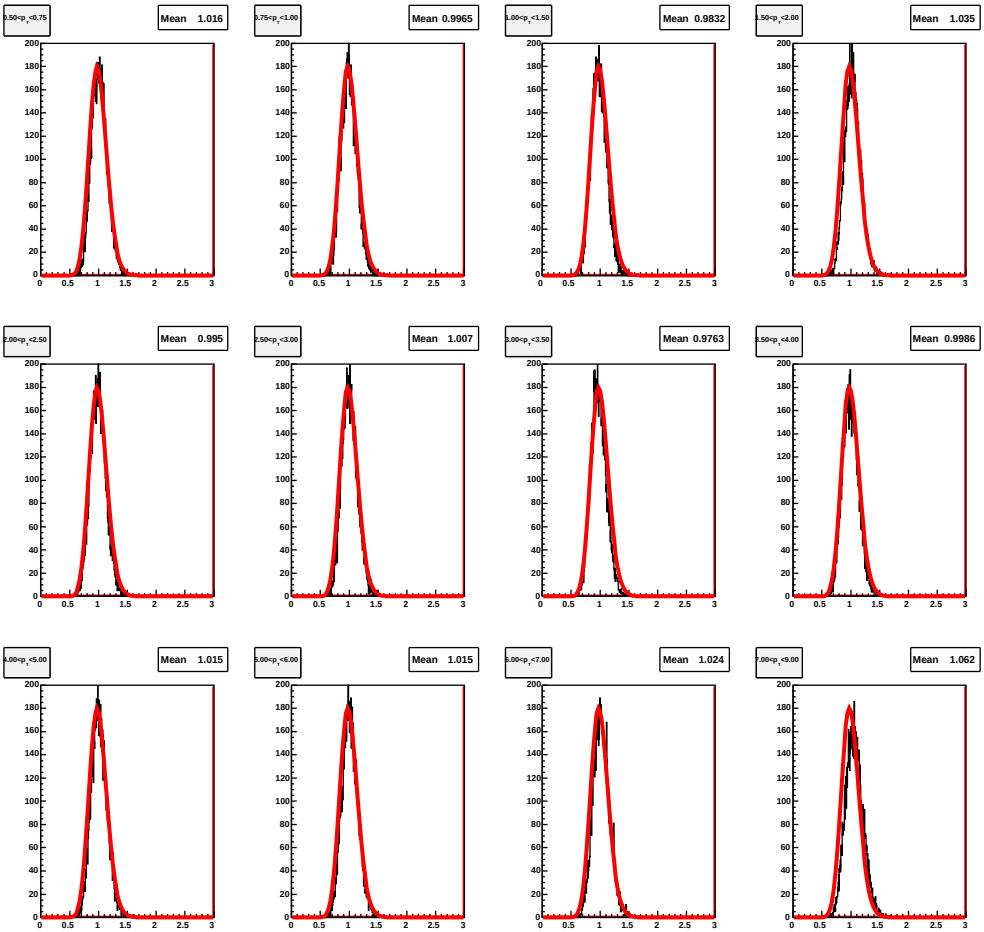

Figure 7.13: χ^2/NDF results from 10000 bunch shuffled samples for $A_{LL}^{\pi^0+BG}$ from Run5. Data used is from ERT triggered events in *even* crossings in the full EMCal (PbSc+PbGl). The expected distribution is plotted in red. Top row, from left to right: 0.5-0.75, 0.75-1.0, 1.0-1.5, 1.5-2.0 GeV/c. Middle row, from left to right: 2.0-2.5, 2.5-3.0, 3.0-3.5, 3.5-4.0 GeV/c. Bottom row, from left to right: 4.0-5.0, 5.0-6.0, 6.0-7.0, 7.0-9.0 GeV/c.

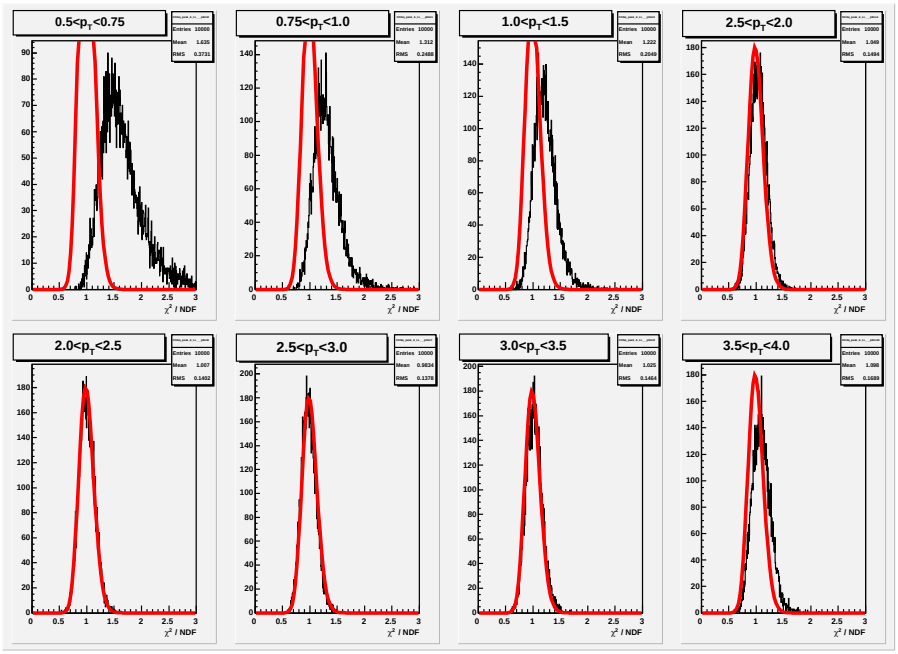

Figure 7.14: χ^2/NDF results from 10000 bunch shuffled samples for $A_{LL}^{\pi^0+BG}$. Data used is from minbias events in the full EMCal (PbSc+PbGl). The expected distribution is plotted in red. The disagreement between expected and actual distributions in the lowest p_T bins is due to ignoring prescales on the minbias trigger. Top row, from left to right: 0.5-0.75, 0.75-1.0, 1.0-1.5, 1.5-2.0 GeV/c. Bottom row, from left to right: 2.0-2.5, 2.5-3.0, 3.0-3.5, 3.5-4.0 GeV/c.

when the prescales are not used properly, and the statistical uncertainty is incorrectly calculated.

The results from minbias data for $p_T < 1$ GeV/c are used for the final result. The results in Fig. 7.15 can be used to estimate a systematic uncertainty for $0.5 < p_T < 0.75$ and $0.75 < p_T < 1.0$ GeV/c. These are given in Table 7.1.

7.7.2 Charged Pions

Results for bunch shuffling for positive and negative charged pion are shown in Fig. 7.16 for the three p_T bins used. The distributions agree with the expected distribution (red curve), and so indicate that any bunch to bunch or fill to fill systematic uncertainties are negligible with respect to the current statistical uncertainties.

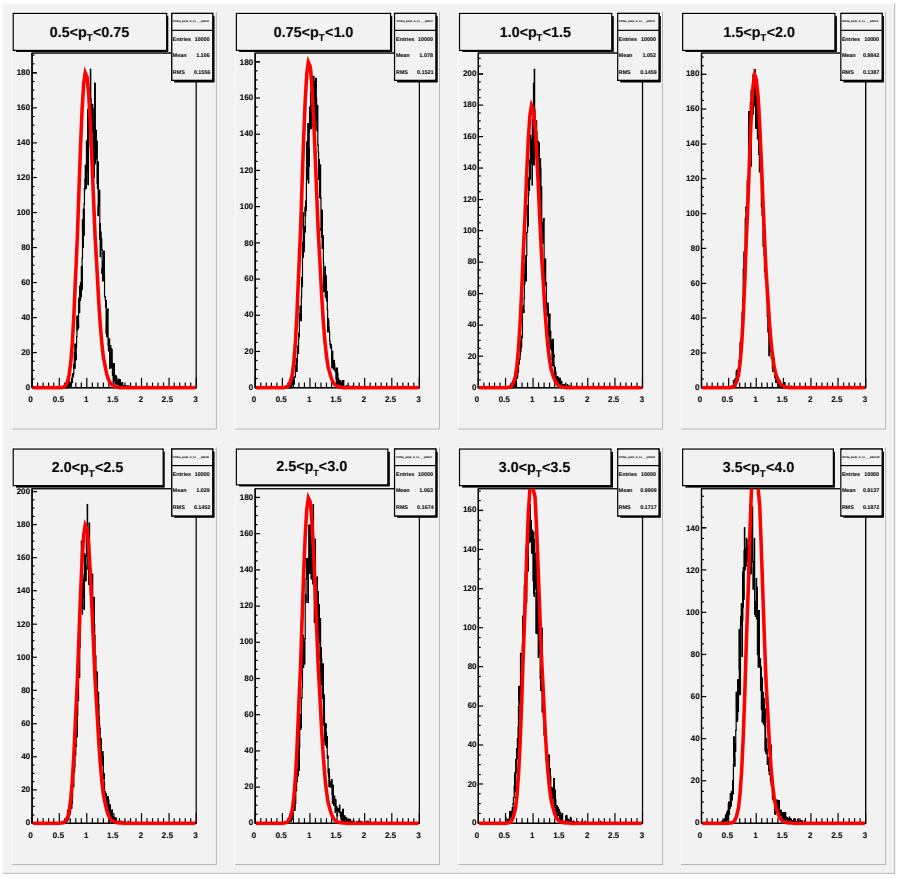

Figure 7.15: χ^2/NDF results from 10000 bunch shuffled samples for $A_{LL}^{\pi^0+BG}$. Data used is from minbias events in the full EMCal (PbSc+PbGl) with luminosity scaled by the minbias prescales. The expected distribution is plotted in red. Top row, from left to right: 0.5-0.75, 0.75-1.0, 1.0-1.5, 1.5-2.0 GeV/c. Bottom row, from left to right: 2.0-2.5, 2.5-3.0, 3.0-3.5, 3.5-4.0 GeV/c.

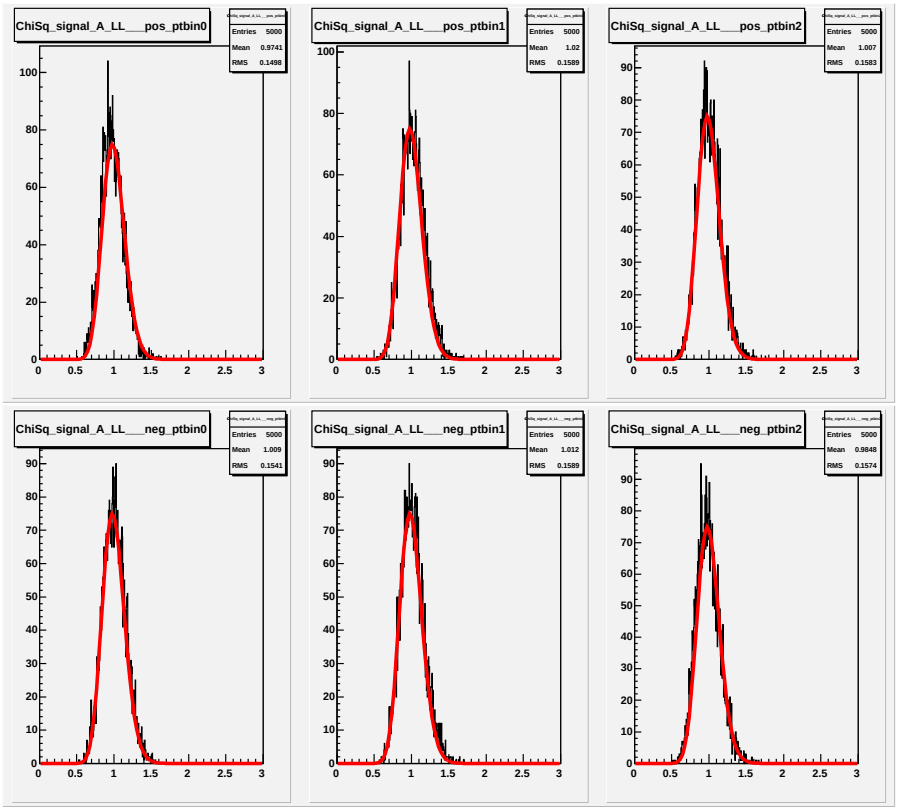

Figure 7.16: χ^2/NDF results from 5000 bunch shuffled samples for positive (top) and negative (bottom) charged pions A_{LL} for the three p_T bins used in the analysis: 5-6 GeV/c, 6-7 GeV/c and 7-10 GeV/c.

7.8 Systematic Uncertainty from Beam Polarization

The uncertainties on beam polarization can be divided into three groups: (1) statistical, which are independent from fill to fill, (2) uncorrelated systematic, which are also independent from fill to fill, and (3) correlated systematic, which were discussed in Chapter 4.2. The fill by fill statistical uncertainty on the polarization, as well as the uncorrelated fill to fill systematic uncertainties, have been included in the uncertainty on $A_{LL}^{\pi^0}$ calculated in Chapter 6.1.4 using

$$\sigma_{A_{LL}} = A_{LL}\sqrt{\left(\frac{\sigma_\epsilon}{\epsilon}\right)^2 + \left(\frac{\sigma_{P_B}}{P_B}\right)^2 + \left(\frac{\sigma_{P_Y}}{P_Y}\right)^2} \tag{7.12}$$

where ϵ is taken to be the raw asymmetry. The resulting values and uncertainties for A_{LL} do not change within the significant digits.

The uncertainties of type (3) are given in Chapter 4.2 ("systB", "systY" and "systG"), and are taken as fully correlated between fills. For A_{LL}, the product of the polarizations is important. In Run6 (Run5), the luminosity weighted average of the product of the two beam polarizations, $\langle P_B \cdot P_Y \rangle$, was 32% (24%) with a relative systematic uncertainty of 8.3% (9.4%).

As both A_{LL} and $\sigma_{A_{LL}}$ depend on polarization in the same way, both scale with this systematic uncertainty.[1] As both the data points and uncertainty scale, it is difficult to plot, and so we do not show it as an uncertainty in the A_{LL} plots, but instead refer to it in the captions. The effect of this uncertainty on the interpretation of A_{LL} in terms of ΔG will be discussed in Chapter 8.5.

7.9 Summary of Systematic Uncertainties

Table 7.1 lists the main systematic uncertainties in the final π^0 and charged pion results. Results from bunch shuffling indicate that all bunch to bunch of fill to fill systematic uncertainties were smaller than the statistical precision of the Run5 and Run6 A_{LL} results for charged and neutral pions for $p_T >$ 1 GeV/c. The results for $A_{LL}^{\pi^0}$ did indicate a non-negligible (with respect to the statistical) systematic uncertainty in the results for $p_T < 1$ GeV/c. These uncertainties are also included in Table 7.1.

The uncertainty from relative luminosity determined in Chapter 4.1.2 is also listed. As this uncertainty is in the luminosity normalization, it is entirely

[1] Systematics of type three will roughly cancel in σ_{P_Y}/P_Y, and so all the $\sigma_{A_{LL}}$ terms in Eq. 7.12 will behave the same way.

Source	Run5	Run6
b. shuffling ($0.5<p_T<0.75$ GeV/c)	0.0014	NA
b. shuffling ($0.75<p_T<1.0$ GeV/c)	0.0012	NA
Relative Luminosity	2.1×10^{-4}	7.5×10^{-4}
Polarization	9.4%	8.3%

Table 7.1: Summary of non-negligible systematic uncertainties in the A_{LL} measurements presented. Uncertainties from bunch (b.) shuffling for all results with $p_T > 1$ GeV/c were found to be negligible.

correlated for all p_T bins in both the π^0 and charged pion result within a given RHIC run. The polarization uncertainty discussed above is similarly correlated. No other systematic uncertainties are significant with the current precision of the data.

7.10 Final Combined Results for Neutral Pion A_{LL} from Run5 and Run6

With the statistical and systematic uncertainties in hand, the results from Run5 and Run6 for $A_{LL}^{\pi^0}$ can be combined. The result is simply the weighted average of the Run5 and Run6 results p_T bin by p_T bin, taking the weights to be the square of the total uncertainty (systematic and statistical summed in quadrature). Final results are listed in Table 7.2 along with the statistical errors (σ_{stat}), the systematic uncertainty from Relative Luminosity (σ_{RL}) and the scaling uncertainty due to beam polarization. As the data with $p_T <$ 1 GeV/c and $p_T > 9$ GeV/c were only measured in 1 year, the values are the same as in Table 6.1. The results for Run5, Run6 and Combined Run5+6 are plotted in Fig 7.17.

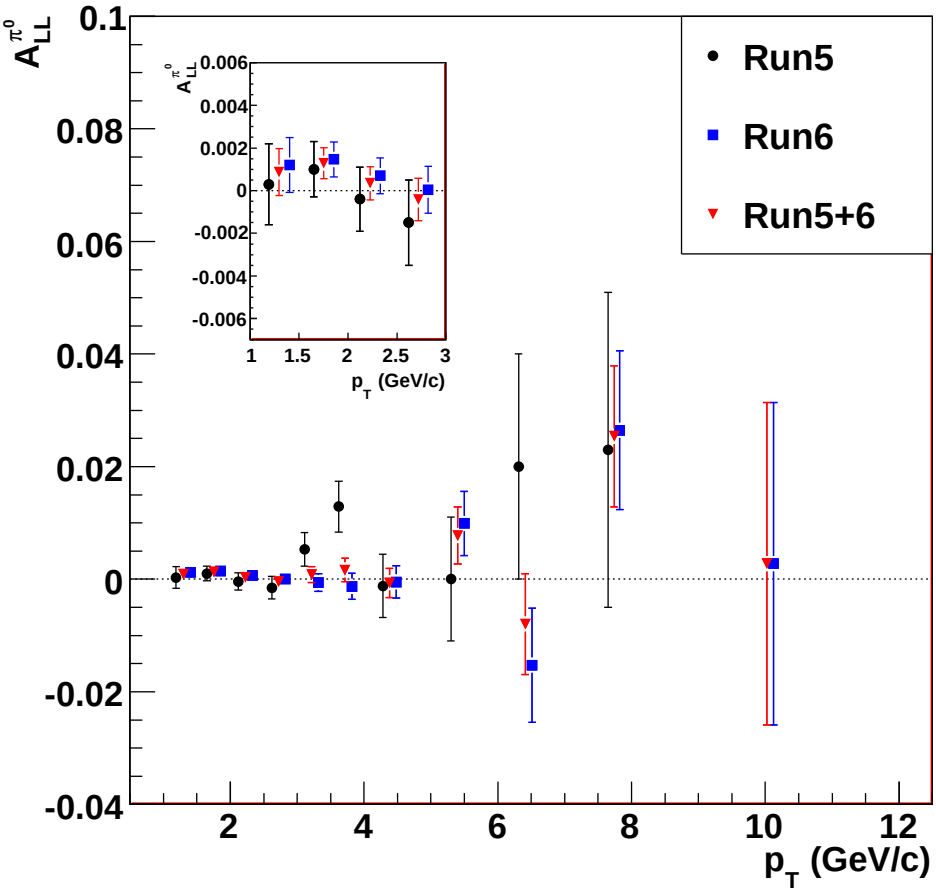

Figure 7.17: $A_{LL}^{\pi^0}$ vs. p_T results from Run5 (black circle), Run6 (blue square) and Combined (Run5+6, red triangle). Only statistical errors are shown.

p_T bin ($\langle p_T \rangle$) (GeV/c)	$A_{LL}^{\pi^0}$ (%)	σ_{stat} (%)	σ_{RL} (%)	Scaling Uncertainty (%)
0.5-0.75 (0.62)	0.21	0.32	0.021	9.4
0.75-1.0 (0.86)	0.40	0.33	0.021	9.4
1.0-1.5 (1.30)	0.086	0.11	0.043	6.8
1.5-2.0 (1.75)	0.127	0.074	0.042	6.8
2.0-2.5 (2.23)	0.031	0.079	0.043	6.8
2.5-3.0 (2.72)	-0.05	0.10	0.045	6.7
3.0-3.5 (3.22)	0.09	0.14	0.046	6.7
3.5-4.0 (3.72)	0.17	0.21	0.047	6.7
4.0-5.0 (4.38)	-0.07	0.26	0.047	6.7
5.0-6.0 (5.40)	0.77	0.51	0.047	6.7
6.0-7.0 (6.41)	-0.79	0.90	0.047	6.7
7.0-9.0 (7.74)	2.5	1.3	0.047	6.7
9.0-12.0 (10.02)	0.3	2.9	0.075	8.3

Table 7.2: Combined π^0 A_{LL} from Run5 and Run6. Values are weighted average using total uncertainty. Statistical and dominant systematic uncertainties are also given.

Chapter 8

Interpretation of A_{LL} Results

Results for the double helicity asymmetry in neutral and charged pion production have been presented, and the systematic uncertainties have been considered. However, the goal was not solely to measure A_{LL}, but to glean information about the spin structure of the proton, with a focus on the gluon spin contribution. In this chapter, we consider the applicability of the theoretical formulation discussed in Chapter 1, and what can be learned from applying this formalism given the results presented previously. We also consider how the interpretation of A_{LL} in terms of ΔG depends on a number of experimental and theoretical uncertainties.

8.1 Cross Section

The basic concept of a cross section measurement was described in Chapter 1.8. While measurement of the cross section is not a requirement for measuring an A_{LL}, it is necessary to show that the framework of PDFs, FFs, and NLO pQCD described in Chapter 1.6 is valid for interpreting our result to extract ΔG.

8.1.1 Comparison with Theory

The π^0 cross section measured with the central arms from Run5 [70] is shown in Fig. 8.1 as a function of p_T. Three NLO pQCD calculations using CTEQ6M PDFs and KKP FFs [77] overlay the data.[1] The solid, dashed and dotted curves are calculated with all theoretical scales (μ_F, μ_R and μ'_F) set to μ=p_T,

[1] Comparisons of the data with either KKP or DSS FFs show equally good agreement. The good description by DSS is not surprising, as the π^0 cross section shown was used in the FF fit.

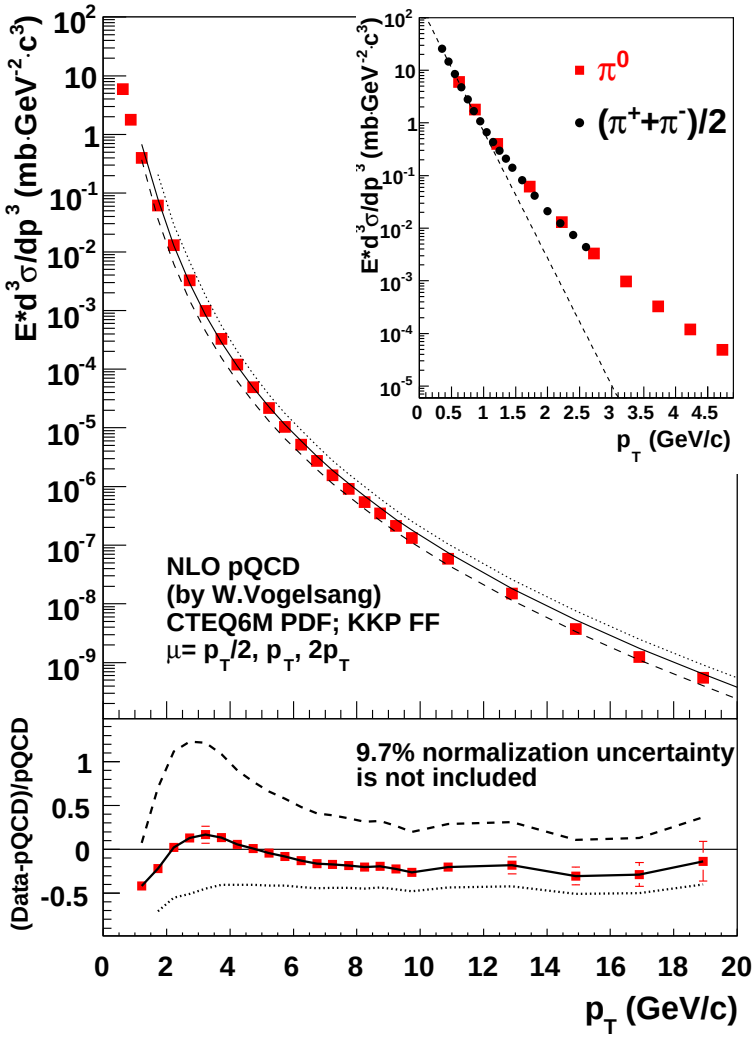

Figure 8.1: Neutral pion cross section (red squares) as a function of p_T measured at midrapidity ($|\eta| < 0.35$) at PHENIX in Run5. A normalization uncertainty in the BBC cross section of 9.7% is not shown. Solid, dashed and dotted line are NLO pQCD calculations with all theory scales set to μ=p_T, $2p_T$ and $p_T/2$, respectively. All calculations use CTEQ6M PDFs and KKP FFs. Lower panel shows the percentage difference between the three theory curves and the data, with error bars calculated assuming the central curve. Top right panel shows comparison of π^0 data with (low p_T) charge pion cross section measured at PHENIX [72]. Dashed line is a fit to an exponential of the charged pion data with $p_T < 1$ GeV/c.

$2p_T$ and $p_T/2$, respectively. The μ=$2p_T$ and μ=$p_T/2$ calculations are normally taken as an uncertainty band on the pQCD calculation with μ^2=p_T^2; *i. e.* the calculation to all orders in pQCD should lay between the $2p_T$ and $p_T/2$ curves. The bottom panel shows the relative difference between the data and the three theory curves, and indicate that within theoretical scale uncertainties, NLO pQCD describes the data across a wide range in p_T. This agreement confirms that the asymmetries measured in this work can be interpreted in the NLO pQCD framework to extract ΔG.

However, before moving on to extract ΔG from our results for A_{LL}, it is important to consider the appropriate p_T range to use. At some low p_T cutoff, the contribution from soft physics, which is not describable in pQCD, will be too large. In order to examine what p_T should be chosen as the minimal p_T for extracting information about ΔG from A_{LL}, the π^0 cross section is compared with the sum of the low p_T charged pion cross section. Due to isospin invariance, the sum of the charged pion cross section divided by two should be the same as the π^0 cross section. The inset in Fig. 8.1 shows the charged pion cross section measured at PHENIX [72] in the same rapidity range compared with the low p_T π^0 cross section. The data agree well in the overlapping p_T range. A possible transition in the p_T dependence of the charged pion data can be seen around $p_T = 1$ GeV/c. The results below this transition are most likely dominated by soft physics, and so by fitting the results from this data with an exponential function ($Ae^{-\alpha p_T}$), an estimate of the soft physics contribution can be derived. While such a fit is not possible for the π^0 data, the high precision, finely binned charged pion data can be used. The fit, using only statistical uncertainty, gives $\alpha = 5.56 \pm 0.02$ (GeV/c)$^{-1}$ with a χ^2/DOF= 6.2/3. For $p_T > 1$ GeV/c, the fit result, shown in Fig. 8.1 as a dashed line in the inset, underestimates the actual cross section. In the p_T bin 2.0-2.5 GeV/c, the soft physics contribution estimated by extrapolating the fit is less than 10%, and falls off quickly at higher p_T. Therefore, we limit our interpretation of A_{LL} in terms of ΔG to $p_T > 2$ GeV/c.

8.1.2 Charged Pions

Currently, there are no results of the cross section for high p_T charged pions. The applicability of NLO pQCD for RHIC data has been shown using the π^0 cross section (as well as other probes [78, 79]), and the p_T range measured should have little influence from soft physics. However, the lack of a cross section does limit the interpretation of the charged pion A_{LL} in terms of ΔG. The main goal of the charged pion A_{LL} measurement is to reduce the sign ambiguity in ΔG inherent in the π^0 result due to the gluon-gluon interactions. For such an interpretation to be used, we must be sure that NLO pQCD along

with the FFs give the proper relative cross sections for π^+, π^0 and π^-. Only with this in hand can we really interpret any difference in the A_{LL} results as an indication of the gluon spin distribution sign.

The charged pion A_{LL} results from Run5 are not statistically significant enough to offer much constraint on ΔG anyway, and were pursued primarily as a proof of principle measurement. Results from Run6, and future runs, will offer a better constraint, but will still require a cross section to ensure proper interpretation. For the rest of this work, we focus primarily on the constraint on ΔG from $A_{LL}^{\pi^0}$, and only briefly discuss charged pion A_{LL} to indicate where future constraints can have an impact.

8.2 Comparison of Double Helicity Results with Expectations from Different Polarized DIS Fits

The combined Run5+6 results for $A_{LL}^{\pi^0}$ are plotted in Fig. 8.2 along with a number of curves calculated[2] with Eq. 1.31 using the CTEQ6 unpolarized PDFs, the DSS FFs and the best fit results for polarized PDFs from several different groups. The grey band gives the systematic uncertainty from relative luminosity. The scaling uncertainty from the polarization listed in Table 7.2 is not shown. In the following section, we will examine the different fits, and what we can learn from comparing them with the present result.

8.3 Earlier Calculations of Spin Dependent PDFs

In Chapter 1.6, the present knowledge of polarized PDFs was described, and results from a number of different fits to the polarized DIS data were shown (see Fig. 1.10). Here we consider briefly the basic motivation behind these fits.

The exact functional forms used by the different groups discussed below are given in Appendix C. When fitting polarized PDFs, the basic functional form is

$$x\Delta f = \eta x^{\alpha}(1-x)^{\beta}h(x)f(x) \tag{8.1}$$

where f is the parton (for example: u, d_v, g, $\bar{s}$), η, α and β are fit parameters, $h(x)$ is some function that may or may not have additional fit parameters, and

[2]Curves were calculated using code from M. Stratmann for producing $A_{LL}^{\pi^0}$ expectations from grids given at [17] using the method described in [6].

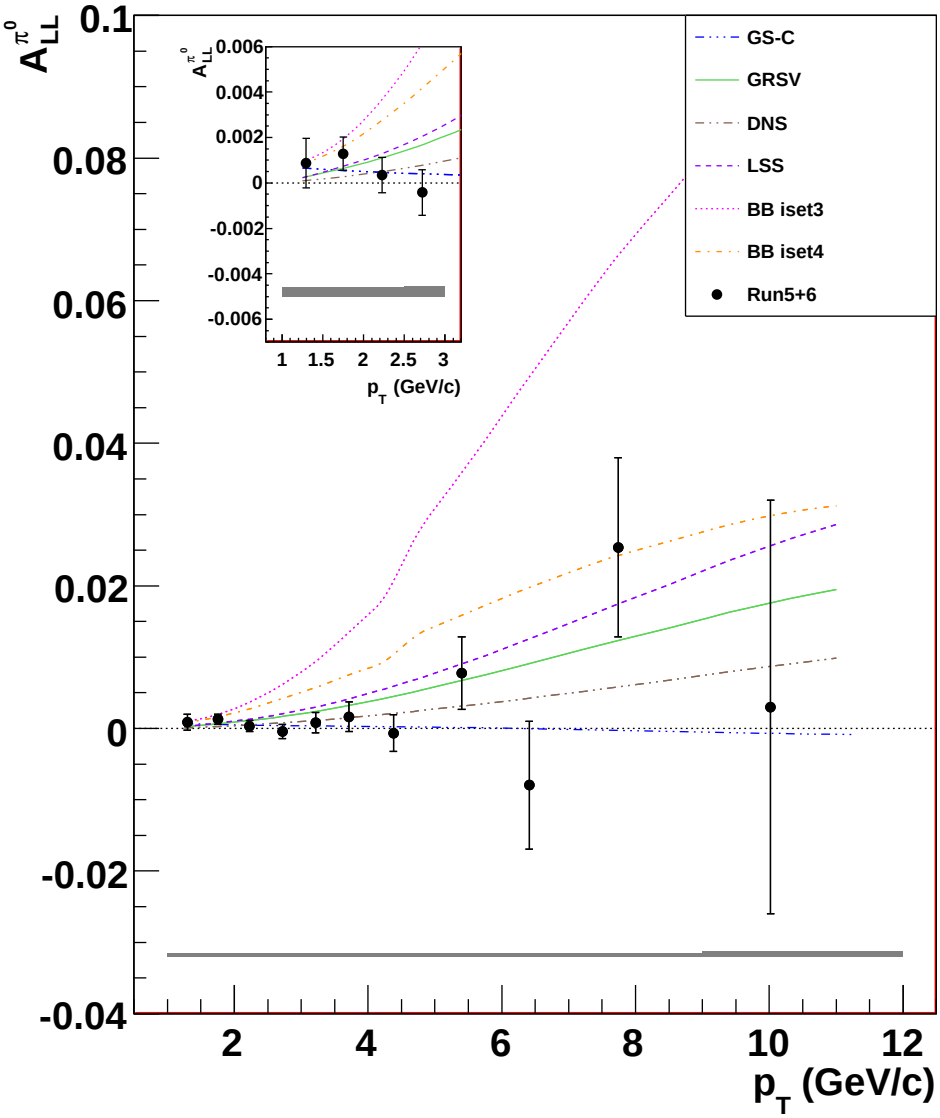

Figure 8.2: π^0 A_{LL} vs. p_T from Run5+6 plotted with expected A_{LL} curves based on the best fit results from several theory groups. Inset shows lower p_T data so that statistical uncertainties are visible. Grey band is systematic uncertainty due to relative luminosity. Scaling error due to polarization is not shown.

$f(x)$ is the unpolarized distribution function. Not all fits use $h(x)$ or $f(x)$.

As $x \to 1$, the factor $(1-x)^{\beta}$,[3] with $\beta > 0$, ensures that $x\Delta f \to 0$ since the likelihood to find any particle goes to zero as the fractional momentum goes to one, and so the difference between the probabilities should also go to zero. For more detailed discussion, see [80].

A detailed discussion of the low x behavior, which is dominated by x^{α}, is given in [81]. In the case of the unpolarized PDFs, for example the gluon, α has been found to be negative, indicating that the probability to find particles increase as $x \to 0$. However, as the momentum is finite, $\int_0^1 dx\, xg(x)$ must be finite and so $\alpha + 1 > 0$. In the case of the polarized distributions, $\int_0^1 dx \Delta g(x)$ must be finite as the proton spin is finite. Therefore, $\alpha > 0$ in the polarized fits. All other shape information is contained in $h(x)$ and $f(x)$, and can lead to significant differences, such as zero crossings for $x \in (0, 1)$.

The results for $\Delta\Sigma$ and ΔG from the different fits are shown in Fig. 1.10. As is discussed in Appendix C, the resulting constraints on ΔG are limited by the small polarized DIS data sample available, and the small range in Q^2 of the data. Therefore, in most fits, a number of assumptions were used and a number of parameters were set constant which are detailed in Appendix C.

In Table C.1, the year of each fit (and so the DIS data available as of the fit) and the number of free parameters are given, as well as information on the different constraints applied.

8.4 Implications of A_{LL} for the Gluon Spin Distribution

The results for $A_{LL}^{\pi^0}$ are plotted in Fig. 8.3 with several different A_{LL} expectations based on different input values of ΔG at the input scale in the GRSV framework. The "std" curve is the result of the GRSV best fit to DIS. It is clear from this plot that the very large values of ΔG are ruled out in this framework.

Figure 8.4a and b show final results for A_{LL} vs. p_T for positive and negative charged pions, respectively, along with curves similar to Fig. 8.3, except now calculated for the respective charged pion. Again, with the much more limited statistics of Run5, the data is not able to significantly constrain the size of ΔG.

While plots such as Fig. 8.3 and 8.4 are useful for getting a sense of the

[3] If $f(x)$ is used, then here we take β to be the sum of the β defined in Eq. 8.1 and the β from the unpolarized fit, which has a similar term. This also holds for the discussion of α in the next paragraph.

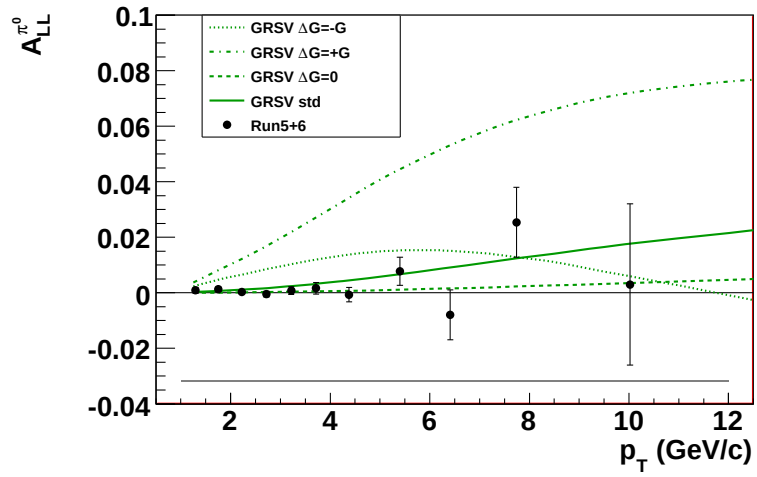

Figure 8.3: π^0 A_{LL} vs. p_T from Run5+6 plotted with expected A_{LL} curves based on different input values of ΔG at Q^2=0.4 GeV^2 in the GRSV framework. GRSV "std" is the GRSV best fit to DIS discussed in Appendix C. Grey band is systematic uncertainty due to relative luminosity. Scaling error due to polarization is not shown.

size of ΔG, in order to estimate the constraint on ΔG from the $A_{LL}^{\pi^0}$ results, we present a χ^2 fitting method first used in [70]. The idea is to use the fit results from polarized DIS, vary ΔG, propagate this variation to A_{LL}, and then calculate the χ^2 for different values of ΔG. The resulting χ^2 values can then be plotted as a function of the value of ΔG.

There are two possible approaches that can be used here. First we consider the method used in [70]. In this method, the value of the first moment of ΔG, $\Delta G(Q^2) = \int_0^1 dx \Delta g(x, Q^2)$, is set to a specific value at initial Q_0^2=0.4 GeV^2. This roughly fixes N_g in Eq. C.8.[4] Then the polarized DIS data was refit in the GRSV framework by W. Vogelsang and M. Stratmann using the same method described in Appendix C.2, but now with N_g effectively fixed. The resulting polarized PDFs were then used to calculate $A_{LL}^{\pi^0}$. This process was then repeated for a number of possible values between $\Delta G = G$ and $\Delta G = -G$ where $G = \int_0^1 dx g(x, Q_0^2 = 0.4\ GeV^2)$ is the unpolarized gluon distribution. Therefore $\Delta G = G$ and $\Delta G = -G$ give a type of limit on the total size of the polarized gluon distribution.

Figure 8.5a show $\Delta g(x, Q^2 = 1$ GeV$^2)$ calculated in the GRSV framework

[4]Technically, this fixes η_g, where η_q is N_g scaled by a normalization factor dependent on α_g and β_g.

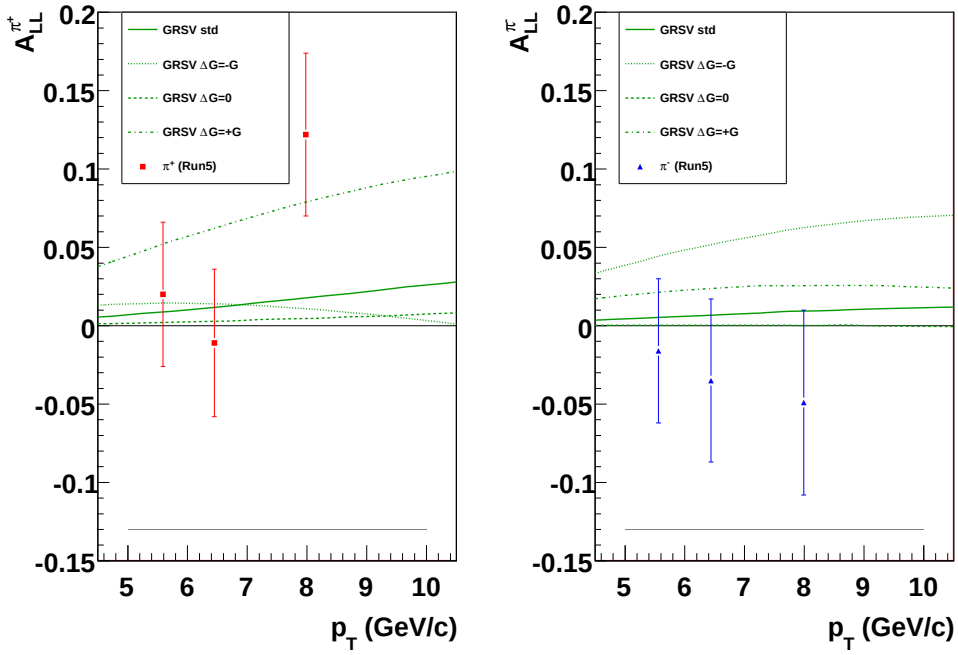

(a) (b)

Figure 8.4: A_{LL} vs. p_T for (a) π^+ and (b) π^- plotted with expected A_{LL} curves based on different input values of ΔG at Q^2=0.4 GeV^2 in the GRSV framework. GRSV std is the GRSV best fit. Grey band is systematic uncertainty due to relative luminosity. Scaling error due to polarization is not shown.

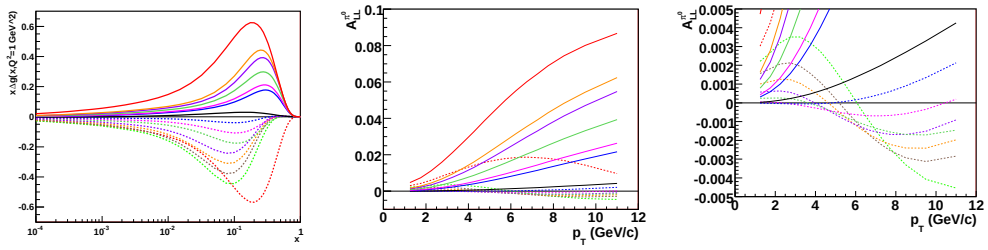

(a) **(b)** **(b)**

Figure 8.5: (a) $x\Delta g(x)$ vs. x at Q^2=1 GeV^2 from fits in the GRSV framework assuming different input values of ΔG (at input scale). (b) A_{LL} vs. p_T calculated from corresponding $\Delta g(x)$ curve. (c) Closer view of curves near $A_{LL} = 0$ in (b). Solid blue line in all cases in GRSV std, the DIS best fit result.

for different input values of the full first moment, ΔG. The resulting A_{LL} curves have been calculated using the method described in [82], and are plotted in Fig. 8.5b. Figure 8.5c shows a expanded view of the same curves near $A_{LL} = 0$.

A χ^2 value was calculated for each $A_{LL}^{\pi^0}$ expectation curve with the Run5, Run6 and Run5+6 $A_{LL}^{\pi^0}$ results for p_T >2 GeV/c, using only the statistical uncertainty given in Tables 6.1 and 7.2. Figure 8.6 shows the value of χ^2 for the $A_{LL}^{\pi^0}$ result from Run5 (red), Run6 (blue) and Run5+6 (black) as a function of the $\Delta G_{\rm GRSV}^{x\in[0.02,0.3]}$ at Q^2=1 GeV^2. Later, we will see that the resulting constraint on ΔG is model dependent, and so the subscript "GRSV" indicates that this result is valid within the GRSV framework. The values of ΔG shown were calculated by evolving (using the DGLAP equations) the GRSV fit results described above to Q^2=1 GeV^2.

It is important to recognize the limitation of this data set, which do not cover the whole of $0<x<1$, but instead a more limited range. Figures 8.7a-c [83] show the $x_{\rm gluon}$ distributions for three p_T ranges used in the π^0 analysis. The distributions are quite wide, and there is significant overlap between the different p_T bins used. Therefore, we simply define the constraint on ΔG in the total x range covered by our π^0 data, which we estimate as $0.02<x<0.3$. The superscript on ΔG in Fig. 8.6 indicates that this constraint is only applicable in the x region sampled by the π^0 data.

From Fig. 8.6, when considering only statistical uncertainties, it is clear that the $A_{LL}^{\pi^0}$ data does constrain the size of ΔG in the measured x range significantly better than fixed target polarized DIS, which allowed a myriad of possibilities in the x range covered by the $A_{LL}^{\pi^0}$ data (see Fig. 1.10). In the following sections, we will consider what effect both the largest experimental

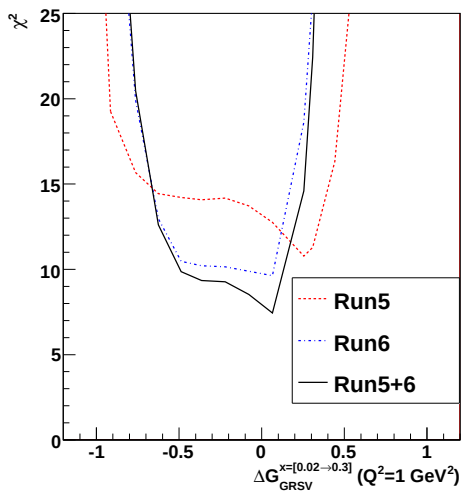

Figure 8.6: χ^2 vs. $\Delta G_{\mathrm{GRSV}}^{x\in[0.02,0.3]}$ at Q^2=1 GeV^2 using results for $A_{LL}^{\pi^0}$ with $p_T > 2$ GeV/c from Run5 (red dashed), Run6 (blue dotted) and Run5+6 (black).

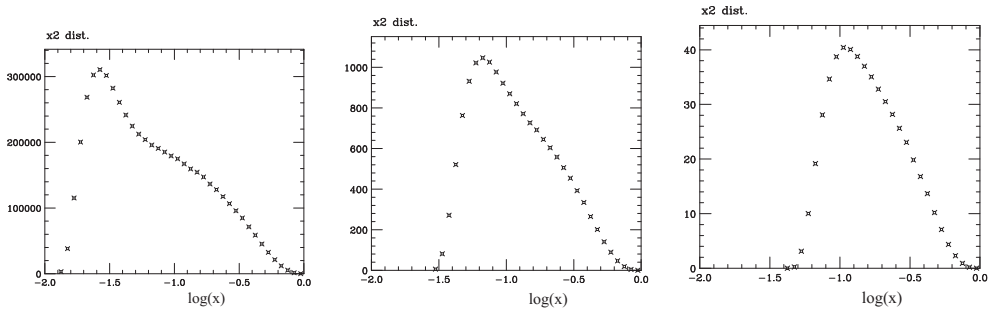

(a) **(b)** **(c)**

Figure 8.7: x_{gluon} distributions in π^0 production at midrapidity for (a) $2<p_T<3$, (b) $5<p_T<6$ and (c) $8<p_T<9$ GeV/c.

systematic uncertainties and the large theoretical uncertainties that arise in this interpretation have on this conclusion.

8.5 Effect of Experimental Systematic Uncertainties

As discussed in Chapter 7.9, the two largest systematic uncertainties on the $A_{LL}^{\pi^0}$ results are from beam polarization normalization uncertainty and relative luminosity. Here we consider the effects of both on the interpretation of A_{LL} in terms of ΔG using the χ^2 method described above. For all of the following plots, the summed results from the Run5+6 data given in Table 7.2 are used.

In Fig. 8.8, two curves are shown in red, which take into account the uncertainty from the polarization, compared with the statistical uncertainty only in black. As is discussed in Chapter 7.8, the only significant polarization uncertainty is an overall systematic uncertainty for each running year. This uncertainty scales both the data and the statistical uncertainties in the same way, and so directly impact the comparison with the A_{LL} expectations used to calculate the χ^2. The dashed (dotted) line is the resulting χ^2 distribution when scaling the polarization value up (down) by the stated uncertainties in Table 7.1. It is clear that this uncertainty has only a small effect on the constraint of ΔG from $A_{LL}^{\pi^0}$. In this, and all later comparisons of the data, only results with $p_T > 2$ GeV/c were used.

In Fig. 8.9, the uncertainty from relative luminosity is taken into account. This uncertainty is completely correlated between all points, and so results in a constant shift in the A_{LL} results. Again, the black line is the same as in Fig. 8.6, and assumes only statistical uncertainty, while the dashed (dotted) lines assume a positive (negative) shift. Even though this uncertainty is small, the interpretation of A_{LL} in terms of ΔG is sensitive to it. Reducing this uncertainty will be key to future measurements.

It may seem surprising that the Relative Luminosity uncertainty leads to a more significant variation in the extraction of ΔG than the polarization uncertainty. This is mainly a product of where the data lie. The Relative Luminosity uncertainty shifts all the data in the same direction, while the polarization uncertainty shifts positive data up and negative down. If the all of the A_{LL} data were positive (and large), then the conclusion of which systematic is more important may change.

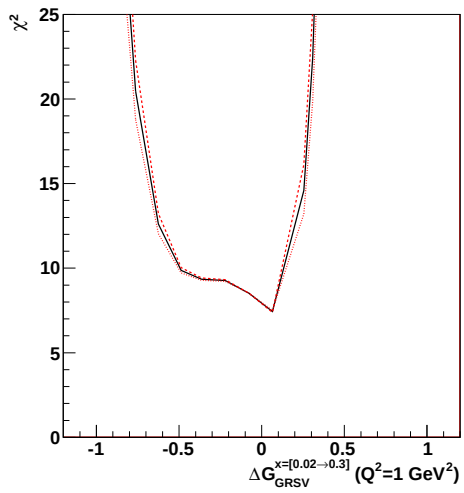

Figure 8.8: χ^2 profile vs. $\Delta G_{\mathrm{GRSV}}^{x\in[0.02,0.3]}$ calculated with only statistical errors (black) or after scaling the polarization value up (red dashed) or down (red dotted) by the polarization uncertainty listed in Table 7.2.

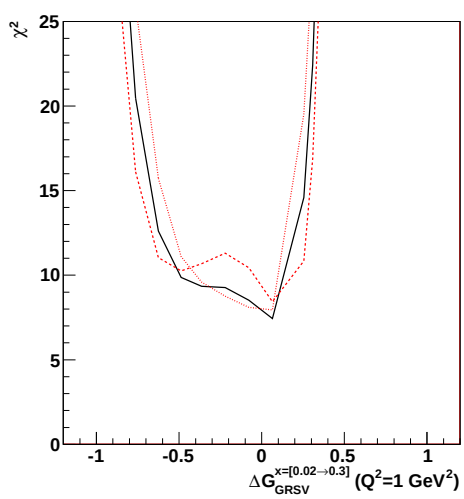

Figure 8.9: χ^2 profile vs. $\Delta G_{\mathrm{GRSV}}^{x\in[0.02,0.3]}$ calculated with only statistical errors (black) or after shifting the $A_{LL}^{\pi^0}$ results up (red dashed) or down (red dotted) by the Relative Luminosity uncertainty listed in Table 7.2.

8.6 Effect of Theoretical Uncertainties

There are a number of theoretical uncertainties which can directly influence the interpretation of our A_{LL} results:

- theoretical scale (μ_F, μ_R, μ'_F) uncertainty,
- uncertainty on polarized quark PDFs,
- functional form used in the fit,
- uncertainty from α_s,
- uncertainty in the x range not measured in the data set
- positivity constraints applied during the fitting procedure.

Here we consider a number of these individually using this χ^2 approach, and discuss the effect from the others on any final estimate of ΔG derived from the $A_{LL}^{\pi^0}$ results. Note that all of these uncertainties *also* apply to fits to DIS and SIDIS data.

8.6.1 Theoretical Scale Uncertainty

As discussed above with respect to the cross section, there are several theoretical scales used in any pQCD calculation: factorization, renormalization and, in the case of a final state hadron, fragmentation. As can be seen in Fig 8.1, a different choice of these scales can lead to a sizable difference in the theoretical expectation. Therefore, varying this scale can give a sense of the uncertainty in the theoretical calculation due to a certain choice. In the fits described in Appendix C, the standard choice of scale in DIS is $\mu^2 = Q^2$ where all the theory scales are taken as equal to μ ($\mu = \mu_F = \mu_R = \mu'_F$). As with the unpolarized cross section, the scale in A_{LL} calculations is taken as the p_T of the final state observable, in this case the p_T of the pion.

While the fits discussed in Appendix C do not include this uncertainty, it is known to be large. The SMC experiment found in their fit to polarized DIS data [84] that this scale uncertainty is one of the dominant uncertainties when extracting ΔG. To give a sense of the size of this scale uncertainty in A_{LL}, two sets of $A_{LL}^{\pi^0}$ expectation curves based on the GRSV best fit (std) and the fit result for fixing ΔG =0 are shown in Fig 8.10 with choice of scale μ=p_T, $p_T/2$ and $2p_T$. The χ^2 analysis above was repeated with these three scale choices and the results are shown in Fig. 8.11. It is clear that this uncertainty is large, and reduces the sensitivity of $A_{LL}^{\pi^0}$ to ΔG, especially for negative values of ΔG

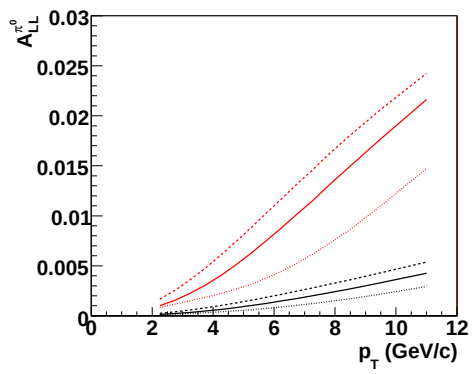

Figure 8.10: $A_{LL}^{\pi^0}$ vs. p_T for GRSV std (red) and $\Delta G = 0$ (black) in the GRSV framework with all theoretical scales set to μ=p_T (solid), $2p_T$ (dashed) and $p_T/2$ (dotted).

in the GRSV framework. No matter the framework, though, the uncertainty due to the choice of theoretical scale can be large, and must be considered when extracting ΔG from A_{LL} (as well as from DIS and SIDIS).

8.6.2 Sensitivity to the Gluon and Quark Spin Distribution

While it is clear from Fig. 8.6 that $A_{LL}^{\pi^0}$ is sensitive to ΔG, Eq. 1.31 indicates that it is also dependent on the quark helicity distributions. In order to explore how sensitive the results are to the quark polarization, we consider a second approach to varying ΔG. Above, the polarized DIS data was refit for each value of ΔG, allowing the shape of the gluon polarization, as well as the quark distributions, to vary. Here, effectively all parameters are fixed except N_g in Eq. C.8, using the best fit quark polarized distribution and gluon shape (α_g, β_g). This is equivalent to setting

$$\Delta g'(x, Q_0^2) = \lambda \Delta g(x, Q_0^2) \tag{8.2}$$

and varying λ. The difference between the two approaches indicates the sensitivity of $A_{LL}^{\pi^0}$ to the gluon shape and the quark distributions.

The values of the polarized PDFs were calculated for each new value of N_g using the QCD-Pegasus Parton Distribution Evolution code [85]. From the output, $A_{LL}^{\pi^0}$ expectations were generated using the method of [82]. The results from this approach are plotted in Fig. 8.12, along with the method in which the polarized DIS data is refit. For positive ΔG, the two curves agree

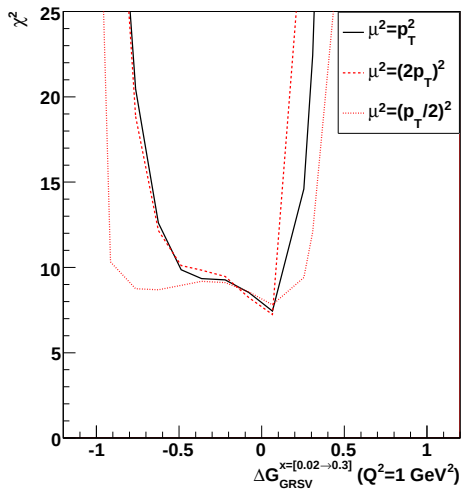

Figure 8.11: χ^2 profile vs. $\Delta G_{\mathrm{GRSV}}^{x\in[0.02,0.3]}$ in the GRSV framework with choice of theory scale $\mu^2 = p_T^2$ (black solid line), $\mu^2 = (2p_T)^2$ (red dashed line), and $\mu^2 = (p_T/2)^2$ (red dotted line).

well, indicating that the A_{LL} results are primarily sensitive to ΔG, as allowing the quark polarization to vary yields little difference. However, in the region of ΔG less than or near zero, there is a significant difference between the results for the two methods, indicating that the A_{LL} results are sensitive to more than simply the size of the gluon spin distribution. Therefore, when using this method without refitting to DIS, we must take care of interpreting the results for negative values of ΔG.

8.6.3 Sensitivity to Functional Form

A significant source of uncertainty in a PDF fit will arise from the use of different functional forms. In the unpolarized case, the large x and Q^2 range of the data significantly constrain the possible functional forms used. Due to the limited Q^2 and x range of the fixed target polarized DIS data, the functional form of the gluon (and the sea quarks) is not well constrained. A number of different functional forms have been considered, and are discussed in Appendix C. Here we examine the dependence of the ΔG extracted above from our data on functional form.

Similar to the procedure described in the previous section, $A_{LL}^{\pi^0}$ was calculated based on the best fit results from BB, LSS, and GS-A, B, and C for multiple values of ΔG, changed at the input scale, while fixing all other

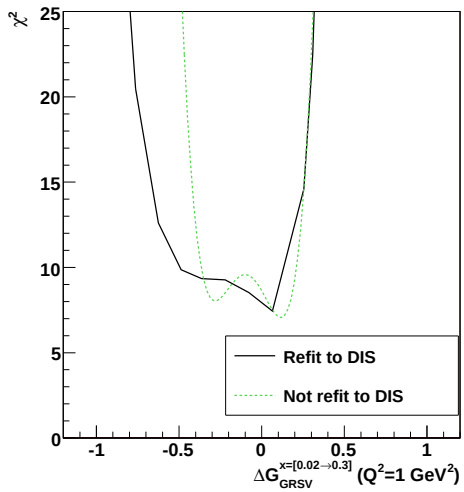

Figure 8.12: χ^2 profile vs. $\Delta G_{\mathrm{GRSV}}^{x\in[0.02,0.3]}$ in the GRSV framework calculated with (black solid line) and without (green dashed line) refitting the DIS data after fixing the value of ΔG.

parameters to the best fit values. In most cases, this affects only the quark sector, as most gluon parameters were already fixed. From these expectations, the χ^2 as a function of ΔG (in the measured x range) were calculated, and are plotted in Fig. 8.13. In each case, the new gluon polarization $\Delta g'(x, Q_0^2)$ has been evolved to Q^2=1 GeV^2, so that all the theories can be easily compared. Note that, as in seen in Fig. 8.12, this method can underestimate the variation allowed in χ^2 in the region of ΔG corresponding to small A_{LL} values (roughly -0.6<ΔG <0.1).

As discussed in Appendix C, all of the fits considered except GS-C did not contain nodes for $0 < x < 1$. Here we will discuss these "nodeless" forms, and leave GS-C for later. In Fig. 8.13, the results for all the different "nodeless" fits are seen to be very consistent with each other. This again indicates that the data do constrain ΔG. Secondly, we see that differences in the quark helicity distribution or gluon shape between the BB iset3 and 4, GRSV, LSS and GS-A and -B functional forms do not lead to any significant dilution of this constraint. In the case of a "nodeless" functional form, the π^0 data indicate a negative or small positive ΔG, ruling out large gluonic contributions postulated [28–30] after the EMC result.

In Fig. 8.13, there is also a very wide χ^2 profile corresponding to the result from varying ΔG in the GS-C framework. In this model, there is a node at $x = \frac{1}{9}$ (see Fig. 1.10, which lies within the x range covered by the π^0

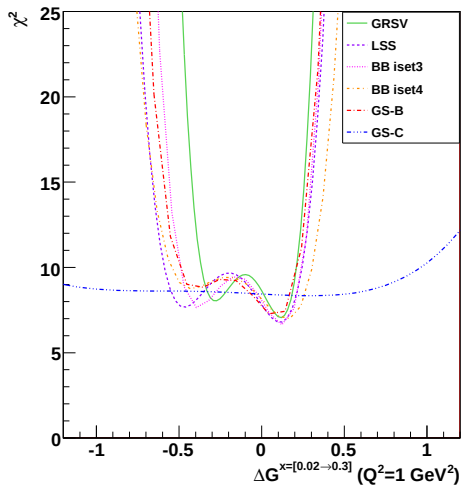

Figure 8.13: χ^2 profile vs. $\Delta G^{x\in[0.02,0.3]}$ for different models done without refitting DIS data in all cases.

measurement. Due to the wide distribution in x sampled in each p_T bin, as can be seen in Fig. 8.7a-c, A_{LL} at all p_T values from 2-12 GeV/c are sensitive to this node, and so the expectation for A_{LL} is quite small (see Fig. 8.2).

To study the effect of a node crossing, and the dependence on the location of the node in x, the parameter in GS-C that gives the node, ρ_g (see Appendix C.6), has been varied, and the procedure above redone. The results are shown in Fig. 8.14 for ρ=-1.5, -3 (initial value), -6 and -12 resulting in a node at x=0.44, 0.11, 0.028 and 0.007, respectively. Note that in GS-C, the node was chosen and not the result of the fit. Here, we have neglected the fact that changing the location of the node will change the quark sector fit via DGLAP evolution. However, this gives a sense of how the location of the node can affect the extraction of ΔG from A_{LL}. Figure 8.14 indicates that if the node lies at a small value of x below the measured x range or such that the higher p_T points do not sample this x value, the result is very similar to the results of the "nodeless" fits in Fig. 8.13.

Any estimate on the uncertainty from functional form from Fig. 8.2 and 8.14 only give a sense of the total uncertainty. In order to more thoroughly examine this uncertainty, these different functional forms must be considered in a "global analysis", or fit, to all available data: polarized DIS, SIDIS and $p+p$ scattering.

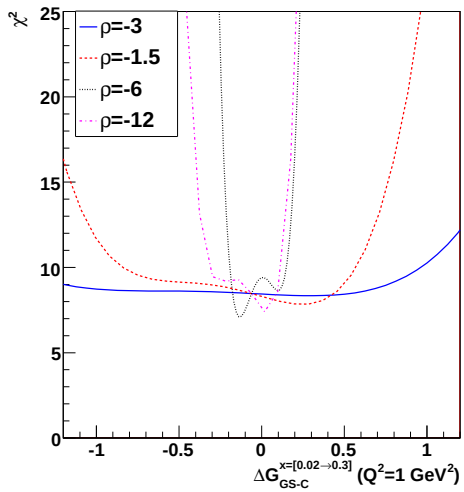

Figure 8.14: χ^2 profile vs. $\Delta G^{x\in[0.02,0.3]}$ for different values of the parameter ρ in Eq. C.28 assuming all other best fit values from the GS-C fit.

8.6.4 Uncertainty from α_s

The strong coupling constant, α_s, has been measured precisely at the Z pole [12]. However, the uncertainty at the energy scale of the current polarized DIS (as well as SIDIS and $p+p$ scattering) data is large. This uncertainty will impact the pQCD calculations, and therefore the extracted PDFs. The value on α_s used in PEGASUS and the calculation of A_{LL} can be set to take into account the uncertainty on α_s, but as the uncertainty will directly impact the fit to the DIS data also, it would not account for the total uncertainty from α_s. Therefore, we leave estimates of the effects of this uncertainty for future fits, and only highlight its importance in the total uncertainty in the (polarized) PDFs.

8.6.5 Uncertainty from the Unmeasured x Region

As stated above, the $A_{LL}^{\pi^0}$ data cover a limited x range, as does the fixed target polarized DIS measurements, and so the PDFs are only constrained in these ranges. The total first moment however depends on the entire x range ($0 < x < 1$), and so will depend significantly on the assumed behavior of the functional form used in the unmeasured and unconstrained region. This lesson has been learned several times. Prior to data from HERA, there was large uncertainty in the low x unpolarized gluon distribution, with some predictions expecting it to go to zero as $x \rightarrow 0$ [86], while others predicted that it would

continue to rise [87], which turned out to be correct.

Similarly, as was discussed in Chapter 1.6.2, the low x extrapolation from SLAC polarized DIS data at high x indicated agreement with the Ellis-Jaffe sum rule. The results from EMC however showed that the extrapolation was an over estimate and the sum rule was indeed violated, producing the "proton spin crisis". As this extrapolation is by its very nature outside of the measured x range, it is difficult to estimate it based on our results. In Sec. 8.8, we will see this clearly in a result from the AAC collaboration. Again, here we simply highlight the sizable uncertainty that can come from this extrapolation. While such extrapolations are always needed (there is always some minimal x measurable), extending the x reach of both the A_{LL} data and the DIS data are essential to constraining this uncertainty. Future prospects for achieving this are discussed in the next chapter.

8.6.6 Constraints on Positivity

As the polarized and unpolarized PDFs are the difference and sum, respectively, of the positive helicity and negative helicity distributions, we should expect that positivity should hold, *i. e.*[5]

$$|\Delta f(x, Q^2)| \leq f(x, Q^2) \; . \tag{8.3}$$

In the BB fit, the authors found that they did not have to impose positivity, and only checked that it was not violated after the fit. Other groups have imposed it as a constraint during the fit. (See Appendix C for details of how it was handled in the different fits.) However, in a fit with so many parameters, it is difficult to know how such a constraint on one parameter may propagate to constraints on other parameters.

Figure 8.15 [89] shows the χ^2 distribution from the DNS fit when varying ΔG. The dashed dotted line is from their fit to polarized inclusive data only, while the solid (dashed) line correspond to the fit to both the DIS and SIDIS data using Kretzer [90] (KKP) FFs. While the SIDIS data does show some preference for the value of ΔG, the sharp edges of the distribution, even when only using inclusive data, indicate that the inclusion of SIDIS data do not lead to a much more significant constraint, as has been claimed. Instead, much of the constraint comes from the application of the positivity constraint during the fit. For the gluon, this constraint is not very strong, except at large x as the unpolarized gluon distribution is very large at even moderate

[5] As the authors of [88] point out, the physical observables are $\Delta\sigma$ and σ, and so we must have $|\Delta\sigma| \leq \sigma$. One way to ensure this, which they and most other groups use, is to instead assume Eq. 8.3

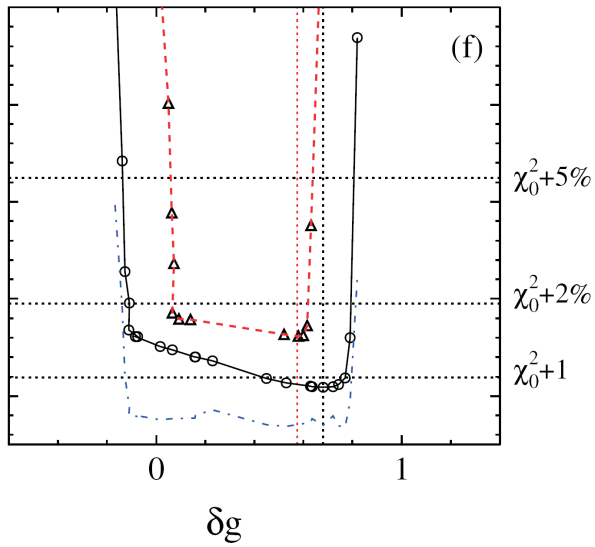

Figure 8.15: χ^2 profiles for the different polarized PDFs in the DNS framework. Sharp boundaries on the gluon distribution arise from the method of constraining positivity of the sea quarks in the fit. Taken from [89].

x (see Fig. 1.4 or 1.5). However, the positivity constraint on the sea quarks is significant, and directly impacts the gluon though the DGLAP evolution equations. Therefore, constraining the positivity of the sea quarks effectively imposes a constraint on the gluon, but how this constraint behaves is not obvious. Clearly, constraining positivity can lead to an overstated result.

8.7 Extracting ΔG

From the above studies, a value of ΔG can be determined in the measured x range. From the χ^2 profile using Run5+6 data in Fig. 8.6, a best fit value of 0.0 ± 0.1 can be determined assuming a one sigma uncertainty given by the change in ΔG for an increase of one unit in χ^2. However, as discussed above, the are several experimental systematic and theoretical uncertainties that we also need to consider.

From the variation in the value of χ^2 when taking into account the Relative Luminosity and polarization uncertainties (Fig. 8.9 and 8.8), the total effect of the systematic uncertainties on ΔG is estimated as $^{+0.1}_{-0.2}$. This is primarily due to the uncertainty in Relative Luminosity.

For theoretical uncertainties, we consider only three sources of uncertainty:

choice of theoretical scale, functional form and the method used to vary ΔG. The variations in the χ^2 profiles in Fig. 8.11, 8.13 and 8.12 lead to an uncertainty in ΔG of $^{+0.2}_{-0.9}$ in the case of a simple "nodeless" functional form. In the case of a node, a significantly larger uncertainty of $^{+0.7}_{-1.5}$ is estimated, based on comparison with the GS-C result.

Therefore, we find in the "nodeless" case

$$\int_{0.02}^{0.3} dx \Delta g(x) = 0.0 \pm 0.1(\text{stat.})^{+0.1}_{-0.2}(\text{syst.})^{+0.2}_{-0.9}(\text{theo.}). \tag{8.4}$$

Some of the uncertainties in ΔG discussed above have been neglected in this result, such as the uncertainty in α_s. Note that we have limited the result to the measured region. As discussed above, large uncertainties from extrapolation to the unmeasured x regions, particularly at low x, can lead to significant uncertainties in the final value of $\Delta G = \int_0^1 dx \Delta g(x)$.

8.8 Recent Theoretical Studies

Since the release of the Run5 $A_{LL}^{\pi^0}$ results, several theory groups have studied how well the data can constrain ΔG. In 2006, the Asymmetry Analysis Collaboration (AAC) [91] considered what additional constraint came from the Run5 Preliminary π^0 result [92]. Their best fit to DIS data alone and one sigma statistical error bands are shown in Fig. 8.16 as green dashed and dotted lines, respectively. From additionally including the π^0 A_{LL} result, they found two possible solutions with essentially the same χ^2: positive ΔG (red line with shaded statistical error bands) and negative ΔG (dashed dotted blue line with solid blue line giving statistical error band). From this plot, the large uncertainty in the behavior at low x (below the measured region in $A_{LL}^{\pi^0}$) is quite clear.

Also in 2006, DNS [89] fit the polarized DIS and SIDIS data. From initial comparison of their results with the Run5 Preliminary $A_{LL}^{\pi^0}$ result, they concluded that $A_{LL}^{\pi^0}$ was not sensitive to ΔG. However this was a misunderstanding of the scaling uncertainty in the beam polarization. When taking the errors into account properly, they found that $A_{LL}^{\pi^0}$ was sensitive to ΔG, but was not a better constraint than SIDIS+DIS. However, as was discussed above, the majority of this constraint on ΔG actually arises via DGLAP evolution from strong positivity constraints on the sea quark.

In spring 2008, De Florian and Sassot of DNS and Stratmann and Vogelsang of GRSV (DSSV) [93] performed for the first time a global analysis including A_{LL} results from $p+p$ scattering on an equal footing with DIS and

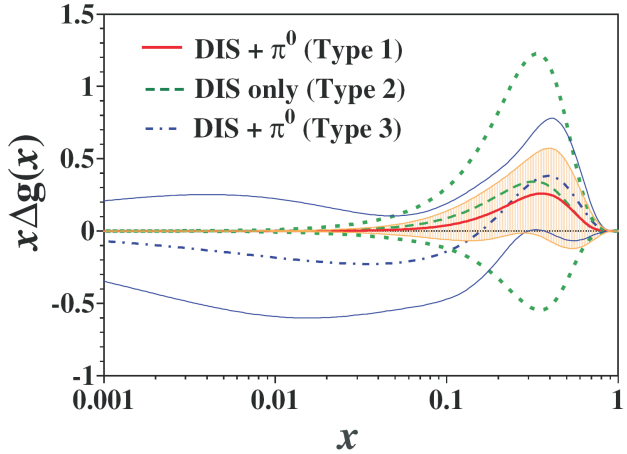

Figure 8.16: Gluon spin distribution vs. x from AAC for DIS data only (green dashed) along with two fits after including the $A_{LL}^{\pi^0}$ data. Large uncertainty in the extrapolation to low x can be seen by comparing the blue and red curves, which give roughly equal χ^2. Taken from [91].

SIDIS data. This analysis was effectively a proof of principle that A_{LL} results could be used directly in constraining the polarized PDFs. However, serious consideration of the experimental and theoretical uncertainties has not yet been done, and so the results must be considered in this context.

Figure 8.17 shows the best fit result for the different polarized PDFs at Q^2=10 GeV^2, along with a statistical uncertainty from the fit given as $\Delta\chi^2$ =1 (green band), which is a one sigma error if all errors are handled properly, or $\Delta\chi^2/\chi^2$ =2%, which is about the difference between unpolarized PDF fit results. Theoretical uncertainties have not been considered, and experimental statistical and systematic errors were simply summed in quadrature. The node at $x \sim 0.1$ is driven primarily by the small A_{LL} results from both π^0 at PHENIX and STAR jets [94]. Comparison with the results from DNS and GRSV are also seen.

The DSSV result for χ^2 vs. ΔG[6] is plotted in Fig. 8.18 along with the relative deviations for the different subsets of data: DIS, SIDIS, $A_{LL}^{\pi^0}$ (final Run5 and Preliminary Run6 at $\sqrt{s}$ =200 GeV and Preliminary Run6 [95] at $\sqrt{s}$ =62.4 GeV [96]) and inclusive jet A_{LL} from STAR. The constraint of the A_{LL} results are significant, and drive the fit in the range $0.02 < x < 0.2$

When comparing the SIDIS and DIS χ^2 profile in Fig. 8.15 and Fig. 8.18,

[6]DSSV uses a different notation for $\int_{x_{min}}^{x_{max}} dx\Delta g(x)$, namely Δg, whereas we use ΔG.

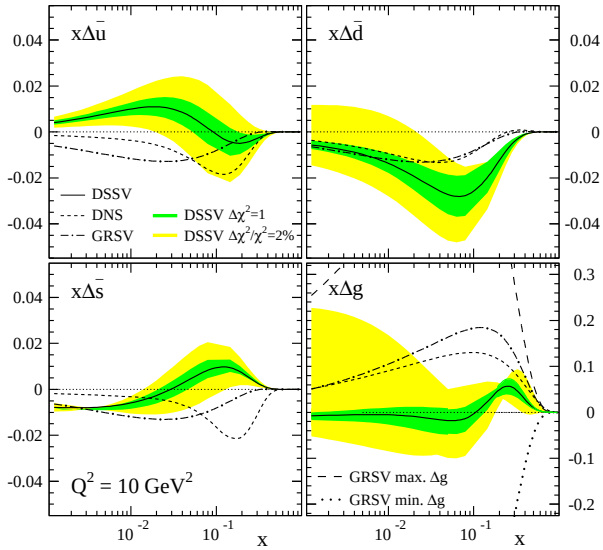

Figure 8.17: Polarized PDFs from DSSV fit. Best fit is solid line. Statistical error bands for $\Delta\chi^2 = 1$ (green) and $\Delta\chi^2/\chi^2 = 2\%$ are shown. Best fit results for GRSV and DNS are also shown for comparison. Taken from [93].

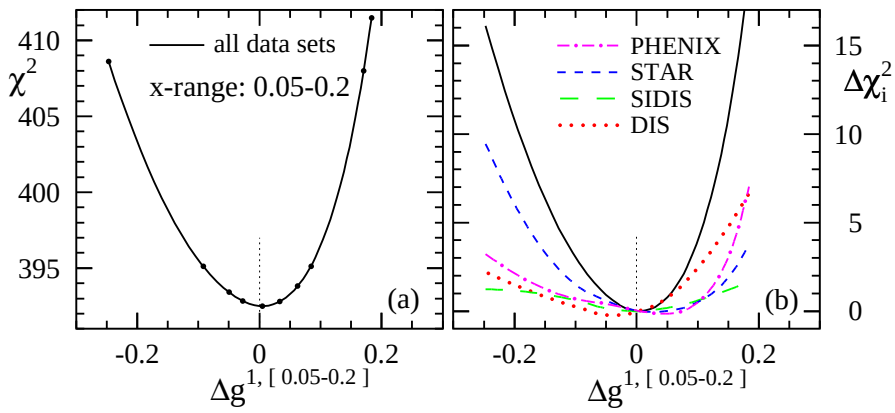

Figure 8.18: Left: χ^2 profile as a function of ΔG at Q^2=1 GeV and $0.05 < x < 0.2$. Right: Change in χ^2 ($\Delta\chi^2$) for the different subsets of data as a function of the ΔG. Taken from [93].

the sharp edges of the distribution seen in DNS are no longer present. This is primarily due to the choice of FF. In the DNS result, Kretzer FFs were used, which did not well describe some SIDIS results, and therefore ended up falsely constraining the quark sea and through evolution the gluon. The use of DSS FFs, which were fit to SIDIS, $p+p$ and e^+e^- data, in DSSV did not suffer this problem.

Chapter 9

Conclusions and Prospects

The measurement of the double helicity asymmetry in neutral pion production in polarized proton collisions at $\sqrt{s} = 200$ GeV from the 2005 and 2006 RHIC runs has been presented. A number of systematic cross checks have been performed. The dominant systematic uncertainties, due to luminosity normalization and polarization, have been studied.

The π^0 A_{LL} results have been compared with expectations based on NLO pQCD calculations in order to constrain the size of the polarized gluon distribution in the proton. A simple method that calculates χ^2 while varying the size of ΔG has been used to estimate the sensitivity of the A_{LL} results to ΔG. The π^0 A_{LL} measurement from the Run5+6 data set is precise enough to offer a significant constraint on ΔG. The inclusion of the primary experimental systematic uncertainties has a minimal effect on this constraint, though reduction of these uncertainties as the statistical precision of the data increases in future years will be important. A number of theoretical uncertainties in the interpretation of A_{LL} have been examined using this χ^2 method, and found to be much more significant than any current experimental uncertainties. From these different studies, in the case of a simple "nodeless" functional form, the value of ΔG can be extracted, and in the measured x range is found to be

$$\int_{0.02}^{0.3} dx \Delta g(x) = 0.0 \pm 0.1(\text{stat.})^{+0.1}_{-0.2}(\text{syst.})^{+0.2}_{-0.9}(\text{theo.}) \tag{9.1}$$

where the first uncertainty is statistical, the second in due to experimental systematic uncertainties, and the third is due to theoretical uncertainties. In the case of a node in the measured region, such as for GS-C, the theoretical uncertainty is significantly larger ($^{+0.7}_{-1.5}$). This value is only for the measured range. There are also significant uncertainties in the extrapolation to the full integral ($\int_0^1 dx \Delta g(x)$), especially in the low x region.

The effect of the A_{LL} data in extracting ΔG was also examined in view of several recent studies. The recent inclusion in a true global analysis (DSSV) including DIS, SIDIS and $p+p$ results clearly shows the power of this new result.

A second exploratory measurement from the 2005 RHIC run of charged pion A_{LL} has also been described. With the statistical precision from the Run5 data set, the charged pion result is unable to offer much constraint on ΔG. Increased statistics from Run6 and beyond will add to the significance of this channel, though statistical limitations do to trigger efficiency mean that any constraint from charged pions will be limited. A charged pion trigger would be an important development. However, for comparison with theory, a cross section measurement must be completed to ensure correct interpretation in terms of ΔG.

9.1 Prospects for Constraining ΔG

The first true global analysis from DSSV indicates that ΔG can be constrained in $p+p$ collisions. However, a full and complete error analysis is still needed. This process is now beginning with both experimentalists and theorist involved, and will hopefully ensure that all uncertainties are considered and handled properly.

From the experimental side, the most significant advance will come from extension of the x region covered by experiment. A first measurement has been made at $\sqrt{s}$ =62.4 GeV [96], which can offer higher precision data than the larger center of mass energies at a given x_T[1]. This effectively allows access to higher x, though overlap with the x range at $\sqrt{s}$ = 200 GeV is sizable. Also, the applicability of NLO pQCD at this lower energy must be studied.

Another option available at RHIC is to move to larger center of mass energy, namely $\sqrt{s}$ =500 GeV. This will allow access to a lower x range (down to $x \sim 0.007$) not currently probed at $\sqrt{s} = 200$ GeV. This will offer additional insight into ΔG, as the effect of any node in the measured x range at $\sqrt{s} = 200$ GeV will differ at $\sqrt{s}$ =500 GeV. However, the small uncertainties expected will require a significant reduction in the systematic uncertainties, namely Relative Luminosity.

While extending the measured x range will be significant, the use of correlation measurements between jets at STAR or hadrons at PHENIX may reduce the smearing out of x across multiple p_T bins. Correlations between particles at different pseudorapidities will allow different regions in the x range probed

[1] x_T is the equivalent of x_F (Eq. 4.18), but with p_T interchanged for p_z.

by the inclusive π^0 and jet measurements to be examined.

In the longer term, the most significant constraints on the polarized gluon distribution will largely come via the same method used for the unpolarized distribution, namely a large Q^2 and x range. This will require us to return to polarized DIS, and so a new polarized electron polarized hadron collider, the Electron Ion Collider (EIC) [97], is currently being planned. The EIC is expected to cover a large range in x, reaching a minimum x of 10^{-4}. Such an collider will offer significant insight, not only into the polarized gluon distribution, but perhaps the entire spin structure of the proton.

Appendix A

Useful Mathematical Calculations

A.1 k Factor Derivation

Assume that we want the uncertainty in N, where N can be written as

$$N = \sum_{i=1}^{N_{ev}} k_i = \bar{k} N_{ev} \tag{A.1}$$

where k_i is the multiplicity per event, N_{ev} is the number of events and $\bar{k}$ is the average multiplicity. Then by standard error propagation, the uncertainty in N is written as

$$\sigma_N^2 = N_{ev}^2 \sigma_{\bar{k}}^2 + \bar{k}^2 \sigma_{N_{ev}} \ . \tag{A.2}$$

As N_{ev} is Poissonian, $\sigma_{N_{ev}} = \sqrt{N_{ev}}$. For the uncertainty in the average multiplicity, we look at

$$\sigma_k^2 = E[k^2] - (E[k])^2 \tag{A.3}$$

where $E[k]$ is the expectation value of k.

Several useful identities about expectation values are:

A. $E[cX] = cE[X]$

B. $E[X + Y] = E[X] + E[Y]$

C. $E[XY] = \sigma_{XY}$

where c is a constant, X and Y are independent distributions. Further, if X and Y are from the same parent distribution, then:

D. $\sigma_X = \sigma_Y$

E. $\sigma_{XY} - \sigma_X \sigma_Y = 0$, *i. e.* the covariance is zero.

Using $\bar{k}$ in place of k in Eq. A.3, we start with

$$\sigma_{\bar{k}}^2 = E[\bar{k}^2] - (E[\bar{k}])^2$$

which by the definition of $\bar{k}$ can be rewritten as

$$\begin{aligned}\sigma_{\bar{k}}^2 &= E[(\frac{1}{N}\sum k)^2] - (E[\frac{1}{N}\sum k])^2 \\ &= E[\frac{1}{N^2}(k_1 + k_2 + \ldots + k_N)^2] - (\frac{1}{N}E[(k_1 + k_2 + \ldots + k_N)])^2 \,.\end{aligned}$$

Using A and B from above and expanding $(\sum k)^2$, this becomes

$$\begin{aligned}\sigma_{\bar{k}}^2 = \quad & \frac{1}{N^2}(E[k_1^2] + E[k_2^2] + \ldots + E[k_N^2] + \sum_{i \neq j} E[k_i k_j]) \\ - \quad & \frac{1}{N^2}(E[k_1]^2 + E[k_2]^2 + \ldots + E[k_N]^2 + \sum_{i \neq j} E[k_i]E[k_j]) \,.\end{aligned}$$

Regrouping like terms gives

$$\begin{aligned}\sigma_{\bar{k}}^2 = \quad & \frac{1}{N^2}\{(E[k_1^2] - E[k_1]^2) + (E[k_2^2] - E[k_2]^2) + \ldots + (E[k_N^2] - E[k_N]^2)\} \\ + \quad & \frac{1}{N^2}\sum_{i \neq j}\{E[k_i k_j] - E[k_i]E[k_j]\} \,.\end{aligned}$$

Now, using Eq. A.3 for each k_i, we get

$$\begin{aligned}\sigma_{\bar{k}}^2 = \quad & \frac{1}{N^2}(\sigma_{k_1}^2 + \sigma_{k_2}^2 + \ldots + \sigma_{k_N}^2) \\ + \quad & \frac{1}{N^2}(\sum_{i \neq j} \sigma_{k_i k_j} - \sigma_{k_i}\sigma_{k_j}) \,.\end{aligned}$$

As k_i and k_j are independent distributions from the same parent distribution, using D and E we have

$$\sigma_{\bar{k}}^2 = \frac{1}{N^2}(N\sigma_k^2) + \frac{1}{N^2}(0)$$

which finally reduces to

$$\sigma_{\bar{k}}^2 = \frac{1}{N}\sigma_k^2 \tag{A.4}$$

Plugging this result and $\sigma_{N_{ev}} = \sqrt{N_{ev}}$ into Eq. A.2, we find

$$\sigma_N^2 = N_{ev}\sigma_k^2 + \bar{k}^2 N_{ev} \,. \tag{A.5}$$

Now, using $\sigma_k^2 + \bar{k}^2 = \bar{k^2}$ (a variant of Eq. A.3) and the fact that $N_{ev} = \frac{N}{k}$, we have

$$\sigma_N = \sqrt{\frac{\bar{k^2}}{\bar{k}} N} \,. \tag{A.6}$$

A.2 Relations between Longitudinal Spin Parity Violating Asymmetries

Other parity violating double longitudinal asymmetries have been calculated in the past as a check on our data, namely

$$A_{LL}^{++vs--} = \frac{\sigma_{++} - \sigma_{--}}{\sigma_{++} + \sigma_{--}} \tag{A.7}$$

$$A_{LL}^{+-vs-+} = \frac{\sigma_{+-} - \sigma_{-+}}{\sigma_{+-} + \sigma_{-+}} \,. \tag{A.8}$$

From Fig. 4.14, one can see that if in (a) we consider two positive helicity protons interacting, the result after applying parity and rotation in (d) is two negative helicity protons interacting. Any difference measured between (a) and (d) is parity violating, and so, as the strong force does not violate parity, Eq. A.7 must be zero. The same argument holds for Eq. A.8.

As there are four independent variables (σ_{++}, σ_{+-}, σ_{-+} and σ_{--}), there are four independent calculable qualities: total cross section ($\sigma_{++} + \sigma_{+-} + \sigma_{-+} + \sigma_{--}$), A_{LL} (the ratio of Eq. 1.27 and 1.28) and single spin asymmetry A_L for each beam. This is clearer if we rewrite Eq. 7.1 as a function of the four independent variables separately for the two beams:

$$A_L^{blue} = -\frac{\sigma_{++} + \sigma_{+-} - \sigma_{--} - \sigma_{-+}}{\sigma_{++} + \sigma_{+-} + \sigma_{--} + \sigma_{-+}} \tag{A.9}$$

$$A_L^{yellow} = -\frac{\sigma_{++} + \sigma_{-+} - \sigma_{--} - \sigma_{+-}}{\sigma_{++} + \sigma_{-+} + \sigma_{--} + \sigma_{+-}} \,. \tag{A.10}$$

Adding (subtracting) Eq. A.9 and Eq. A.10 gives Eq. A.7 (Eq. A.8) scaled by a ratio of sums of cross sections. Thus, A_{LL}^{++vs--} and A_{LL}^{+-vs-+} are not independent quantities.

Therefore, we do not calculate these asymmetries as they contain no new

information.

A.3 Relation between Asymmetries in FBF and Bunch Fitting Methods

In Chapters 4.1 and 6, two different methods for measuring an asymmetry are used. In Bunch Fitting, the ratio of yields to luminosity,

$$r(i) = \frac{N(i)}{L(i)} \ , \tag{A.11}$$

is fit with Eq. 4.10:

$$r(i) = c[1 \pm \epsilon_{BF}] \ . \tag{A.12}$$

Note that the form is written in a simplified manner where the $\pm$ sign depends on the spin state of the bunch i. In the Fill by Fill (FBF) method, the asymmetry is measured using Eq. 1.35, which we rewrite here ignoring polarization and defining two spin states '+' and '−' for simplicity:

$$\epsilon_{FBF} = \frac{\frac{N^+}{L^+} - \frac{N^-}{L^-}}{\frac{N^+}{L^+} + \frac{N^-}{L^-}} \tag{A.13}$$

In this section, we show that the ϵ_{BF} and ϵ_{FBF} are mathematically the same, allowing the two methods to be used interchangeably as needed.

Equating the right sides of Eq. A.11 and A.12, and multiplying by $L(i)$, we have

$$N^{\pm}(i) = c[1 \pm \epsilon_{BF}]L^{\pm}(i) \ . \tag{A.14}$$

For Eq. A.13, we are interested in the ratio N/L for the two spin states, where N and L are summed over all crossings. Therefore,

$$\begin{aligned} \frac{N^+}{L^+} &= \frac{\sum_i N^+(i)}{\sum_i L^+(i)} \\ &= \frac{\sum_i c[1+\epsilon_{BF}]L^+(i)}{\sum_i L^+(i)} \\ &= \frac{c[1+\epsilon_{BF}]\sum_i L^+(i)}{\sum_i L^+(i)} \\ &= c[1+\epsilon_{BF}] \ . \end{aligned} \tag{A.15}$$

Similarly

$$\frac{N^-}{L^-} = c[1 - \epsilon_{BF}] \tag{A.16}$$

and so Eq. A.13 becomes

$$\begin{aligned} \epsilon_{FBF} &= \frac{c[1 + \epsilon_{BF}] - c[1 - \epsilon_{BF}]}{c[1 + \epsilon_{BF}] + c[1 - \epsilon_{BF}]} \\ &= \frac{2\epsilon_{BF}}{2} \\ &= \epsilon_{BF} \ . \end{aligned} \tag{A.17}$$

Appendix B

Data Tables

Table B.1: Number of non-edge masked towers (hot, dead, uncalibrated and their neighbors) and edge towers from warn map study in Run5. The number in parenthesis is the percentage of the total.

sector	masked towers	edge towers	total
W0	246 (9%)	212 (8%)	2592
W1	213 (8%)	212 (8%)	2592
W2	256 (10%)	212 (8%)	2592
W3	515 (20%)	212 (8%)	2592
E0	864 (18%)	284 (6%)	4608
E1	648 (14%)	284 (6%)	4608
E2	484 (19%)	212 (8%)	2592
E3	343 (13%)	212 (8%)	2592
PbSc	2057 (13%)	1272 (8%)	15552
PbGl	1512 (16%)	568 (6%)	9216
Total	3569 (14%)	1840 (7%)	24768

Table B.2: Number of non-edge masked towers (hot, dead, uncalibrated and their neighbors) and edge towers from warn map study in Run6. The number in parenthesis is the percentage of the total.

sector	masked towers	edge towers	total
W0	248 (10%)	212 (8%)	2592
W1	274 (11%)	212 (8%)	2592
W2	306 (12%)	212 (8%)	2592
W3	498 (19%)	212 (8%)	2592
E0	1010 (22%)	284 (6%)	4608
E1	769 (17%)	284 (6%)	4608
E2	445 (17%)	212 (8%)	2592
E3	433 (17%)	212 (8%)	2592
PbSc	2204 (14%)	1272 (8%)	15552
PbGl	1779 (19%)	568 (6%)	9216
Total	3983 (15%)	1840 (7%)	24768

Table B.3: π^0 shower shape cut for Run5: Efficiency, Background Suppression, and remaining background fraction for 10 p_T bins above 1 GeV/c, separately for PbSc and PbGl.

	efficiency (%)		BG suppress (%)		BG cont. (%)	
p_T (GeV)	PbSc	PbGl	PbSc	PbGl	PbSc	PbGl
1.00-1.50	94	94	42	22	63	36
1.50-2.00	94	93	33	24	44	23
2.00-2.50	96	93	24	24	28	16
2.50-3.00	96	93	20	23	19	12
3.00-3.50	96	93	18	22	15	10
3.50-4.00	96	93	18	20	13	9
4.00-5.00	95	96	19	18	11	12
5.00-6.00	96	94	20	23	11	8
6.00-7.00	96	95	23	30	11	8
7.00-9.00	99	97	37	30	10	10

Table B.4: π^0 shower shape cut for Run6: Efficiency, Background Suppression, and remaining background fraction for 11 p_T bins above 1 GeV/c, separately for PbSc and PbGl.

	efficiency (%)		BG suppress (%)		BG cont. (%)	
p_T (GeV)	PbSc	PbGl	PbSc	PbGl	PbSc	PbGl
1.00-1.50	95	94	42	23	63	36
1.50-2.00	95	93	33	24	44	24
2.00-2.50	96	93	24	24	29	17
2.50-3.00	96	93	20	24	20	13
3.00-3.50	96	93	18	23	15	11
3.50-4.00	96	93	18	22	13	9
4.00-5.00	96	96	19	19	11	11
5.00-6.00	96	94	20	23	11	8
6.00-7.00	96	95	24	30	11	7
7.00-9.00	97	97	35	30	9	10
9.00-12.00	97	96	46	53	9	6

Table B.5: π^0 Time of Flight cut in Run5: Efficiency, Background Suppression, and remaining background fraction for 10 p_T bins above 1 GeV/c, separately for PbSc and PbGl.

	efficiency (%)		BG suppress (%)		BG cont. (%)	
p_T (GeV)	PbSc	PbGl	PbSc	PbGl	PbSc	PbGl
1.0 - 1.5	85	92	38	26	56	32
1.5 - 2.0	91	95	30	20	38	21
2.0 - 2.5	95	97	23	16	24	15
2.5 - 3.0	97	98	20	14	17	11
3.0 - 3.5	98	98	19	13	13	9
3.5 - 4.0	98	99	18	12	12	9
4.0 - 5.0	99	98	16	17	10	10
5.0 - 6.0	98	99	15	11	10	8
6.0 - 7.0	99	99	13	10	9	7
7.0 - 9.0	99	98	13	10	8	10

Table B.6: π^0 Time of Flight cut in Run6: Efficiency, Background Suppression, and remaining background fraction for 11 p_T bins above 1 GeV/c, separately for PbSc and PbGl.

	efficiency (%)		BG suppress (%)		BG cont. (%)	
p_T (GeV)	PbSc	PbGl	PbSc	PbGl	PbSc	PbGl
1.00-1.50	84	91	42	23	54	32
1.50-2.00	89	93	35	19	36	21
2.00-2.50	94	94	29	17	23	15
2.50-3.00	95	94	25	15	16	12
3.00-3.50	96	95	23	14	12	10
3.50-4.00	97	95	22	13	11	8
4.00-5.00	97	97	18	20	9	10
5.00-6.00	97	95	18	11	9	7
6.00-7.00	97	95	16	12	9	7
7.00-9.00	97	98	15	15	8	9
9.00-12.00	98	95	17	18	7	5

Table B.7: π^0 charge veto cut in Run5: Efficiency, Background Suppression, and remaining background fraction for 10 p_T bins above 1 GeV/c, separately for PbSc and PbGl.

	efficiency (%)		BG suppress (%)		BG cont. (%)	
p_T (GeV)	PbSc	PbGl	PbSc	PbGl	PbSc	PbGl
1.0 - 1.5	98	99	38	20	45	27
1.5 - 2.0	98	99	34	17	29	18
2.0 - 2.5	98	100	30	14	19	13
2.5 - 3.0	98	100	26	13	13	10
3.0 - 3.5	99	100	24	11	11	8
3.5 - 4.0	99	100	23	11	9	8
4.0 - 5.0	99	99	19	21	8	8
5.0 - 6.0	99	100	20	10	8	7
6.0 - 7.0	99	100	19	11	8	7
7.0 - 9.0	99	100	20	20	8	8

Table B.8: π^0 charge veto cut in Run6: Efficiency, Background Suppression, and remaining background fraction for 11 p_T bins above 1 GeV/c, separately for PbSc and PbGl.

	efficiency (%)		BG suppress (%)		BG cont. (%)	
p_T (GeV)	PbSc	PbGl	PbSc	PbGl	PbSc	PbGl
1.00-1.50	97	97	37	21	43	27
1.50-2.00	97	97	33	17	28	18
2.00-2.50	97	98	28	15	18	13
2.50-3.00	98	98	25	14	13	10
3.00-3.50	98	99	23	12	10	9
3.50-4.00	98	99	22	11	8	7
4.00-5.00	99	98	19	20	7	8
5.00-6.00	99	99	20	10	8	6
6.00-7.00	99	99	20	12	7	6
7.00-9.00	99	99	17	18	7	7
9.00-12.00	99	99	21	5	6	5

Table B.9: Two photon yield in signal and background mass ranges as well as background percentage (r in Eq. 6.2) for Run5 ERT triggered events.

p_T bin (GeV/c)	peak yield (112-162 MeV/c^2)	background yield (47-97 + 177-227 MeV/c^2)	background %
1.0-1.5	17061814	11165470	0.373
1.5-2.0	22481562	10270055	0.261
2.0-2.5	13890459	4194302	0.175
2.5-3.0	6230789	1339250	0.127
3.0-3.5	2595443	445468	0.102
3.5-4.0	1093299	166402	0.089
4.0-5.0	713390	101369	0.084
5.0-6.0	175797	23818	0.081
6.0-7.0	53718	7128	0.081
7.0-9.0	28161	3453	0.079

Table B.10: Two photon yield in signal and background mass ranges as well as background percentage (r in Eq. 6.2) for Run6 ERT triggered events.

p_T bin (GeV/c)	peak yield (112-162 MeV/c^2)	background yield (47-97 + 177-227 MeV/c^2)	background %
1.00-1.50	21081329	14336413	0.387
1.50-2.00	33609294	15705719	0.266
2.00-2.50	23655949	7264167	0.178
2.50-3.00	11656472	2515618	0.128
3.00-3.50	5165175	878295	0.102
3.50-4.00	2265137	334442	0.089
4.00-5.00	1515597	204589	0.082
5.00-6.00	380058	48938	0.080
6.00-7.00	117689	14651	0.078
7.00-9.00	61413	7335	0.077
9.00-12.00	14418	1540	0.063

Table B.11: Charged pion yields and background percentage estimated with Eq. 5.9 with a Type 2 (Eq. 5.12) background.

	π^+		π^-	
p_T bin (GeV/c)	Yield	Background %	Yield	Background %
5-6	9589	1.9	9289	1.8
6-7	9108	2.5	7563	2.0
7-10	7399	3.3	5887	2.6

Table B.12: $k^2_{enhance}$ for N^{π^0+BG} (N^{BG}) from Run5.

p_T bin (GeV/c)	PbSc	PbGl	Combined (PbSc+PbGl)
0.5-0.75	1.21 (1.29)	1.06 (1.09)	1.17 (1.24)
0.75-1.0	1.15 (1.22)	1.05 (1.09)	1.11 (1.17)
1.0-1.5	1.14 (1.21)	1.07 (1.11)	1.12 (1.19)
1.5-2.0	1.11 (1.18)	1.05 (1.10)	1.10 (1.17)
2.0-2.5	1.07 (1.15)	1.03 (1.09)	1.06 (1.15)
2.5-3.0	1.04 (1.13)	1.02 (1.08)	1.04 (1.13)
3.0-3.5	1.03 (1.12)	1.02 (1.08)	1.03 (1.12)
3.5-4.0	1.03 (1.11)	1.02 (1.07)	1.03 (1.11)
4.0-5.0	1.04 (1.15)	1.02 (1.11)	1.03 (1.15)
5.0-6.0	1.03 (1.14)	1.02 (1.10)	1.03 (1.14)
6.0-7.0	1.03 (1.16)	1.02 (1.11)	1.02 (1.15)
7.0-9.0	1.03 (1.17)	1.03 (1.15)	1.03 (1.16)

Table B.13: $k^2_{enhance}$ for N^{π^0+BG} (N^{BG}) from Run6.

p_T bin (GeV/c)	PbSc	PbGl	Combined (PbSc+PbGl)
1.0-1.5	1.13 (1.20)	1.06 (1.10)	1.11 (1.18)
1.5-2.0	1.10 (1.17)	1.05 (1.09)	1.09 (1.16)
2.0-2.5	1.06 (1.14)	1.03 (1.08)	1.06 (1.14)
2.5-3.0	1.04 (1.12)	1.02 (1.08)	1.04 (1.12)
3.0-3.5	1.03 (1.11)	1.02 (1.08)	1.03 (1.11)
3.5-4.0	1.03 (1.10)	1.02 (1.07)	1.02 (1.10)
4.0-5.0	1.03 (1.14)	1.02 (1.11)	1.03 (1.14)
5.0-6.0	1.03 (1.14)	1.02 (1.09)	1.03 (1.13)
6.0-7.0	1.03 (1.14)	1.02 (1.07)	1.02 (1.13)
7.0-9.0	1.04 (1.14)	1.03 (1.12)	1.03 (1.14)
9.0-12.0	1.04 (1.15)	1.03 (1.07)	1.04 (1.14)

Table B.14: Run5 Single Spin Asymmetry A_L values and statistical uncertainties for π^0 for the Blue and Yellow beam, as well as the combined result, using ERT triggered events.

p_T bin (GeV/c)	Blue Beam (10^{-3})	Yellow Beam (10^{-3})	Combined (10^{-3})
1.0-1.5	1.3 ± 1.1	0.16 ± 0.95	0.71 ± 0.70
1.5-2.0	-0.54 ± 0.73	0.61 ± 0.68	0.07 ± 0.50
2.0-2.5	-0.33 ± 0.80	1.00 ± 0.75	0.38 ± 0.55
2.5-3.0	0.2 ± 1.1	-0.8 ± 1.0	0.30 ± 0.75
3.0-3.5	1.9 ± 1.6	-1.9 ± 1.5	-0.2 ± 1.1
3.5-4.0	-4.4 ± 2.5	1.3 ± 2.3	-1.4 ± 1.7
4.0-5.0	-1.8 ± 3.1	0.0 ± 2.9	-0.8 ± 2.1
5.0-6.0	-3.4 ± 6.1	-3.4 ± 5.7	-3.4 ± 4.2
6.0-7.0	-11 ± 11	-9 ± 10	-10.0 ± 7.5
7.0-9.0	-1 ± 15	3 ± 14	1 ± 10

Table B.15: Run6 Single Spin Asymmetry A_L values and statistical uncertainties for π^0 for the Blue and Yellow beam, as well as the combined result, using ERT triggered events.

p_T bin (GeV/c)	Blue Beam (10^{-3})	Yellow Beam (10^{-3})	Combined (10^{-3})
1.00-1.50	-0.78±0.73	-0.65±0.74	-0.72±0.52
1.50-2.00	0.51±0.46	-0.65±0.47	-0.06±0.33
2.00-2.50	-0.14±0.47	-0.55±0.48	-0.34±0.34
2.50-3.00	-0.33±0.62	-0.27±0.63	-0.30±0.44
3.00-3.50	1.80±0.89	-0.43±0.91	0.71±0.64
3.50-4.00	2.7±1.3	1.2±1.4	1.98±0.94
4.00-5.00	-2.4±1.6	-1.0±1.6	-1.7±1.1
5.00-6.00	-0.5±3.2	-5.1±3.3	-2.7±2.3
6.00-7.00	3.5±5.7	1.3±5.8	2.4±4.1
7.00-9.00	-0.2±7.9	-15.0±8.1	-7.4±5.7
9.00-12.00	16±16	18±16	17±11

Table B.16: Run5 Single Spin Asymmetry A_L values and statistical uncertainties for π^+ and π^- for the Blue and Yellow beam.

	π^+ A_L (10^{-3})		π^- A_L (10^{-3})	
p_T bin (GeV/c)	Blue Beam	Yellow Beam	Blue Beam	Yellow Beam
5-6	2±25	15±23	12±25	21±24
6-7	5±26	-25±24	-9±28	1±26
7-10	16±29	2±27	4±33	32±31

Table B.17: π^0 A_{TT} values and statistical uncertainties from Run5. The width of the p_T bin is listed in the first column while the average p_T ($\langle p_T \rangle$) for each bin is shown in the second.

p_T bin (GeV/c)	$\langle p_T \rangle$ (GeV/c)	$A_{TT}^{\pi^0}$ (10^{-3})	$\sigma_{A_{TT}^{\pi^0}}$ (10^{-3})
1.0-1.5	1.29	-0.4	8.9
1.5-2.0	1.75	9.8	6.2
2.0-2.5	2.22	-2.4	6.8
2.5-3.0	2.72	3.9	9.4
3.0-3.5	3.21	3	14
3.5-4.0	3.71	15	21
4.0-5.0	4.38	-20	26
5.0-6.0	5.40	-4	52
6.0-7.0	6.41	18	93

Appendix C

Functional Forms Used in Fits of Polarized PDFs

In this appendix, the functional forms used in the different fits to polarized DIS discussed in Chapters 1 and 8 are given. Unless otherwise stated, all fits are based on the asymmetry measured in polarized DIS.

C.1 Common Assumptions

In most of these fits, due to the limited amount of polarized DIS data, two assumptions are standard: a symmetric (polarized) sea and SU(3) symmetry. The symmetric sea assumes that all sea quark distributions are the same, i.e.

$$\Delta\bar{q} = \Delta\bar{u} = \Delta u_{\text{sea}} = \Delta\bar{d} = \Delta d_{\text{sea}} = \Delta\bar{s} = \Delta s \ . \tag{C.1}$$

Note that this has been shown not to hold in recent unpolarized PDF fits [18, 98].

SU(3) symmetry assumes that the up, down and strange quark polarizations are related through three separate equations:

$$a_0 = \Delta\Sigma = \Delta u + \Delta\bar{u} + \Delta d + \Delta\bar{d} + \Delta s + \Delta\bar{s}, \tag{C.2}$$

$$a_3 = \Delta u + \Delta\bar{u} - \Delta d - \Delta\bar{d}, \tag{C.3}$$

$$a_8 = \Delta u + \Delta\bar{u} + \Delta d + \Delta\bar{d} - 2\Delta s - 2\Delta\bar{s}. \tag{C.4}$$

a_3 can be determined from neutron beta decay, a_8 can be determined from Hyperon beta decay, and a_0 can be determined from g_1, which is a linear combination of a_0, a_3 and a_8, if SU(3) symmetry holds. In general, the use of SU(3) symmetry is normally taken as fixing the first moment of the polarized

up and down quark distributions, Δu and Δd. Note that if the symmetric sea is assumed, Eq. C.3 and C.4 are the redundant. Hence the symmetric sea assumption effectively assumes SU(3) symmetry.

A third constraint in most of the fits is due to positivity, defined in Eq. 8.3. Normally, this condition is imposed at the initial scale and through evolution would not be violated. This condition can be imposed as a constraint during the fit, or used as a requirement after the fit. The effects of using positivity as a constraint are considered in Chapter 8.6.6

In general, groups fitting the unpolarized PDFs do not use data with $Q^2 <$ 4 GeV^2. However, due to the small amount of polarized DIS data with $Q^2 >$ 4 GeV^2, all fits discussed here use data with $Q^2 > 1$ GeV^2.

Note that the standard method for calculating the uncertainties for the data points is to simply add the statistical and systematic errors in quadrature for all data points, regardless of the correlation in systematic uncertainties between points.[1] This certainly overestimates the error, and leads to a smaller χ^2 value than if the errors were correctly handled. Therefore, the exact χ^2 value, and its closeness to one is not very meaningful. Instead, relative differences are more important.

C.2 GRSV

Glück, Reya, Stratmann, and Vogelsang (GRSV) [99] performed two NLO pQCD fits to the polarized DIS data as of 2000 with two different sets of assumptions: "standard", with a symmetric sea and "valence", with a model dependent broken sea, in which $\Delta s = \Delta\bar{s} = 0$ for all x at the input scale. Here we consider only the "standard" scenario.

The functional forms used in the "standard" GRSV polarized DIS fit [99] are

$$x\Delta u(x,\mu^2) = N_u x^{\alpha_u}(1-x)^{\beta_u} u(x,\mu^2)_{\rm GRV} \quad \text{(C.5)}$$

$$x\Delta d(x,\mu^2) = N_d x^{\alpha_d}(1-x)^{\beta_d} d(x,\mu^2)_{\rm GRV} \quad \text{(C.6)}$$

$$x\Delta \bar{q}(x,\mu^2) = N_{\bar{q}} x^{\alpha_{\bar{q}}}(1-x)^{\beta_{\bar{q}}} \bar{q}(x,\mu^2)_{\rm GRV} \quad \text{(C.7)}$$

$$x\Delta g(x,\mu^2) = N_g x^{\alpha_g}(1-x)^{\beta_g} g(x,\mu^2)_{\rm GRV} \quad \text{(C.8)}$$

where N_f, α_f and β_f are fit parameters, and $f(x,\mu^2)_{\rm GRV}$ is taken to be the unpolarized PDF fit result from GRV98 [100]. The GRSV fit is done at an input scale of $\mu^2 = 0.40$ GeV^2.

[1] A number of the papers indicate that the exact point to point correlations are not always clearly defined. However, it also makes the analysis easier.

From Eq. C.2-C.4, the size of the u and d distributions are fixed. β_d and $\beta_{\bar{q}}$ were found to be consistent with zero, and were fixed to zero after initial tests [101].

C.3 BB

Blümlein and Böttcher (BB) [102] performed two NLO pQCD fits to the polarized DIS data as of 2002 with a single set of functional forms:

$$x\Delta u(x,\mu^2)_v = \eta_u A_u x^{\alpha_u}(1-x)^{\beta_u}(1+\gamma_u x+\rho_u x^{1/2}) \quad \text{(C.9)}$$

$$x\Delta d(x,\mu^2)_v = \eta_d A_d x^{\alpha_d}(1-x)^{\beta_d}(1+\gamma_d x+\rho_d x^{1/2}) \quad \text{(C.10)}$$

$$x\Delta \bar{q}(x,\mu^2) = \eta_{\bar{q}} A_{\bar{q}} x^{\alpha_{\bar{q}}}(1-x)^{\beta_{\bar{q}}}(1+\gamma_{\bar{q}} x+\rho_{\bar{q}} x^{1/2}) \quad \text{(C.11)}$$

$$x\Delta g(x,\mu^2) = \eta_g A_g x^{\alpha_g}(1-x)^{\beta_g}(1+\gamma_g x+\rho_g x^{1/2}) \quad \text{(C.12)}$$

where η_f, α_f, β_f, γ_f and ρ_f are fit parameters, and A_f are normalization constants set such that η_f give the first moment of the distribution, $\int_0^1 dx\Delta f(x,Q_0^2)$.

A symmetric sea and SU(3) symmetry were assumed. A number of parameters were fixed in the fits, due to the insensitivity of the data: $\rho_u = \rho_d = 0$, $\gamma_{\bar{q}} = \rho_{\bar{q}} = 0$, and $\gamma_g = \rho_g = 0$, while $\Lambda_{\rm QCD}$ was taken as a parameter in the fit. Also, varying γ_u, γ_d, $\beta_{\bar{q}}$ and β_g had little impact on the χ^2, and so were fixed after the initial fit. Similarly, the sea quark and gluon low x behaviors were related using $\alpha_g = \alpha_{\bar{q}} + C$. Two separate fits were performed, using $C = 0.9$ in the "iset3" fit and $C = 0.5$ in the "iset4" fit. A positivity constraint was not applied for Δu or Δd. For $\Delta\bar{q}$ and Δg, positivity was not strictly enforced, but the fixed parameters were set such that positivity should be preserved by assuming that $\beta_{\bar{q}}/\beta_g|_{\rm pol} = \beta_{\bar{q}}/\beta_g|_{\rm unpol}$, using [100].

Note that, for the χ^2 determination, BB used statistical errors only (instead of the quadrature sum of statistical and systematic) but did allow for normalization shifts within the quoted normalization uncertainty range for each data set. In general, this accounts for a significant part of the systematic uncertainties, and should be a more correct approach.

C.4 DNS

De Florian, Navarro and Sassot (DNS) [89] performed a NLO pQCD fit to the polarized (inclusive) DIS and SIDIS data as of 2005 with the following

functional forms:

$$
\begin{aligned}
x(\Delta q(x,Q^2)+\Delta\bar{q}(x,Q^2)) &= \eta_q A_q x^{\alpha_q}(1-x)^{\beta_q}(1+\gamma_q x^{\delta_q})\,, \quad q=u,d && \text{(C.13)}\\
x\Delta\bar{q}(x,Q^2) &= \eta_{\bar{q}} A_{\bar{q}} x^{\alpha_{\bar{q}}}(1-x)^{\beta_{\bar{q}}}\,, \quad \bar{q}=\bar{u},\bar{d} && \text{(C.14)}\\
x(\Delta s(x,Q^2)+\Delta\bar{s}(x,Q^2)) &= \eta_s A_s x^{\alpha_s}(1-x)^{\beta_s} && \text{(C.15)}\\
x\Delta g(x,Q^2) &= \eta_g A_g x^{\alpha_g}(1-x)^{\beta_g} && \text{(C.16)}
\end{aligned}
$$

where η_f, α_f, β_f, γ_f and δ_f are fit parameters, and A_f are normalization constants such that η_f give the first moment of the distribution. Neither the symmetric sea nor SU(3) symmetry are assumed. Instead, two extra parameters are used to account for the breaking of these symmetries.

DNS fixed the large x anti quark distributions, requiring that $\beta_s{=}\beta_{\bar{u}}{=}\beta_{\bar{d}}$. The other major constraint was positivity, which was imposed in the fit by using MRST02 unpolarized distributions [98]. As is evident from the paper, this assumption strongly constrains the gluon polarization indirectly through the sea quark positivity constraint. In order to account for fragmentation to final state hadrons in the SIDIS data, FFs were required. Two sets of FFs, Kretzer [90] and KKP, were used and the χ^2 were essentially the same (431 and 436, respectively, for 458 degrees of freedom).

C.5 LSS

Leader, Sidorov, and Stamenov (LSS) [103] performed four different NLO pQCD fits to the polarized DIS data as of 2006. The functional forms used are

$$
\begin{aligned}
x\Delta u_v(x,Q_0^2) &= \eta_u A_u x^{\alpha_u} x u_v(x,Q_0^2)_{\mathrm{MRST}} && \text{(C.17)}\\
x\Delta d_v(x,Q_0^2) &= \eta_d A_d x^{\alpha_d} x d_v(x,Q_0^2)_{\mathrm{MRST}} && \text{(C.18)}\\
x\Delta s(x,Q_0^2) &= \eta_s A_s x^{\alpha_s} x s(x,Q_0^2)_{\mathrm{MRST}} && \text{(C.19)}\\
x\Delta g(x,Q_0^2) &= \eta_g A_g x^{\alpha_g} x g(x,Q_0^2)_{\mathrm{MRST}}\,. && \text{(C.20)}
\end{aligned}
$$

where η_f and α_f are fit parameters, A_f is a normalization constant such that η_f is the first moment of Δf, and $f(x,Q^2)_{\mathrm{MRST}}$ is taken to be the unpolarized PDF fit result from MRST99 [104]. A symmetric sea and SU(3) symmetry are assumed.

LSS fit the data using either the normal NLO pQCD description of the g_1 structure function in "Set1" or an extended form with an additional theoretical term to account for possible high twist contributions in "Set2". With each set, either the $\overline{\mathrm{MS}}$ or JET factorization scheme was used. In the present study, only

"Set1" with the $\overline{\text{MS}}$ factorization scheme is used. For details on the differences in these schemes, or discussion of the possible higher twist effects, see [103].

Due to the assumption of SU(3) symmetry, η_u and η_d were constrained. In addition, LSS used the MRST02(NLO) unpolarized parton distributions [98] as a positivity constraint in the fit. Note that, as the functional forms of LSS do not have a $(1-x)^\beta$ factor, the large x behavior is assumed to be the same as the unpolarized function.

C.6 GS-A,B,C

Gehrmann and Stirling (GS) [105] did three different fits to very limited polarized DIS data available in 1996, using one set of functional forms:

$$x\Delta u_v(x,Q_0^2) = \eta_u A_u x^{\alpha_u}(1-x)^{\beta_u}(1+\gamma_u x+\rho_u x^{1/2}) \quad \text{(C.21)}$$
$$x\Delta d_v(x,Q_0^2) = \eta_d A_d x^{\alpha_d}(1-x)^{\beta_d}(1+\gamma_d x+\rho_d x^{1/2}) \quad \text{(C.22)}$$
$$x\Delta \bar{q}(x,Q_0^2) = \eta_{\bar{q}} A_{\bar{q}} x^{\alpha_{\bar{q}}}(1-x)^{\beta_{\bar{q}}}(1+\gamma_{\bar{q}} x+\rho_{\bar{q}} x^{1/2}) \quad \text{(C.23)}$$
$$x\Delta g(x,Q_0^2) = \eta_g A_g x^{\alpha_g}(1-x)^{\beta_g}(1+\gamma_g x+\rho_g x^{1/2}) \; . \quad \text{(C.24)}$$

where η_f, α_f, β_f, γ_f and ρ_f are fit parameters, and A_f is a normalization constant such that η_f is the first moment of Δf. Like the other fits, Eq. C.1 and SU(3) symmetry are assumed. The functional form in this case can allow for a zero crossing at

$$x = \frac{1}{2\gamma^2}\left[\rho^2 - 2\gamma \pm \rho\sqrt{\rho^2-4\gamma}\right] . \quad \text{(C.25)}$$

In the case where γ=0, then there is a node at

$$x = \frac{1}{\rho^2}. \quad \text{(C.26)}$$

GS defined three different fits based on different values of γ_g and ρ_g:

$$\begin{aligned} \text{GS-A: } \gamma_g = 0, \quad \rho_g = 0 \; , \\ \text{GS-B: } \gamma_g = 1, \quad \rho_g = -2 \; , \\ \text{GS-C: } \gamma_g = 0, \quad \rho_g = -3 \; . \end{aligned} \quad \text{(C.27)}$$

while GS-A and GS-B do not have nodes in $0<x<1$, GS-C has a node fixed at $x=\frac{1}{9}$ at the input scale.

Based on SU(3) symmetry, η_u and η_d are fixed, as are γ_g and ρ_g by Eq. C.28. In addition, in all three GS fits, $\eta_{\bar{q}}$, β_u and β_d are fixed, and it is assumed that

$\alpha_g = \alpha_{\bar{q}}$. A positivity constraint was applied, using the GRV95 unpolarized PDFs, which limited the size of β_g and $\beta_{\bar{q}}$, and in particular $\gamma_d + \rho_d$[2], in the fit.

C.7 Summary Table

Group	Year	# of par	constraints		
			SU(3)	sym. sea	positivity
GRSV	2002	8	Y	Y	Y
BB	2002	7	Y	Y	N
LSS	2005	6	Y	Y	Y
DNS	2006	20	N	N	Y
GS	1996	12	Y	Y	Y

Table C.1: Information on number of parameters used in the fits discussed above, as well as whether other constraints were applied.

[2] As $x \to 1$, $(1+\gamma x+\rho x^{\frac{1}{2}}) \to (1+\gamma+\rho)$ which simply scales the distribution. Therefore the size of these parameters are limited if positivity is imposed.

Bibliography

[1] D. H. Perkins. *Introduction to High Energy Physics*. Cambridge Univ. Pr., 2000.

[2] F. Halzen and A. D. Martin. *Quarks & Leptons: An Introductory Course in Modern Particle Physics*. John Wiley & Sons, Inc., 1984.

[3] D. Griffiths. *Introduction to Elementary Particles*. John Wiley & Sons, Inc., 1987.

[4] M. E. Peskin and D. V. Schroeder. *An Introduction to Quantum Field Theory*. Westview Pr., 1995.

[5] G. Sterman. *An Introduction to Quantum Field Theory*. Cambridge Univ. Pr., 1993.

[6] B. Jäger, A. Schäfer, M. Stratmann, and W. Vogelsang. Next-to-leading order QCD corrections to high-p_T pion production in longitudinally polarized pp collisions. *Phys. Rev.*, D67:054005, 2003.

[7] A. H. Mueller, editor. *Perturbative Quantum Chromodynamics*. World Scientific Publ., Singapore, 1989.

[8] B. A. Kniehl, G. Kramer, and B. Pötter. Testing the universality of fragmentation functions. *Nucl. Phys.*, B597:337–369, 2001.

[9] S. Albino, B. A. Kniehl, G. Kramer, and C. Sandoval. Confronting fragmentation function universality with single hadron inclusive production at HERA and e^+e^- colliders. *Phys. Rev.*, D75:034018, 2007.

[10] D. de Florian, R. Sassot, and M. Stratmann. Global analysis of fragmentation functions for pions and kaons and their uncertainties. *Phys. Rev.*, D75:114010, 2007.

[11] A. Airapetian et al. Quark helicity distributions in the nucleon for up, down, and strange quarks from semi-inclusive deep-inelastic scattering. *Phys. Rev.*, D71:012003, 2005.

[12] W. M. Yao et al. Review of particle physics. *J. Phys.*, G33:1–1232, 2006.

[13] V. N. Gribov and L. N. Lipatov. Deep inelastic *ep* scattering in perturbation theory. *Yad. Fiz.*, 15:781–807, 1972.

[14] Yu. L. Dokshitzer. Calculation of the structure functions for deep inelastic scattering and e^+e^- annihilation by perturbation theory in Quantum Chromodynamics. (in Russian). *Sov. Phys. JETP*, 46:641–653, 1977.

[15] G. Altarelli and G. Parisi. Asymptotic freedom in parton language. *Nucl. Phys.*, B126:298, 1977.

[16] A. D. Martin, W. J. Stirling, R. S. Thorne, and G. Watt. Update of parton distributions at NNLO. *Phys. Lett.*, B652:292–299, 2007. doi: 10.1016/j.physletb.2007.07.040.

[17] HEPDATA: The Durham HEP Databases, 2003. URL http://durpdg.dur.ac.uk/.

[18] J. Pumplin et al. New generation of parton distributions with uncertainties from global QCD analysis. *JHEP*, 07:012, 2002.

[19] S. D. Bass. The spin structure of the proton. *Rev. Mod. Phys.*, 77: 1257–1302, 2005.

[20] J. R. Ellis and R. L. Jaffe. A sum rule for deep inelastic electroproduction from polarized protons. *Phys. Rev.*, D9:1444, 1974. Erratum-ibid.D10:1669,1974.

[21] R. L. Jaffe and A. Manohar. The g_1 problem: deep inelastic electron scattering and the spin of the proton. *Nucl. Phys.*, B337:509–546, 1990.

[22] L. M. Sehgal. Angular momentum composition of the proton in the quark parton model. *Phys. Rev.*, D10:1663, 1974.

[23] M. J. Alguard et al. Deep inelastic scattering of polarized electrons by polarized protons. *Phys. Rev. Lett.*, 37:1261, 1976.

[24] M. J. Alguard et al. Deep inelastic *ep* asymmetry measurements and comparison with the Bjorken sum rule and models of the proton spin structure. *Phys. Rev. Lett.*, 41:70, 1978.

[25] G. Baum et al. A new measurement of deep inelastic e p asymmetries. *Phys. Rev. Lett.*, 51:1135, 1983.

[26] J. Ashman et al. A measurement of the spin asymmetry and determination of the structure function g_1 in deep inelastic muon proton scattering. *Phys. Lett.*, B206:364, 1988.

[27] J. Ashman et al. An investigation of the spin structure of the proton in deep inelastic scattering of polarized muons on polarized protons. *Nucl. Phys.*, B328:1, 1989.

[28] G. Altarelli and W. J. Stirling. Phenomenology of the anomalous gluon contribution to polarized leptoproduction. *Part. World.*, 1:40–52, 1989.

[29] G. Altarelli and G. G. Ross. The anomalous gluon contribution to polarized leptoproduction. *Phys. Lett.*, B212:391, 1988. doi: 10.1016/0370-2693(88)91335-4.

[30] R. D. Carlitz, J. C. Collins, and A. H. Mueller. The role of the axial anomaly in measuring spin dependent parton distributions. *Phys. Lett.*, B214:229, 1988. doi: 10.1016/0370-2693(88)91474-8.

[31] B. Adeva et al. Spin asymmetries A(1) and structure functions g1 of the proton and the deuteron from polarized high energy muon scattering. *Phys. Rev.*, D58:112001, 1998. doi: 10.1103/PhysRevD.58.112001.

[32] P. L. Anthony et al. Deep inelastic scattering of polarized electrons by polarized He-3 and the study of the neutron spin structure. *Phys. Rev.*, D54:6620–6650, 1996. doi: 10.1103/PhysRevD.54.6620.

[33] K. Abe et al. Measurements of R = sigma(L)/sigma(T) for $0.03 < x < 0.1$ and fit to world data. *Phys. Lett.*, B452:194–200, 1999. doi: 10.1016/S0370-2693(99)00244-0.

[34] P. L. Anthony et al. Measurements of the Q^2 dependence of the proton and neutron spin structure functions g1(p) and g1(n). *Phys. Lett.*, B493: 19–28, 2000. doi: 10.1016/S0370-2693(00)01014-5.

[35] A. Airapetian et al. Measurement of the proton spin structure function g1(p) with a pure hydrogen target. *Phys. Lett.*, B442:484–492, 1998. doi: 10.1016/S0370-2693(98)01341-0.

[36] M. Stratmann and W. Vogelsang. Exploring the polarization of gluons in the nucleon. *J. Phys. Conf. Ser.*, 69:012035, 2007. doi: 10.1088/1742-6596/69/1/012035.

[37] I. Alekseev et al. Polarized proton collider at RHIC. *Nucl. Instrum. Meth.*, A499:392–414, 2003. doi: 10.1016/S0168-9002(02)01946-0.

[38] T. Roser. Acceleration of polarized beams using multiple strong partial snakes. In *Proceedings of the 16th International Spin Physics Symposium (SPIN 2004)*, page 687, Singapore, 2005. World Scientific.

[39] I. Nakagawa et al. Run05 proton beam polarization measurements by pC-polarimeter. *RHIC/CAD Accelerator Physics Note*, 275, 2007.

[40] H. Okada et al. Measurement of the analyzing power in p p elastic scattering in the peak CNI region at RHIC. *Phys. Lett.*, B638:450–454, 2006. doi: 10.1016/j.physletb.2006.06.008.

[41] K. Adcox et al. PHENIX detector overview. *Nucl. Instrum. Meth.*, A499: 469–479, 2003.

[42] M. Allen et al. PHENIX inner detectors. *Nucl. Instrum. Meth.*, A499: 549–559, 2003.

[43] M. Aizawa et al. PHENIX central arm particle ID detectors. *Nucl. Instrum. Meth.*, A499:508–520, 2003.

[44] S. Abeytunge et al. Proposal for a Silicon Vertex Tracker (VTX) for the PHENIX experiment. *http://www.phenix.bnl.gov/WWW/publish/akiba/2006VTXReview/VTXProposal.pdf*, 2006.

[45] M. Allen et al. ZDC. *Nucl. Instrum. Meth.*, A470:488, 2001.

[46] M. Togawa. *Measurements of the leading neutron production in polarized pp collision at* $\sqrt{s} = 200$ *GeV*. PhD thesis, Kyoto Univ., 2008.

[47] L. Aphecetche et al. PHENIX calorimeter. *Nucl. Instrum. Meth.*, A499: 521–536, 2003.

[48] S. Belikov et al. Determination of the absolute luminosity for the proton-proton data at $\sqrt{s}$=200 GeV recorded by PHENIX during RHIC run-02. *PHENIX Analysis Note*, 184:1, 2003.

[49] S. S. Frank, C. L. Britton, A. L. Witenberg, and G. R. Young. Trigger circuits for the PHENIX electromagnetic calorimeter. *Nuclear Science Symposium, IEEE*, 1:680–684, 1997.

[50] S. S. Adler et al. PHENIX on-line systems. *Nucl. Instrum. Meth.*, A499: 560–592, 2003.

[51] S. H. Aronson et al. PHENIX magnet system. *Nucl. Instrum. Meth.*, A499:480–488, 2003. doi: 10.1016/S0168-9002(02)01951-4.

[52] K. Adcox et al. PHENIX central arm tracking detectors. *Nucl. Instrum. Meth.*, A499:489–507, 2003.

[53] Z. Fraenkel et al. A hadron blind detector for the PHENIX experiment at RHIC. *Nucl. Instrum. Meth.*, A546:466–480, 2005. doi: 10.1016/j.nima.2005.02.039.

[54] K. Tanida. Relative luminosity in Run3 pp. *PHENIX Analysis Note*, 222:1, 2003.

[55] A. Datta and D Kawall. Multiple collision effect on relative luminosity measurement at PHENIX. *Riken Accel. Prog. Rep.*, 41, 2008.

[56] M. Bai, A. U. Luccio, W. W. MacKay, T. Roser, and V. Ranjbar. RHIC spin flipper commissioning. *AIP Conf. Proc.*, 675:771–775, 2003.

[57] N. H. Buttimore, E. Gotsman, and E. Leader. Spin dependent phenomena induced by electromagnetic hadronic interference at high-energies. *Phys. Rev.*, D18:694–716, 1978. doi: 10.1103/PhysRevD.18.694.

[58] C. Bourrely and J. Soffer. On the size of the Coulomb - nuclear interference polarization in hadronic reactions at high-energy and large momentum transfer. *Nuovo Cim. Lett.*, 19:569, 1977.

[59] K. O. Eyser et al. Absolute polarization determination at RHIC in 2005. *RHIC/CAD Accelerator Physics Note*, 274, 2007.

[60] K. Boyle et al. Absolute polarization determination at RHIC in 2006. *RHIC/CAD Accelerator Physics Note*, preliminary, 2008.

[61] C. M. Camacho et al. Run06 proton beam polarization measurements by pC-polarimeter. *RHIC/CAD Accelerator Physics Note*, preliminary, 2008.

[62] O. Jinnouchi et al. Measurement of the analyzing power of proton-carbon elastic-scattering. 2004.

[63] M. Anselmino. Lectures at the ECT* doctoral training program on QCD Spin Physics, November 13-17, 2006.

[64] D. L. Adams et al. Analyzing power in inclusive π^+ and π^- production at high x_F with a 200 GeV polarized proton beam. *Phys. Lett.*, B264: 462–466, 1991.

[65] J. Adams et al. Cross sections and transverse single-spin asymmetries in forward neutral pion production from proton collisions at $\sqrt{s} = 200$ GeV. *Phys. Rev. Lett.*, 92:171801, 2004.

[66] I. Arsene et al. Single transverse spin asymmetries of identified charged hadrons in polarized p+p collisions at $\sqrt{s} = 62.4$ GeV. 2008.

[67] A. Bazilevsky et al. Single transverse-spin asymmetry in very forward and very backward neutral particle production for polarized proton collisions at $\sqrt{s} = 200$ GeV. *Phys. Lett.*, B650:325–330, 2007.

[68] M. Togawa et al. Phenix local polarimeter analysis for RUN5 pp data. *PHENIX Analysis Note*, 462:1, 2005.

[69] G. G. Ohlsen and P. W. Keaton. Techniques for measurement of spin-1/2 and spin-1 polarization analyzing tensors. *Nucl. Instrum. Meth.*, 109:41–59, 1973. doi: 10.1016/0029-554X(73)90450-3.

[70] A. Adare et al. Inclusive cross section and double helicity asymmetry for π^0 production in $p + p$ collisions at $\sqrt{s}$=200 GeV: Implications for the polarized gluon distribution in the proton. *Phys. Rev.*, D76:051106, 2007.

[71] A Bazilevsky, A. Deshpande, Y. Fukao, and O. Zaudtke. Results on double longitudinal spin asymmetry (A_{LL}) in π^0 production in polarized proton-proton collisions at $\sqrt{s}$=200 GeV from Run-3 (for PPG031). *PHENIX Analysis Note*, 225:1, 2003.

[72] S. S. Adler et al. Nuclear effects on hadron production in d + Au and p + p collisions at $sqrts_{NN} = 200$ GeV. *Phys. Rev.*, C74:024904, 2006.

[73] A. Adare et al. Measurement of high-p_T single electrons from heavy-flavor decays in $p + p$ collisions at $\sqrt{s} = 200$ GeV. *Phys. Rev. Lett.*, 97: 252002, 2006. doi: 10.1103/PhysRevLett.97.252002.

[74] J. Jia and B. Cole. R_{cp} for charged high p_T pions in $d - Au$ collisions at $\sqrt{s_{NN}} = 200$ GeV. *PHENIX Analysis Note*, 311:1, 2004.

[75] A. Mukherjee, M. Stratmann, and W. Vogelsang. Next-to-leading order QCD corrections to single-inclusive hadron production in transversely

polarized p p and anti-p p collisions. *Phys. Rev.*, D72:034011, 2005. doi: 10.1103/PhysRevD.72.034011.

[76] J. Soffer. Positivity constraints for spin dependent parton distributions. *Phys. Rev. Lett.*, 74:1292–1294, 1995.

[77] B. A. Kniehl, G. Kramer, and B. Potter. Fragmentation functions for pions, kaons, and protons at next-to-leading order. *Nucl. Phys.*, B582: 514–536, 2000. doi: 10.1016/S0550-3213(00)00303-5.

[78] S. S. Adler et al. Mid-rapidity direct-photon production in $p+p$ collisions at $\sqrt{s} = 200$ GeV. *Phys. Rev.*, D71:071102, 2005.

[79] B. I. Abelev et al. Longitudinal double-spin asymmetry and cross section for inclusive jet production in polarized proton collisions at $\sqrt{s} = 200$ GeV. *Phys. Rev. Lett.*, 97:252001, 2006. doi: 10.1103/PhysRevLett.97.252001.

[80] S. J. Brodsky, M. Burkardt, and I. Schmidt. Perturbative QCD constraints on the shape of polarized quark and gluon distributions. *Nucl. Phys.*, B441:197–214, 1995. doi: 10.1016/0550-3213(95)00009-H.

[81] Richard D. Ball, Stefano Forte, and Giovanni Ridolfi. A next-to-leading determination of the singlet axial charge and the polarized gluon content of the nucleon. *Phys. Lett.*, B378:255–266, 1996. doi: 10.1016/0370-2693(96)00376-0.

[82] B. Jager, M. Stratmann, and W. Vogelsang. Single-inclusive jet production in polarized p p collisions at O($alpha_s^3$). *Phys. Rev.*, D70:034010, 2004.

[83] M. Stratmann. Lectures at the RIKEN Spin Summer School, July, 2007. http://ribf.riken.jp/spinfest/2007/lecture/stratmann_wako07-3.pdf.

[84] B. Adeva et al. A next-to-leading order QCD analysis of the spin structure function g1. *Phys. Rev.*, D58:112002, 1998. doi: 10.1103/PhysRevD.58.112002.

[85] A. Vogt. Efficient evolution of unpolarized and polarized parton distributions with QCD-PEGASUS. *Comput. Phys. Commun.*, 170:65–92, 2005. doi: 10.1016/j.cpc.2005.03.103.

[86] D. W. Duke and J. F. Owens. q^2 dependent parametrizations of parton distribution functions. *Phys. Rev.*, D30:49–54, 1984. doi: 10.1103/PhysRevD.30.49.

[87] M. Gluck, E. Reya, and A. Vogt. Dynamical parton distributions of the proton and small x physics. *Z. Phys.*, C67:433–448, 1995. doi: 10.1007/BF01624586.

[88] M. Hirai, S. Kumano, and N. Saito. Determination of polarized parton distribution functions and their uncertainties. *Phys. Rev.*, D69:054021, 2004.

[89] D. de Florian, G. A. Navarro, and R. Sassot. Sea quark and gluon polarization in the nucleon at NLO accuracy. *Phys. Rev.*, D71:094018, 2005.

[90] S. Kretzer. Fragmentation functions from flavour-inclusive and flavour-tagged e^+e^- annihilations. *Phys. Rev.*, D62:054001, 2000.

[91] M. Hirai, S. Kumano, and N. Saito. Determination of polarized parton distribution functions with recent data on polarization asymmetries. *Phys. Rev.*, D74:014015, 2006. doi: 10.1103/PhysRevD.74.014015.

[92] K. Boyle. Neutral pion double longitudinal spin asymmetry in proton proton collisions at $\sqrt{s}$ = 200 GeV using the PHENIX detector. *AIP Conf. Proc.*, 842:351–353, 2006.

[93] D. de Florian, R. Sassot, M. Stratmann, and W. Vogelsang. Global analysis of helicity parton densities and their uncertainties. 2008.

[94] B. I. Abelev et al. Longitudinal double-spin asymmetry for inclusive jet production in p+p collisions at $\sqrt{s}$=200 GeV. 2007.

[95] K. Boyle. Neutral pion double longitudinal spin asymmetry in proton proton collisions at $\sqrt{s}$ = 200 GeV using the PHENIX detector. *Talk at the 2007 RHIC & AGS Users' Meeting*, BNL, June 2007.

[96] K. Aoki. Double helicity asymmetry of inclusive π^0 production in polarized pp collisions at $\sqrt{s}$ = 62.4 GeV. *AIP Conf. Proc.*, 915:339–342, 2007. doi: 10.1063/1.2750791.

[97] Abhay Deshpande, Richard Milner, Raju Venugopalan, and Werner Vogelsang. Study of the fundamental structure of matter with an electron ion collider. *Ann. Rev. Nucl. Part. Sci.*, 55:165–228, 2005.

[98] A. D. Martin, R. G. Roberts, W. J. Stirling, and R. S. Thorne. Uncertainties of predictions from parton distributions. i: Experimental errors. *Eur. Phys. J.*, C28:455–473, 2003.

[99] M. Glück, E. Reya, M. Stratmann, and W. Vogelsang. Models for the polarized parton distributions of the nucleon. *Phys. Rev.*, D63:094005, 2001.

[100] M. Gluck, E. Reya, and A. Vogt. Dynamical parton distributions revisited. *Eur. Phys. J.*, C5:461–470, 1998.

[101] W. Vogelsang, April 2008. Private communication.

[102] J. Bluemlein and H. Bottcher. QCD analysis of polarized deep inelastic scattering data and parton distributions. *Nucl. Phys.*, B636:225–263, 2002.

[103] Elliot Leader, Aleksander V. Sidorov, and Dimiter B. Stamenov. Longitudinal polarized parton densities updated. *Phys. Rev.*, D73:034023, 2006.

[104] Alan D. Martin, R. G. Roberts, W. James Stirling, and R. S. Thorne. Parton distributions and the LHC: W and Z production. *Eur. Phys. J.*, C14:133–145, 2000.

[105] T. Gehrmann and W. James Stirling. Polarized parton distributions in the nucleon. *Phys. Rev.*, D53:6100–6109, 1996.